Band Engineering in Thermoelectric Materials Using Optical, Electronic, and Ab-Initio Computed Properties

Thesis by

Zachary M. Gibbs

In Partial Fulfillment of the Requirements

For the Degree of

Doctor of Philosophy

California Institute of Technology

Pasadena, California

2015

(Defense Date: May 11, 2015)

Acknowledgements

I would like to acknowledge many people who helped me along the way during this PhD thesis. First, I would like to thank my lovely wife Gina for loving and supporting me during my time at Caltech. I would also like to thank my Australian cattle dog, Aspen, for understanding that I could not play fetch because I had to do more thermoelectrics research. I would like to thank my family for their support (even from afar) during my PhD.

Professionally, I have many colleagues to thank and acknowledge. Of course the entirety of the Snyder group has been wonderful over the years. I would like to especially thank Yanzhong Pei and Heng Wang (for mentoring me through the band engineering concepts); Nick Heinz, Tristan Day, Wolfgang Zeier, and Hyun Sik Kim (for providing endless entertainment at lunch time); and collaborators and coauthors Yinglu Tang, Hyun Sik Kim, Min Zhou, Wolfgang Zeier, and Jennifer Schmitt. I would like to acknowledge Jeff Snyder for always being willing to talk about a project and being an overall wonderful adviser. I would like to acknowledge the Molecular Materials Research Center (MMRC) in the Beckman Institute at Caltech for allowing use of their optical measurement systems free-of-charge. I would like to acknowledge several collaborators who performed DFT calculations in this thesis including Hyoungchul Kim, Massoud Kaviany (University of Michigan), and Luis Agapito (University of North Texas). I would also like to acknowledge funding and support from the Materials Project; I would like to especially acknowledge useful discussions with Geoffroy Hautier, Anubhav Jain, and Hong Zhu.

Abstract

Thermoelectric materials have demanded a significant amount of attention for their ability to convert waste heat directly to electricity with no moving parts. A resurgence in thermoelectrics research has led to significant enhancements in the thermoelectric figure of merit, zT, even for materials that were already well studied. This thesis approaches thermoelectric zT optimization by developing a detailed understanding of the electronic structure using a combination of electronic/thermoelectric properties, optical properties, and ab-initio computed electronic band structures. This is accomplished by applying these techniques to three important classes of thermoelectric materials: IV-VI materials (the lead chalcogenides), Half-Heusler's (XNiSn where X=Zr, Ti, Hf), and $CoSb_3$ skutterudites.

In the IV-VI materials (PbTe, PbSe, PbS) I present a shifting temperature-dependent optical absorption edge which correlates well to the computed *ab-initio* molecular dynamics result. Contrary to prior literature that suggests convergence of the primary and secondary bands at 400 K, I suggest a higher convergence temperature of 700, 900, and 1000 K for PbTe, PbSe, and PbS, respectively. This finding can help guide electronic properties modelling by providing a concrete value for the band gap and valence band offset as a function of temperature.

Another important thermoelectric material, ZrNiSn (half-Heusler), is analyzed for both its optical and electronic properties; transport properties indicate a largely different band gap depending on whether the material is doped n-type or p-type. By measuring and reporting the optical band gap value of 0.13 eV, I resolve the discrepancy in the gap calculated from electronic properties (maximum Seebeck and resistivity) by correlating these estimates to the electron-to-hole weighted mobility ratio, A, in narrow gap materials (A is found to be approximately 5.0 in ZrNiSn).

I also show that $CoSb_3$ contains multiple conduction bands that contribute to the thermoelectric properties. These bands are also observed to shift towards each other with temperature, eventually reaching effective convergence for $T>500$ K. This implies that the electronic structure in $CoSb_3$ is critically important (and possibly engineerable) with regards to its high thermoelectric figure of merit.

Contents

List of Figures

List of Tables

List of Symbols and Notation

Fundamental Constants

- e – Fundamental electron charge
- $\hbar$ – Planck's constant (h) divided by 2π
- m_e – Electron rest mass
- k_B – Boltzmann constant
- c – Speed of light

Transport Properties

- V – Voltage
- R– Resistance
- I – Electric Current
- V_H – Hall voltage
- B – Magnetic Field
- n – Carrier concentration (electrons)
- p – Carrier concentration (holes)
- R_H – Hall coefficient
- r_H – Hall factor (n/n_H)
- n_H – Carrier concentration ($\frac{1}{R_H e}$)
- σ – Electrical conductivity ($ne\mu$)
- ρ – Electrical resistivity ($1/\sigma$)
- μ – Carrier drift mobility
- μ_H – Hall Mobility (σR_H)
- τ – Scattering time
- λ – Scattering coefficient (exponent)
- v – Drift velocity of electrons
- S – Seebeck coefficient
- $|S|$ – Thermopower (magnitude of S)
- L – Lorenz number
- κ – Total thermal conductivity
- κ_e – Electronic thermal conductivity ($L\sigma T + \kappa_{bipolar}$)
- $\kappa_{bipolar}$ – Bipolar thermal conductivity
- C_p – Heat capacity (constant pressure)
- d – Density
- D – Thermal diffusivity
- zT –Thermoelectric figure of merit
- $S^2\sigma$ –Thermoelectric power factor
- L^* – Sample dimension

- A^* – Sample cross sectional area
- t – Sample thickness
- α_L – Linear thermal expansion coefficient
- K_B – Bulk modulus

Band Engineering

- v_l – Longitudinal speed of sound
- E_{def} – Deformation potential
- C_l – Average longitudinal elastic moduli ($v_l^2 d$)
- τ_0 – Scattering time prefactor
- μ_0 – Mobility prefactor ($e\tau_0/m_c^*$)
- n_0 – Carrier concentration prefactor
- σ_0 – Conductivity prefactor ($n_0 e \mu_0$)
- m^* – Effective mass
- m_c^* – Conductivity effective mass
- m_d^* – Density of states effective mass
- m_b^* – Single valley effective mass
- m_P^* – Effective mass obtained from electronic momentum
- m_S^* – Effective mass obtained from Seebeck coefficient (single parabolic band)
- $m_\parallel^*$ – Effective mass along the longitudinal ellipsoid direction
- $m_\perp^*$ – Effective mass along the transverse ellipsoid direction
- $\mu_0 m_S^{*3/2}$ – Weighted mobility
- B– Thermoelectric quality factor ($\frac{\mu_0 m_S^{*\frac{3}{2}}}{\kappa_L}$)
- A – Majority-to-minority carrier weighted mobility ratio
- N_v – Valley degeneracy
- N_v^* – Effective valley degeneracy
- K – Ellipsoidal mass anisotropy parameter ($\frac{m_\parallel^*}{m_\perp^*}$)
- K^* – Effective anisotropy parameter
- f – Fermi distribution function
- F_j – Fermi integral of order j
- ${}^nF_l^m$ – Generalized Fermi integral
- E_g – Band gap
- $E_{g,thermal}$ – Thermal band gap
- ΔE – Band offset
- T_{cvg} – Band convergence temperature
- β – Dimensionless Kane band parameter ($\approx k_B T/E_g$)
- m_0^* – Band edge effective mass (Kane bands)
- P– Kane band interaction matrix element

- $D(E)$ – Density of states
- N_A – Number of acceptors
- N_d – Number of donors
- s_i – Sign of the charge carriers in the i^{th} band
- E – Electron energy
- ϵ – Dimensionless energy (E/k_BT)
- ξ – Chemical potential
- E_F – Fermi level
- η – Dimensionless chemical potential (ξ/k_BT)
- A_k – Fermi surface area
- V_k – Volume enclosed by the Fermi surface

Optical Properties

- $F(R)$ – Kubelka Munk Function, equivalently: $\frac{\alpha}{\widetilde{K}}$
- α – Absorption coefficient
- $\widetilde{K}$ – Scattering coefficient
- ω – Photon frequency
- $\hbar\omega$ – Photon energy
- ϵ_c – Complex dielectric constant ($\epsilon_1 + i\epsilon_2$)
- ϵ_1 – Real dielectric constant
- ϵ_2 – Imaginary dielectric constant
- n_r – Real part of the refractive index
- κ_r – Imaginary part of the refractive index
- $\boldsymbol{E}$ – Electric field
- ω_p – Plasma frequency
- ϵ_∞ – Screening dielectric constant
- $E_{g,opt}$ – Optical band gap
- Δ_{RN} – Band gap renormalization

Chapter 1: Introduction

1.1 - Thermoelectric Motivation and Applications

In a world where renewable energy is becoming an increasingly hot topic, new and different strategies have been investigated for producing it. In addition to approaches such as wind and solar power, several other approaches that focus primarily on increasing energy utilization efficiency or recovering waste heat are also being pursued. Thermoelectric materials have received a considerable amount of attention in terms of waste-heat recovery for a wide range of applications including automobiles (General Motors [1] and BMW [2]), ships and boats [3, 4], industrial processes [5], remote sensing (oil and gas [6], nuclear [7]), thermonuclear power for space missions [8, 9], or as cathodic protection devices to reduce corrosion in oil and gas pipelines [10]. Another useful application of thermoelectric materials is for solid-state refrigeration, which is useful for applications where vibrations involved with conventional refrigeration techniques are detrimental (medicinal storage, wine refrigerators, etc.) or where precisely controlled spot-cooling (or heating) is desired. Because of the broad range of potential applications and wide academic and scientific impact (in a range of fields including: thermal/electronic transport processes, metallurgical techniques, solid-state chemistry, and others), thermoelectric materials have received a significant amount of interest over the last 50-60 years.

The fundamental process responsible for thermoelectric power generation (or efficiency) is known as the Seebeck effect. Metals or doped semiconductors contain free charge carriers and produce the Seebeck effect in the presence of a temperature gradient. If we consider these carriers as a gas of charged particles, the gas will be most dense at the cold side of the material (Figure 1-1). At equilibrium, an electric field (voltage) will be generated to balance the chemical, diffusive driving force provided by the temperature difference. The Seebeck coefficient can be written as the ratio of the measured voltage across the sample to the temperature difference, $S \approx -\frac{\Delta V}{\Delta T}$. The Seebeck effect is also often used in thermocouples for precise temperature measurements. While Figure 1-1 shows the effect for a single material, two unlike-materials (for example, chromel and alumel in a K-type thermocouple) coupled together will produce a voltage that depends very precisely on the temperature at their union. However, unlike precise thermocouple measurement instrumentation where the value of the Seebeck does not need to be particularly large, thermoelectric devices for waste heat recovery applications prefer a specific combination of material parameters (including large Seebeck coefficient).

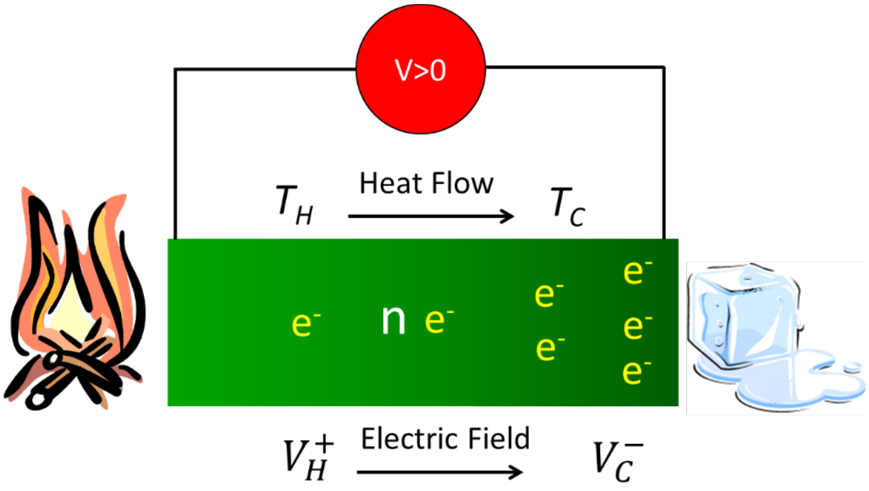

Figure 1-1: Schematic diagram of the Seebeck effect in which charge carriers diffuse towards the cold end of a heated material—the resulting voltage that develops determines the Seebeck coefficient: $S = -\frac{\Delta V}{\Delta T}$.

Thermoelectric efficiency is determined by the thermoelectric figure of merit: $zT = \frac{S^2\sigma}{\kappa}T$, where *S* is the Seebeck coefficient, σ is the electrical conductivity, κ is the thermal conductivity, and *T* is the temperature of operation. This relation is derived by considering all of the modes of heat and current transfer through a theoretical device. Of course, a high Seebeck coefficient is preferred since this directly leads to a higher voltage across the device; good electrical conductivity is desired in order to minimize resistive losses due to Joule heating (which generates heat, reducing the overall ΔT across the device), and a low thermal conductivity is necessary to allow the largest possible temperature gradient. Current state-of-the-art thermoelectric materials that are used for waste heat recovery have *zT* values near 1.0, which corresponds to less than 12% energy conversion efficiency (for high temperature power generation) once devices losses are taken into account [6]. An average *zT* of 1.25 would enable substantial waste-heat harvesting and up to a 10% fuel reduction in the case of automotive applications [6]. Since the early 1990s, a wave of new nanotechnology related research has ushered in a new era for thermoelectric materials as well [11]; nanoscale features had been theorized to provide revolutionary advances beyond conventional bulk solids by either lowering thermal conductivity through modes of additional phonon-scattering or by altering the electronic structure which is known to benefit from low-dimensional features [11]. While nanoscale features have led to advances in some areas [12-14], the renewed interest in thermoelectric materials has also revitalized research efforts towards developing advanced bulk materials through conventional solid-state chemistry and physics techniques. This thesis will highlight several examples where traditional semiconductor physics including optical, electronic, and *ab-initio* computed properties are utilized in common thermoelectric materials to guide new strategies for enhancing *zT* using “Band Engineering.”

1.2 - Thermoelectric Materials, Band Engineering, and Summary of Work

Even though the scientific community’s renewed interest in thermoelectrics may have been sparked by the promise of benefits due to nanoscale features, a large number of recent advanced material discoveries involve bulk materials and alloys which owe their extraordinary performance to superior electronic properties. These discoveries can be explained in the context of semiconductor transport physics and doping without nanoscale features. The “Band Engineering” concept uses a variety of strategies for optimizing *zT* including either carrier concentration tuning or altering the electronic structure using alloying in order to utilize additional electronic states through band convergence. Here, I will apply band engineering techniques to resolve discrepancies observed in the literature regarding the electronic band structure parameters (band gap, secondary band offset, effective masses, etc.) in a variety of thermoelectric materials, including IV-VI materials and their alloys (Chapter 3 and 4), ZrNiSn half Heusler's (Chapter 5), and $CoSb_3$ skutterudite and A_5M_2Sb6 Zintl materials (Chapter 6). This is accomplished with a combination of optical absorption measurements (absorption edge), electronic/thermal/thermoelectric transport properties measurement (and corresponding semi-empirical modelling), and *ab-initio* electronic band structure calculations (traditional density functional theory, DFT, *ab-initio* molecular dynamics, AIMD, and numerical solutions to the Boltzmann transport equation, Boltztrap). Furthermore, in the context of band engineering, I develop theoretical techniques to provide a framework for analyzing DFT-computed thermoelectric transport properties (Chapter 7). Work in this thesis provides insight into the electronic band structure contributions to the thermoelectric properties for a few systems of materials of great interest to the thermoelectrics community, namely IV-VI materials, half-Heuslers, and skutterudites.

Until recently, PbTe and the IV-VI materials were thought to have a mediocre peak *zT* with values lower than 1.0; however, in the last five years many works have shown some of the highest recorded *zT* values in its alloys, approaching and exceeding 2.0 [14-21]. These recent advancements are attributed both to improvement in high temperature thermal conductivity measurements (through development of the new standard for these measurements: the laser flash technique discussed in Chapter 2) and electronic band structure engineering by doping and alloying these materials with other elements. This wave of new work on the IV-VI materials has spurred additional discussion of their band structures (particularly as a function of temperature); Chapter 4 provides a series of optical measurements, electronic properties measurements, and AIMD calculations which provide new insight into the temperature at which the primary and secondary valence bands converge (which is commonly cited as the reason for the superior performance of PbTe and its alloys).

Another family of materials, the half Heusler's with the general formula XYZ, where X=Zr, Ti, Hf, ..., Y=Ni, Co, …, and Z=Sn, Sb, …, have also been shown to be good thermoelectric materials. Half Heuslers are often favored over other materials because of their ability to attain high zT (~1.0) without toxic or rare elements [22, 23]. In Chapter 5 of this thesis, I use experimentally measured optical and electronic properties in ZrNiSn to determine both the value of the band gap ($E_g \approx 0.13\ eV$) and the electron-to-hole weighted mobility ratio ($A \approx 5$). The low hole mobility agrees with some recent observations that the valence band may be composed of in-gap states resulting from interstitial Ni atoms, which is not captured in conventional DFT calculations. Further, A=5 helps to explain the good performance of n-type ZrNiSn at high temperatures despite its narrow band gap. I also develop theory which relates the maximum in the temperature-dependent thermopower to the band gap for low gap materials with electron-to-hole weighted mobility ratios not equal to 1.0.

Another popular bulk material is $CoSb_3$, which has proven itself a leader in commercial applications for waste heat recovery. By filling voids in the crystal structure with dopant atoms (Yb, La, In, etc.), simultaneous doping and phonon scattering (sometimes attributed to rattling of the filler atoms) leads to high *zT*s greater than 1.0 around 400°C. Chapter 6 of this thesis thoroughly investigates this material as a multiple-band electronic conductor. Using electronic transport measurements in a doping study, I show that the thermoelectric properties are not explainable using single band properties (even if that band is a non-parabolic Kane-type band). This is supported by the observation of multiple absorption edges observed in optical measurements. The thermoelectrics community generally attributes high *zT* in these materials to the reduction in thermal conductivity; however, results from this thesis indicate that it also has a superb (and possibly engineerable) electronic structure that is at least partially responsible for its high *zT*.

These thermoelectric material systems are quite important to the thermoelectric community. By characterizing their electronic structure, we can pave the way for band engineering and further improvement of their properties. The remainder of this introductory chapter will detail some of the fundamental concepts that link electronic and thermoelectric transport properties to a material's underlying electronic structure.

1.3 - Doping and zT Optimization

Extrinsic doping involves the substitution of impurity atoms, which contain a different charge state than the native lattice. In order to maintain charge neutrality, additional holes or electrons are added, creating a p-type or n-type material, respectively. In thermoelectric materials, doping can lead to drastic changes in the properties and is therefore critical for optimizing zT. Figure 1-2 shows the dependence of zT and the other thermoelectric parameters on carrier concentration by assuming a single parabolic band and acoustic phonon scattering [24]. As the carrier concentration is lowered, say in the case of an insulator, the Seebeck coefficient becomes quite high, but the electrical conductivity is lowered significantly, resulting in poor zT. For high carrier concentration (as in a metal), the electrical conductivity is high, but the Seebeck is lower. For this reason, zT and power factor ($S^2\sigma$) are usually optimized in the 10^{19}-10^{20} cm^{-3} range (usually described as a heavily doped semiconductor). In the absence of extrinsic doping, the doping level for a given material is set by its intrinsic defect level, which can depend upon sample preparation procedures (annealing temperature, quench vs. slow cool) and can be quite sensitive to sample stoichiometry and defect formation energetics. Doping (intrinsic or extrinsic) often serves as a good first check to determine whether a given material's properties can be further optimized.

Using the single parabolic band (SPB) model [24] (Figure 1-2), it is straightforward to obtain information like the effective mass (m^*), deformation potential (E_{def}, which determines the strength of electron scattering by acoustic phonons), and lattice thermal conductivity (κ_L); the combination of these parameters can be used to determine the maximum attainable *zT* (and the carrier concentration at which it occurs). The SPB model is a useful tool because it is easily generated from a small amount of experimental data, and it can be extremely useful when determining a *zT* optimization strategy for a new material.

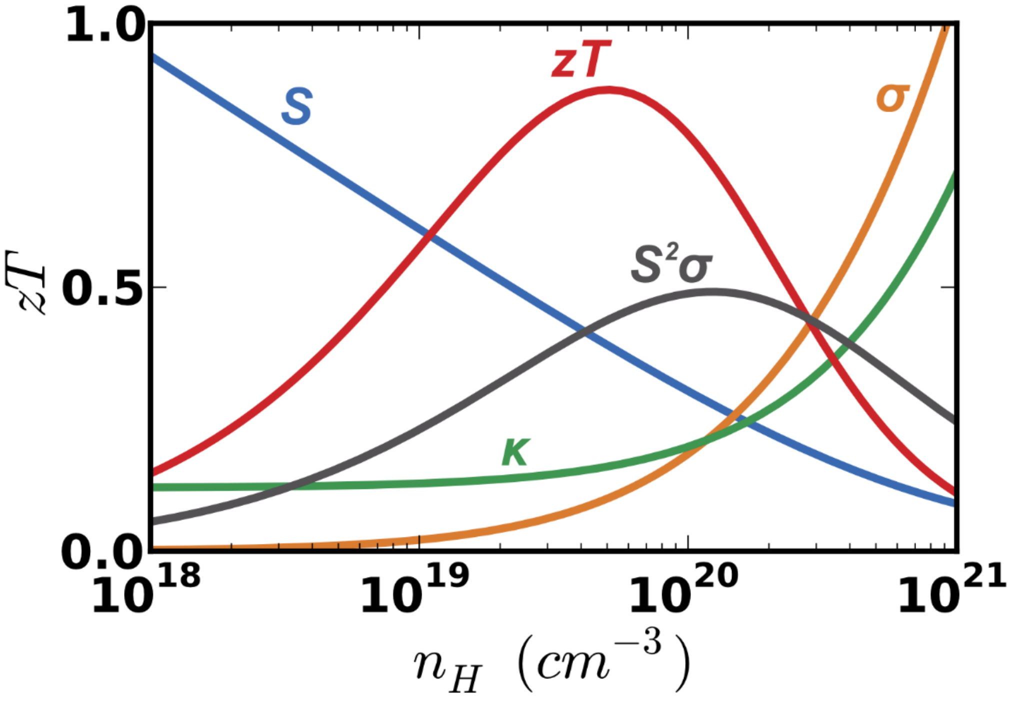

Figure 1-2: Carrier concentration dependence of zT and other thermoelectric properties.

1.4 - Multiple Band Phenomena in Thermoelectric Materials

While the single parabolic band works well for a variety of systems, many of the best thermoelectric materials contain multiple electronic bands. Multi-valence band phenomena are believed to be responsible for the superior *zT*s in several systems, including PbTe [15-18], PbSe [25], Mg_2Si [26], and others. Each band can be treated as a parallel circuit; their electrical conductivities add, but each band maintains its own high Seebeck coefficient. This leads to a greatly enhanced performance, particularly when multiple bands are occupied and at similar energy levels (converged bands lead to the largest enhancements). One of the most successful examples where converging electronic bands are beneficial to thermoelectric performance is in

PbTe. PbTe has two valence bands offset by ~0.15 eV (ΔE) at 300 K as shown in Figure 1-3. The band positions are thought to change as a function of temperature, resulting in band convergence at around 400 K according to Tauber et al. [27] However, work shown in this thesis disagrees with this finding, showing an optical band gap that continues to increase with temperature until the highest measured temperature of 673K, which is supported by AIMD calculations. Alloying has also been shown to improve the thermoelectric properties for lead chalcogenide materials; the improvement is usually attributed to both reduction in the lattice thermal conductivity due to point defect scattering of phonons and an $L-\Sigma$ band offset (ΔE) reduction (in the case of alkaline earth alloying on the lead site). I show one case in particular where significantly improved properties are attained using alloys of the lead-chalcogenide materials (PbSe/SrSe- Chapter 4.3, $zT_{max} \approx 1.5$). This thesis includes several other examples of multiple band behavior.

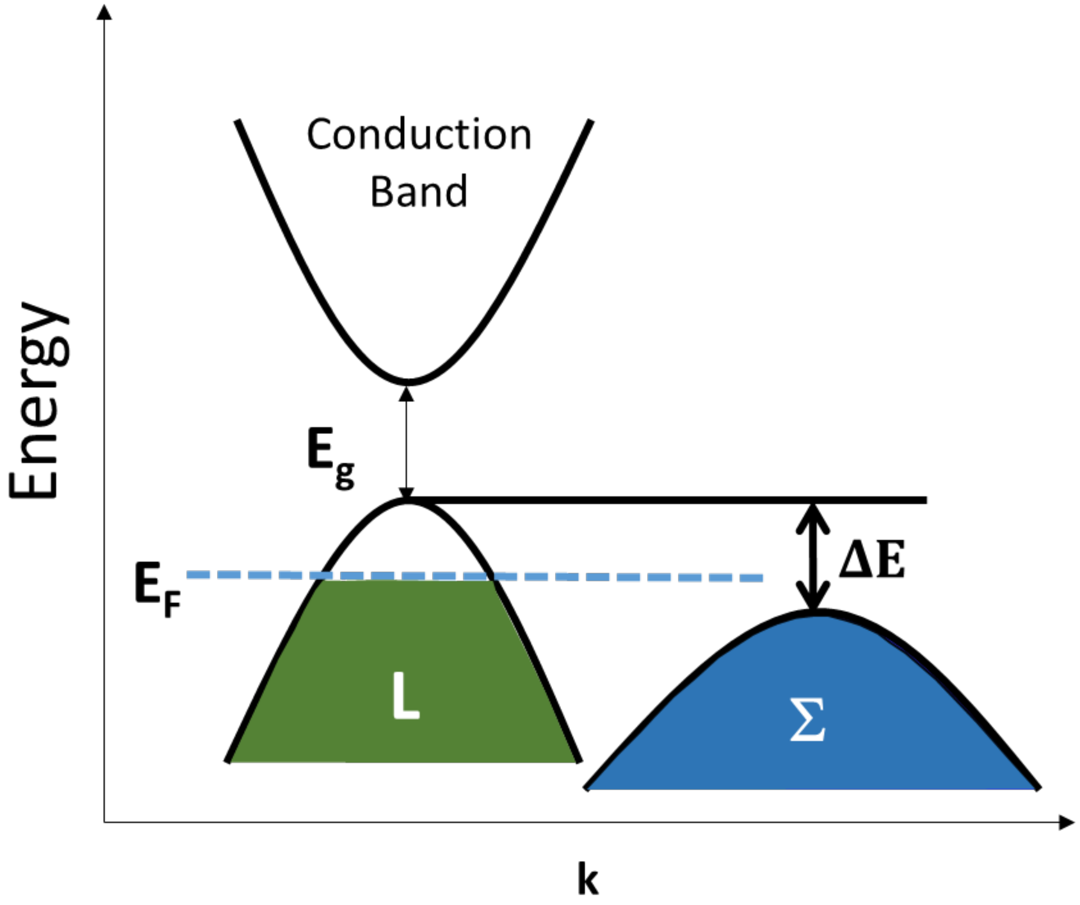

Figure 1-3: Near-edge band structure in the lead chalcogenides indicating multi-band behavior for p-type.

Besides the lead chalcogenides, Chapter 6 includes optical, electronic, and *ab-initio* calculation evidence of multi band behavior in the conduction band of $CoSb_3$. High temperature electronic and optical properties show band convergence, which is likely extraordinary thermoelectric performance in Yb filled $CoSb_3$. Otherwise, multi-band behavior is also evident in the optical and transport properties of two other systems: the 5-2-6 family of Zintl compounds, $Ca_5In_2Sb_6$ (Chapter 6.3), and in SnTe (Chapter 4.4). By understanding the nature of the band structure, we open the door for future band engineering studies through isoelectronic alloying of these systems, which can lead to large zT enhancements.

1.5 - Band Gap in Thermoelectric Materials

Because many thermoelectric materials are narrow gap semiconductors (E_g<0.5 eV), their high temperature properties are often subject to strong bipolar effects. Bipolar effects occur in doped semiconductors when minority carrier states become populated and their conductivities become comparable in magnitude to the majority carrier. Because these carriers have opposite signs, the temperature dependent thermopower (defined as the magnitude of the Seebeck coefficient, $|S|$) increases to a maximum and then decreases (Figure 1-4a). This is accompanied by an increase in electrical conductivity (and the electronic contribution to the total thermal conductivity, κ_{total}, Figure 1-4b) due to the presence of both electrons and holes. The Goldsmid-Sharp band gap allows us to relate the maximum in the temperature dependent thermopower to the band gap of a semiconductor: $E_g = 2e|S|_{max}T_{max}$. In terms of thermoelectric performance, this maximum in the thermopower often leads to a corresponding maximum in the zT. Because the peak zT is the metric by which most thermoelectric materials are compared, understanding the value of the band gap and the onset of bipolar conduction is critical for optimizing the temperature dependent zT.

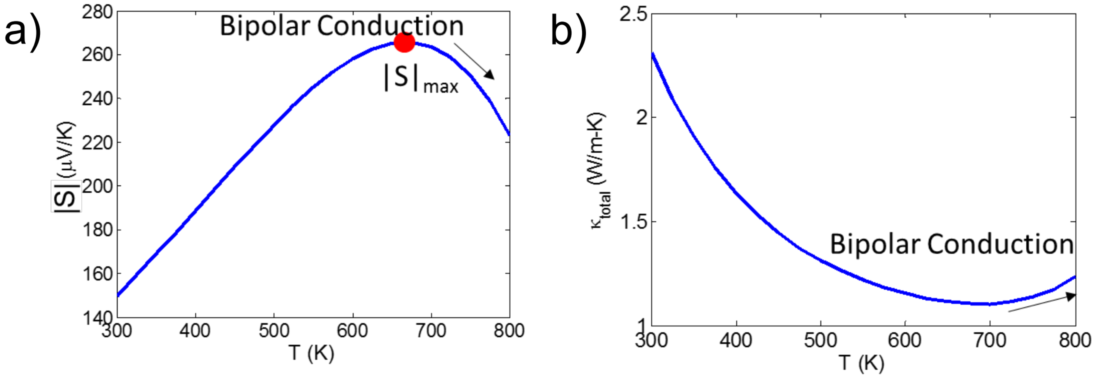

Figure 1-4: Bipolar conduction example in I-doped PbTe including a) Temperature dependent Seebeck coefficient and b) temperature dependent thermal conductivity [28].

Besides the Goldsmid-Sharp band gap, the temperature dependent resistivity can also be used to estimate the band gap for semiconductors in the intrinsic region of conductivity (low doping levels). The electrical resistivity is related to the temperature following $\sigma(T) = \sigma_0 \exp(-\frac{E_g}{2k_BT})$ where σ_0 is related to both the density of states and mobility for the material.

Other than transport measurements, optical measurements such as absorption edge, photoconductivity, and photoluminescence are the most direct methods of obtaining an estimate of the band gap. In optical absorption edge measurements, a sample is illuminated by light of different frequencies (which correspond to a photon energy: $E = \hbar\omega$) that can be absorbed by electrons in the valence band (Figure 1-5a). If $\hbar\omega$ is less than the band gap energy, no absorption is observed because there are no states within the band gap to excite the valence band electrons into. However, for photon energies equal to or larger than the band gap, we observe a rapid rise in the absorption coefficient (Figure 1-5b).

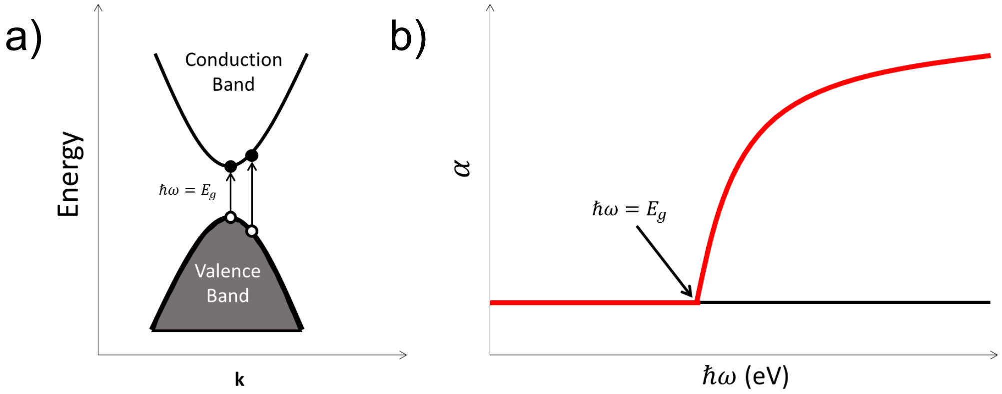

Figure 1-5: Optical absorption edge illustrating the illumination of the valence band by a photon with energy ($\hbar\omega$), which excited an electron to the conduction band if $\hbar\omega \geq E_g$.

Experimentally, the energy at which the absorption coefficient, α, begins to rise indicates the band gap energy. Usually, band gap obtained from optical measurements is understood to be more accurate (and more direct) than those obtained through electronic measurements, especially if E_g is temperature dependent. Chapter 3 of this thesis shows how sensitive optical measurements can be by investigating slight shifts in the optical absorption edge with small changes in doping level, known as the Burstein-Moss shift.

Because band gap is such an important parameter in thermoelectric materials, both in terms of bipolar conduction and band engineering strategies, estimates of the band gap are useful regardless of whether they come from electronic or optical results. Sources of discrepancies for the Goldsmid-Sharp (maximum thermopower) band gap are described in detail in Chapter 5. I show that the largest discrepancies in the computed value occurs for large electron-to-hole weighted mobility ratio (A) and narrow band gaps. In this thesis, a large difference in the Goldsmid-Sharp band gap for p-type and n-type ZrNiSn Half-Heusler thermoelectric materials is explained by invoking a weighted mobility ratio (A) of 5.0 (rather than 1.0, which is assumed in the derivation of Goldsmid-Sharp's $E_g = 2eS_{max}T_{max}$ formula). The theory is developed to extend this analysis to any general A-value or measured band gap using full Fermi statistics (which are useful for thermoelectric materials which contain narrow gaps).

1.6 - Band Engineering from *Ab-Initio* Calculations

Ab-initio calculations are a useful tool for mapping the electronic structure for a material. Because this thesis focuses on connecting measured electronic, thermoelectric, and optical properties to the electronic band structure, *ab-initio* electronic band structure calculations are a crucial tool for helping to explain the results. For example, Chapter 4 shows results regarding the temperature-dependent band gap in PbTe computed using AIMD calculations that mimic the effect of atomic vibrations (phonons) on the computed electronic band structure; coupled with thermal expansion of the lattice, we correlate these calculations to the measured optical results. In another example of *ab-initio* calculations, Chapter 6 shows an electronic band structure calculation and Fermi surface mapping for $CoSb_3$, which provide the insight needed to explain the two observed absorption edges that were measured optically. Another natural extension of *ab-initio* electronic structure calculations is to directly predict thermoelectric properties by solving the Boltzmann transport equation.

Boltztrap is a useful, open-source code that uses calculated band structures to generate Fermi-level dependent thermoelectric transport data which can be used to discover new compounds in a high-throughput sense [29, 30]. In Chapter 7 of this thesis I discuss the application of many of the band engineering strategies to Boltztrap calculations from the Material Project (materialsproject.org). I define a new, easily computed parameter known as the "Fermi surface complexity factor", $(N_v^* K^*)$ which is composed of both the effective valley degeneracy (N_v^*) and the effective anisotropy factor (K^*). N_v^* reflects the influences of multiple bands when they are near the Fermi level, while K^* is enhanced for complex Fermi surfaces (as observed in the valence bands of the III-V and IV-VI semiconductors). Further $(N_v^* K^*)$ improves upon existing Boltztrap results by bypassing the constant relaxation time approximation (CRTA) to provide a parameter (unlike Seebeck coefficient or power factor) that reflects the electronic structure directly, is proportional to the maximum attainable power factor, and does not depend on the observed scattering mechanism.

1.7 - Conclusions

In this thesis, I will focus on explaining the electronic band structure origin of the thermoelectric properties in the context of band engineering for three heavily studied groups of thermoelectric materials: IV-VI semiconductors (PbTe, PbSe, PbS, SnTe), ZrNiSn half Heuslers, and $CoSb_3$ skutterudites. I have utilized a variety of experimental (optical, electronic, and thermoelectric measurements) and theoretical (band engineering/models, *ab-initio* calculations) techniques to provide these insights, and I have characterized their results in the framework of existing physical models. I have developed theoretical models, as needed, to explain the large discrepancy in the computed Goldsmid-Sharp band gap for n-type and p-type ZrNiSn compounds, and I have generalized the findings to be useful for any arbitrary electron-to-hole weighted mobility ratio (*A*). Through a combination of experimental measurements and a thorough application of electron band/transport physics I provide a novel interpretation to the properties in these systems.

Chapter 2: Theoretical and Experimental Methods:

2.1 - Electronic/Thermal Transport Properties Measurement

Thermoelectric efficiency depends on the relevant transport properties: S, ρ, κ being the Seebeck coefficient, resistivity, and thermal conductivity, respectively. These properties are each measureable to give the thermoelectric figure of merit, *zT*. Measurements were performed on disc-shaped samples synthesized according to the techniques described in a later section.

2.1a - Electrical Resistivity/Conductivity and Hall Effect

The electrical resistance is a quantity that is simply measured with a multi-meter, but resistivity is an intrinsic material property that does not depend on the amount of material present. The traditional method of measuring resistivity is accomplished with a rectangular prism sample with known cross sectional area, *A*, as detailed in Figure 2-1a. Here, a known current, *I*, is passed through the sample through contacts at either end of the prism. The voltage, *V*, is measured by probes with a known distance between them, L^*, from which the resistance, *R,* can be estimated from Ohm's law: $R = \frac{V}{I}$. The resistivity, ρ, then is simply calculated using $\rho = \frac{RA^*}{L^*}$. This technique is preferred for samples which are either single crystals or ones with anisotropic properties. For polycrystalline or cubic samples, the Van Der Pauw method is a simpler way to obtain the resistivity(Figure 2-1b). Here, a known current is passed through two leads attached to a disc shaped sample with known thickness, *t*. The voltage is measured perpendicular to the current flow. In a second step, the current is flowed perpendicular to the first step's current, and the voltage is measured on the remaining two leads. The resistivity can be calculated using the Van der Pauw formula $e^{-\frac{\pi R_1 t}{\rho}} + e^{-\frac{\pi R_2 t}{\rho}} = 1$, where R_1 and R_2 are the measured resistances. In addition to measuring the resistivity for the sample, additional information can be obtained upon performing these measurements under a magnetic field. The Hall voltage can be measured by applying a magnetic field, *B*, perpendicular to the flowing current, *I*, in both the bar sample or in the Van der Pauw arrangement. The Hall voltage, V_H, can be measured perpendicular to both I and B, from which the carrier concentration can be estimated: $n_H = -\frac{IB}{teV_H}$. Once the number of carriers is known, the mobility (μ_H) of those carriers can also be expressed from the measured conductivity (inverse of resistivity): $\sigma = n_H e \mu_H$. While the simple measurement of the resistivity is all that is required for estimation of the thermoelectric performance (zT), the Hall carrier concentration and mobility provide much needed additional information about the underlying transport and charge carrier scattering mechanisms (also the sign of the Hall coefficient—$R_H = \frac{1}{n_H e}$—indicates the sign of the majority charge carrier).

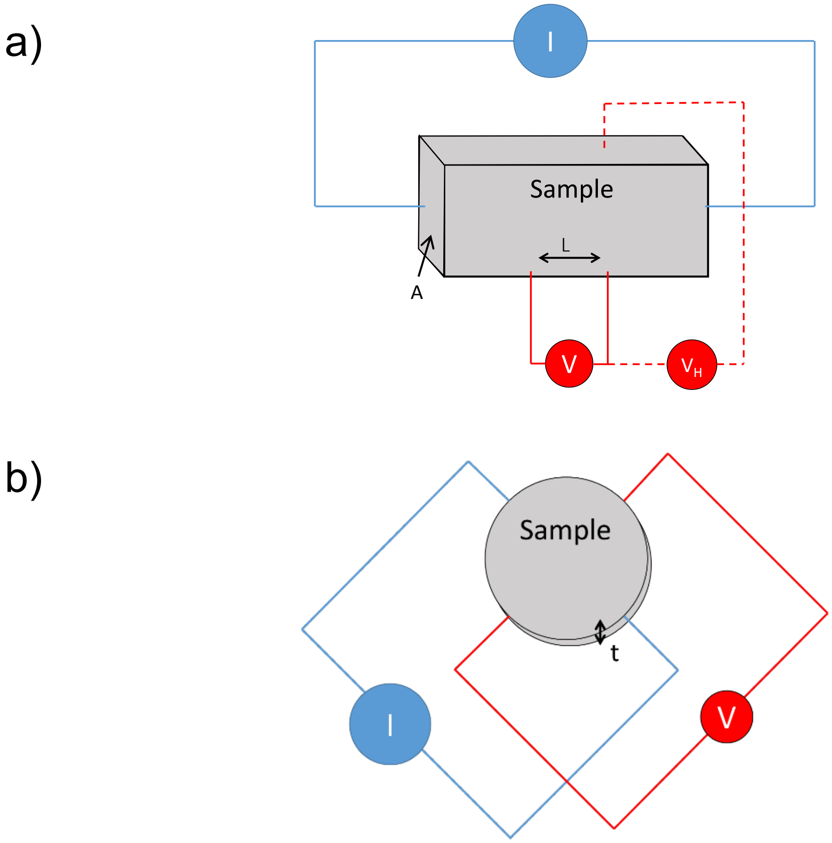

Figure 2-1: Electrical resistivity measurement schematic a) Conventional bar sample, b) disc-shaped sample via the Van Der Pauw method.

In this thesis, all of the measurements are performed on polycrystalline hot-pressed disc-shaped samples (synthesis procedure described in a later section) in the Van der Pauw arrangement in a ±2 T magnetic field using niobium pressure contacts [31]. The temperature is varied from room temperature up to ~500-600°C with the entire setup under high vacuum to avoid sample oxidation.

2.1b - Seebeck Coefficient

The Seebeck coefficient is measured in an instrument built and designed in the Snyder group lab as described in detail by Iwanga et al. [32] Essentially, two thermocouples are constructed by passing two unlike metal wires (chromel–niobium) through thin rods with 4 narrow holes. The wires are threaded through at the end of the ceramic rod (Figure 2-2) to form a single point of contact (which is pushed onto the sample using a spring); this contact allows for both voltage and temperature to be measured at the sample surface. Temperature is measured by measuring the voltage difference between the two thermocouple wires (which are on the same side of the sample) and comparing this voltage to a reference junction at a known temperature. The Seebeck voltage is found by measuring the voltage difference across the sample with two alike wire types, i.e., niobium only. The thermocouples and narrow ceramic rod (both top and bottom) are passed through a larger, heated ceramic block which also makes direct contact to the sample. The heating serves two purposes: first, the cold-finger effect through the thermocouple probe is reduced so that the temperature at the sample surface can be accurately deduced, and second, to maintain good thermal contact with the sample to establish the temperature gradient.

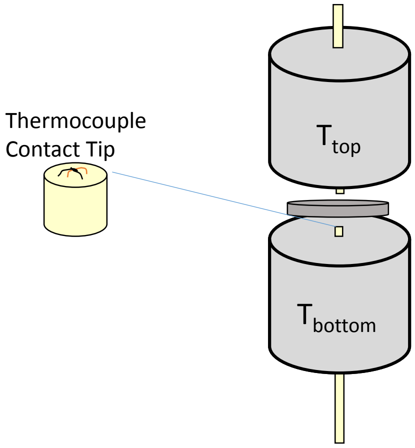

Figure 2-2: Schematic of the uniaxial Seebeck coefficient measurement setup.

During high temperature Seebeck coefficient measurements, rather than simply heating one side to a slightly higher temperature, taking a voltage measurement, and calculating the Seebeck coefficient as the voltage divided by the temperature difference, we perform temperature oscillation sequences. Here, the top and bottom temperatures are made to oscillate giving a range of different temperature differences within $\pm 10\,K$. The resulting voltages and temperature differences are plotted and a linear fit is performed to extract the Seebeck coefficient. We find that this method compensates for any systematic errors and gives accurate and reproducible results. Because the Seebeck coefficient is squared in the final estimate of *zT*, it is critical to reduce error in this measurement (a 10% error in Seebeck propagates to a 20% error in zT). Several “round robin” measurement cycles have been performed to determine what spread of properties measured on different instruments can be observed [33].

2.1c - Thermal Conductivity

Thermal conductivity has, of the three properties in *zT*, been one of the more difficult to accurately measure over the years. In the simplest case, the measurement is performed by passing a known power through a well-insulated sample and measuring the temperature at different points. Unfortunately, careful calibration is required to account for radiative losses, especially at high temperatures. Recently, the standard for thermal measurements in the thermoelectrics community has changed towards measuring the thermal diffusivity using the commercial Netzsch Laser Flash Apparatus (LFA 457). In this technique, a laser pulse slightly heats the sample surface inside of a furnace (which is heated to the desired measurement temperature). An optical detector carefully measures the time-dependent temperature increase and decrease at the sample surface. A model (Cowan Model with Pulse Correction) is used to correlate this time-dependence directly to the thermal diffusivity, $D = \frac{\kappa}{dC_p}$, where κ is the thermal conductivity, d is the sample density, and C_p is the heat capacity. The sample density is usually either measured directly (by estimating the volume from the sample thickness and diameter, and the mass by weighing with a scale), or it is estimated from the lattice parameter (which can be obtained from x-ray diffraction). All of the samples were coated with a thin layer of graphite to minimize emissivity errors. The heat capacity is sometimes estimated using the Dulong–Petit method (C_p = 3 k_B per atom) (as in the ZrNiSn case), or it is extracted from previous literature in the case of the IV-VI materials [34].

2.2 - Optical Properties Measurement and Analysis

Optical properties measurements have been used extensively in this work to provide information about the electronic states near the band gap. I do this by analyzing the optical absorption edge (as discussed in the introduction). In order to experimentally measure the frequency dependent absorption coefficient, several techniques can be used. In this thesis, I have chosen to focus on Diffuse Reflectance Infrared Fourier Transform Spectroscopy (DRIFTS), which is straightforward to perform and yields consistent results. In DRIFTS, a light source (black body radiator) illuminates a sample by way of an ellipsoidally shaped mirror (See Figure 2-3). The sample, which is usually a finely ground powder, diffusely reflects the light in all directions. The reflected light is collected with the ellipsoidal mirror and refocused onto a detector. Kubelka Munk theory derives a simple relation between the fraction of reflected light (R) and the absorption coefficient (α):

$$F(R) = \frac{\alpha}{\widetilde{K}} = \frac{(1-R)^2}{2R} \qquad \text{Equation 2-1}$$

where $\widetilde{K}$ is the scattering coefficient (an unknown parameter). Figure 2-3b shows some measurement results from a few relevant thermoelectric materials. I observe the correct ordering of the absorption edges in these materials: Bi_2Te_3 (~0.1 eV), PbSe (~0.27 eV), PbTe (~0.29 eV), and PbS (~0.42 eV), consistent with literature results.

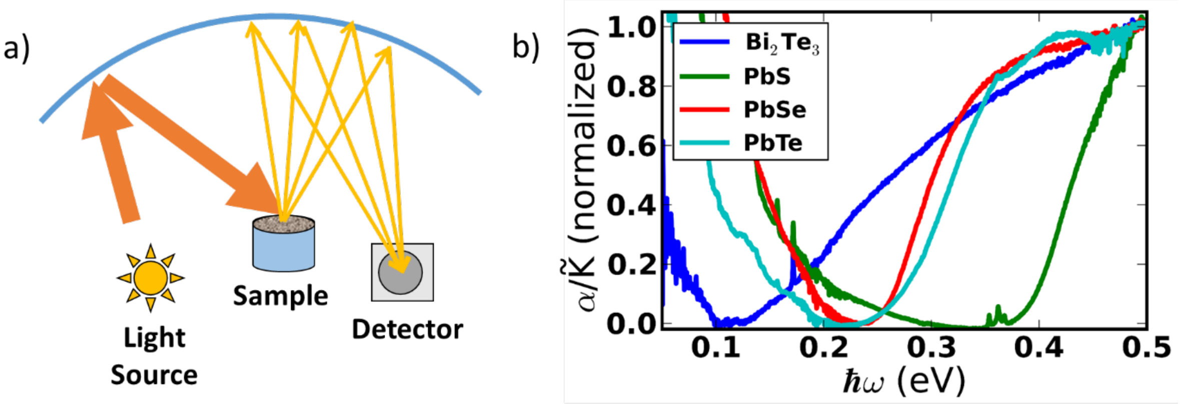

Figure 2-3: a) Schematic of the Diffuse Reflectance technique for measuring spectral absorption. b) Representative DRIFTS results for several relevant thermoelectric materials (at 300 K).

For particle sizes greater than the light wavelengths measured (20 - 2 μm), the scattering coefficient is understood to be approximately independent of frequency [35]. For all measurements in this thesis, I use a Nicolet 6700 FTIR Spectrometer with a deuterated triglycine sulfate (DTGS) detector equipped with a KBr beamsplitter. All samples were referenced to the provided alignment mirror, this was found to give nearly same results as when referenced to KBr powder without the added impurity features from KBr itself. This optical setup gave good spectral intensity for photon energies between ~0.05 eV up to 0.8 eV (with severely deteriorating spectral quality above ~0.6 eV). This range was ideal for studying most thermoelectric materials, which are usually narrow gap (E_g<0.5 eV) semiconductors. Several other methods for measuring the optical properties are available for materials with gaps in this range.

Many of the previous reports of optical band gap measurements on PbTe have used single crystal samples measured in transmission [27, 36-42]. Transmission experiments have a few disadvantages: first, optically transparent single crystals are often used to avoid internal reflections and light scattering at the grain boundaries, which are generally more difficult to prepare than polycrystalline powder samples. Second, the samples must be polished quite thin since the absorbance scales exponentially with the absorption coefficient and sample thickness through Beer's law, $A = \exp(\alpha t)$, where α is the absorption coefficient and t is the sample thickness. This limits the highest absorption coefficient that can be measured for a given sample thickness. Lastly, in cases where the samples were sufficiently thin (i.e., thin film samples with thicknesses on the order of the light wavelength), oscillations can result in the measured absorbance. These Fabry-Perot fringes are related to interference during internal reflection. While the effect can be mitigated through mathematical models, additional analysis is required.

Diffuse reflectance infrared Fourier transform spectroscopy (DRIFTS) was used exclusively in this work for optical measurements due to its ease of sample preparation and data analysis. Diffuse reflectance can be obtained in a thin sample layer of a ground powder. The measurement requires only a small amount of polycrystalline sample (200 mg or less). Because of the Fourier transform analysis, light at all frequencies can be measured simultaneously, greatly reducing sampling time relative to techniques which vary frequency using a diffraction grating. Relating the diffuse reflectance to sample absorption can be performed using the Kubelka-Munk function (Equation 2-1). Chapter 3 of this thesis shows that DRIFTS is very sensitive to small changes in the energy of direct transitions across the band gap due to progressively higher doping levels. With proper extrapolation the small shifts associated with doping can be shown and understood according to existing optical analysis techniques. Additionally, small, temperature-dependent shifts in the band structure can be detected using a high temperature stage (as shown in Chapter 4 and Chapter 6). A Praying Mantis attachment (Harrick) was used to collect the DRIFTS spectra. A high/low temperature stage, also from Harrick (CHC), was also used to vary the sample temperature from 120 to 673 K. Measurements were performed under an argon atmosphere after rough pumping and purging the sample chamber several times. Temperature dependent scans were referenced to either KBr standard samples taken at the same temperatures or a room temperature scan of the alignment mirror (although both references gave similar results).

2.2a - Optical Band Gap Extraction

The theory of optical transitions in semiconducting materials is discussed in detail in many references [43-45]. Typically, the method of extraction of the optical band gap depends on the type of transition observed. In the case of direct transitions, electron crystal momentum, *k*, is conserved. As is the case in PbTe, which has its valence band maximum and conduction band minimum at the same points in *k*-space (the *L*-point), direct transitions simply require the incoming photon to impart its energy on the valence-band electron. In this case, the absorption coefficient is proportional to the joint density of states, which in the case of two parabolic bands has the form:

$$\boldsymbol{\alpha\hbar\omega} \propto \left(\boldsymbol{\hbar\omega} - \boldsymbol{E_g}\right)^{\mathbf{1/2}} \qquad \text{Equation 2-2}$$

for $\hbar\omega > E_g$ according to the Tauc method [45, 46]. Other authors have plotted α^2 vs. $\hbar\omega$ for fitting the direct gap[37], but both methods give similar results (within the measurement error ~0.005 eV).

Many semiconducting systems contain indirect band gaps. For example, silicon has an indirect gap from the valence band at the Γ point to the conduction band which lies along the $\Gamma-X$ line [47]. For indirect gaps, i.e., where the initial and final electron momentum is not the same, either emission or absorption of a phonon (a lattice vibration) is required in order to shift *k* to its final value. Generally, even the highest energy phonons have energies on the order of 10-50 meV, and therefore do not impart much energy in comparison to the photons required for excitation. In the case of indirect absorption the absorption coefficient is known to scale as:

$$\boldsymbol{\alpha\hbar\omega} \propto \left(\boldsymbol{\hbar\omega} - \boldsymbol{E_g}\right)^{\mathbf{2}} \qquad \text{Equation 2-3}$$

following the same Tauc-formula as direct gap, but with a different exponent. Some works suggest $\alpha \propto \left(\hbar\omega - E_g\right)^2$, but as was the case in direct gaps, the results do not change significantly. Nonetheless, because indirect gaps require both a phonon and a photon simultaneously, their transitions often occur with much lower probability (a factor of 10-100x less [48]). However, because the transition frequency inherently depends on the number of valence and conduction band states, indirect transitions from states with significantly larger density of states than direct ones can still have a large absorption magnitude, as we will show in $CoSb_3$ and other systems in Chapter 6.

Optical band gaps in this work were generally obtained using the Tauc method (unless otherwise specified), where $(\alpha\hbar\omega)^n$ and where *n*=2 for direct transitions and *n*=1/2 for indirect. The Tauc function is extrapolated on a plot versus photon energy, $\hbar\omega$, to zero (normalized) absorption; the zero is determined by either normalizing the sample to the minimum absorption coefficient value or by fitting and subtracting the free carrier absorption contribution: $\alpha_{FC} = a(\hbar\omega)^b + c$ (which will be discussed more thoroughly in Chapter 3).

2.3 - Estimating Band Gap from Temperature Dependent Electronic Properties

As mentioned in Chapter 1, there are several experimental methods of measuring the band gap, both using electronic and optical properties.

2.3a - Resistivity

First, the band gap can be estimated from electronic resistivity for an intrinsic semiconductor (where the number of holes and electrons are approximately equal). In the case where the electron and hole mobilities the same, one can derive that the temperature dependent resistivity should decrease in the intrinsic region as:

$$\boldsymbol{\rho \propto \exp(\frac{E_g}{2k_BT})} \qquad \text{Equation 2-4}$$

where E_g is the band gap, and T is the temperature. The band gap can be extracted from the slope of a plot of log of resistivity as a function of $1/T$. This is a common technique for determining the band gap in semiconductor materials in the absence of other estimates, but the linear region will not be reached if the materials is too heavily doped. In that case, the resistivity will behave as a metal, i.e., increasing resistivity with temperature.

2.3b - Band Gap Estimate from the Maximum Seebeck Coefficient

Alternatively, the peak in the Seebeck coefficient can be used to estimate the band gap of a material. At low temperatures, a sufficiently doped sample will have an increasing Seebeck coefficient with temperature (approximately linear with temperature in the degenerate limit). At sufficiently high temperatures (i.e., when E_g~O(k_BT)), a sufficient population of minority carriers develops which slows the increase in Seebeck coefficient, eventually resulting in a maximum in the thermopower. Goldsmid and Sharp have developed a relationship between the maximum Seebeck coefficient and the band gap [49-51]:

$$\boldsymbol{E_g = 2S_{max}T_{max}} \qquad \text{Equation 2-5}$$

Similar to the temperature-dependent resistivity, this requires similar assumptions about the relative mobility of holes and electrons. This assumption turns out to be quite important for materials such as ZrNiSn [52], which I will explore in detail during this thesis in Chapter 5. I also developed a method for determining how far the band gap will deviate from the Goldsmid-Sharp estimate as a function of the electron-to-hole weighted mobility ratio, *A*, even for materials with narrow gaps (or moderate gaps at high temperature) [50]. The Goldsmid-Sharp band gap is usually assumed to be, at best, a qualitative estimate (within ~20%). For a more direct measurement of band gap, optical methods are preferred, although they are not always feasible in doped samples.

2.4 - Band Engineering

Band engineering is a common topic in this thesis which involves optimization of thermoelectric efficiency through modifications in the electronic band structure. This can involve either tuning the Fermi level (E_F) through doping to optimize the thermoelectric properties or alloying the material with another to alter the electronic structure to improve thermoelectric properties (possibly through band convergence).

2.4a - Single Parabolic Band Model – Carrier Concentration Optimization

The most straightforward way to optimize a thermoelectric material is by varying the doping content and charge carrier concentration. Improvements in this context are often explained using the "single parabolic band model" where the material properties are assumed to be described by a free electron-like band with a certain effective mass (some multiple of the mass of a free electron). In terms of the thermoelectric figure of merit, zT, the optimum value can be found to scale with the quality factor:

$$\boldsymbol{B = \frac{2k_B^2\hbar}{3\pi}\frac{N_v C_l}{m_c^* E_{def}^2\, \kappa_L}} \qquad \text{Equation 2-6}$$

where k_B is the Boltzmann constant, $\hbar$ is Planck's constant ratioed to 2π, N_v is the valley degeneracy, $C_l = dv_l^2$ (where d is the density and v_l is the longitudinal speed of sound), m_c^* is the inertial effective mass, E_{def} is the deformation potential (which is a measure of the strength of coupling between lattice vibrations and electronic structure), and κ_L is the lattice thermal conductivity.

The single parabolic band model is derived from the Boltzmann transport equation using the relaxation time approximation to obtain the thermoelectric parameters as a function of the reduced chemical potential [24, 53, 54], $\eta = \frac{\xi}{k_B T}$, where ξ is the electronic chemical potential (which reduces to the Fermi level, E_F, at T=0 K). The resulting relations for the thermoelectric transport properties are written below for an arbitrary power law dependence of the scattering time: $\tau(\epsilon) = \tau_0 \epsilon^{\lambda - 1/2}$ [24].

$$\boldsymbol{S(\eta) = \frac{k_B}{e}\left[\frac{(2+\lambda)}{(1+\lambda)}\frac{F_{1+\lambda}(\eta)}{F_{\lambda}(\eta)} - \eta\right]} \qquad \text{Equation 2-7}$$

$$\boldsymbol{n(\eta) = \frac{1}{2\pi^2}\left(\frac{2m_d^* k_B T}{\hbar^2}\right)^{\frac{3}{2}} F_{1/2}(\eta)} \qquad \text{Equation 2-8}$$

$$\boldsymbol{r_H(\eta) = \frac{3}{2} F_{1/2}(\eta) \frac{\left(\frac{1}{2} + 2\lambda\right) F_{2\lambda - 1/2}(\eta)}{(1+\lambda)^2 F_{\lambda}^2(\eta)}} \qquad \text{Equation 2-9}$$

where λ determines the scattering exponent, n is the charge carrier concentration, m_d^* is the density of states effective mass, r_H is the Hall coefficient, which determines the relationship between the measured $n_H = \frac{1}{R_H e}$ and the chemical carrier concentration ($\frac{n}{n_H} = r_H$), and $\epsilon = \frac{E}{k_B T}$. $F_j(\eta) = \int_0^{\infty} \frac{\epsilon^j d\epsilon}{1+\exp(\epsilon - \eta)}$, which is defined as the *jth* order Fermi integral. While there are analytical expressions for the transport integrals in either the non-degenerate (semiconducting/insulating $\eta \ll 0$) or the degenerate (heavily doped semiconducting/metallic $\eta \gg 0$) limits, the best thermoelectric materials tend to have Fermi levels somewhere in the intermediate region (η near the band edge), requiring a full, numerical solution to the Fermi integrals (Python, Matlab, Mathematica, Excel/VBA). For most thermoelectric materials at or above room temperature, acoustic phonon scattering is the dominant scattering mechanism, and it usually works well to describe transport in thermoelectric materials, requiring: $\lambda = 0$ and $\tau_0 = \frac{\pi\hbar^4 C_l}{\sqrt{2}E_{def}^2(m_b{*}k_BT)^{3/2}}$. Here, m_b^* is the single valley effective mass (neglecting the effects of valley degeneracy). For systems where acoustic phonon scattering dominates, mobility decreases with temperature roughly as $T^{-3/2}$ (although some variation can exist if the effective mass is also temperature dependent). The real usefulness of Equation 2-7 through Equation 2-9 is that they relate experimentally measured parameters (Seebeck coefficient and Hall carrier concentration) back to the electronic band structure. The effectivez mass (which when estimated from the SPB Seebeck and carrier concentration, we will call m_S^*) is directly related to the band curvature and valley degeneracy ($m_d^* = N_v^{2/3}m_b^*$). In order to obtain m_S^*, first, the measured Seebeck coefficient will be used to estimate the reduced chemical potential (η) using Equation 2-7. η can be substituted into the measured $n_H = \frac{n}{r_H}$, the ratio of n (Equation 2-8) to r_H (Equation 2-9), to solve for the experimental effective mass (m_S^*). m_S^* is believed to represent the density of states m_d^*, rather than the conductivity mass defined previously or the single band mass m_b^*.

However, the effective mass is not the only useful parameter obtained in the single parabolic band model. Because Hall-effect measurements also yield the charge carrier mobility, $\mu_H = \mu_0 \frac{\left(\frac{1}{2}+2\lambda\right)F_{2\lambda-\frac{1}{2}}(\eta)}{(1+\lambda)F_\lambda(\eta)}$, it is straightforward to determine the parameter which scales the mobility, $\mu_0 = \frac{e\tau_0}{m_c^*}$, if the value has been measured experimentally. In fact, the band parameters in τ_0 (and the parameters that make it up as indicated in the previous paragraph) can also be determined if we assume that $m_c^* = m_b^* = m_d^*$, essentially requiring a single spherical Fermi surface. The thermoelectric quality factor, B (Equation 2-6), can be expressed in terms of μ_0:

$$\boldsymbol{B} = \frac{\boldsymbol{\mu_0 m_S^*}^{3/2}}{\boldsymbol{\kappa_L}}$$ Equation 2-10

In addition, the lattice thermal conductivity can be estimated using the Wiedemann-Franz law, $\kappa_L = \kappa - \kappa_e = \kappa - L\sigma T$, where $\kappa_e = L\sigma T$ is the electronic thermal conductivity. The expression for the Lorenz number, *L* is given by:

$$\boldsymbol{L} = \frac{\boldsymbol{k}^2}{\boldsymbol{e}^2}\frac{(\boldsymbol{1}+\boldsymbol{\lambda})(\boldsymbol{3}+\boldsymbol{\lambda})\boldsymbol{F_\lambda}(\boldsymbol{\eta})\boldsymbol{F_{\lambda+2}}(\boldsymbol{\eta}) - (\boldsymbol{2}+\boldsymbol{\lambda})^2\boldsymbol{F}^2_{\boldsymbol{\lambda+1}}(\boldsymbol{\eta})}{(\boldsymbol{1}+\boldsymbol{\lambda})^2\boldsymbol{F}^2_{\boldsymbol{\lambda}}(\boldsymbol{\eta})}$$ Equation 2-11

By computing m_S^*, μ_0, and κ_L from experimental data, we can make a plot of the carrier concentration dependent thermoelectric properties, as shown in Figure 1-2. The power of this simple method is that this plot can be generated after making and measuring the *zT* for a single sample. We can immediately determine the value of the maximum *zT*, and whether the charge carrier concentration needs to increase or decrease to yield the optimum *zT*. Usually, a series of samples is made with different doping concentrations to reduce the uncertainty of the m_S^*, μ_0, and κ_L values.

2.4b - Valley Degeneracy and Band Anisotropy

Higher levels of complexity can be added to the single parabolic band transport model. To begin with, perhaps the most profound in terms of thermoelectric enhancement are the valley degeneracy (N_v) and band anisotropy (K). Each of these show up during several chapters of this thesis. The valley degeneracy, N_v, is defined as the number of distinct charge carrier pockets (of the same sign) which exist at the Fermi level. The origin of these degeneracies can be broken down into two parts: $N_v = N_{v,symmetry}N_{v,band}$, where $N_{v,symmetry}$ is related to the degeneracy of a given point in the Brillouin zone due to that point's symmetry and $N_{v,band}$ which is the number of individual bands that are converged at that energy. Valley degeneracy manifests itself by increasing the density of states effective mass, $m_d^* = N_v^{2/3}m_b^*$, relative to the single valley effective mass (m_b^*). This is beneficial for the thermoelectric properties because each individual pocket conducts in parallel while the overall Fermi level does not rise too quickly (allowing the material to maintain a high Seebeck coefficient). In order to maximize N_v, a highly symmetric Brillouin zone (usually found in high symmetry materials) with band extrema that exist at low symmetry points lead to the highest degeneracy. For PbTe and other IV-VI materials, the primary valence band exists at the L-point with $N_{v,symmetry}$=4, and a $N_{v,band}$=1, and a secondary band exists along the Σ line with a high degeneracy of $N_{v,symmetry}$=12, and a $N_{v,band}$=1.

The common definition for the effective mass is $m^* = \hbar^2 \left(\frac{d^2E}{dk^2}\right)^{-1}$, which is the inverse of the curvature of the band in energy vs. *k*-space (light bands have high curvature, heavy bands have shallow). In the simplest case, this Fermi surface will have the same curvature along all directions in *k*-space, producing a single, spherically shaped pocket. However, for many common materials this is not the case (Si/Ge [55, 56], III-V [57], and the lead chalcogenides [58-60]). In general, the effective mass can be different along all three directions. For example, when describing the density of states in that band, the geometric average along these directions is most appropriate: $m_d^* = N_v^{2/3} m_b^* = N_v^{2/3}(m_1^* m_2^* m_3^*)^{1/3}$, where N_v is the valley degeneracy, m_b^* is the single valley effective mass, and $m_{1,2,3}^*$ are the effective masses along the different directions. While the density of states effective mass is the appropriate scaling parameter for the carrier concentration, the electrical conductivity and mobility are governed by the harmonic average over the different directions, yielding the conductivity (or inertial) effective mas: $m_c^* = \frac{3}{\frac{1}{m_1^*}+\frac{1}{m_2^*}+\frac{1}{m_3^*}}$, which weights the lighter (higher conductivity) directions more. Most often experimentally, Fermi surfaces are believed to be ellipsoidal, implying $m_1^* = m_2^* = m_\perp^*$ and $m_3^* = m_\parallel$. Often, the anisotropy is described by the parameter $K = \frac{m_\perp^*}{m_\parallel^*}$. While it is possible to obtain information about the band anisotropy directly from experiments (Faraday rotation [55, 56], Shubnikov De Haas

[61]), for new materials these experiments have usually not been performed; therefore *K* is assumed to be 1.

2.4c - Multiple Band Effects

As is the case in p-type PbTe, many good thermoelectric materials exhibit multiple band effects. While semiconductors are inherently multi-band systems (one valence, one conduction band), good thermoelectric materials are sufficiently doped, meaning that their Fermi levels are far enough from the minority carrier band to not have detrimental effects to the majority carrier properties. In systems such as PbTe, where a secondary valence band exists about 0.12 eV below the primary, the effects are almost always beneficial to the thermoelectric properties. This can be understood by considering the quality factor, *B* (Equation 2-6), which is proportional to the valley degeneracy. Any electron (or hole for p-type material) population in an additional band which contributes to the electronic transport properties (i.e., the band's energy is within ~4 $k_B T$ of the chemical potential) can be regarded as an increase in the effective valley degeneracy (a topic that will be discussed in detail in Chapter 7). This increase ultimately results in a better *zT* than could have been obtained by either band separately; however, the details depend significantly upon the energy offset (ΔE) between the bands. This thesis will focus, in a large part, on the details of these multiple band effects and their characterization and potential enhancement to *zT* in both an experimentally measureable and theoretical sense.

In order to compute multi-band effects, conductivity weighted averages over the properties of the individual bands (the i^{th} band) are used, as suggested by Putley [62]:

$$\boldsymbol{\sigma} = \sum_i \boldsymbol{\sigma_i}$$ Equation 2-12

$$\boldsymbol{S} = \frac{\sum_i \boldsymbol{S_i \sigma_i}}{\sum_i \boldsymbol{\sigma_i}}$$ Equation 2-13

$$\boldsymbol{R_H} = \frac{\sum_i \boldsymbol{\sigma_i^2 R_{H_i}}}{\left(\sum_i \boldsymbol{\sigma_i}\right)^2}$$ Equation 2-14

$$\boldsymbol{\kappa} = \boldsymbol{\kappa_L} + \sum_i \boldsymbol{L_i \sigma_i T} + \boldsymbol{T}(\sum_i \boldsymbol{\sigma_i S_i^2} - \boldsymbol{S^2 \sigma})$$ Equation 2-15

where $R_{H,i}$ is the Hall coefficient for the i^{th} band, defined as $R_{H,i} = \frac{1}{n_{H,i}e} = \frac{r_{H,i}}{n_i e}$ (where r_H and n were defined in Equation 2-8 and Equation 2-9). Interestingly, the thermal conductivity shows a non-trivial effect: $\kappa = \kappa_L + \kappa_{e,Lorenz} + \kappa_{bipolar}$. Essentially, the Wiedemann-Franz law accounts for only part of the electronic thermal conductivity in the region where multiple bands exist. The bipolar term is a result of a difference in the total power factor and the power factors of each individual band. In the region where two charge carriers exist with opposite signs (valence and conduction band), the bipolar thermal conductivity is observed rather strongly and is quite important in many thermoelectric materials. In fact, the bipolar effect at high temperature is readily observed in the thermal conductivity (Figure 1-4b) and is one physical origin of the maximum in *zT*. The Seebeck coefficient also is decreased in this bipolar region (Figure 1-4a).

Additionally, the charge neutrality equation:

$$\boldsymbol{N_D} + \sum_i \boldsymbol{p_i} = \boldsymbol{N_A} + \sum_i \boldsymbol{n_i}$$ Equation 2-16

can be solved with a known number of donors (N_D) and/or acceptors (N_A) (or difference between their concentrations) for the chemical potential dependent electron and hole concentrations (which is only be a function of η given $m_{d,i}^*$ and ΔE are specified for each of the *i* bands at a given T). The charge neutrality equation is useful for determining temperature-dependent thermoelectric properties (assuming N_D-N_A is constant), and it is used in several chapters of this thesis.

It should be noted that the reduced chemical potential for the *ith* band should be defined relative to the first band in order to reduce the overall number of variables (given that the offset between the bands, ΔE, is known). This can be defined as $\eta_i = s_i\eta_1 - \Delta E_{i-1}$, where s_i is the sign of the band (which should be specified relative to that of band 1), ΔE_{i-1} is the band offset between the i^{th} and first bands, and η_i represents the reduced chemical potential for that band (which should be substituted into the Fermi integral equations specified previously with the sign of the Seebeck coefficient reflecting the sign of the band, s_i).

2.4d - Band Non-Parabolicity

In this thesis, non-parabolic bands will also be used to describe the thermoelectric transport properties. The two-band Kane model (which Kane originally developed for InSb [63]) involves interacting valence and conduction bands through the $k \cdot p$ method. This model's application to describing electronic transport properties is described in great detail by Zawadski [64] and Ravich [58]. While Zawadski takes a more general approach which includes examples across many material systems and considers a wide range of properties, Ravich's more simple approach is geared towards thermoelectric lead chalcogenides. The equations for the transport properties are outlined in detail in previous work by Wang et al. and will not be repeated here [65], but the relevant Fermi integral is generalized to:

$$\boldsymbol{{}^{n}F_{l}^{m} = \int_{0}^{\infty}\left(-\frac{df}{d\epsilon}\right)\epsilon^{n}\left(\epsilon+\beta\epsilon^{2}\right)^{m}\left[(1+2\beta\epsilon)^{2}+2\right]^{l/2}d\epsilon} \qquad \text{Equation 2-17}$$

The degree of non-parabolicity is related to the band gap using the parameter $\beta = \frac{k_B T}{E_g}$; therefore materials with small gaps will exhibit large non-parabolicity. In fact, the band edge effective mass can be shown to scale as, $m_0^* = \frac{\hbar^2 E_g}{2P^2}$, where *P* is the interaction matrix element between electrons and holes. In this thesis, I will apply non-parabolic models for the lead and tin chalcogenides and $CoSb_3$. In Chapter 6, I discuss the effect of non-parabolicity on the effective mass, which is obtained through the Seebeck coefficient (m_S^*) by deriving the Mott relation for

Kane-type bands. The generalized Fermi integrals for non-parabolic bands can be used in place of parabolic ones (in fact, if we take $\beta = 0$ the result reduces to the parabolic expression) when computing the properties for either a single or a multi-band transport model.

2.5 - Ab-Initio Calculations

Density functional theory (DFT) calculations are commonplace in materials and chemistry research. In the context of thermoelectric materials, they give a detailed description of the materials' electronic structure, which is critically important to characterizing experimentally measured results. This thesis uses these calculations throughout to guide the research and provide a framework for which to understand the results. Because of the range of methods used by our collaborators, specific details of each calculation will be given within each chapter on the *ab-initio* results obtained.

2.6 - Sample Preparation

Thermoelectric samples were prepared using conventional solid-state chemistry techniques. The IV-VI materials (PbTe, PbSe, SnTe, and their alloys) were prepared by first weighing stoichiometric quantities of the elements, loading them into a quartz ampule, sealing under vacuum, and melting in a tube furnace for approximately 1 day at 1000 – 1100°C. The melted samples were quenched in water followed by annealing for ~ 3 days at 600°C to homogenize the sample.

$CoSb_3$ samples were synthesized in a similar manner to the IV-VI materials where the elements were melted (1080°C) and annealed (for 7 days at 600°C) within boron nitride crucibles that were sealed within quartz ampules.

Half-Heusler (ZrNiSn) samples were prepared via arc-melting due to the high melting point of Zr. The arc-melting of the elements occurred in an Ar atmosphere within a water-cooled copper crucible. To ensure compositional homogeneity, samples were flipped and remelted five times.

The as-cast samples were annealed in evacuated quartz tubes at 1220 K for 7 d, followed by quenching in ice water to ensure the crystalline order.

For each of the materials, the samples were quenched after annealing and the ingots were recovered and ground into a fine powder (in the glove box). Samples were prepared by loading this powder into a graphite dye (1/2” outer diameter) which was used for induction hot-pressing [66]. The resulting samples were high quality (>95% theoretical density) ½” discs which were polished and prepared for the electrical, thermoelectric, and thermal measurements required to estimate *zT*. X-ray diffraction was performed to ensure that the expected crystal structure was obtained and to discover any possible secondary phases (detection limit of ~1%). Additional details regarding the synthesis, as needed, will be included at the end of each section.

Chapter 3: Optical Properties of Doped Semiconductors

3.1 - Introduction

Because thermoelectric materials require doping for optimization of the thermoelectric properties, understanding how free carriers in a material affect its optical absorption spectrum is quite important. Figure 3-1 illustrates several ways that free carriers affect the optical absorption edge spectrum. Region 1 involves absorption of light via plasma oscillation of the bulk free electrons, the magnitude of which depends on the free carrier concentration. Region 2, 3, and 4 are associated with interband transitions from the valence to conduction band, as indicated by the increase in absorption beginning around 0.28 eV. Region 2 precedes the onset of the absorption edge and is known as the Urbach tail, which is associated with randomly distributed impurities within the semiconductor. Regions 3 and 4 are associated with an increase or decrease in the band edge position, which occurs at high doping levels. The increase shown in Region 3 is known as the Burstein Moss shift, which occurs due to occupation of the conduction band edge upon heavy n-type doping. Region 4 indicates a decrease in the absorption edge energy (renormalization), which is thought to occur due to electron-electron repulsion. Each of these effects will be described in detail in the following sections.

The difference between the optical (Burstein-Moss shifted) and true band gaps have been studied in many material systems [47, 67, 68] . It is important to have an understanding of the Burstein Moss shifts and band gap renormalization for a variety of semiconductor device applications where both the majority and minority carrier concentrations and band energies are necessary to optimize performance. In thermoelectric materials, though, there is often no distinction made between the true and optical gaps in doped materials [69, 70]. While the differences can be circumvented in the case of an undoped material (PbTe undoped binary), some thermoelectric materials may include simultaneous shifts in the doping level and the band structure during doping that we would like to characterize in the context of band engineering. In this thesis chapter, I quantify the Burstein-Moss shift to the optical gap, and gap renormalization in Iodine doped PbTe measured using DRIFTS. We use measured Seebeck coefficients to estimate the chemical potential (ξ), which is an improvement to simply measuring the Hall carrier concentration. Further, we attempt to improve upon renormalization estimates by self-consistently considering the band gap parameter for non-parabolic systems.

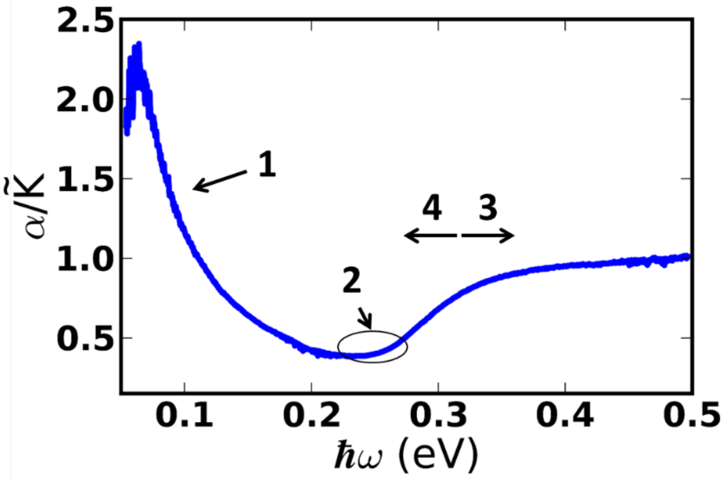

Figure 3-1: Optical absorption edge spectrum of an Iodine doped PbTe sample indicating the four regions that are present when considering optical processes relevant to free carriers: 1. Free carrier absorption, 2. Urbach edge, 3. increase in the interband transition energy (Burstein Moss Shift), and 4. band gap reduction as a result of doping (renormalization).

3.2 - Theory of Free Carrier Contributions to Optical Spectra

3.2a - Free Carrier Absorption

In n-type doped PbTe, a population of free carriers exists near the bottom of the conduction band, which can be excited to higher levels within the conduction via intraband transitions. The free electron cloud is perturbed by an incoming electric field, $\boldsymbol{E}$. Solutions to the Maxwell equations take the form of: $\boldsymbol{E} = \boldsymbol{E_0} e^{i(\boldsymbol{k}\cdot\boldsymbol{r}-\omega\tilde{t})}$, (where $\tilde{t}$ is the time), which yields the following form of the complex dielectric function ($\epsilon_c = \epsilon_1 + i\epsilon_2$) [43]:

$$\boldsymbol{\epsilon_c = \epsilon_\infty + \frac{4\pi i}{\omega}\left(\frac{ne^2\tau}{m(1-i\omega\tau)}\right) = \epsilon_\infty\left(1-\frac{\omega_p^2\tau^2}{1+\omega^2\tau^2}\right) + i(\frac{\epsilon_\infty\omega_p^2}{\omega(1+\omega^2\tau^2)})} \qquad \text{Equation 3-1}$$

Here, τ is the Drude scattering time and the plasma frequency is defined as $\omega_p = \sqrt{\frac{ne^2}{m^*\epsilon_\infty}}$. Using this model for the complex dielectric function, it is straightforward to obtain both the real and imaginary components of the refractive index, which can then be used to obtain the frequency dependent reflectivity and absorption coefficient. In the case of specular reflection (perfect mirror reflection), the measured reflectivity can be compared to the result expected from the real and imaginary components of the refractive index, which can be derived from the dielectric function using [43]:

$$\boldsymbol{\epsilon_1 = n_r^2 - \kappa_r^2} \qquad \text{Equation 3-2}$$

$$\boldsymbol{\epsilon_2 = 2n_r\kappa_r} \qquad \text{Equation 3-3}$$

and

$$\boldsymbol{R = \frac{(1-n_r)^2+\kappa_r^2}{(1+n_r)^2+\kappa_r^2}} \qquad \text{Equation 3-4}$$

which can be shown to yield a minimum in *R* near ω_p as a result of resonance between the photon and the bulk free electrons. The frequency at which the minimum occurs is roughly equal to ω_p (minor corrections have been shown by Lyden et al. [71]). In a diffuse reflectance spectrum, which is transformed by the Kubelka Munk function (Equation 2-1), this instead yields a maximum in *F(R)*. These maxima are observed in the more heavily doped PbTe samples ($n_H > 2 \times 10^{19}$ cm^{-3}) where the plasma frequency becomes larger than 0.05 eV as shown in Figure 3-2a. The measured peak in the Kubelka Munk function occurs even though the Praying Mantis diffuse reflectance instrument attempts to minimize the specular component of the reflection.

In terms of the absorption coefficient, α, (which Diffuse Reflectance attempts to capture), when $\omega \gg \tau^{-1}$: $\alpha_{FC} \propto \frac{ne^2}{n_r\, c\, m^*\, \tau\, \omega^2}$ where *n* is the number of free carriers, *e* is the elementary charge of an electron, n_r is the real refractive index, and *c* is the speed of light [43]. In order to isolate interband transitions, these features were fit and subtracted with a power law ($y = ax^b + c$). In almost all cases, the exponent, *b*, followed the expectation for Drude carriers of *b* = -2.

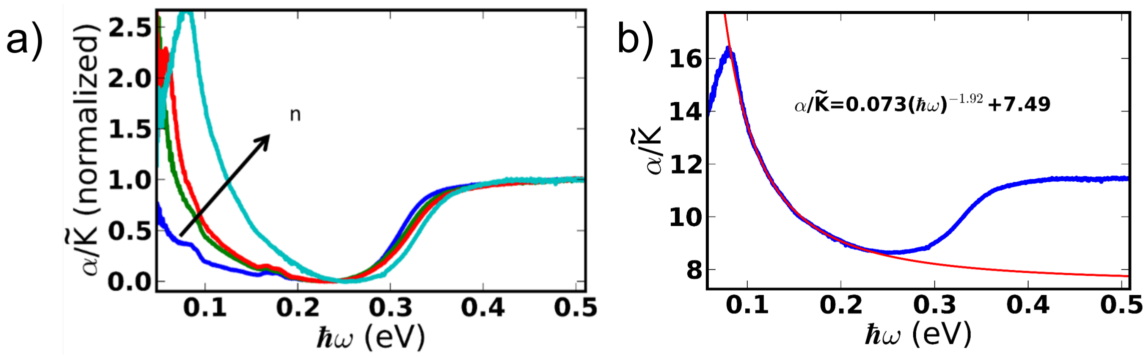

Figure 3-2: DRIFTS Spectra showing free carrier absorption contributions in Iodine doped PbTe. a) an increasing free carrier absorption with doping level, b) an example of a power law fit to the free carrier absorption.

3.2b - Urbach Edge

The second region of Figure 3-1 shows the exponential onset of absorption just below the fundamental absorption edge, known as the Urbach Edge (or Urbach tail). This effect is known to occur across a wide range of semiconductors, although ones with high impurity contents (or disordered alloys) have the largest Urbach tails (shown later in Chapter 4.3 for PbSe/SrSe alloys). The Urbach tail is thought to be related to the random distribution of impurity atoms in the material. For measurements done in this thesis, we also observe an approximately exponential increase in absorption just below the band edge [44, 45]. In this chapter, we will not treat the Urbach edge explicitly as we will attempt to fit the direct transitions instead, although its implications will be discussed.

3.2c - Burstein Moss Shift/Renormalization

Region 3, shown in Figure 3-1, indicates an upward shift in the absorption edge energy with doping. Heavily doped semiconductors (most good thermoelectric materials) have free carrier contributions to the optical absorption that can complicate the estimate of the band gap. In the case of degenerately doped semiconductors, this can cause large errors in the estimate of the true band gap on the order of the value of the chemical potential, ξ (which can be more than 0.1 eV in heavily doped samples). Since the early 1950's, it has been known that the measured optical band gap ($E_{g,opt}$) tends to change with increasing doping [72, 73]. These effects have even been considered in lead chalcogenides by some authors [74-77].

In the case of a degenerately doped n-type semiconductor, states near the conduction band edge become partially occupied. As a result, the photon energy required for excitation across a direct band gap becomes higher, increasing by $\left(1+\frac{m_{cb}^*}{m_{vb}^*}\right)\xi$ in the case of direct transitions (where $m_{cb,vb}^*$ are the conduction and valence band effective mass respectively, see Figure 3-3). This results in an increase in the optical band gap ($E_{g,opt}$), known as the Burstein-Moss shift [45, 72, 75, 78]. The thermal gap, $E_{g,thermal} = E_g + \xi$, is relevant to transport properties and minority carrier excitation across the gap. The true band gap, E_g, has been shown both experimentally through optical measurements [47, 79, 80] and theoretically [47, 79, 80] to be reduced as the carrier concentration increases in heavily doped semiconductors, known as band gap renormalization (Δ_{RN})[12,35-37]. Renormalization has been attributed to Coulombic repulsion of the electrons and/or exchange interactions. Thus, the optical band gap can be expressed as:

$$\boldsymbol{E_{g,opt} = E_g + \left(1+\frac{m_{cb}^*}{m_{vb}^*}\right)\xi - \Delta_{RN}} \qquad \text{Equation 3-5}$$

which is illustrated in Figure 3-3.

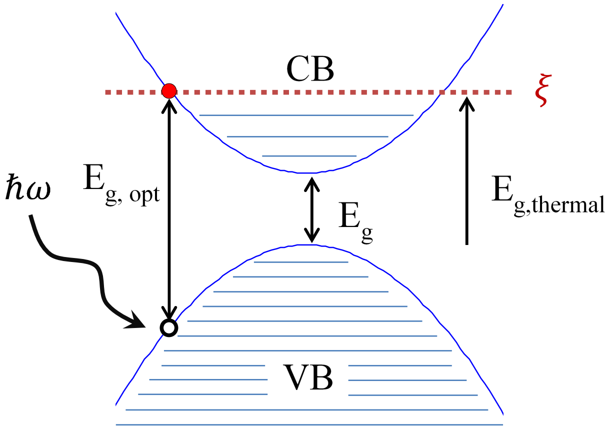

Figure 3-3: Optical excitations across the gap in a direct gap n-type degenerately doped semiconductor illustrating the Burstein-Moss shift and the different estimates of the band gap. Dashed line indicates the chemical potential, ξ.

While the accepted view of PbTe is as a direct gap semiconductor, with evidence shown both experimentally [77, 81-83] and theoretically [84-86], some confusion existed in the early optical measurements. Some authors had also obtained good, linear fits to $\alpha^{1/2}$ vs. $\hbar\omega$ expected for indirect transitions [27, 37]. Similar to these reports, the absorption spectra in this thesis also provide a linear $\alpha^{1/2}$ vs. $\hbar\omega$ region where the extrapolated band-gap energy is slightly lower (~30-60 meV) than those fit for direct transitions. Scanlon suggests that this difference can be attributed to indirect transitions where a phonon is absorbed [37, 58], although single phonon energies are at most 12 meV or less based on a Debye temperature of 140 K [87] and neutron scattering experiments [88]. Prakash suggests Scanlon's observation could also be interpreted as merely a coincidental fit due to the Urbach tail (exponential decrease in density of states below the band edge) [39]. Although we believe that Prakash's interpretation is correct in PbTe, many materials do exhibit both indirect and direct transitions with some energy separation. For example, in germanium, both direct and indirect transitions exist with the indirect gap occurring first at about 0.63 eV and direct transitions beginning at 0.81 eV [89]. The indirect portion involves a slow rise in absorption coefficient over a long energy range (~100 cm^{-1} over ~0.2 eV) while the direct absorption on the other hand gives a much steeper rise over a shorter period (~10^{4} cm^{-1} over ~0.05 eV). As a result, the direct gap is much more easily observed, particularly if both direct and indirect transitions occur at close to the same energies. The absorption coefficient of PbTe changes ~10^4 cm^{-1} over ~0.05 eV [76, 90], suggesting that it is a direct gap semiconductor.

Recently, it has been suggested that the true gap value is convoluted by mid-gap defect states [91]. While these states may affect the measured optical band gap, we see no significant contribution from localized states in the transport properties; transport measurements are characteristic of itinerant (delocalized) carriers giving metal-like transport behavior (implying that the suggestion of mid-gap states is incorrect). Therefore, the measured absorption edge was assumed to be associated with the band edge in PbTe and not mid gap defect states, although defect states near the band edge could certainly play a role in band gap renormalization.

3.3 - Results and Discussion

Figure 3-4a shows the raw absorption spectra for a series of Iodine doped PbTe samples. A steady shift in the absorption edge to higher energies is observed with an increase in dopant concentration. Upon fitting and subtracting the free carrier absorption portions at low energies and applying the Tauc transformation for direct gaps, the gaps can be extrapolated as shown in Figure 3-4b. The results of the extrapolations are plotted (Figure 3-4c) as the optical band gap ($E_{g,opt}$) as a function of charge carrier concentration for Iodine and Lanthanum doped PbTe and Bromine doped PbSe.

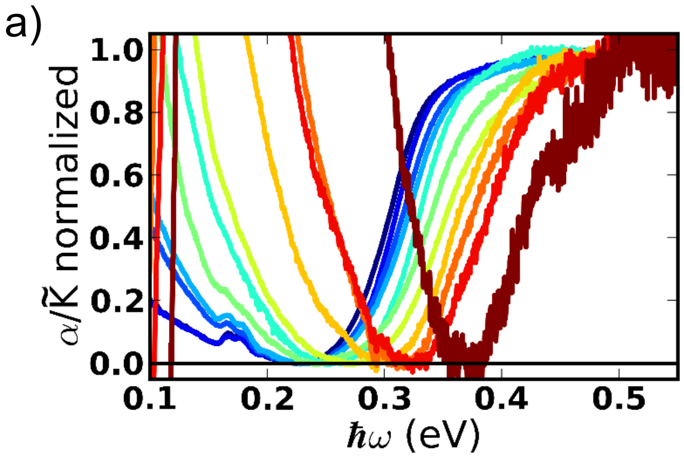

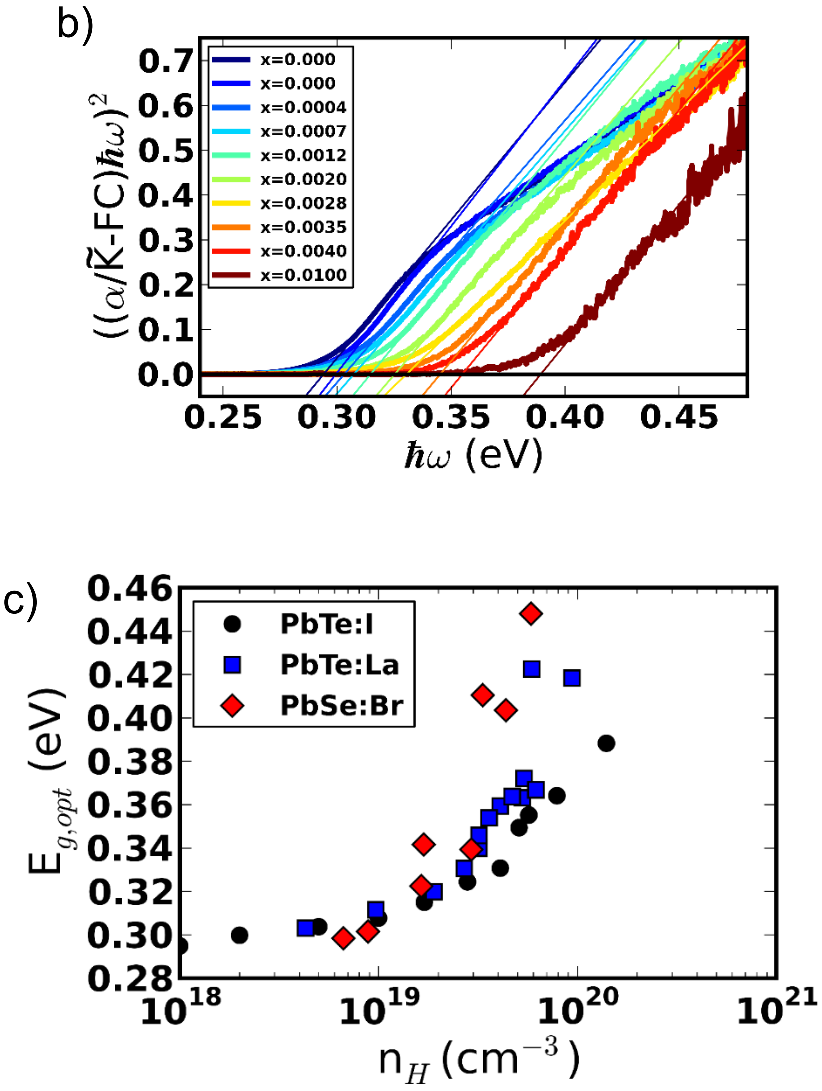

Figure 3-4: Normalized Kubelka Munk function for $PbTe_{1-x}I_x$ for a) raw data, and b) absorption coefficient direct gap extrapolation using the Tauc method. c) the resulting optical band gaps for n-type PbTe doped w/ either Iodine or Lanthanum and PbSe doped with Bromine.

Figure 3-4 clearly shows the increasing optical band gap with doping level; in order to quantify this effect, ξ must be determined. In many cases, the chemical potential is estimated by the 0 K limit of the parabolic band (Fermi energy, *E_F*): $E_F = \frac{\hbar^2}{2m^*}(3\pi^2 n)^{2/3}$ [68, 92, 93]. While this may be a good estimate for degenerate systems (at low temperature, high doping) with parabolic band shapes, a better estimate involves solving the more general temperature-dependent expression, $n = \int_0^\infty D(E) f(E, \xi, T) dE$, where *D* is the density of states and *f* is the Fermi distribution function. It is well known that many semiconductors, including lead chalcogenides, deviate significantly from parabolic behavior. Ravich has developed an adaptation of the Kane band model for application to the lead chalcogenides, which has shown excellent agreement to experimental transport data [16, 28, 58]. Using Ravich's solution of the Kane band model applied to lead chalcogenides, *n* can be calculated by numerically integrating Equation 3-6:

$$\boldsymbol{n} = \frac{(\mathbf{2m}^{*}\boldsymbol{k_B T})^{\frac{3}{2}}}{\mathbf{3}\boldsymbol{\pi}^{\mathbf{2}}\hbar^{\mathbf{3}}}\ {}^{\mathbf{0}}\boldsymbol{F}_{\mathbf{0}}^{\mathbf{3/2}} \qquad \text{Equation 3-6}$$

where $m_{d,0}^{*}$ is the band edge density of states effective mass, ϵ is the dimensionless energy ($\epsilon = \frac{E}{k_B T}$), β is the non-parabolicity parameter ($\beta = \frac{k_B T}{E_g}$ from Ravich), η is the reduced chemical potential $\eta = \frac{\xi}{k_B T}$, and ${}^{n}F_{l}^{m} = \int_0^\infty \left(-\frac{df}{d\varepsilon}\right)\epsilon^n(\epsilon + \beta\epsilon^2)^m[(1 + 2\beta\epsilon) + 2]^{l/2}d\epsilon$ (a modified version of the Fermi integrals, Equation 2-17, from Wang et al [65]). The band gap parameter in the Kane model was assumed to have a constant value equal to that of the undoped PbTe, 0.295 eV, for this analysis. Calculation of the chemical potential as a function of the true carrier concentration is rather straightforward, but in order to compare to the Hall carrier concentration the Hall factor, r_H, is needed [58, 65]:

$$\boldsymbol{r_H} = \frac{\mathbf{3}\boldsymbol{K}(\boldsymbol{K}+\mathbf{2})}{(\mathbf{2}\boldsymbol{K}+\mathbf{1})^{\mathbf{2}}}\frac{{}^{\mathbf{0}}\boldsymbol{F}_{\mathbf{0}}^{\mathbf{1/2}}\ {}^{\mathbf{0}}\boldsymbol{F}_{\mathbf{0}}^{\mathbf{3/2}}}{\left({}^{\mathbf{0}}\boldsymbol{F}_{\mathbf{-2}}^{\mathbf{1}}\right)^{\mathbf{2}}} \qquad \text{Equation 3-7}$$

where *K* (as defined in Chapter 2) is the anisotropy factor ($K = \frac{m_{\parallel}^{*}}{m_{\perp}^{*}} = 3.58$ [16]). By combining Equation 3-6 and Equation 3-7 to obtain $n_H = n/r_H$, we can plot the chemical potential dependent carrier concentration in Figure 3-5b (blue line) for $m_{d,0}^{*} = 0.276\, m_e$.

Alternatively, using the Boltzmann transport equation, it is possible to obtain an estimate for the chemical potential, ξ, directly from the measured Seebeck coefficient with no assumption about the band edge effective mass (Equation 3-8) [58, 65]. The raw Seebeck data as a function of Hall carrier concentration is plotted in Figure 3-5a along with an *S* vs n_H (Pisarenko plot) estimate using the SKB model (Red line derived using Equation 3-6, Equation 3-7, and Equation 3-8).

$$\boldsymbol{S} = \frac{\boldsymbol{k_B}}{\boldsymbol{e}}\left(\frac{{}^{1}\boldsymbol{F}^{1}_{-2}}{{}^{0}\boldsymbol{F}^{1}_{-2}} - \boldsymbol{\eta}\right) \qquad \text{Equation 3-8}$$

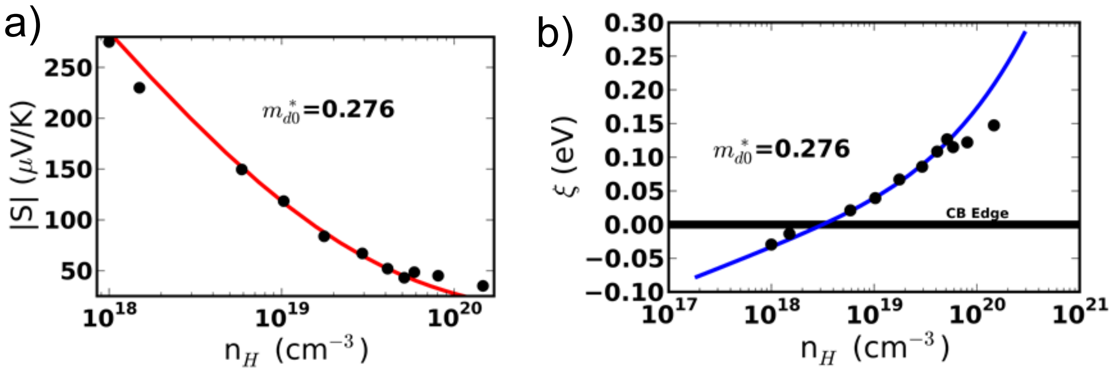

Figure 3-5: a) Seebeck Pisarenko plot for PbTe:I with the SKB model curve (m^*_{d0}=0.276) shown. b) The change in electrochemical potential (calculated from the Seebeck coefficient) with Hall carrier concentration as a result of doping.

Figure 3-5b shows the calculated chemical potential for each iodine doped sample calculated using a single Kane band model both from the room temperature Seebeck measurements (solid points) along with the result assuming $m^*_{d0} = 0.276\, m_0$ (best fit of the Seebeck vs. n_H Pisarenko plot). Here, we can see the chemical potential for the most heavily doped samples increases to ~0.15 eV from the band edge. It is important to note that the chemical potential estimate can vary significantly depending on the particular band model. In the case of a single parabolic band, the chemical potential can change to be as much as 50% higher for the same doping level and effective mass (this is a consequence of the Kane band effective mass increasing with increasing ξ). Once ξ is known, it is possible to estimate the true gap from the optical gap measurement (Figure 3-4). As an alternative to the Tauc method, the gap can also be fit using the spectral Fermi distribution.

The Fermi distribution can be projected onto the unperturbed interband absorption as a multiplicative factor, shown in Equation 3-9. This technique and similar methods have been performed on a variety of materials, including lead chalcogenides [75, 76] and other materials [47, 67, 72, 94].

$$\boldsymbol{\alpha}(\hbar\boldsymbol{\omega}) \propto \boldsymbol{\alpha_0}(\hbar\boldsymbol{\omega})\ [\mathbf{1} - \boldsymbol{f}(\hbar\boldsymbol{\omega}, \boldsymbol{\zeta}, \boldsymbol{T})\ ] \qquad \text{Equation 3-9}$$

Here, α_0 is the absorption for an unpopulated conduction band at T = 0 K, which for parabolic bands is proportional to $\alpha_0 = \frac{\sqrt{\hbar\omega - E_g}}{\hbar\omega} = \frac{\sqrt{\hbar\omega - \left[E_{g,opt} - \left(1 + \frac{m_{cb}^*}{m_{vb}^*}\right)\xi\right]}}{\hbar\omega}$. f is the Fermi distribution, which is related to the photon energy as $f(\hbar\omega, \xi, T) = \left[1 + \exp\left(\frac{\hbar\omega - E_{g,opt}}{\left(1 + \frac{m_{cb}^*}{m_{vb}^*}\right)k_B T}\right)\right]^{-1}$. The second term in Equation 3-9 represents the electronic excitation probability based on the electron population from Fermi distribution.

Using the proportionality factor and the band gap value as a fitting parameter, it is possible to obtain an estimate for the optical band gap using Equation 3-9 from the measured absorption spectra for a given estimate of the chemical potential, ξ (as estimated from either room temperature Seebeck and n_H measurements). A resulting fit of the absorption spectrum is shown in Figure 3-6. The Fermi projection method gives the optical band gap near the inflection point in the absorption (where the slope is the largest) which agrees approximately in trend obtained directly from extrapolation (Figure 3-7a) using the Tauc method (although is ~0.01-0.02 eV higher in energy than the Tauc extrapolation method). Results regarding the Fermi broadening method are included in a separate work on the subject [95], but in the remainder of this thesis I will only present results using the Tauc extrapolations (Figure 3-4).

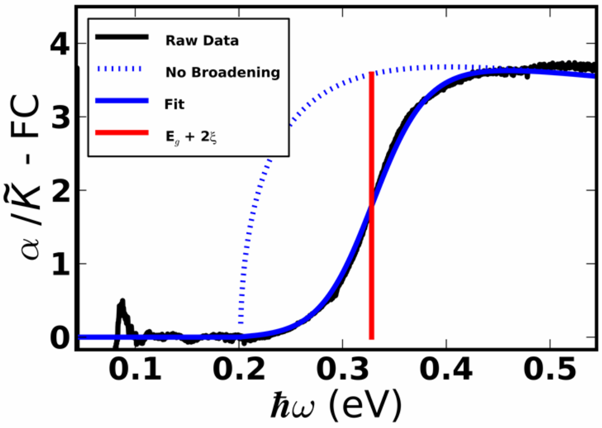

Figure 3-6: Fermi spectra method projecting the Fermi distribution onto the absorption edge in $PbTe_{1-y}I_y$, y =0.0012 fit with a Fermi function.

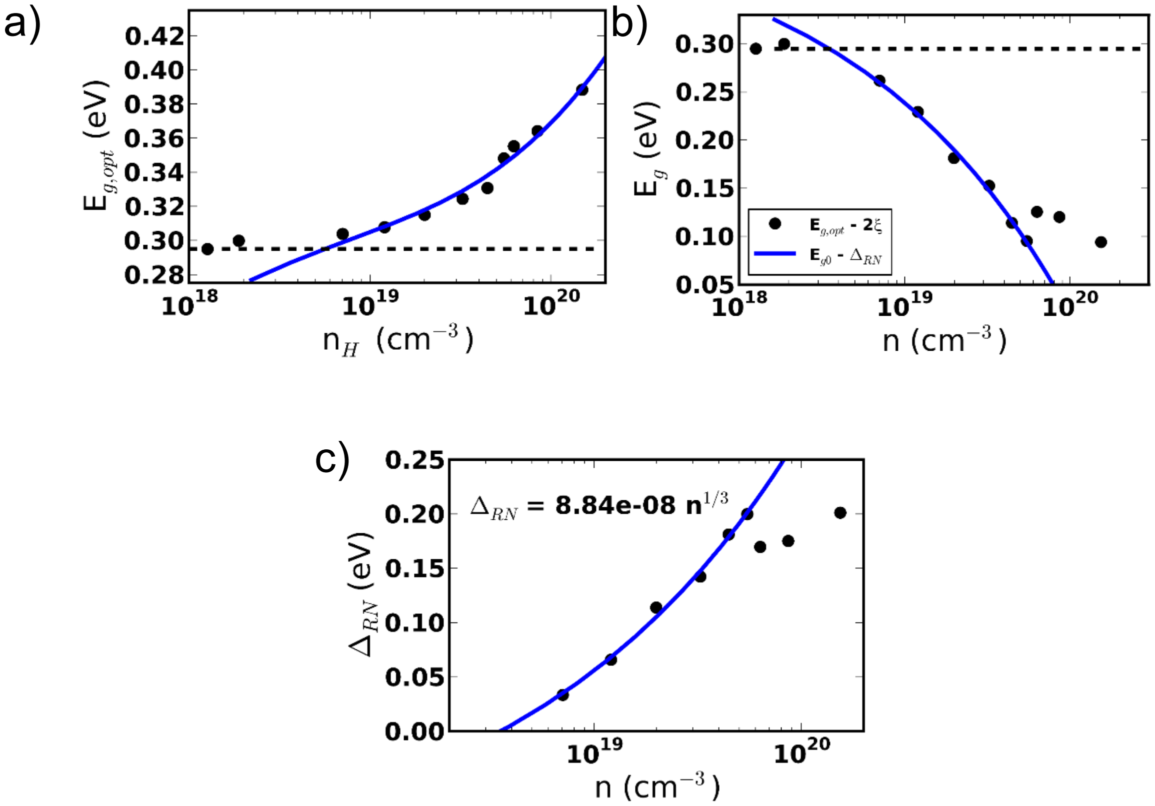

Figure 3-7: a) Optical band gaps fit from optical data via extrapolation by the Tauc plot method along with the curve fit from Equation 3-5. b) The true band gap, calculated from the optical gaps by $E_g = E_{g,opt} - 2\xi$ and the curve, which is given by $E_g = E_{g,0} - \Delta_{RN}$, c) Band gap renormalization fit: experimental data is $\Delta_{RN} = E_{g,0} - (E_{g,opt} - 2\xi)$, and the curve is given by the best fit: $\Delta_{RN} = An^{1/3} + \Delta_{RN,0}$.

Figure 3-7a shows an increasing optical gap with doping level, known as a Burstein-Moss shift. As the doping level increases, the chemical potential in the conduction band moves upward, which creates occupied states nearest the band edge, requiring a higher energy photon for excitation of a carrier across the gap. Following Figure 3-3 (and Equation 3-5) we can relate the optical gap to the true gap, E_g.

Figure 3-7b shows the calculated true band gap with respect to doping level. In the case of direct transitions and similar valence and conduction band effective masses, the true band gap is related to the optical gap and the chemical potential as $E_g = E_{g,opt} - 2\xi$. The result shows a true gap that decreases significantly with doping level relative to the undoped sample. This is a result of the measured optical gap not increasing as quickly as expected based on the calculated ξ. Over the same doping range, the optical band gap is expected to increase by 2ξ, which is as much as 0.25 eV at the highest doping levels (see Figure 3-5b). The measured optical band gap, however, only increases by about 0.1 eV (about 40% of ξ) at the highest doping levels, as shown in Figure 3-4c/Figure 3-7c/Table 3-1. The relatively small change of the optical band gap can be explained by the renormalization effect, which is an estimate of band gap shrinkage with doping.

The true band gap in Equation 3-5 can also be represented by $E_g = E_{g0} - \Delta_{RN}$, which accounts for a shrinking band gap with increasing doping level as shown in Figure 3-7b. Both experimental and theoretical work has been done to determine how the band gap should shrink due to renormalization with increasing electron concentration in many semiconductors, including Si [47, 67, 80, 96, 97], Ge [96, 98], GaAs [68, 99], InP [79], ZnO [100], and other materials. The effect has proven important in semiconductor device applications where the material's band gap determines many device characteristics and careful engineering is required to optimize performance. Gap narrowing is thought to be due to a combination of effects, including electron-electron exchange interactions, electron-donor interactions, and band tailing [92, 96, 99, 101]. Electron-electron exchange has been shown to scale as $n^{1/3}$ in a weakly interacting free electron gas [96, 100]; this model is often used empirically, although the specific form may vary with crystal and energy band structure. The effect can be thought of as Coulombic repulsion between free electrons in the material, which scales as 1/*r* where *r* is the mean distance between electrons. Experimentally, attempts have been made to empirically fit the theoretical models. Most use a combination of power laws whose prefactors can in theory be calculated, but are most often used as fitting parameters [92, 96, 101]. Drabkin et al., for example, suggest that for PbTe a shift on the order of 10 meV is reasonable for doping levels on the order of 1×10^{19} cm^{-3} [76]. When using the method of Mahan [101], however, the predicted reduction is actually 1 meV or less due to the large static dielectric constant ($\epsilon(0) \approx 400$) for PbTe. Following other references [47, 67], I fit the experimental renormalization to an $n^{1/3}$ power law, including an additional constant term: $\Delta_{RN} = An^{1/3} + \Delta_{RN,0}$. The resulting renormalized fits to the optical and true band gap are plotted in Figure 3-7a and b and are also shown in Table I. Figure 3-7c shows the fitting result for the band gap renormalization. Note that the renormalization does not become non-zero until ξ becomes greater than the conduction band edge ($n > 3 \times 10^{18} cm^{-3}$), which is likely the origin of the $\Delta_{RN,0}$ term.

As mentioned previously, Figure 3-7b shows that the true band gap is rather significantly reduced at high doping levels due to renormalization. For the three most heavily doped samples, ξ, as estimated from Seebeck coefficient measurements, does not continue to increase at the same rate. As a result, the true gap approaches an approximately constant value of close to 0.12 eV. The $n^{1/3}$ model (blue curve Figure 3-7c) deviates significantly for carrier concentrations > ~ 6×10^{19} cm^{-3}, resulting in an estimated gap (blue curve in Figure 3-7b) that rapidly approaches zero above this value. While the magnitude of the gap reduction is consistent with previously published results for heavily doped n-type PbTe [76], Si [47, 67, 80], Ge [98], and III-V semiconductors [68, 79, 92, 99, 102], the apparent discrepancy at high doping is not easily explained using the simple $n^{1/3}$ empirical model.

Table 3-1: Band gap and transport measurement results and chemical potential estimates for this series of samples. All Kane band calculations assume a constant β parameter of ~ 0.087 corresponding to the undoped sample band gap of 0.295 eV. Chemical potentials are presented for the experimental results (ξ_{Seeb}) and model curve fit (ξ_{SKB}) as shown in Figure 3-5b.

x	n_H (10^{18} cm^{-3})	S (μV/K)	ξ_{Seeb}(eV)	$\xi_{SKB}(m^*$=0.276) (eV)	$E_{g, opt}$ (eV)	$\Delta_{RN,Seeb}$ (eV)
0.0000	-	-275.0	-0.030	-0.033	0.295	-
0.0000	-	-230.0	-0.014	-0.022	0.300	-
0.0004	5.87	-141.4	0.021	0.020	0.304	0.033
0.0007	1.03	-109.6	0.039	0.040	0.308	0.066
0.0012	1.76	-81.9	0.067	0.063	0.315	0.114
0.0020	2.94	-66.9	0.086	0.089	0.324	0.142
0.0028	41.1	-52.0	0.108	0.108	0.331	0.181
0.0035	51.4	-43.0	0.126	0.123	0.349	0.199
0.0040	58.7	-42.9	0.115	0.132	0.355	0.170
0.0055	80.8	-41.5	0.122	0.156	0.364	0.175

0.0100	147	-33.7	0.147	0.208	0.388	0.201

In Ravich's adapation of the Kane band model for lead chalcogenides, the band gap is a necessary parameter as it determines the non-parabolicity parameter: $\beta = \frac{k_B T}{E_g}$. Because optical measurements have shown evidence that the band gap in PbTe decreases with doping as a result of band gap renormalization, it might be expected to affect the band structure. The band edge effective mass in narrow gap semiconductors has been suggested to scale with the band gap itself [43, 58]. Ravich suggests that the energy dependent effective mass for a Kane type band should scale with energy as:

$$\boldsymbol{m}^{*}\ (\mathbf{E}) = \frac{\hbar^{2} \boldsymbol{E_g}}{\mathbf{2}\boldsymbol{P}^{2}}\left(\mathbf{1} + \frac{\mathbf{2}\boldsymbol{E}}{\boldsymbol{E_g}}\right) \qquad \text{Equation 3-10}$$

where P is the $k{\cdot}p$ matrix element coupling states between the valence and conduction band states. The first term in Equation 3-10 will scale proportional to the band gap, while the second will scale with E, the electron energy. More often, the prefactor in Equation 3-10 is treated as a constant, m_0^*, the band edge effective mass, which can be fit from the Seebeck coefficient vs. carrier concentration Pisarenko plot. Because m_0^* appears to be independent of carrier concentration, we will only consider the effect of the changing band gap with carrier concentration through the β parameter. In order to probe the effect that this might have on the estimate of ξ and on the transport properties, a self-consistent approach should be taken.

For all of the previous calculations, ξ has been estimated from Seebeck coefficient (Equation 3-8) assuming a constant Kane-band non parabolicity parameter (β used in Equation 3-6 and Equation 3-8) given by assuming a constant band gap of 0.295 eV equal to that of the undoped PbTe sample. Using the fitted n-dependent gap, $E_g(n) = E_{g0} - \Delta_{RN}(n)$, we can self-consistently calculate n as a function of chemical potential with an n-dependent nonparabolicity parameter, $\beta = \frac{k_B T}{E_g(n)}$. The new value of chemical potential was used to recalculate the gap renormalization using the measured optical gaps, which was again fit to an $n^{1/3}$ model. After several iterations, the true gap appeared to converge to a self-consistent value that was slightly higher than the previous result which assumed constant gap. The self-consistent solution yielded renormalization fitting parameters of 5.6×10^{-8} eV-cm and -0.068 eV for A and $\Delta_{RN,0}$ respectively. The band gap, both fit (solid lines) and values from measurements (circles), for the model assuming either constant β or an n-dependent band gap (self-consistent) are shown Figure 3-8a. Renormalized gap estimates were obtained using measured optical gaps and estimates of the chemical potential, ξ (shown in Figure 3-8b). Here, we can see the effect of the band-nonparabolicity as an increasing band mass (which increases even faster as a result of the increasing $\beta(n)$) as the chemical potential rises. At higher carrier concentrations (> 6×10^{19} cm^{-3}), the renormalized band gap value becomes quite small, and errors become larger. Therefore, the fact that $E_g(n)$ levels out at about 0.15 eV may not be entirely accurate since the renormalization effect is probably overestimated at these doping levels. Further, PbTe is known to deviate from the Kane model for carrier concentrations greater than this value [103]. As in the constant β case, the empirical $n^{1/3}$ model may be an oversimplification in the case of increasingly narrow gap and/or the simplified Kane model of Ravich may also be an oversimplification that cannot account for these narrowing phenomena.

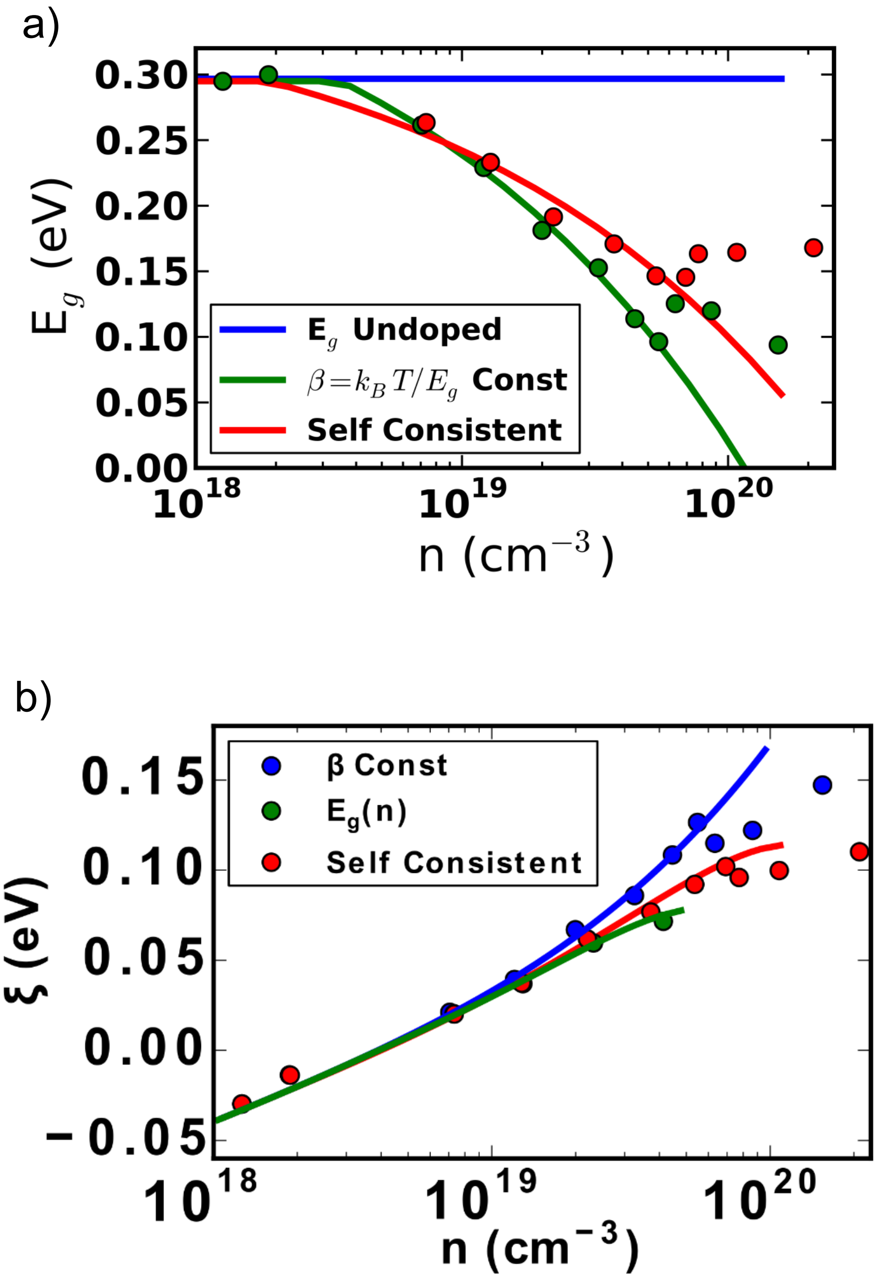

Figure 3-8: Iterative self-consistent calculation of the true gap $E_g(n)$ in accordance with the Kane band model. a) The result of different n-dependences of the Kane β parameter solid points represent $E_g(n)$ in accordance with eq. 5 (using the measured optical gaps and chemical potential estimates from Seebeck coefficient measurements). b) The estimated chemical potential as a function of doping level for different dependence of β on n; lines represent constant effective band edge mass (Eq 3, m^*_0 = 0.276 m_0) and points are calculated from Seebeck coefficient (Equation 3-8).

In the discussion of electronic band structure it is typically a good first approximation to assume the energy bands remain unaltered with doping, which is known as the rigid band approximation. Lee, Mahanti et al. give some examples where this may not be a good assumption in Na doped PbTe [104], although the picture here is complicated by the variability in supercell calculations [105]. Experimental measurements of effective mass can show small changes in band structure when using different dopants (I or La) in PbTe, which may be related to a shift in band gap [106]. With the goal of band engineering in mind it is important to be able to determine how the band structure is altered as the materials are doped or alloyed. While the rigid band approximation works reasonably well for many purposes, this work demonstrates that the differences between true, optical, and thermal band gaps can be different of the order 0.1 eV (which is quite large considering that the true gap is ~0.3 eV). Most thermoelectric materials are heavily doped semiconductors, where $E_{\mathrm{g,thermal}} >> k_{\mathrm{B}}T$. In this case, the electronic transport properties (electrical conductivity, Seebeck coefficient) are determined by a single band. The most obvious effect of a narrower band gap is the increased concentration of minority carriers. In the case of most thermoelectric materials, though, the chemical potential (and thermal band gap) is deep enough into the band to where the minority carrier population is still very small compared to majority carriers. The effects become more apparent at high temperatures when $k_{\mathrm{B}}T \sim E_{g,th}$.

While band gap renormalization is a well-known effect that has been studied in many materials, it is generally ignored in thermoelectric materials in favor of the rigid band approximation. This work suggests that in PbTe, both approximations may play a role. While it seems unlikely that the band gap in these materials might become very small (or even approach zero), it is possible that if the material is sufficiently doped that bipolar effects can be suppressed and a reduced band gap would not be observed by measuring transport properties alone.

Ultimately, the apparent discrepancy between the rigid band approximation and band gap renormalization may need to be resolved with either better estimates of the *n*-dependent chemical potential, or by developing models that more accurately represent renormalization in narrow gap semiconductors. Perhaps more experimental and theoretical work should be done to investigate what is different in narrow gap, heavily doped semiconductors from other wider gap materials.

3.4 - Conclusions

While the DRIFTS method of measuring the optical absorption has been thoroughly explored in catalysis research and has shown some promise for quantifying chemical reactions [107, 108], as a technique for precisely determining band gaps in semiconductors diffuse reflectance has only proven semi quantitative (±0.1 eV) [109]. In this work, we detect shifts in band gap with doping of smaller than 0.01 eV in PbTe, which can be analyzed and understood by methods consistent with current optical literature.

While electronic transport measurements are essential to determine the thermoelectric properties for a materials, optical properties can provide more direct knowledge about the band structure. Although diffuse reflectance measurements have been used in the thermoelectric literature, it is important to account for the effects of electron population on the absorption edge that alters the observed optical band gap. I have shown a series of iodine doped PbTe samples which show a Burstein-Moss shift in the absorption edge to higher frequencies. Using estimates of the chemical potential from transport measurements, it is possible to estimate that a gap shrinkage of up to 0.15 eV occurs at the highest doping levels appropriate to thermoelectrics. An attempt is made to fit the true gap self-consistently using a single band Kane model, which results in a slight reduction in the renormalization. While renormalization has been shown to fit well-behaved empirical models for many semiconductors, PbTe (and possibly other narrow gap materials) exhibits a Burstein-Moss shift and renormalization that are not readily explained with existing theory.

Ultimately, even though the effects of doping on the value of the band gap can be accounted for using the Burstein Moss shift and renormalization effects, measuring undoped samples is preferred when trying to distinguish small shifts due to temperature or alloying. But, because it is not always possible to make undoped samples due to intrinsic defects, it is important to be able to recognize the effects of doping on optical absorption edge measurements and to be able to account for differences that they may cause.

Chapter 4: Multi Band Behavior, Optical, and Electronic Properties in IV-VI materials

4.1 - Introduction

In this chapter, I will give a detailed account of my work in the IV-VI materials (PbTe, PbSe, PbS, and SnTe). Because this family of materials has been extensively studied since the 1950's, an account of some of the historical findings along with the current state of the field will be outlined. My contribution comes in largely in the context of band engineering in these materials, both through optimization of the electronic properties (SnTe, PbSe/SrSe alloys) and through determining the nature and effects of the temperature-dependent shifts in the band structure which are known result in improved performance at high temperatures.

Even though there is a wealth of historical work on the lead and tin chalcogenides over the last 60 years, the topic has received resurging interest over the last few years. This is largely due to the newly established method for measuring the thermal conductivity: the Laser Flash Apparatus (LFA, discussed in Chapter 2). LaLonde et al. reports that some of the more commonly cited zT estimates for the lead chalcogenides did not explicitly measure the high temperature thermal properties; rather, they were extrapolated from a room temperature lattice thermal conductivity and a high temperature resistivity (using the Wiedemann-Franz law)—this resulted in an overestimation in κ of ~30% [110]. In fact, the LFA method (even though it was available beginning in the 1960's) was not widely applied to the lead chalcogenides until recently. With the combination of optimal doping levels and the more modern and accurate method for measuring the thermal conductivity at high temperatures it has been found that optimally doped binary PbTe can reach zT of up to ~1.4 for n-type and up to 1.5 for p-type at high temperatures; the modern result is nearly double that of many of the 1960's measurements. Since then, many groups around the world have been reporting high zT values, many even higher than the doped binary samples through alloying with other elements. Recent reports on PbTe and its alloys have suggested an extraordinarily high peak *zT* of between 1.0 and 2.2 in the temperature range useful for waste heat recovery depending on the specific dopant and alloy [18, 28, 34, 111-113].

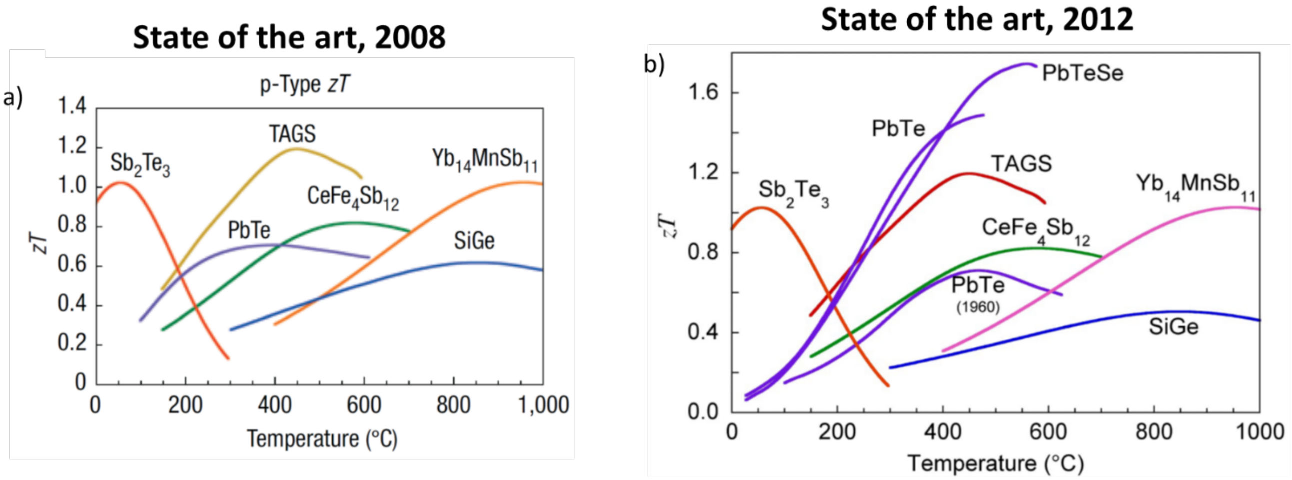

Figure 4-1: Illustration of the rapidly changing state of the thermoelectrics field which until ~2010 believed that the optimum in zT was much less than 1.0. a) was taken from [114], and b) from [110].

4.2 - Lead Chalcogenides, Band Engineering, and Band Convergence

While optical properties measurements are commonly used for characterizing semiconducting materials, electronic measurements are much more commonly performed for thermoelectric materials (neglecting optical properties). This is likely because the goal is to produce a large *zT*, but not necessarily to understand the electronic structure which produced it. In this section, I will apply a combination of optical and *ab-initio* computational analyses to understand the electronic band positions in the lead chalcogenides, particularly how they change as a function of temperature. Multiple band effects have been identified as being responsible for enhancing thermoelectric properties; I will thoroughly review the literature on this topic in the lead chalcogenides as well as provide insight using a combination of optical properties, electronic properties, and *ab-initio* calculations.

4.2a - Lead Chalcogenide Literature Review

In p-type PbTe a complex valence band structure exists that has been described with two valence bands: a lighter band at the *L* point (direct) and a heavier along the *Σ* line in the Brillouin zone [15, 16, 58, 85, 86, 115-120] as shown in a later chapter (Figure 7-1). The enhanced thermoelectric efficiency in PbTe is attributed to valley degeneracy arising from band convergence, which yields higher thermopower without greatly reducing carrier mobility [16]. The region of electronic states along the *Σ* line has been described and modeled as a separate, heavy band, even though recent work suggests that it may be associated with the band at *L* [91, 117, 121]. However, two-band transport analysis, e.g., when both bands are considered separately, is consistent with most experimental observations and is useful for rational thermoelectric material design; therefore, in this chapter we will refer to these states as a separate band at *Σ* [15, 16, 18, 122]. Based on historical evidence [123-125] and calculations [84, 86, 91, 117], the band extremum at *Σ* is believed to lie about 0.1 – 0.15 eV below that of the band at L at room temperature (See Figure 1-3 and Figure 4-2). Still, the exact band energies and their temperature dependence continue to be disputed [16, 91, 117, 121]. The other IV-VI materials are known to have larger *L*-*Σ* offsets of approximately 0.25 [126, 127], 0.5 [126], and 0.4 [128-130] eV for PbSe, PbS, and SnTe at room temperature, respectively. The band offset in all of the IV-VI materials is known to be temperature dependent, and the primary and secondary valence bands are thought to move towards each other at a rate of ~$2-4\times10^{-4}$ eV/K [16, 27, 39, 60, 87]. Both the temperature dependence and the offset can be modified through alloying with a variety of elements (cation: Sr, Ca, Mg, Mn or anion: S, Se, Te) [15-18, 21, 25, 42, 131], often resulting in very good performance. While several groups have discussed nano/micro-structuring to improve thermoelectric performance [12, 21, 131, 132], which is generally thought to be a result of reduction of thermal conductivity through additional phonon scattering, a fully optimized thermoelectric material will likely require some combination of alloying/nano-microstructure to benefit from the effects of reduced thermal conductivity as well as band engineering. Furthermore, it is important to be able to separate the nano-structuring effects in order to better quantify them; in this thesis I will be focusing on understanding the electronic band structure and band engineering in these materials and I will therefore avoid samples which have detectable amounts of precipitates (nano or otherwise). Knowledge of the specific band offset and its temperature dependence in these materials is crucial since band convergence is thought to be responsible for the improved thermoelectric properties. Hence, this work is motivated by the hope that a more accurate understanding of the electronic band structure can provide a clearer route forward to band structure engineering in the lead chalcogenides for further improvement of *zT*.

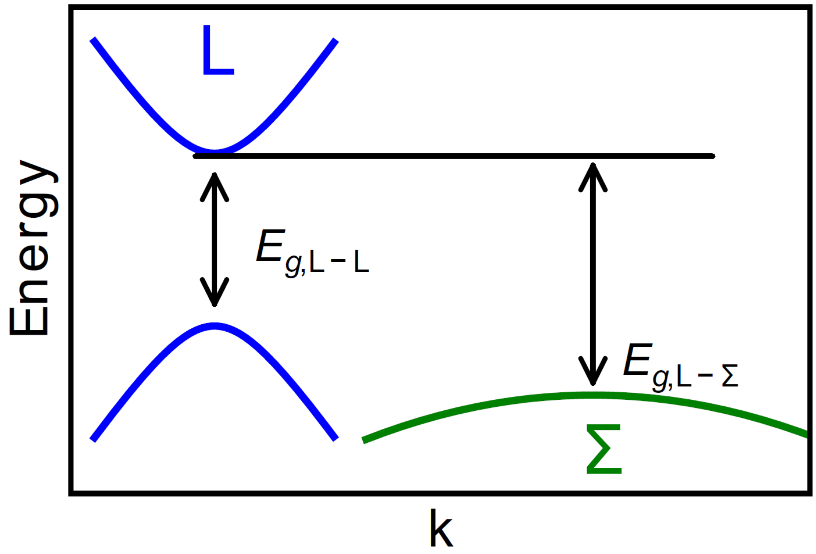

Figure 4-2: Schematic representation of the L and Σ band extrema in PbX (X=Te, Se, S) and SnTe (as presented in previous work[126]).

Electrical and magnetic measurements have been performed previously to characterize the energy band structure, including estimates of the valence band offsets and their temperature dependence [115, 121, 123-125, 133-137]. Nevertheless, interpretation of the results depends upon transport models. Optical absorption edge spectroscopy in semiconductors is a more direct route to obtain information about electronic states near the band edge (E_g), which can be used in conjunction with transport models to experimentally map out the electronic structure.

Historically, optical data on the PbX materials have been plentiful. Early data from the 1950's and 60's [27, 36-39, 74, 75, 138-149] provided a good foundation for both the low temperature [27, 38], room temperature [37, 38, 74], and temperature dependent band gaps [27, 36, 39, 141, 143, 145] are widely cited in the field. Many works since then have aimed to perform more careful characterization of the IV-VI materials and their alloys [41, 42, 81, 148, 150-153], including estimates of the valence band offset (though interband-valence band absorption [38, 90]), additional comments on the origin of their temperature-dependence [87, 154], band non-parabolicities [151], possible resonant/impurity states with In [155-157] and Tl [157, 158], and some helpful reviews [60]. As mentioned in Chapter 2, many of the previous reports of optical band gap measurements on PbTe have used single crystal samples measured in transmission [27, 36-42], which, in many cases, limited their maximum measureable absorption coefficients. Spectroscopic ellipsometry can bypass the necessity for the Kramers-Kronig analysis by measuring both the real and imaginary components of the dielectric function simultaneously, and some studies of lead chalcogenides as photodetectors or infrared lasers use these techniques [159, 160].

Regarding thermoelectric efficiency, the main point that comes into question for these materials is their L-Σ band offset, temperature dependent shifts in ΔE, and the temperature at which the bands are effectively converged, T_{cvg}. The most widely cited article that reports T_{cvg} for the lead chalcogenides is one of the earlier reports by Tauber et al. in 1966 [27] indicating a plateau in the indirect band gap at approximately 400 K for PbTe (Gibson et al. observe the plateau for all of the lead chalcogenides around this temperature [36]). The band offset and convergence temperature supposed by Tauber et al. has been widely used in the field and has been supported by other evidence, including a peak in the Hall coefficient at around this temperature [16, 135]. However, recent work points out some discrepancies in the literature data [91, 121]: poor resolution of the early optical data (Miller et al. have a resolution of 7 meV [161]), improper extrapolation of the absorption edge (often incorrectly assumed to be indirect [27, 161]), and that a wide range of values for $\frac{d\Delta E}{dT}$ (where ΔE is the offset between the L and Σ bands) that are reported from $2-4\times10^{-4}\,\frac{eV}{K}$. In order to help resolve some of these questions, I have performed measurements using diffuse reflectance infrared Fourier transform spectroscopy (DRIFTS) on polycrystalline samples for the lead chalcogenides over a broad range of temperatures; I compare the results to *ab initio* molecular dynamics (AIMD) calculations to study the temperature dependent gap and examine the band structure at high temperatures.

The positive temperature coefficient of the band gap in lead chalcogenides, unlike many common semiconductors, is favorable for thermoelectric materials. An increasing gap with temperature can act to suppress bipolar effects caused by intrinsic carrier activation, increasing the optimum *zT*. The temperature dependent gap in PbX is known to be due to both lattice expansion and electron-phonon interactions [39, 87, 162]. The effect can be described by:

$$\boldsymbol{\frac{dE_g}{dT} = \left(\frac{dE_g}{dT}\right)_V - 3\alpha_L K_B \left(\frac{dE_g}{dP}\right)_T} \qquad \text{Equation 4-1}$$

where α_L is the linear thermal expansion coefficient ($\frac{1}{L^*}\left(\frac{dL^*}{dT}\right)_P$), K_B is the bulk modulus ($-\frac{1}{V}\left(\frac{dV}{dP}\right)_T$), $\left(\frac{dE_g}{dT}\right)_V$ describes the electron-phonon interactions, and $\left(\frac{dE_g}{dP}\right)_T$ is the band gap dependence on pressure [39, 60, 87]. Prakash et al. performed detailed pressure dependent optical measurements to determine that $\left(\frac{dE_g}{dP}\right)_{T=300K}$ was equal to -9.15, -9.1, and -7.4 x10^{-6} eV/bar for PbS, PbSe, and PbTe respectively. This measurement is comparable with *ab-initio* calculated figures obtained in a more recent reference, which obtained -6.85 x10^{-6} eV/bar for PbTe [163]. Prakash estimated that the electron-phonon interaction term $\left(\frac{dE_g}{dT}\right)_V$ was approximately 40%, 40%, and 60% of the overall change in dE_g/dT for PbS, PbSe, and PbTe, respectively.

4.2b - Results

AIMD Calculations

In order to probe the effects of temperature on the electronic bands, I took a two-pronged approach involving both temperature-dependent optical measurements and *ab-initio* calculations performed by our collaborators Hyunchul Kim and Massoud Kaviany (University of Michigan). *Ab-initio* molecular dynamics (AIMD) calculations combine electronic structure calculations (DFT) with molecular dynamics (MD) calculations. While ab-initio calculations are inherently performed at T=0 K (no lattice vibrations, simply minimizing the energy of the system), MD allows us to simulate how a material might actually look at high temperature by allowing the atomic positions to move from their equilibrium values. Snapshots are taken once the computed temperature is equal to the desired one, and a DFT calculation is performed on the perturbed supercell. By performing AIMD simulations coupled with DFT band structure calculations on supercells, we were able to calculate the effect of the thermal motion of the atoms in PbX on both the direct (*L*) and indirect (*Σ*) band gaps, the results of which are shown in Figure 4-3 (points and solid lines). For all of the lead chalcogenides, the direct (*L*-*L*) band gap increases from low temperature with a slope (dE_g/dT) that decreases as temperature is increased. The indirect (*L*-*Σ*) gap increases at a slower rate with temperature for PbTe, but decreases with temperature in PbSe and PbS, resulting in a convergence temperature (T_{cvg}) of about 700, 900, and 1000 K for PbTe, PbSe, and PbS, respectively. The dashed line in Figure 4-3 represents the effect of lattice expansion alone; it is clear that both electron-phonon interaction and lattice expansion make significant contributions to dE_g/dT. The electron-phonon contribution does appear to grow weaker as the temperature increases for all materials in comparison to contributions to dE_g/dT due to expansion only. Still, in the absence of electron-phonon interactions, the bands would not converge until a temperature greater than the melting point of PbX. Hence, the presence of electron-phonon interactions, exclusive to AIMD calculations, is required in order predict band convergence at the temperatures that we observe experimentally. In comparison to Prakash's estimate, we obtain that the portion of the electron-phonon contribution to dE_g/dT, $\left(\frac{dE_g}{dT}\right)_V$, is 37%, 41%, and 67% for PbS, PbSe, and PbTe, respectively, all of which agree well with Prakash's estimates [39]. Furthermore, our calculations show that the gap at Σ changes relatively little (particularly in PbTe) and that band convergence is primarily the result of electron-phonon interaction on the L bands.

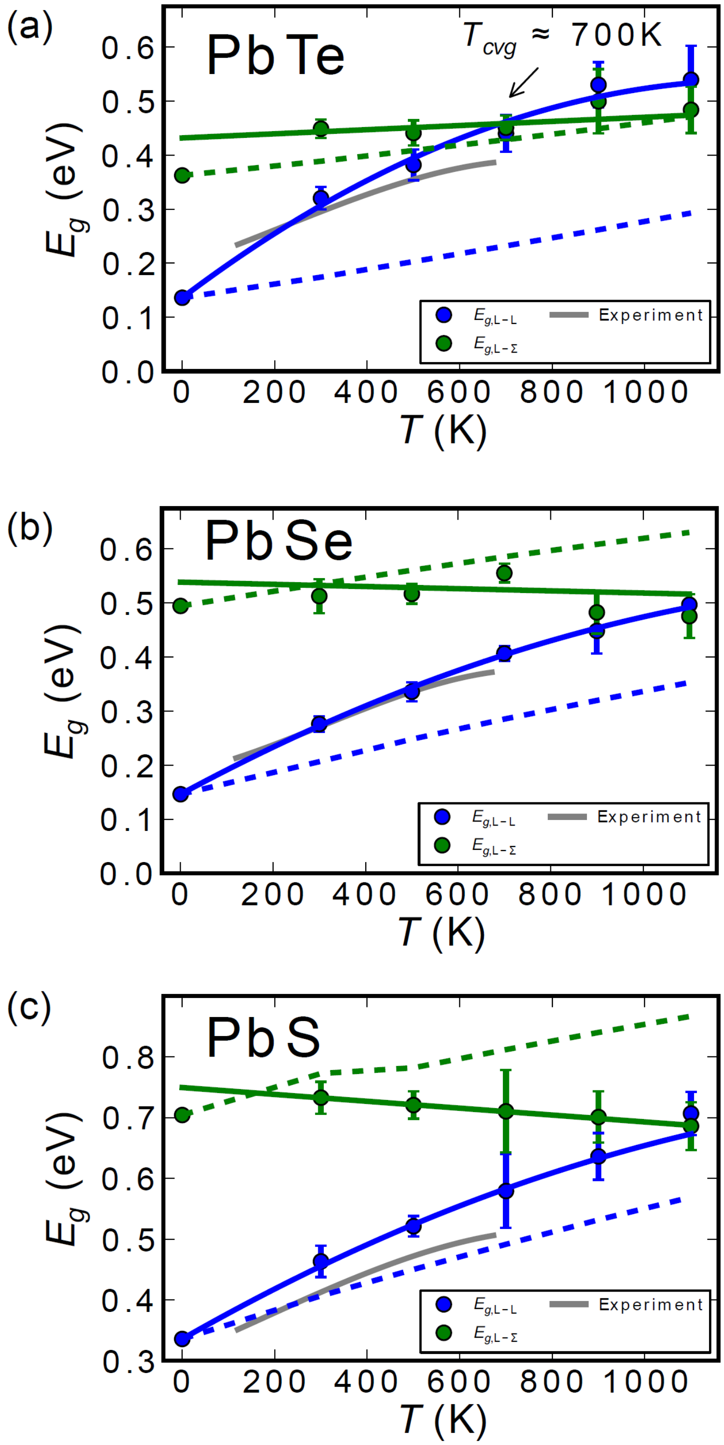

Figure 4-3: AIMD calculated temperature dependent band gap for a) PbTe, b) PbSe, and c) PbS. Circular points represent the computed (electron-phonon + expansion) average value over several snap shots (along with the error bar plotted as a standard deviation), and solid lines represent a guide to the eye. Dashed lines show the change in band gap when electron-phonon interactions are not considered (thermal expansion only). The grey line indicates a best fit to the experimental result.

Experimental results are also obtained in the form of temperature dependent optical absorption spectra (Figure 4-4a). It should be noted that undoped samples were measured in order to avoid the Burstein Moss shift and other complexities that are encountered when trying to interpret optical results in doped samples (as detailed in Chapter 3). Figure 4-4b and c show the extrapolated direct gaps, as well as reported values from the literature. A linear fit of the changing gap up to 500 K returns a value for dE_g/dT = 3.2 ± 0.1 (10^{-4} eV / K), which is almost the same for all PbX (X=S, Se, Te). Several works report a value for dE_g/dT in the range 3.0 to 4.9×10^{-4} eV/K [27, 36, 39, 87, 140, 164, 165], although generally the values are on the higher end of this range. In agreement with the references, the rate of change is mostly linear from low temperature (100 K) to room temperature and does not vary depending on the particular chalcogen atom. However, the actual band gap value depends on how it is obtained from the absorption edge. In addition to the value of the band gap, its temperature dependence is important because of what it implies about the relative positions of *L* and *Σ* extrema and their contributions to the thermoelectric properties, which optical band gap measurements have played a role in determining [27].

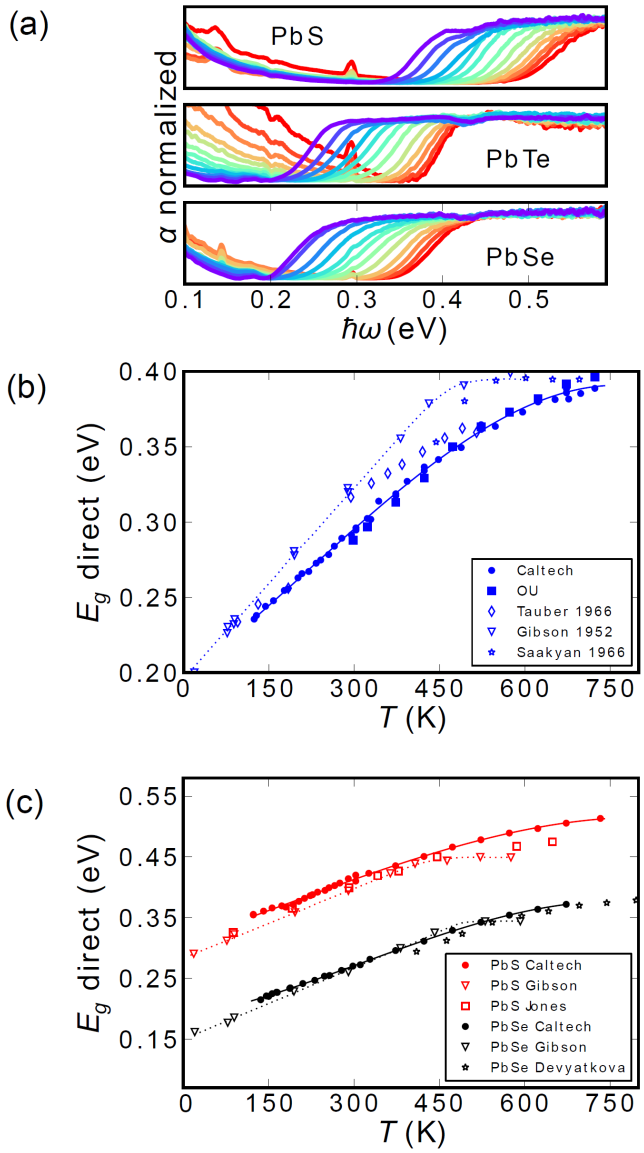

Figure 4-4: a) Temperature-dependent optical absorption spectra for PbS, PbTe, and PbSe. b) Extrapolated direct band gap as a function of temperature for PbTe measured at Caltech, OU (University of Oklahoma), Tauber et al. [27], Gibson et al. [36], and Saakyan et al. [166]. c) Extrapolated results for PbSe and PbS measured at Caltech along with references from Jones et al. [143] and Devyatkova et al [136].

4.2c - Discussion, Impact, and interpretation of the results

As mentioned previously, both Gibson (1952) and Tauber (1966) both showed an increasing band gap that stopped changing above 400 K [27, 36]. Tauber interpreted this as a shifting primary valence band (which is now known as a direct gap at the L point) that is replaced by the secondary valence band (*Σ*) above 400 or 500 K in PbTe. Tauber's work is widely cited as evidence of the convergence temperature, T_{cvg}, in PbTe. Band convergence, however, does not require a plateauing optical band gap. Direct transitions (*L*-*L*) have been shown to be 10-100x as strong as indirect ones, which require both photon and phonon participation [48]. In fact, without sufficient separation between the indirect and direct gaps, it may be difficult to distinguish the smaller indirect absorption edge from the exponential Urbach tail (an exponential tail in density of states into the band gap resulting from impurities and disorder in the material, discussed in Chapter 3.2b). Consequently, we expect that the temperature dependent optical band gap should continue to increase even if the *L* and Σ bands had converged—suggesting that Tauber's aforementioned results cannot be used as direct evidence of *L* and Σ valence band convergence. Upon re-extrapolating the Tauber et al. absorption spectra (which was necessary since only indirect transitions were fit) using Tauc extrapolation, the resulting band gaps do continue to increase, contrary to the conclusions of Gibson and Tauber. Our results, shown in Figure 4-4b and c, show that the optical gap continues to increase for temperatures greater than 673 K, albeit at a lower rate above 500 K. In fact, several other authors have observed no plateau in the band gap via optical measurements in PbTe [154, 167], PbSe [127], and PbS [143]; however, these articles are not generally cited in more modern investigations. In this thesis, both experimental and AIMD results suggest that the band convergence temperature is much higher than 400 K, suggested by Gibson and Tauber et al., and that T_{cvg} is actually closer to 700 K in PbTe.

The temperature dependence of electronic transport properties (resistivity, Hall effect, and Seebeck) can also be used to estimate the band gap. Devyatkova and Saakyan et al. [136, 166] (also shown in Figure 4-4b and c) measured the electronic/thermoelectric properties of both n and p-type samples in the bipolar regime to estimate the temperature dependent gap using an extrapolation technique for the single parabolic band model. They obtained a constant gap for temperatures greater than 550 K in PbTe and one that increased continuously until 800 K in PbSe. These estimates seem to be consistent with results from this work, although both calculation and optical measurement from this work suggest a somewhat higher convergence temperature. This may be a result of the fact that effective convergence (as in the bands are within a few k_BT of each other and both contribute significantly to transport) can occur at temperatures lower than the true convergence temperature, which will be discussed in detail in Figure 4-6a-c.

The question of whether the absorption edge can provide evidence of band convergence is an interesting one that is of great importance for both the scientific community and this thesis. Usually, one will make a Tauc plot scaled to the appropriate power in order to determine whether a material shows direct or indirect transitions (as outlined in Chapter 2). This is usually determined by fitting the linear portion of the appropriate Tauc plot and extrapolating back to zero absorption. In the case of the lead chalcogenides, however, this simple exercise seems to yield confusing results. Part of the reason that many of the early works on the subject concluded that PbX had an indirect band gap is because the absorption edges (even though we know that the primary band gap is direct) give good linear extrapolation fits for both direct and indirect gaps. This has been observed and discussed by a few authors [37, 39] who provide different explanations. Because the extrapolated indirect gap usually falls ~ 0.02-0.05 eV below the extrapolated direct one, Scanlon et al. proposed that the indirect edge could be a result of k=0 phonons imparting their energy (but not their wave vector) to the excited electron, resulting in some indirect contribution to the *L-L* direct gap transitions [37]. Prakash tends to believe that this linear indirect region is actually a coincidental fit in the region between the Urbach edge, and the direct absorption edge [39]. Regardless, of who is correct, it is necessary to understand why Tauber and Gibson's data yields a maximum in band gap. We suspect that it may be related to the fact that both Gibson and Tauber et al. used optical transmission through relatively thick samples, limiting the maximum measurable absorption coefficient to hundreds of cm^{-1}. Combined with an increasing baseline absorption coefficient as temperature increases, Gibson and Tauber were only observing the very bottom of the absorption spectrum at high temperatures. DRIFTS, however, seems to measure a broader range of absorption coefficient. To test this hypothesis, we will consider both the direct and indirect extrapolations (Figure 4-5). Due to the nature of the transformations, direct transition extrapolations tend to favor higher absorption coefficients (absorption coefficient is squared), while indirect ones tend to enhance the lower magnitude absorption coefficient.

In order to investigate whether the assumption of direct gap may have resulted in overlooking the indirect L-Σ gap, I have plotted the extrapolation for both the direct and indirect gaps as a function of temperature for each of the lead chalcogenides in Figure 4-5. Here we can see that the temperature-dependent slope of the indirect and direct gaps are very close to the same values in all of the lead chalcogenides, indicating that the two extrapolations are intimately linked. In order to determine whether the indirect L-Σ band gap actually becomes the primary one, we would be looking for some break in this pattern, perhaps a maximum in the indirect gap as observed by Tauber (while the direct one continues to grow). However, in all of the lead chalcogenides, both the direct and indirect extrapolations seem to change together, with the only exception being the very highest PbTe data points; between 350 and 400°C the direct gap seems to grow more slowly than the indirect gap—resulting a nearly constant indirect gap. While this could indicate that the indirect, L-Σ gap is becoming the primary one for PbTe above these temperatures, a single data point does not constitute a trend. Further, the sample could not be taken to temperatures much higher than ~400°C because of significant evaporation that quickly coated the windows. Therefore, we have concluded that all of the lead chalcogenides show direct-gap behavior over the entire temperature range (up to 400°C) with no evidence of indirect transitions becoming the primary ones. This finding is consistent with the AIMD calculations, but differs from Gibson and Tauber's conclusions, which we attribute to their low maximum measurable absorption coefficients due to a relatively large sample thickness measured in transmission.

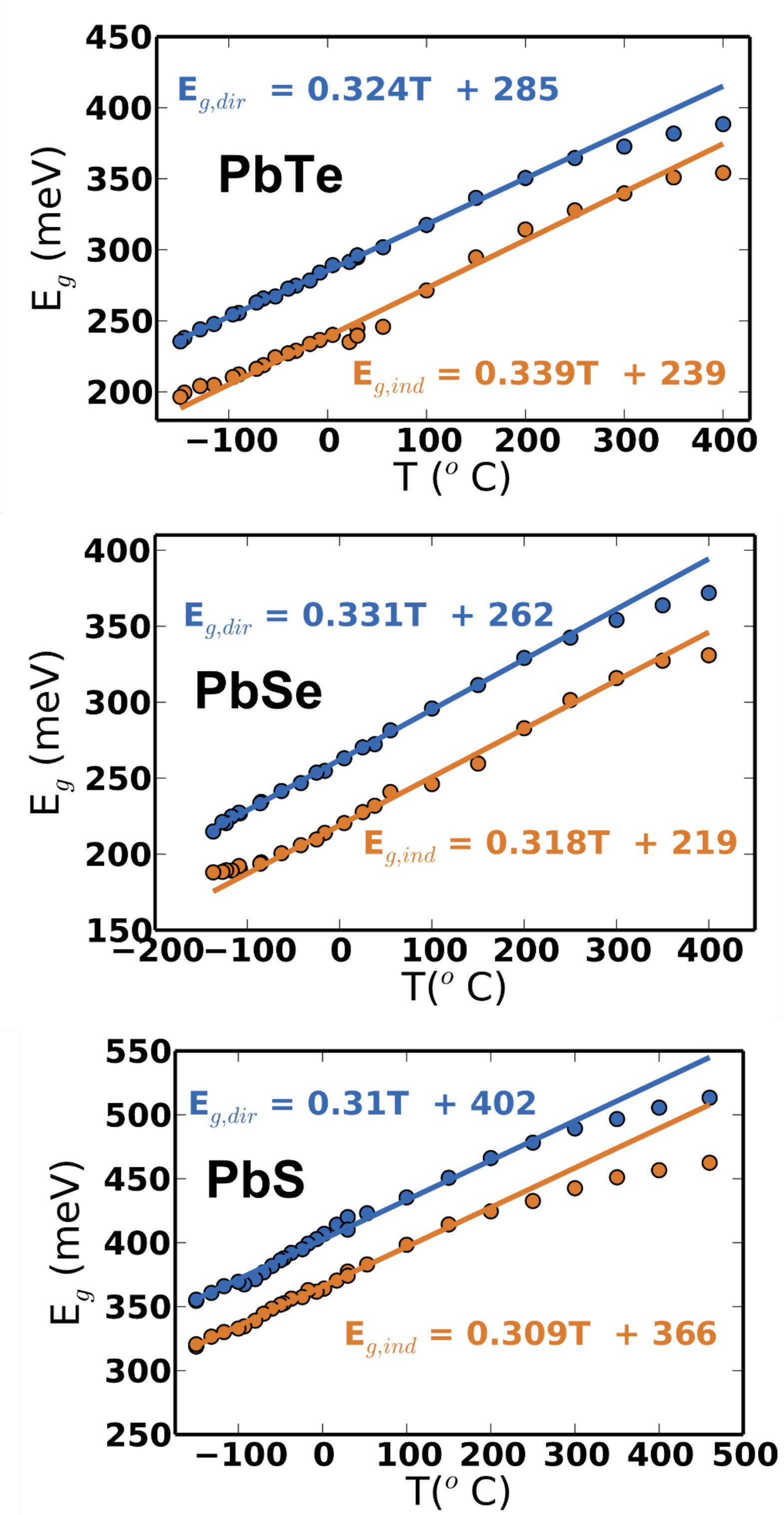

Figure 4-5: Temperature dependent band gap for the direct (dir) and indirect (ind) extrapolations of the absorption edge along with linear fits as functions of temperature for PbTe, PbSe, and PbS.

The implications that a higher T_{cvg} has on other conclusions about the temperature dependent band structure of PbTe are that the temperature-depdnent L-Σ offset should be reconsidered. Historically, valence band offsets in PbX samples have been determined by intra and inter-valence band free carrier absorption measurements with photon energies less than the fundamental gap [74, 90, 116]; this is an experimental method for determining the L-Σ energy offset directly. Values of 2-4×10^{-4} eV/K were reported for the temperature dependence of the offset between the two valence bands using these techniques [90, 127], which approximately agree with estimates from transport properties [121]. However, the range of values mean that the answer is still an open one. Several methods of estimating the L-Σ offset (ΔE) and T_{cvg} are available, including free carrier absorption, band gap measurements as shown in this work (which can be used to indirectly infer the inter-valence band behavior), and temperature-dependent electronic transport properties.

As an example of how electronic transport measurements have been used to estimate the band offset, it has been suggested that a peak in the Hall resistance with temperature implies band convergence and can be used as an estimate of T_{cvg} [15, 16, 123, 124]. Interestingly, these results show a peak around 450 K for p-type PbTe, consistent with the T_{cvg} estimate of Tauber et al. However, as pointed out by Jaworski et al., this represents the temperature at which the conductivity of carriers in either band are equal and not necessarily when the bands are at the same energy [121]. We tested this hypothesis using a two valence band transport model consistent with Pei et al [16] with a different band convergence temperature (consistent with the 3.2×10^{-4} eV/K, convergence at 700 K and a slightly lower L-band effective mass of 0.26 m_0). We modeled a Hall coefficient peak at around 450 K (approximately where the L and Σ band conductivities are equal), even though the band convergence does not occur until 700 K. This result suggests that a higher convergence temperature is not in conflict with the Hall coefficient peak observed around 450 K.

While this study shows that the band convergence temperature is higher than previously believed, it also confirms that such a convergence should indeed occur at high temperatures. However, just because the actual convergence may not occur until 700 K in PbTe, this does not mean that the electronic transport properties will not reflect contributions from the Σ band at lower temperatures. It is understood that electronic transport properties are determined by the bands within 3-4 k_BT of the chemical potential. This means that effective convergence can occur when the L and Σ bands are within this energy-range of each other. In order to illustrate effective convergence, I plot the projected Fermi distribution along with the calculated temperature-dependent Fermi distribution in Figure 4-6 a-c. In this figure, we see a lower effective convergence temperature of ~600, 800, and 850 K for PbTe, PbSe, and PbS, respectively, consistent with the observations of high zT in these materials at high temperatures.

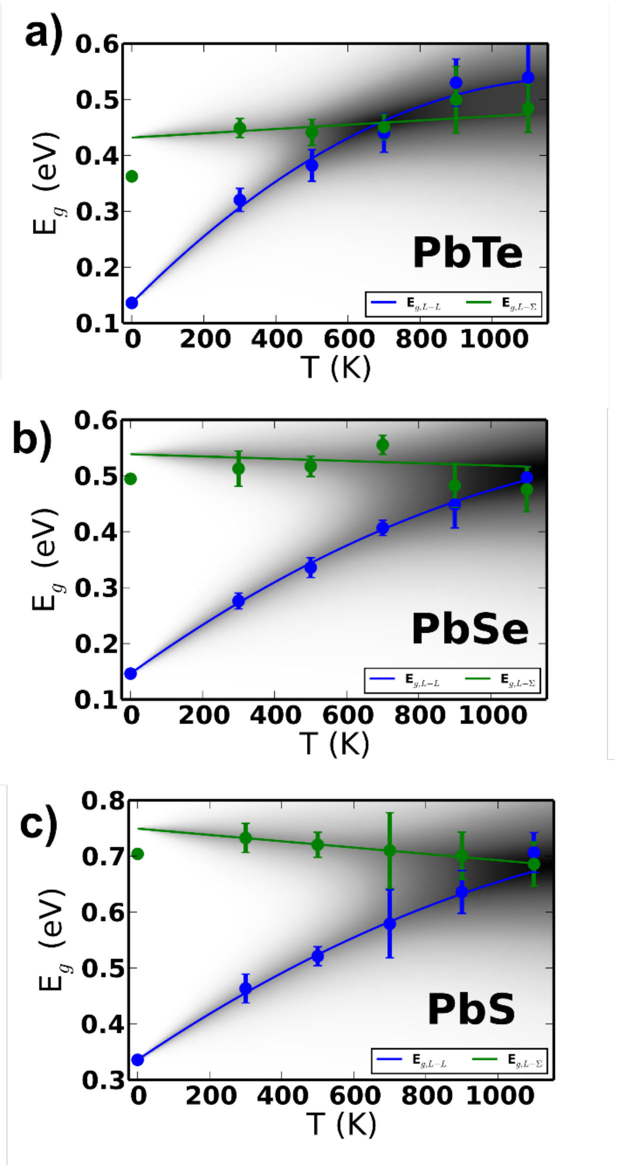

Figure 4-6: Calculated temperature dependent gap between either the L or Σ valence bands and L conduction bands for a) PbTe, b) PbSe, and c)PbS with temperature-dependent Fermi distrubtion overlayed indicating that the region of effective convergence occurs at temperatures below the actual T_{cvg}.

4.2d - Conclusions

While electronic transport models have used band convergence temperatures of 400-500 K to adequately describe the transport properties in PbTe [16], a higher convergence temperature is not necessarily inconsistent with these results. The observance of effective convergence at ~600 K indicates that the effect of the Σ band is still significant for transport in binary PbTe. Optical absorption edge data show an increasing optical gap with temperature at a rate of ~3.2×10^{-4} eV/K for all three lead chalcogenides up to 500 K (whereas the slope above that is smaller and steadily decreasing). AIMD calculations deduce that about half of the contribution is due to lattice expansion, while the rest is due to electron-phonon interaction. Contrary to prior temperature dependent optical absorption literature, this work suggests that the optical gap continues to increase for temperatures up to 673 K. While previous work used the E_g plateau in PbTe as evidence of the convergence temperature, our results suggest that the plateau does not occur at such low temperatures. Optical absorption and AIMD DFT calculations in this work both suggest that the band convergence in PbTe occurs at about 700K a temperature higher than concluded previously. Future sections of this thesis will focus on strategies for enhancing thermoelectric properties through band convergence by alloying.

4.2e - Methods

Optical characterization for this section was done using DRIFTS. Direct and indirect extrapolations of the optical band gaps were performed using the Tauc method as described in detail in Chapter 2.

AIMD simulations were performed by my collaborator Hyounchul Kim and Massoud Kaviany of the University of Michigan to describe the effects of temperature on the band structures of the lead chalcogenides according to the methods described in a previous work[162]. The temperature-dependent lattice dynamics were calculated using AIMD considering the Fermi-Dirac smearing factor and the thermally expanded lattice parameter from experimental results: $a(T) = 6.422 + (0.9545\times10^{-4})T + (2.615\times10^{-8})T^2$ [168]. Calculations were performed on large supercells (54 atoms) and the near edge band positions were averaged over three snapshots per temperature. In the calculations of band gap energy as a function of temperature, we only consider the maxima of the valence and conduction bands at the L and Σ points in the band structure. This is done to exclude some band splitting and shifting. We note that above-mentioned choices (data averaging of several snapshots and the different calculation schemes) result in a spread of values for which error bars are plotted. Sample synthesis details are given both in Chapter 2 and in the original paper on this topic [126].

4.3 - Band Engineering and Band Convergence through Alloying in the Lead Chalcogenides

4.3a - Introduction

Thermoelectric performance in the lead chalcogenides has proved to be among the best of any potential thermoelectric material in the 600K – 800K range. As mentioned previously, many attempts at engineering the electronic band structure in PbTe and other IV-VI materials have been successful at improving the thermoelectric properties [15-17, 21, 25, 131, 169, 170] . In this section, I will highlight a successful band engineering attempt in PbSe by alloying with SrSe, which I did in collaboration with my colleagues Heng Wang and Yoshiki Takagiwa [25]. Alloying in this case improves the properties by pushing the valence bands closer together (as a result of the widening L-L band gap), which we observe through electronic/optical properties and computed *ab-initio* density of states.

In PbSe and PbTe, the secondary valence band maximum (along the Σ line of the Brillouin zone) contributes significantly to the thermoelectric performance at high temperatures [58, 127, 136, 166]. The best thermoelectric performance is found around temperatures where the two valence bands are converged (within a few k_BT of one another) [16, 26]. For PbTe the convergence temperature (T_{cvg}) has been shown in the previous section to be around 700 K (with effective convergence occurring above ~600 K—Figure 4-6a). In PbSe, the Σ band is further away [127, 171] (~ 0.25 eV at 300 K) from the primary band maximum at L, resulting in a higher T_{cvg} (~900 K, ~800K for effective convergence; Figure 4-6). Early works [58, 137, 172, 173] based on Hall coefficient data confirm this result, suggesting a T_{cvg} around 750 K for binary PbSe. In order to enhance thermoelectric performance in PbSe, it is beneficial to reduce T_{cvg} by tuning the secondary valence band position; in this section we accomplish this by alloying with SrSe.

One strategy that has been successful at reducing ΔE in PbTe [14, 15] has been alloying with alkaline-earth chalcogenides (MgTe) that also have the rock salt crystal structure and wide band gaps. Previous results have shown that it is possible to grow $Pb_{1-x}Sr_xSe$ thin films via molecular beam epitaxy (MBE) where the lattice constant changes gradually following the Vegard's law; this is accompanied by a tunable band gap in a wide range with different SrSe content [174-176]. Given the rock-salt structure and the lattice parameter of 6.25 Å for SrSe, it is highly probable that an appreciable solubility of SrSe in PbSe in the bulk material could exist as well. In addition, recent studies regarding thermoelectric PbTe with SrTe addition resulted in a noticeable thermal conductivity reduction without significantly impairing the carrier mobility[14, 120], indicating that SrSe in PbSe may yield beneficial alloying results as well.

4.3b - Results and Discussion

A series of PbSe/SrSe samples were synthesized with varying sodium (p-type) dopant concentration. SrSe is very effective in changing the band energies in PbSe. As shown in Figure 4-7a and Figure 4-8, the optical band gap (as determined from the absorption edge) of undoped $Pb_{1-x}Sr_xSe$ alloys is noticeably larger than that of PbSe. Band gaps of the alloys increase approximately linearly with Sr content up to 12%, resulting in a band gap that is nearly double that of pure PbSe. The change of band structure consequently affects the transport properties. Figure 4-7d shows measured room temperature Seebeck coefficient as function of Hall carrier density (the Pisarenko relation). For PbSe, due to the large offset between two valence-band maxima at room temperature, the contribution from the secondary Σ band on transport is negligible and the Pisarenko relation (data in black squares) can be explained with a single band model [177] (black curve) using L valence band parameters determined previously [65]. With the addition of Sr, S starts to deviate from the curve at high doping levels, resulting in higher values compared to pure

PbSe given the same carrier density. Among the $Pb_{1-x}Sr_xSe$ alloys, the Seebeck coefficient also increases as the Sr content increases. When considering the origin of the increasing Seebeck coefficient, one possibility is that it is due to increasing L-band effective mass. However, if the increased S were simply due to a larger effective mass, the value would be proportionally larger at all n_H; in this case, however, the low n_H $Pb_{1-x}Sr_xSe$ samples seem to converge with pure PbSe curve. Instead, we attribute the deviation from the single band model (the black curve) at high n_H by considering the contribution from the heavier (Σ) band as the Fermi level moves deeper into the valence band, as is commonly observed in heavily doped p-type PbTe [34]. The continuous change in the direct L-L band gap due to SrSe alloying can explain the gradual change of Pisarenko relation. If the energy of the L valence band is reduced as the band gap increases and this reduces the band offset in PbSe between L and Σ valence bands (meaning $\frac{dE_{g,L-L}}{dx} > \frac{dE_{g,L-\Sigma}}{dx}$), the secondary Σ band will play a more noticeable role in heavily doped, Sr containing PbSe, consistent with our observed Seebeck Pisarenko plot.

In accordance with a literature observation [176] on thin films samples at 77 K, we assume that the L and Σ valence band offset (ΔE) changes as approximately half of the L-L band gap change with strontium content ($\frac{d\Delta E}{dx} = \frac{1}{2}\frac{dE_{gL,L}}{dx}$), as shown in (Figure 4-7e, inset). Using this assumption, the calculated Pisarenko relation for each $Pb_{1-x}Sr_xSe$ alloy can be calculated as shown in Figure 4-7d (solid curves); the resulting two-band transport model curves are in reasonable agreement with the observed experimental Seebeck results over a wide range of chemical potentials (Na doping concentrations).

In addition to shifting the electronic band structure, alloying reduces the electronic and thermal conductivity due to point defect scattering. Figure 4-7b shows the reduction in lattice thermal conductivity as Sr is added (point defect scattering of phonons) at 300 and 850 K. This reduction is often thought to be beneficial for thermoelectric materials, but only if the thermal conductivity is reduced more than the electronic mobility [178]. In this case, the electronic mobility is reduced by more than 50% relative to the undoped sample, meaning that disorder is likely not beneficial to thermoelectric properties in this series of samples.

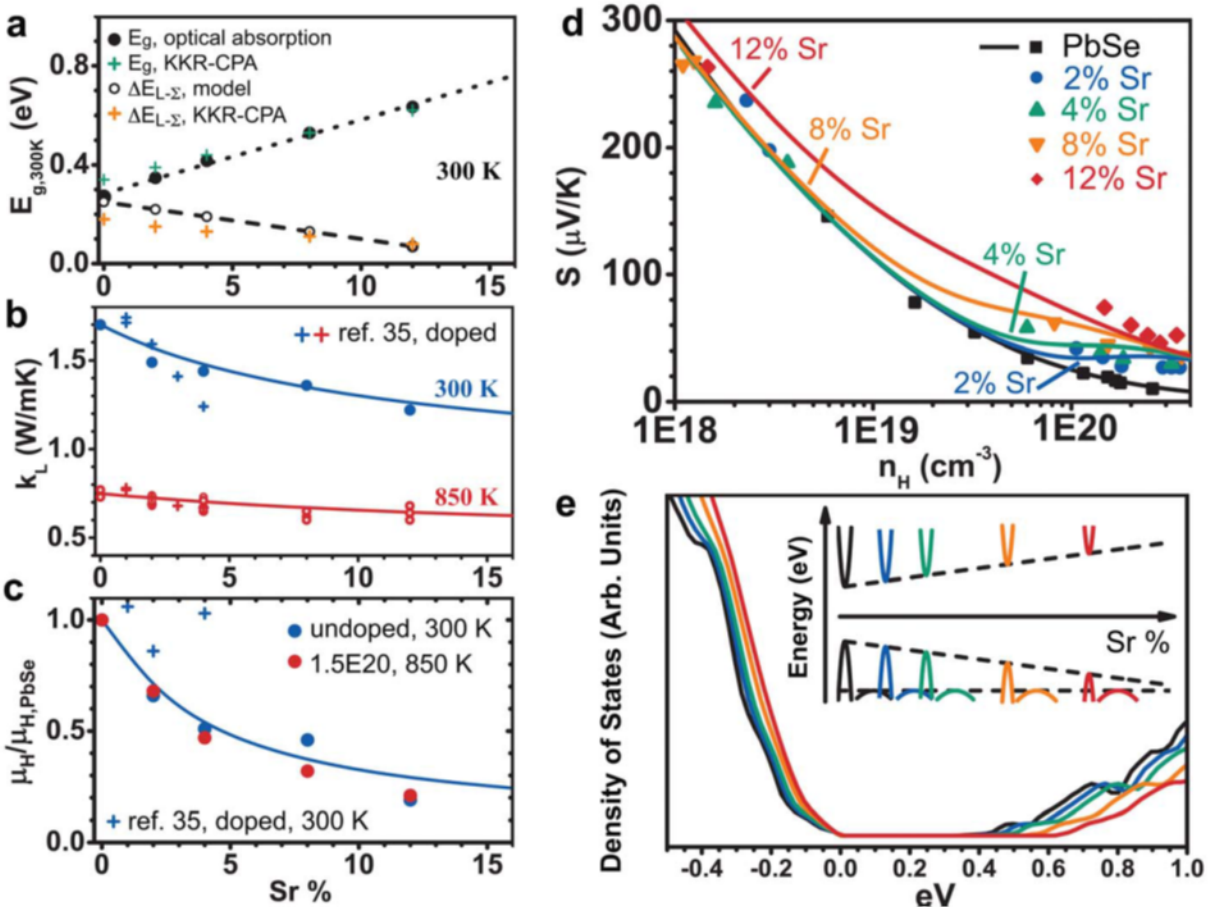

Figure 4-7: a) The measured band gap E_g and the proposed energy separation between two valence bands $\Delta E_{L-\Sigma}$ of $Pb_{1-x}Sr_xSe$ alloys, each is consistent with calculated values. b) Lattice thermal conductivity as function of Sr content at 300 K and 850 K. 300 K values are from undoped samples. c) Normalized Hall mobility as function of Sr content for undoped samples at 300 K and doped samples with same carrier density at 850 K. d) Pisarenko relation of p-type PbSe and $Pb_{1-x}Sr_xSe$ alloys. Lines are calculated using the proposed band model. e) The calculated DOS spectrum of $Pb_{1-x}Sr_xSe$ alloys; kinks in DOS around -0.1 eV are used to estimate $\Delta E_{L-\Sigma}$, and the inset illustrates the proposed band model, which is also given in (a).

The optical absorption edge in the binary lead chalcogenides begins with direct transitions across the fundamental gap at the *L* point. Because these direct transitions do not require phonon participation, they are believed to dominate the absorption spectra compared with the *L-Σ* indirect transitions which should occur at higher energies. This limits traditional optical absorption to accurately determining the direct (fundamental) gap (while missing any *Σ-L-$_c$* indirect transitions).

While inter-valence band optical transitions (Σ-L_v) have been observed and used to estimate the valence band offset in older Russian literature [127], this method requires some analysis to subtract free carrier absorption contributions; however, we did not observe any inter-valence band transitions in this system that might indicate the valence band offset. Instead, we employed *ab-initio* calculations of the electronic band structure to determine how it might change with Sr content. My collaborator, Yoshiki Takagiwa, performed first principle calculation using the Korringa-Kohn-Rostoker Green function formalism under the coherent potential approximation[179-181] (KKR-CPA). The KKR-CPA method is a powerful tool for visualizing the electronic density of states (DOS) for disordered materials without establishing a supercell; this technique is widely used in studies of thermoelectrics to imitate random substitutions [105, 182-184]. Calculated DOS spectra of $Pb_{1-x}Sr_xSe$ confirmed both the increase of band gap and the decrease of energy separation between L and Σ bands. These are shown in Figure 4-7 a and e; the results are consistent with regards to the proposed model.

Because of the widening band gap in the PbSe/SrSe alloys, it is possible that the indirect (L-Σ) optical transition might be observable in the optical absorption edge. In the previous section, I showed that even at the highest temperatures I was not able to directly detect the Σ band in any of the pure lead-chalcogenide absorption edges. I present the room temperature optical absorption results along with various transformations of the data in Figure 4-8. The normalized absorption spectra show a steady shift upwards in the absorption edge (as represented in Figure 4-7a) as the strontium content is increased. Along with a shift of the absorption edge to higher energies, the onset of the absorption edge does appear to broaden as the strontium content is increased. Because it is possible that the longer absorption edge tail to low energies is a result of some indirect L-Σ transitions, we need to consider this possibility. The indirect extrapolation is shown in Figure 4-8c, which does show regions of linearity. In fact, the samples with the three largest Sr content (4, 8, and 12%) show two linear regions (potentially consistent with indirect optical absorption associated with absorption/emission of a phonon [43]). However, I believe that it is actually related to disorder due to increased randomness in the alloy, as evidenced by the Urbach edge plotted in Figure 4-8b. By taking the logarithm of the absorption data, exponential features, such as the Urbach absorption edge (discussed in Chapter 3), should appear linear. In this case, we can clearly see the evolution of the Urbach edge, which goes from being quite small in pure PbSe (x=0) to stretching over nearly 0.15 eV in the sample with 12% Sr. This fits well with the supposition of Prakash (mentioned in the previous section) that the observation of a linear region for the indirect extrapolation is simply a coincidental fit resulting from the transition from the exponential Urbach edge to the direct extrapolation [39]. For all alloys the absorption spectra are consistent with direct transitions, which I attribute to the L-L gap as in pure PbSe [171]. It is possible that upon investigating the temperature-dependent gap that these features might arise.

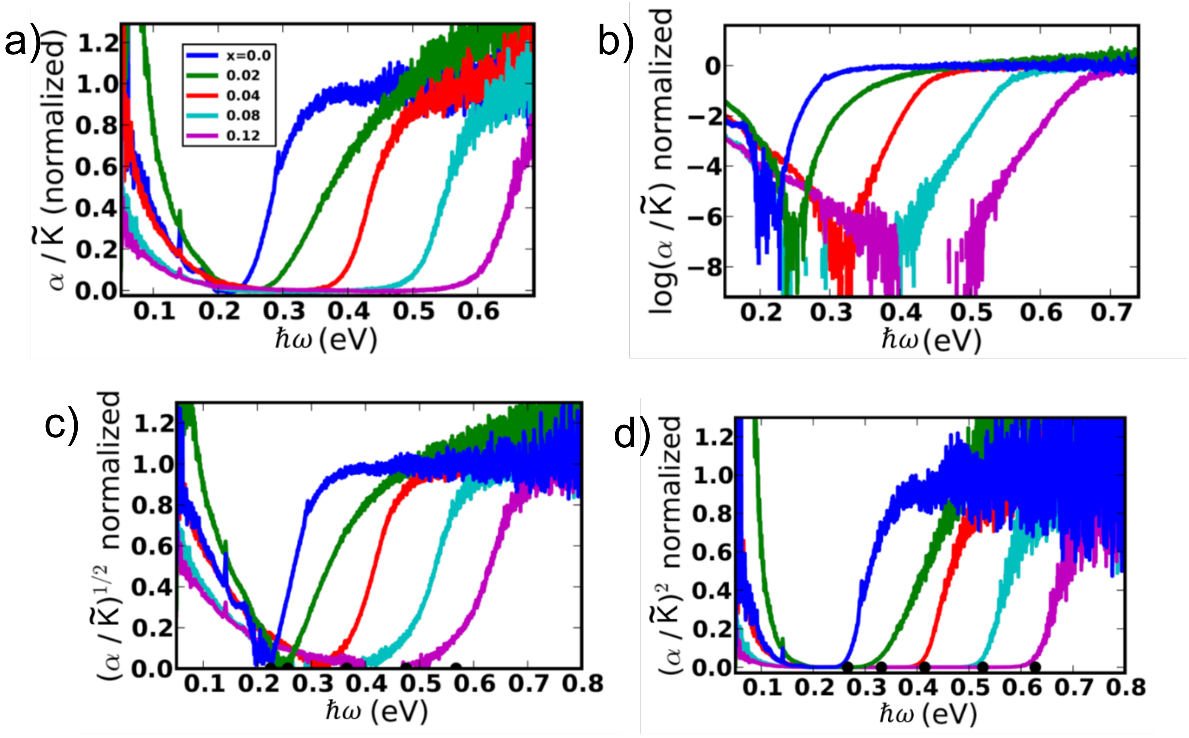

Figure 4-8: Optical data over a series of $(PbSe)_{1-x}/(SrSe)_x$ samples at room temperature—showing a) the normalized Kubelka Munk function, b) the log of the normalized Kubelka Munk function, c) the indirect extrapolation of the normalized Kubelka Munk function, and d) the direct extrapolation. Black dots on the axes indicate the extrapolated values.

The temperature dependent extrapolated direct band gap for each of the Sr-alloyed samples (and pure PbSe) is plotted in Figure 4-9 along with literature data from Shen et al. [174]. Our results are in good agreement with the literature values (which tended to be measured at low temperatures). Perhaps the most significant finding here is that the temperature coefficient (dE_g/dT) seems to decrease as Sr is added. This may be one of the reasons that, even at high temperatures, it is difficult to observe the indirect transition (because the Σ band never overtakes L as the primary valence band). It is important to note, however, that just because the secondary band is not observable using optical properties, the transport properties of doped samples do reflect the increased valley degeneracy and effective mass of the secondary Σ band.

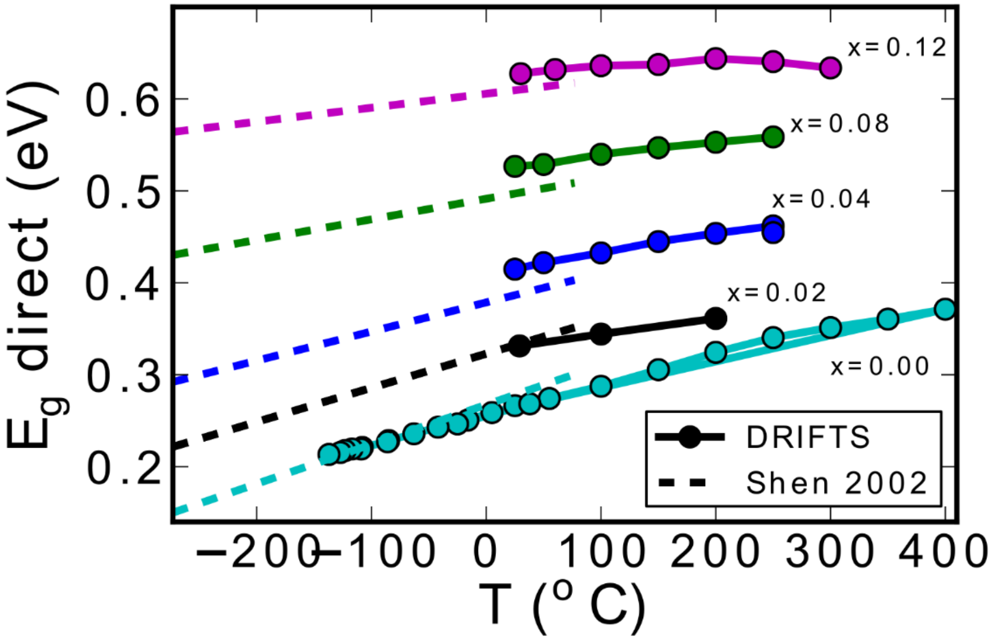

Figure 4-9: Temperature dependent optical band gap (direct extrapolation) in $(PbSe)_{1-x}(SrSe)_x$.from room temperature to~200°C [174].

Ultimately, the optical properties are not critical to optimization of these materials, rather, they serve as a tool to help provide insight into the underlying band structure features which give rise to the measured electronic properties. Of all of the samples which we have measured, the ones with the highest peak *zT* (of all of the sodium doping levels for each Sr content, x) are shown in Figure 4-10. A large maximum *zT* is obtained of up to 1.5 at *T*=900 K for the 8% SrSe sample, nearly 50% larger than the optimum *zT* for binary PbSe at this temperature. Largely, the enhancement is from the Seebeck coefficient (as is observed in the Seebeck Pisarenko plot, Figure 4-7d) as a result of a larger influence from the secondary bands at high doping levels rather than through thermal conductivity reduction through disorder scattering (as mentioned previously). At high temperatures, these effects are enhanced further because an even larger population of charge carriers develops in this high-degeneracy Σ band. In this case, the electronic properties confirm the existence of the secondary band even though optical measurements could not isolate its contribution. The large *zT* enhancement in the alloyed samples illustrates the Σ band's importance for thermoelectric optimization in this system.

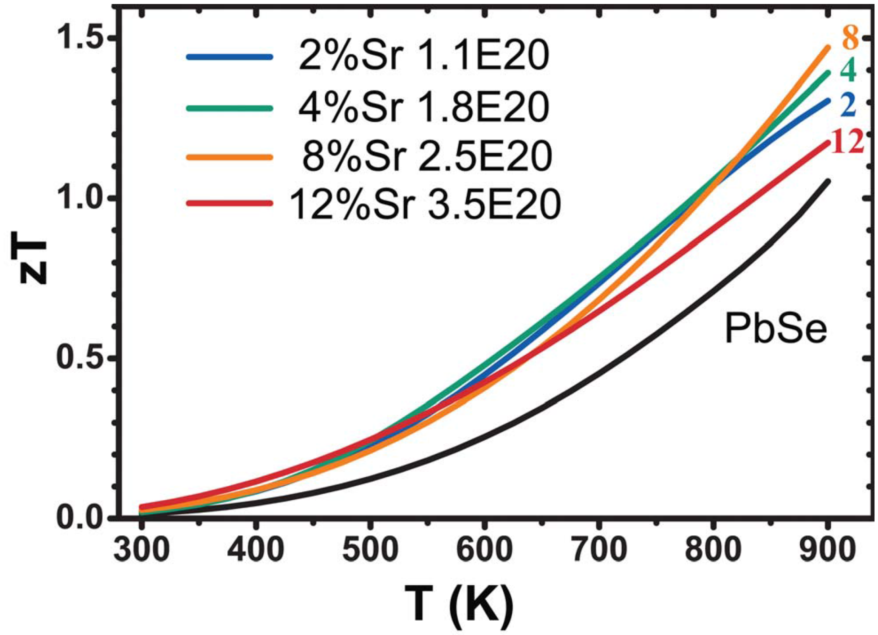

Figure 4-10: The observed zT *of samples that have highest* zT *at 900 K and the corresponding Hall carrier densities at room temperature for* $Pb_{1-x}Sr_xSe$ *with different Sr content (*zT *for samples with different carrier density at each Sr content shown in supplementary), compared to the maximum* zT *evaluated for p-type PbSe.*

4.3c - Conclusion

In this section, I presented a study of bulk $Pb_{1-x}Sr_xSe$ alloys with different *x* up to 12%. For each alloy composition, a p-type dopant, Na (K for two samples), is used to tune the carrier density for each Sr-content. The effect of Sr on band structure is revealed by transport and optical absorption edge measurements as well as first principle calculations. The band structure is sensitive to and gradually tunable with Sr content. Appreciable enhancement in thermoelectric performance was achieved and the maximum *zT* of 1.5 is found at 900 K (1.4 ± 0.1 in multiple samples with different compositions). Analysis further suggests that such enhancement is purely due to the change of band structure. This result provides a significant (~50%) enhancement over pure p-type PbSe, making an alloy which has performance comparable to that of binary p-type PbTe. It also shows how—even in a material that already has good thermoelectric properties, the performance can be significantly enhanced through proper band structure engineering through doping and alloying.

4.3d - Methods

The samples are made via conventional melting and pressing route. Undoped samples in 25g batches were first made. To do so, high purity elements (Pb, 99.999%; Se, 99.999%; Sr, 99.9%) were loaded and sealed in carbon coated quartz ampoules, and then quickly melted for 15 minutes by induction heating. Each ingot was ground and hot pressed, and then sealed in another ampoule and annealed at 1073 K for 14 days. The doped samples of each alloy composition were made by reacting powder (3g) of undoped alloy with Na and Se at 1200 K for 5 days in sealed ampoules, and then hot pressed at 923 K. The disc samples for tests were 12.7 mm in diameter and about 1mm thick with density no less than 97% of theoretical value.

Modelling results shown in the Seebeck Pisarenko plot were obtained using many of the band engineering methods presented in Chapter 2. The density-of-states effective mass ($m_{d,L}^*$) of the light band and the conduction band is taken as 0.27 m_e at 300 K and changes with temperature following $\frac{d\ln(m_{d,L}^*)}{d\ln T} = 0.5$, the anisotropy factor *K* is taken as a constant 1.75 and the valley degeneracy was set to 4. The deformation potential for the conduction band and the light band were determined as 25 and 35 eV. Little is known for the parameters of the heavy band. Based on suggested values from Veis [127] and transport properties of p-type PbSe at high temperatures these parameters are determined to be $m_{d,\Sigma}^* = 4.2\ m_e$, K = 1, $N_{v,\Sigma} = 12$, and E_{def}=28 eV. The band gap and the gap between two valence bands change with temperature and Sr content ($Pb_{1-x}Sr_xSe$) following $E_g = 0.17 + 3 \times 10^{-4}\ T + 3x$ and $\Delta E = 0.32 - 2.2 \times 10^{-4}\ T - 1.5x$. The temperature dependence of E_g is based on results from the previous section on binary, undoped PbSe. The Sr-dependence of the band gap was determined from optical measurements at room temperature for the undoped Sr alloys. The temperature dependence of ΔE is based on Veis' optical measurement result [127] and modeling of transport data of p-type PbSe at high temperatures, and its dependence on Sr content is taken assuming the band gap increase in $Pb_{1-x}Sr_xSe$ alloys is from the movement of two bands at L point simultaneously towards opposite directions (half of dE_g/dx, as mentioned previously). Alloy scattering of electrons was necessary to account for at higher Sr content. The alloy scattering potential, U, is taken as 3 eV for the light valence band, which is estimated from measured Hall mobility of undoped $Pb_{1-x}Sr_xSe$ alloys. The same U is taken for the conduction band because no data is available so far to estimate it more accurately. U for the heavy band is assumed to be 1.5 eV. A smaller U for the heavy band is consistent with the assumption that the heavy band position does not explicitly depend on Sr content. The value of 1.5 eV is used to provide the best overall fitting for all alloy compositions.

4.4 - Two Band Thermoelectric Performance in SnTe—Optimization Towards Single Band Behavior

4.4a - Introduction

As discussed in detail previously, the mechanism for p-type PbTe's outstanding thermoelectric performance is its complex valence band structure, especially at high temperatures where the energy of primary (L) and secondary (Σ) maximums are thought to be aligned, leading to extraordinarily high valley degeneracy[16]. In SnTe [128], one might also expect good thermoelectric performance because it shares many of the same characteristics with PbTe, specifically, both exist in the rock salt crystal structure and both have multiple valence bands [185] which contribute to the thermoelectric properties. However, unlike PbTe, SnTe is riddled with intrinsic defects which results in a heavily doped ($p \sim 10^{20}$–10^{21} cm^{-3}) material and a mediocre zT (around 0.5 at 900 K)[129, 186]. Nonetheless, several works have confirmed the existence of two valence bands (as in PbTe) and have estimated their transport parameters[129, 130, 187-189].

SnTe has a large valence band offset, ΔE, of around 0.3-0.4 eV at room temperature, larger than PbTe, which is closer to 0.1 eV (Figure 4-11c) [90, 130]. The two valence bands in SnTe are known to give rise to a unique Seebeck coefficient behavior as the carrier concentration is varied (Seebeck Pisarenko relation). A minimum Seebeck coefficient is observed in the Pisarenko plot (Figure 4-11a) near n_H=1-2$\times10^{20}$ cm^{-3}, followed by a maximum at about n_H=8$\times10^{20}$ cm^{-3}. Theoretical calculations confirm the position of the two valence bands in k-space (at the L and Σ points as in the lead chalcogenides) and have provided some insight into their character [29, 190-193]. Other than thermoelectric properties, other works have discussed SnTe and its alloys with regards to their uses as long wavelength detectors [194-196], or most recently as topological insulators[191, 197, 198]. Similar to PbTe, SnTe has been studied rather thoroughly over the years for its thermoelectric properties, but in light of a recent resurgence in band-engineering in the lead chalcogenides it is worthwhile to take a closer look at the properties of SnTe as well, especially in regards to optimzation of the carrier concentration.

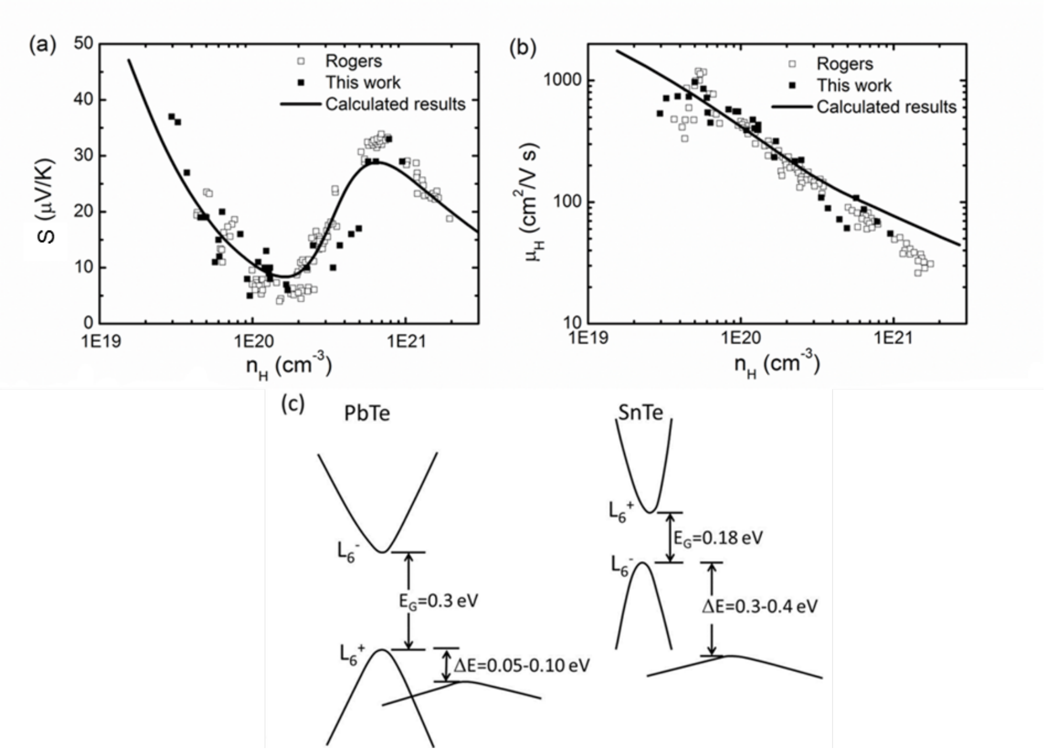

Figure 4-11: a) Seebeck coefficient and b) Hall mobility as a function of Hall carrier concentration at 300 K for $SnTe_{1-x}I_x$ and $SnTe_{1+y}$, $Gd_zSn_{1-z}Te$. Solid squares are our experimental results, open squares are Rogers' reported results [130], solid curves are calculated from a two band model. c) A schematic diagram of the near edge band structure in PbTe and SnTe. (Rogers et al reported a band offset of 0.3 eV for SnTe. Our results yielded different fitting parameters, and we found that 0.4 eV was required for best fit.)

The unique Seebeck coefficient behavior of SnTe as the carrier concentration varies stimulates our interests to explore the nature of electrical transport in SnTe and to optimize the thermoelectric properties. Finding the optimum doping level in semiconductors with complicated band structures is crucial to obtaining a thermoelectric material with the optimum performance. In this work, I will show that both the Seebeck coefficient and zT value increase either by substituting donor (I) or acceptor (extra Te and Gd) dopants. We observe that the peak zT value ($zT_{max,1}$=0.6 at 673 K) of I-doped SnTe with decreased carrier concentration (3×10^{19} cm^{-3}) is higher than the other peak zT value of extra Te or Gd-doped SnTe ($zT_{max,2}$=0.4 at 773 K) with increased carrier concentration (6×10^{20} cm^{-3}), suggesting that the light, primary valence band is most important in these systems. This unique behavior is contrary to the behavior in the lead chalcogenides where the second, heavy band usually leads to improved figure of merit. I would like to acknowledge contributions to this work from Min Zhou, who was an equally contributing author on the original paper [128].

4.4b - Results and Discussion

The measured Hall carrier concentration ($p_H=1/eR_H$) of $SnTe_{1-x}I_x$, $SnTe_{1+y}$, and $Gd_zSn_{1-z}Te$ samples at 300 K are shown in Figure 4-12. The Hall carrier concentration of stoichiometric SnTe was found to be around $1.1 \pm 0.2 \times 10^{20}$ cm^{-3} at 300 K when prepared by using the described method. This value is slightly lower than Zhang's report (about 2×10^{20} cm^{-3}) [199]. Extra Te is thought to induce cation vacancies which act as double acceptors[58, 200]. Brebrick, whose data is also shown in Figure 4-12a, studied closely Te solubility in SnTe and concluded that the phase width always leaned towards the Te rich side due to Sn vacancies; this phase width leads the heavily p-type character of intrinsic SnTe. Our work agrees with the cation vacancy mechanism and yields ~1.7 holes per Te atom, although Brebrick saw more (3 holes per Te atom) [129]. Because Brebrick used carefully controlled and measured data for Te content while we use nominal composition only, Te loss through vaporization during synthesis is a plausible explanation of the difference. Dopant solubility in SnTe has been thoroughly studied by Rogacheva et al.; they investigate the complexities involved with doping phases that are intrinsically nonstoichiometric [201].

Gd with normal valence Gd^{3+} might be expected to substitute for Sn^{2+} and be an electron donor, but instead Gd is observed to cause an increase in p-type, hole carrier concentration. Similar results were reported by Story et al., who suggest that Gd is a resonant dopant; however, no Seebeck increase was observed relative to Te-doped samples which would indicate resonant states, probably due to a lower Gd content (<1%) and higher temperatures than used b Story et al. [202] While the exact mechanism of Gd doping is not clear, the Gd-doped samples showed a linear increase in n_H with Gd doping for $z>0.0025$.

We also attempted to counter dope SnTe by substituting Te with Iodine. While much work has been done on cationic substitutions, far fewer works study how SnTe is affected by anion substitution. As pointed out by Rogacheva et al, the cationic dopants that have the highest solubility are those which have similar ionic radii to Sn. Hence, Iodine (which has a similar ionic radius to Te) should be a good candidate for anionic substitutional doping in SnTe. As observed in Figure 4-12b, the carrier concentration linearly decreased to as low as 3×10^{19} cm^{-3} with ~40% doping efficiency, assuming that one electron is donated per iodine atom. The doping efficiency appears linear until $N_I \sim 25\times10^{19}$cm^{-3} ($x = 0.015$), where the carrier concentration continues to decrease, but at a slower rate. The observed carrier concentration has been achieved by previous authors[203-205] , but their interpretation of it and its significance to the thermoelectric properties was not thoroughly studied.

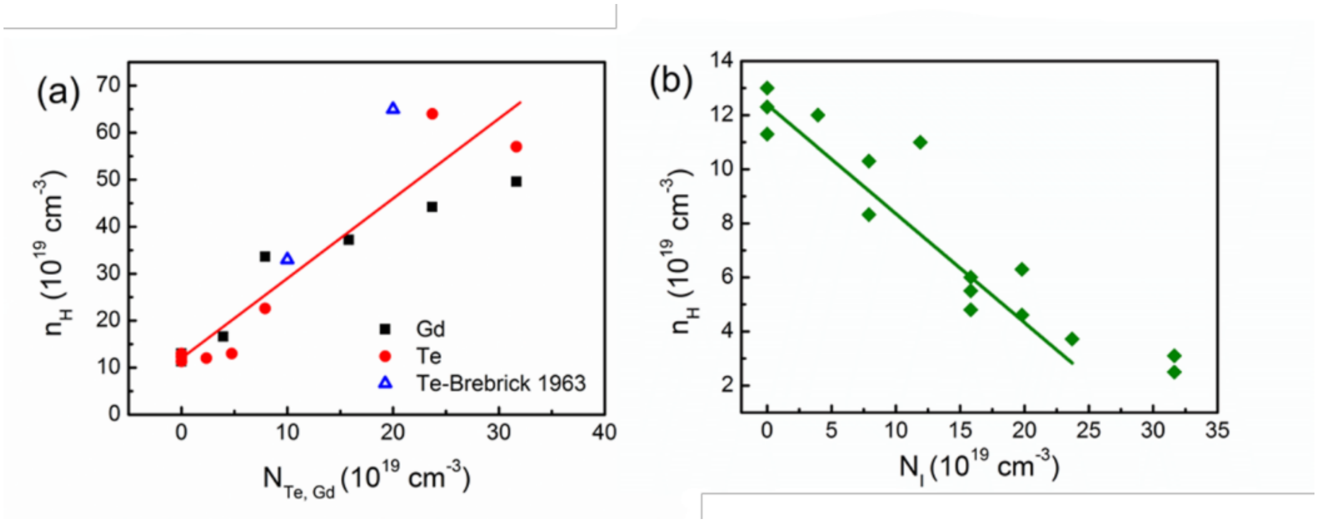

Figure 4-12: Hall carrier concentration as a function of dopant concentration a) Gd, Te excess as acceptors, b) I as donor. Solid lines represent guides to the eye for our data and correspond to 1.7 holes per atom for the Gd/excess Te case shown in a, and 0.4 electrons per Iodine atom as in b.

The measured temperature dependent transport data for samples with nominal composition $SnTe_{1-x}I_x$, $Gd_zSn_{1-z}Te$, and $SnTe_{1+y}$ are shown in Figure 4-13. Stoichiometric

SnTe data reported by Zhang et al (green dashed lines for samples with a slightly different n_H than SnTe in this work) are also shown. Degenerate semiconducting behavior, indicated by an increasing Seebeck coefficient and resistivity with temperature, is observed for all samples. As the iodine content is increased, the measured Seebeck coefficient and electrical resistivity increase, consistent with the decrease of Hall carrier concentrations shown in Figure 4-12. This suggests that I atoms substitute for Te and supply extra electrons which compensate the effect of intrinsic Sn vacancies. Conversely, the p-type dopants (Gd and excess Te) reduce the resistivity, consistent with an increase in carrier concentration. The Seebeck coefficient for these samples, unlike in the I doping case, show an increase with increasing doping level at room temperature, which is a direct consequence of the two band behavior described in Figure 4-11. Further, the most heavily doped sample (6×10^{20} cm^{-3}) also has nearly the highest Seebeck coefficient at room temperature, but it does not increase as much with temperature as samples with lower doping levels.

The total thermal conductivity and the calculated lattice thermal conductivity of $SnTe_{1-x}I_x$ samples are shown in Figure 4-13(e, f). The total thermal conductivity of the undoped SnTe decreases with temperature, reaching 2.3-3.0W/m K at 773K.The thermal conductivities of all the I-doped $SnTe_{1-x}I_x$ are lower than that of undoped SnTe, which comes from the reduction of electronic thermal conductivity as a result of a decreasing hole concentration. The lattice thermal conductivity, κ_L, is calculated by subtracting the electronic contribution ($\kappa_e = LT/\rho$) from the total thermal conductivity, where L is the Lorenz number that was estimated from a two-band model ($L=(L_L\sigma_L T+L_\Sigma\sigma_\Sigma T+\kappa_{bipolar})/(\sigma_L T+\sigma_\Sigma T)$, where $\kappa_{bipolar}=T(\sigma_1 S_1^2+\sigma_2 S_2^2-(\sigma_1 S_1+\sigma_2 S_2)^2/(\sigma_1+\sigma_2))$). The lattice thermal conductivity of all the I-doped $SnTe_{1-x}I_x$ samples decreased with temperature, and then increased when the temperature is over 600 K. This suggests that bipolar effects occur in I-doped $SnTe_{1-x}I_x$

samples with lower carrier concentrations at high temperature. κ_L is not shown for Te and Gd doped samples, which were shown to be additionally complex due to large contributions from the Σ band.

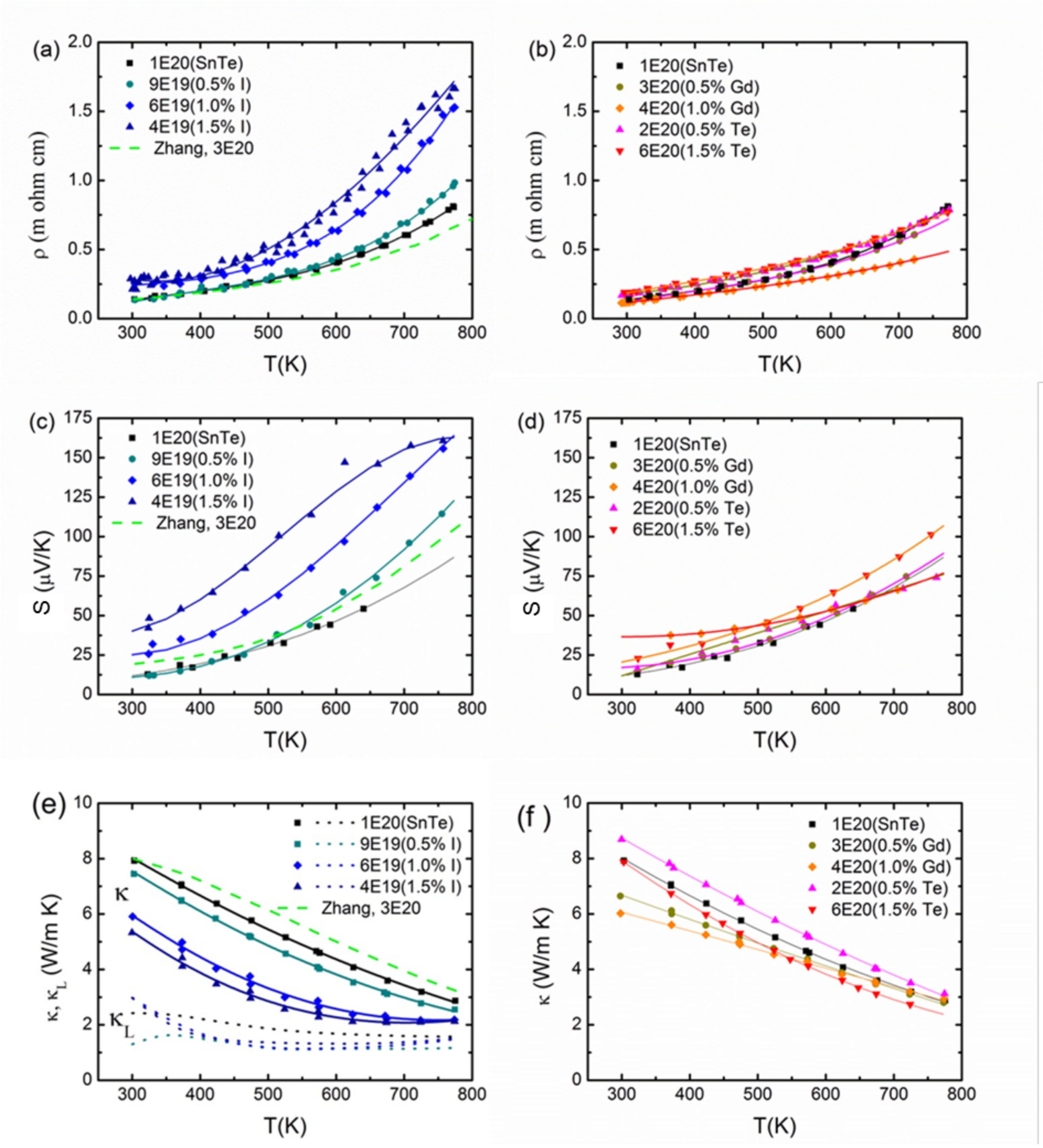

Figure 4-13: Thermoelectric transport properties for various SnTe samples: a) resistivity of SnTe and $SnTe_{1-x}I_x$, b) resistivity of SnTe, $SnTe_{1+y}$, and $Gd_zSn_{1-z}Te$, c) Seebeck of SnTe and $SnTe_{1-x}I_x$, d) Seebeck of SnTe, $SnTe_{1+y}$, and $Gd_zSn_{1-z}Te$, e) thermal conductivity and lattice thermal conductivity of SnTe and $SnTe_{1-x}I_x$, and f) thermal conductivity and lattice thermal conductivity of SnTe, $SnTe_{1+y}$, and $Gd_zSn_{1-z}Te$. Legends indicate

room temperature Hall carrier concentrations and a brief description of the samples as follows: $SnTe_{1-x}I_x$, $Sn_{1-x}Gd_xTe$, and $SnTe_{1+x}$ for Iodine doped (a,c,e), Gd doped (b, d, f), and excess Te (b, d, f) samples, respectively. All plots show both raw experimental data (points) and polynomial fits (lines).

Full optimization of SnTe yields a higher *zT* (average and peak) for samples doped with Iodine. The thermoelectric figure of merit, *zT*, is shown as a function of temperature in Figure 4-14 for Iodine, Gd, and Te rich samples along with results from Zhang et al for an undoped and an In doped sample[199]. We show that the undoped SnTe ($n_H = 1.1\times10^{20}$ cm^{-3}) shows low *zT* values over the measured temperature range yielding a maximum of 0.23 at 773 K. This is lower than the reported *zT* value (0.39) of intrinsic SnTe with a higher carrier concentration ($n_H = 2\times10^{20}$ cm^{-3}) at the same temperature from Zhang et al. (as shown in Figure 4-14a). From Figure 4-14a, *zT* values increased with donor I-dopant and a peak *zT* value of 0.6 was obtained for $SnTe_{0.985}I_{0.015}$ at 700 K, corresponding to an optimum doping level of around 4×10^{19} cm^{-3}, which was the lowest attainable with iodine doping that did not lead to hysteretic behavior in the transport properties. *zT* values of 0.45-0.6 were obtained for several samples with room temperature n_H of $4.0\text{-}6.1\times10^{19}$ cm^{-3}. This means that decreasing carrier concentration is a valid approach to optimize *zT* of SnTe by doping with iodine.

Alternatively, *zT* values increased with acceptor Te or Gd-dopant also. The other peak *zT* value of 0.4 was obtained for the most heavily doped samples ($Gd_{0.01}Sn_{0.99}Te$ and $SnTe_{1.015}$, $n_H = 4\text{-}6\times10^{20}$ cm^{-3}) at 773K, which is about 30% lower than the iodine doped samples. Unlike conventional single band behavior, we show that both I-doped SnTe and Gd-doped SnTe have higher *zT* values than that of stoichiometric SnTe. Figure 4-14c shows the average *zT* value ($\overline{zT} = \frac{\int_{300}^{773} zT dT}{773-300}$) of I-doped and Te-rich SnTe samples along with Zhang et al. $In_{0.0025}Sn_{0.9975}Te$ samples over the temperature range of 300-773 K. $SnTe_{1.015}$ shows an average *zT* of 0.15, but the average *zT* value of best I-doped SnTe (0.35) is about the same as the best In-doped sample (0.32) that contains resonant states.

This indicates that the low-temperature *zT* value in I-doped samples is quite a bit higher than either the intrinsic or In-doped samples from Zhang et al.

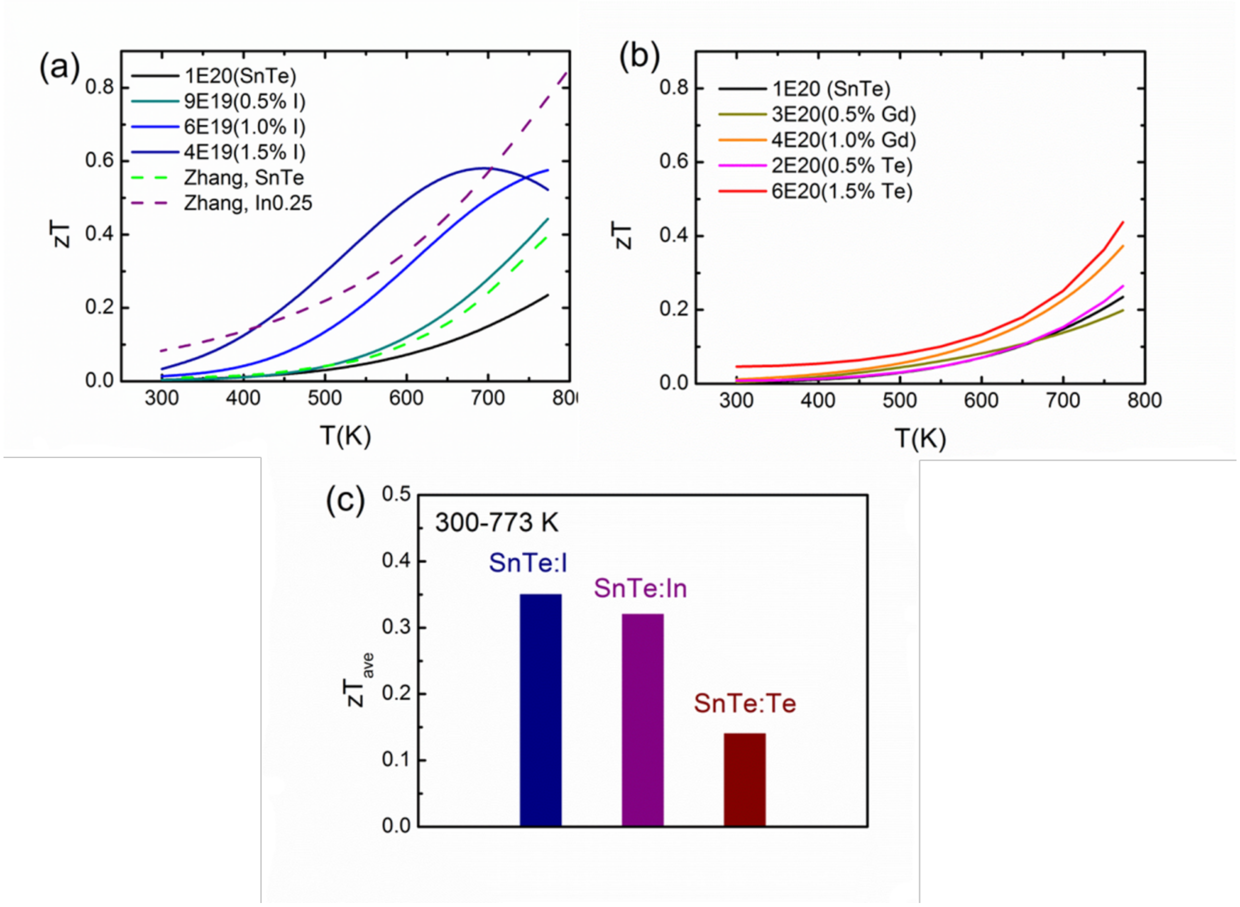

Figure 4-14: a) zT of SnTe$_{1-x}$I$_x$ as function of temperature, data (dashed lines) are from the literature [199]. b) zT of SnTe$_{1+y}$ and Gd$_z$Sn$_{1-z}$Te as function of temperature. c) The average zT between 300 and 773 K for optimally doped samples; data of SnTe:In are from the literature[199]. zT estimates are obtained from polynomial fits of transport data in Figure 3.

The Seebeck coefficient as a function of Hall carrier concentration (Pisarenko plot) is shown in Figure 4-11a for SnTe$_{1-x}$I$_x$ and SnTe$_{1+y}$, Gd$_z$Sn$_{1-z}$Te at 300 K along with reported results from Brebrick and Rogers et al. [129, 130]. The plot shows a unique, non-monotonic n_H dependence brought about by the two interacting valence bands. For carrier concentration of 1-2×10^{20} cm^{-3}, the Seebeck coefficient shows a minimum value of about 5-10 μV/K. The Seebeck coefficient then increases to a maximum of about 30 μV/K at carrier concentration of 6-8×10^{20} cm^{-3}. Figure 4-11b shows the relationship between the carrier mobility and Hall carrier concentration of all the samples as well as data reported by Rogers et al. at 300 K [130]. The carrier mobility of stoichiometric SnTe is about 400-500 cm^2/V-s at room temperature and always decreases with increasing carrier concentration for all $SnTe_{1-x}I_x$ and $SnTe_{1+y}$, $Gd_zSn_{1-z}Te$ samples. The experimental data of both Seebeck coefficient and mobility are fitted by a two band model (the solid curve) using a Kane band (SKB) for the L and a parabolic band (SPB) for the secondary Σ valence band (as described in detail in the Methods section later in this chapter).

As shown in Figure 4-15, the high temperature Seebeck coefficient and carrier mobility could also be explained by the same model, with the valence band offset (ΔE) and band effective masses allowed to change as fitting parameters as a function of temperature. The non-monotonic behavior for the Seebeck coefficient becomes less significant at high temperature (Figure 4-15a), probably a result of a broadening Fermi distribution and temperature dependent shifts in the band structure. By fitting experimental results we determine that the density of states effective mass m_L^* of the L valence band is 0.14 m_e for $SnTe_{1-x}I_x$ at 300 K, and it changes with temperature roughly according to $d\ln m_L^*/d\ln T$=0.55. Similar temperature dependence has been reported in other IV-VI compounds with similar band structure [16, 65, 206]. Little is known about the parameters for the heavier, Σ band, and they are difficult to determine directly using experimental techniques. As a result, they were adjusted to fit the experimental Seebeck and mobility data. The density of states effective mass m_H^* was fit to be 1.7 m_e at 300 K, and it changes with temperature according to $d\ln m_H^*/d\ln T$=0.5. The 300K values are comparable to those reported by Brebrick et al. [129]. The valence band offset energy, ΔE, between the two bands was found to be 0.4 eV at 300 K according to the fitting result; the best fit of the data required ΔE to decrease roughly linearly with temperature at a rate of 3.4×10^{-4} eV/K (similar to the lead chalcogenides in the previous sections). I should note that these values are likely not unique, and that similar fits could also be performed with different sets of parameters.

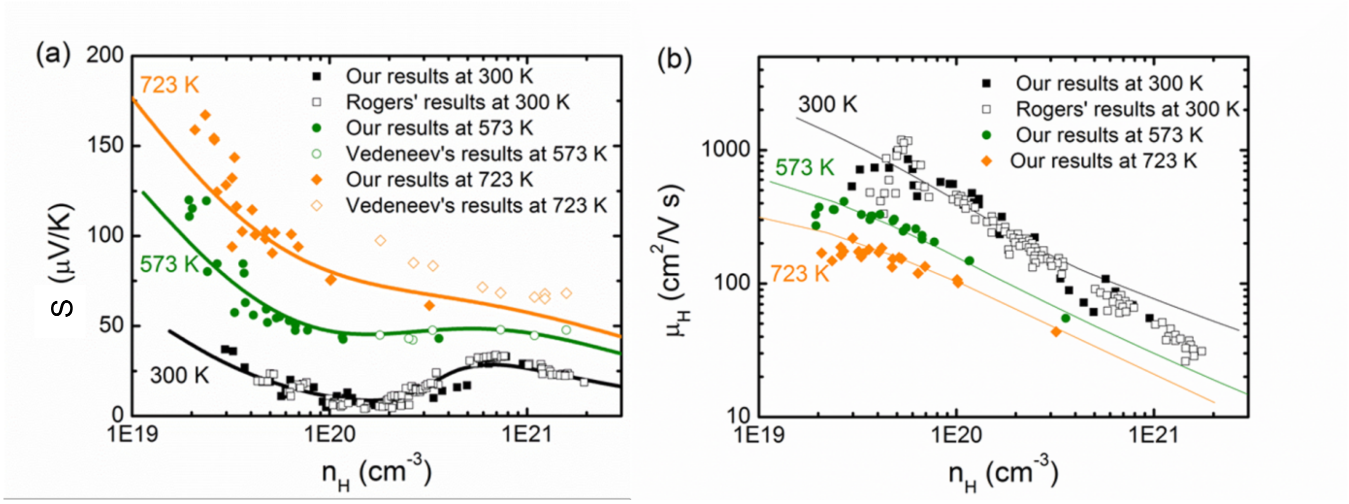

Figure 4-15: a) Seebeck coefficient and b) Hall mobility as a function of Hall carrier concentration at different temperatures. Solid symbols represent our experimental results, open symbols correspond to literature data (Vedeneev {Vedeneev, 1998 #9388} and Rogers {Rogers, 1968 #9294}). Each is presented at three temperatures: 300, 573, and 723 K, which are given by squares, circles, and diamonds, respectively. Solid curves represent the results of the two band model.

Figure 4-16 shows *zT* as a function of Hall carrier concentration for $SnTe_{1-x}I_x$, $SnTe_{1+y}$and $Gd_zSn_{1-z}Te$ samples at different temperatures. Note that a local minimum exists in *zT* vs. n_H for temperatures of 300 and 600 K, which corresponds to a carrier density of ~1×10^{20} cm^{-3}, approximately the composition of stoichiometric SnTe. At a higher temperature of 773 K, the model predicts a single maximum in *zT* as seen in most thermoelectric materials, but the peak is broadened due to the increasing influence of the second band. From Figure 4-16, both the experimental and model results indicate a significant *zT* increase with decreasing carrier concentration, yielding a maximum in the 10^{18} – 10^{19} cm^{-3} range. In this work, the solubility of I in $SnTe_{1-x}I_x$ (x = 0.015, n_H~4×10^{19} cm^{-3}) has limited us from achieving the optimized n_H for the predicted maximum *zT* to be obtained (which requires n_H~8×10^{18} cm^{-3}). While we do expect bipolar effects to begin to play a role at low doping levels and high temperatures, which is not accounted for in this model, the conclusions remains that optimizing SnTe carrier concentration towards the light band results in significant improvement.

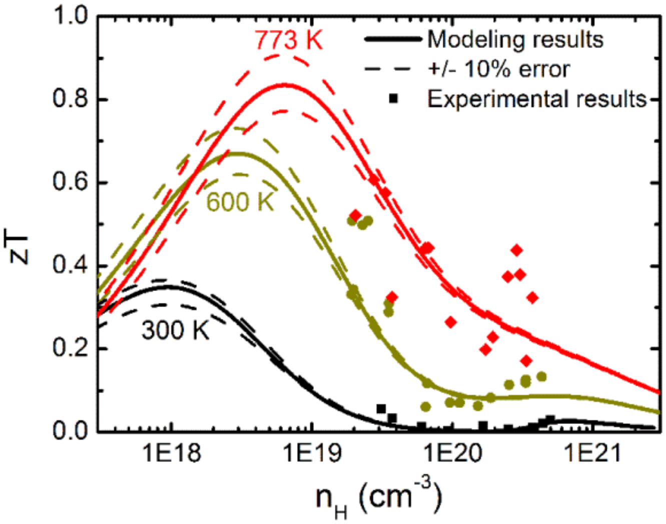

Figure 4-16: zT as a function of Hall carrier concentration for $SnTe_{1-x}I_x$ and $SnTe_{1+y}$, $Gd_zSn_{1-z}Te$. Solid curves are modeling results, and dashed lines are uncertainty values for the model zT which account for a ±10% error in κ_L. The calculated lattice thermal conductivity of 2.5±10% W/m K (300 K), 1.23±10% W/m K (600K), and 1.0±10% W/m K (773 K) were used in the zT calculation as obtained from I-doped samples (Figure 3e).

While both SnTe and PbTe are IV-VI materials have the same crystal structure and similar electronic band structures, their thermoelectric performance and optimization strategies are quite different. At first, one might write off SnTe due to its large intrinsic defect concentration and higher lattice thermal conductivity when compared to PbTe. However, this work suggests that it does in fact give a reasonable *zT* when optimizing towards the low carrier concentration light band rather than the heavier Σ band; this is achieved by doping with iodine. While valley degeneracy and band convergence play a crucial role in the high *zT* for PbTe (more than 1.5 at T ~ 800 K), the larger band offset in SnTe (0.4 eV for SnTe versus 0.1 eV for PbTe at 300 K) makes convergence unattainable in SnTe for temperatures below its melting point. In addition, the thermoelectric quality factor [18, 65], *B* (Equation 2-6), can be used to determine the quality for the *L* and Σ bands to be 0.42 and 0.27, respectively, in SnTe at 600 K. The light band is estimated to have nearly 50% higher quality factor than the heavy band in this system due primarily to the low band mass (and corresponding high mobility). Coupled with a large band offset (~6 $k_B T$ at 600 K), the peak *zT* for SnTe occurs for a chemical potential near to the light valence band edge. This is in contrast to PbTe where the heavy band is believed to have as good or better quality factor than the light band with a much smaller band offset (ΔE~1.5 $k_B T$ at 600 K) [18]. So, while valley degeneracy and the heavy band at Σ play an important role in PbTe [16], they are not viable options for improving *zT* in SnTe.

While intrinsic SnTe seems to have too large of band offset to utilize the heavy band, several successful attempts at band engineering have been achieved. Tan reported a high *zT* of 1.3 for Cd-doped [170] and Hg-doped [169] SnTe, which they attribute to changing ΔE from the addition of Cd/Hg and nanostructuring. Han and Chen et al reported *z*T of 0.9-1 for SnTe-AgSbTe$_2$ alloys [207, 208]. These latest works are encouraging in terms of making a useful thermoelectric device that is lead free.

4.4c - Conclusion

While undoped SnTe has very poor thermoelectric performance, SnTe can be greatly improved through carrier density tuning. We have shown that by either increasing or decreasing the carrier concentration, the *zT* can be improved relative to naturally synthesized, nominally undoped SnTe. A peak *zT* value of 0.6 is obtained for $SnTe_{0.985}I_{0.015}$ sample with a lower carrier concentration of 4×10^{19} cm^{-3}, which is about 50% higher than the other peak *zT* value of 0.4 for $SnTe_{1.015}$ with a higher carrier concentration of p_H = 6×10^{20} cm^{-3}. Transport property models predict higher *zT* if the carrier concentration could be reduced further to 1×10^{19} cm^{-3}. Different from In-doped SnTe that alters the host band structure, this work revealed the inherent merit of SnTe thermoelectric materials. With further band engineering SnTe may become an efficient lead free alternative to lead chalcogenide thermoelectric materials.

4.4d - Methods

Polycrystalline samples of $SnTe_{1-x}I_x$ ($0 \leq x \leq 0.02$,), $SnTe_{1+y}$ ($0 < y \leq 0.015$), $Gd_zSn_{1-z}Te$ ($0 < z \leq 0.02$) were prepared by using a melt alloying and hot pressing technique. Pure elements and TeI_4 (Sn, 99.999%; Te, 99.999%; Gd, 99.99%; TeI_4, 99.999%, ultra dry) were weighed out according to each composition and loaded into quartz ampoules, which were then evacuated and sealed. The sealed ampoules were slowly heated to 1273 K and kept for 24 h followed by water quenching. The ingots obtained were further annealed at 973 K for 120 h before being crushed and ground into fine powders. The powders were then hot pressed at 823 K under 1 atm argon with 40 MPa pressure for 30 min. A typical disc shaped sample obtained is 12 mm in diameter with density no less than 95% of theoretical density (6.46 g/cm^3). Electrical properties were measured as detailed in Chapter 2. The heat capacity, C_p, was determined from: $C_p=C_{p,300}+C_{p1}\times((T/300)^{\alpha}-1)/((T/300)^{\alpha}+C_{p1}/C_{p,300})$ [209], where T is the absolute temperature, $C_{p,300}$ is the specific heat capacity at 300 K. For SnTe, $C_{p,300}$ is 0.1973 J/g K, C_{p1} is 0.115 J/g K, α is 0.63 [209].

A two-band model was used for modeling the light and heavy bands to explain thermoelectric transport properties. Transport properties were modeled following the procedures outlined in previous work [65, 210] and in Chapter 2 of this thesis. The light and heavy valence band properties were calculated by evaluating the full generalized Fermi integrals as a function of chemical potential. The L band was assumed to be a nonparabolic, Kane band, with a nonparabolicity parameter, β, given by k_BT/E_g, where E_g was assumed constant at 0.18 eV [211], while the Σ band was modeled as a parabolic band. More specific details of the modelling results can be viewed in the supplementary material of a paper published on this subject [128].

4.5 - Conclusions

IV-VI materials have proven to have a breadth of interesting and measureable band structure properties which can be used for building world-class thermoelectric materials. In this chapter, I have shown that by using a combination of optical and electronic properties measurements coupled with *ab-initio* calculations we can gather a wealth of information about the electronic band structures in the IV-VI materials. In Section 4.2, I have provided new optical/computational evidence of the convergence temperature in the lead chalcogenides which suggests that convergence occurs at ~700 K in PbTe, much higher than the commonly cited result that claims (~400 K). These experimental results have helped to aid band engineering strategies by providing the data needed to accurately model the band structure at high temperatures. Section 4.3 shows a successful band engineering study in PbSe/SrSe alloys which leads to ~50% enhancement (max *zT* of 1.5) relative to the binary PbSe. In Section 4.4, two band transport behavior in SnTe is characterized in a doping study; here we determine that the *zT* in SnTe can be greatly improved upon decreasing the carrier concentration through iodine doping. My results have expanded upon the current literature by providing band structure properties in the IV-VI materials, allowing a clearer path towards proper optimization. The techniques learned here are generally applicable to other multi-band systems as well, and several will be discussed later in this thesis.

Chapter 5: Resolving the True Band Gap in ZrNiSn: The Effect of the Weighted Mobility Ratio in Bipolar Semiconductors

5.1 - Introduction

Temperature-dependent electronic transport measurements serve as the primary characterization tool for most thermoelectric materials. With regards to the electronic band structure, these measurements can be used to determine things like the effective mass, deformation potential, band offset (ΔE) in the case of two-band systems with the same type of carrier (as discussed in Chapter 4 for the IV-VI materials), or band gap (E_g) for systems where the bipolar effects are large. Particularly in the case of band gap, these estimates are useful for comparing experimental and theoretical (DFT) calculations. Further, understanding the band gap is important for modelling electronic transport properties, primarily to distinguish and quantify band engineering effects. Half Heusler's (HH) have received a lot of attention lately because of their flexibility with regards to composition (XYZ where X=Ti, Zr, Hf, etc., Y=Ni, Co, etc., Z=Sn, Sb, etc.), good electronic properties, earth-abundant elements, and reasonable thermoelectric performance. In this chapter, I explore the relationship between the maximum measured temperature-dependent thermopower ($|S|$), which can be used to estimate the band gap using $E_g=2e|S|_{max}T_{max}$ (the Goldsmid-Sharp band gap), and the electron-to-hole weighted mobility ratio, A [51]. While the Goldsmid Sharp gap estimate is useful, mainly due to its simplicity and ease of application, it gives conflicting results in ZrNiSn and other systems that have large differences in electron and hole weighted mobility (defined as $\mu_0 m^{*3/2}$). By combining optical measurements with the estimated Goldsmid-Sharp band gap in n-type and p-type samples, I am able to resolve the true band gap as well obtain an estimate for the electron-to-hole weighted mobility ratio in ZrNiSn. I also discuss the origins of the large difference in electron and hole weighted mobility in the context of existing literature results and the inherent disorder associated with HH materials.

As an extension of my findings in the ZrNiSn HH system, the second section of this chapter is dedicated to a more thorough theoretical investigation of the Goldsmid-Sharp band gap relationship in the limit of narrow gap materials, where the full Fermi statistics should be considered. I present a chart that can be used to quickly estimate deviations in the $2eS_{max}T_{max}$ relation from the true band gap as a function of the maximum Seebeck coefficient and the majority-to-minority carrier weighted mobility ratio, *A*. I also discuss what deviations in this relation can occur as the band gap is narrowed significantly and the Seebeck rollovers occur while the Fermi level is degenerate.

5.2 - ZrNiSn Half Heusler Thermoelectric Materials– Resolving the True Band Gap

5.2a - Introduction

Half-Heusler (HH) compounds with the general formula *X*NiSn (*X*= Ti, Zr, Hf) have generated significant interest as a promising class of materials for thermoelectric applications because of their high thermopower, reasonable mobility, earth-abundant elements, and good performance [212, 213]. The numerous possibilities to manipulate each of the three lattice sites provide an excellent opportunity to influence the electronic and thermal transport properties. In the case of XNiSn, isoelectronic alloying on the *X* site [214] or partial substitution on the Ni site [215] can lead to thermal conductivity reduction owing to lattice strain and mass fluctuations by point-defect scattering of phonons. Beyond simply alloying, a wide range of HH composites have utilized phase separation, which can result in remarkably low thermal conductivities and even enhanced electrical properties [216-219]. In fact, much of the work on the HH's has involved phase-separating alloys which benefit greatly from the increased phonon scattering from nano/microstructure features. The *X*NiSn system is the most extensively studied *n*-type HH material [23, 212, 213, 219-225] showing good *zT*s of 0.6-1.4 (usually optimizing at high temperatures, T>900 K) [223].

Much of the existing literature focuses on the thermoelectric characterization of *n*-type *X*NiSn, which show the best thermoelectric performance in comparison to their *p*-type analogs. The most promising *p*-type HHs are found in the *X*CoSb system (*X*= Ti, Zr, Hf) [213, 226-228]. However, for the construction of thermoelectric modules, it is desirable for the *n*-type and *p*-type materials to have similar chemical, thermal, and mechanical properties. In order to be most compatible with high-performance HH *n*-type materials that are currently being explored for modules [229], a suitable *p*-type analog in the *X*NiSn system is desirable. Some work has already been done to this end; for example: Xie *et al.* [230] studied the substitution of Ni by Co and demonstrated that a conversion from *n*- to *p*-type behavior for the *X*NiSn system could be achieved. Likewise, Horyn' *et al.* [231] studied the effects of substituting Sc for Ti or Zr; the resulting compounds showed promising positive thermopower at room temperature.

The electronic transport properties of semiconducting materials, such as thermopower and electrical conductivity, are reflections of the electronic energy band structure in *k*-space and the electronic states which make up the valence and conduction bands. A crucial parameter that determines the thermoelectric performance is the band gap. For narrow band-gap semiconductors, the onset of bipolar conduction (both electrons and holes contributing) occurs at lower temperatures than their higher gap analogs. The compensating Seebeck coefficient of the minority carriers leads to a peak in the thermopower, limiting the temperature-dependent *zT* values.

In this work, I aim to extend the existing studies of *p*-type *X*NiSn HH compounds by thoroughly investigating Sc substitutions in $Zr_{1-x}Sc_xNiSn$. Through Sc substitution, we successfully doped ZrNiSn to be *p*-type and then measured its thermoelectric properties up to 850 K. I estimated the band gap size using the commonly used Goldsmid-Sharp formula:

$$E_g = 2e|S|_{max}T_{max} \quad \text{Equation 5-1}$$

where T_{max} is the temperature at which the maximum of the thermopower ($|S|_{max}$) occurs [51]. E_g here is referred to as the Goldsmid-Sharp band gap and is obtained from high temperature thermopower measurements. In this work, synthesized ZrNiSn HH samples give a discrepancy between the values obtained from our *p*-type samples (~0.05 eV) and the *n*-type results from the literature (>0.23 eV), both of which are different from the *ab-initio* calculated result of 0.5 eV [232]. With the aid of the optical measurements, we used the Goldsmid-Sharp formula to resolve this apparent discrepancy by considering a large difference in weighted mobility between electrons and holes. I would like to acknowledge work from Jennifer Schmitt, who was an equally contributing coauthor on the work that this section is based upon [52].

5.2b - Results

X-ray Diffraction

Figure 5-1 shows a representative *XRD* pattern for $Zr_{0.95}Sc_{0.05}NiSn$, which conforms to the well-defined cubic structure typical for the HH phase containing negligible amounts of Sn metal. The calculation of the lattice parameter and the crystal structure refinements were done using the Rietveld method, which yielded a lattice parameter of a = 6.1148 Å for the undoped sample, which is in agreement with the values reported in the literature [233]. The inset in Figure 5-1 shows a roughly monotonic increase with increasing Sc amount, which agrees well with Vegard's law. The increase serves as evidence of the substitution of slightly larger Sc atoms (radius = 1.60 Å) for Zr (radius = 1.55 Å). Each of these observations is consistent with previous synchrotron results on $Ti_{1-x}Sc_xNiSn$ compounds synthesized in a similar way [232].

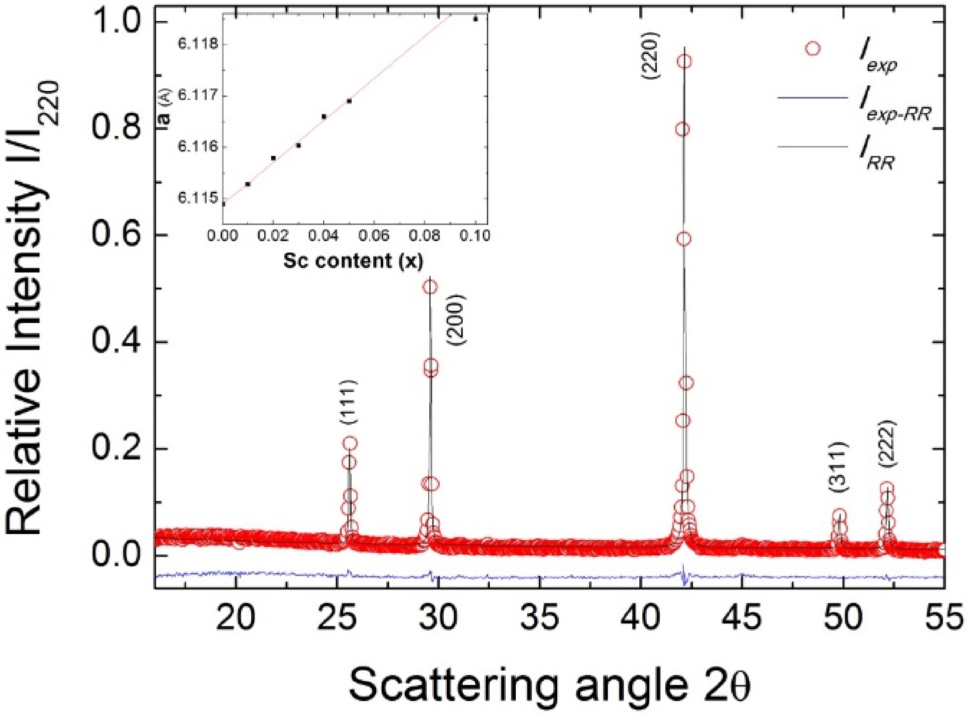

Figure 5-1 Powder XRD pattern for the $Zr_{0.95}Sc_{0.05}NiSn$ sample (I_{exp}) with the Rietveld refinement (I_{RR}) and the difference profile (I_{exp-RR}). The inset shows the dependence of the lattice parameter a (Å) for $Zr_{1-x}Sc_xNiSn$ versus Sc content (x). The straight line represents the linear fit to Vegard's law.

Electrical Transport Properties

The electrical properties of the $Zr_{1-x}Sc_xNiSn$ (x = 0 ,…, 0.10) solid solution are shown in Figure 5-2a. At room temperature, the samples exhibit high electrical resistivity, which decreases with increasing temperature for all the samples, indicating semiconducting behavior. For high substitution levels, both the room temperature value and the temperature dependence of the resistivity decreases, pointing to a shift of the Fermi level towards the valence band as a result of an increasing *p*-type carrier concentration.

It can be seen from Figure 5-2b that for increasing Sc content in the $Zr_{1-x}Sc_xNiSn$ solid solution, the Hall mobility ($\mu_H = \sigma \cdot R_H$ in units of mobility) is suppressed (and eventually becomes positive) by the addition of holes. The parent compound, *n*-type ZrNiSn, exhibits the highest mobility, with a value at room temperature of 25 $cm^2/ V \cdot s$, which is a typical value for *n*-type

*X*NiSn-based systems [234, 235]. This value is still significantly lower than 150 cm^2/ V·s for Bi_2Te_3 or 900-1400 cm^2/ V-s for the lead chalcogenides [58, 236]. If we assume that each replacement of Zr by Sc leads to one hole, the room temperature electron concentration should be completely compensated when the Sc concentration exceeds ~5%. At low Sc content, the samples with $0 \le x \le 0.04$ possess a negative value for $\sigma \cdot R_H$, which is consistent with a substitutional doping explanation.

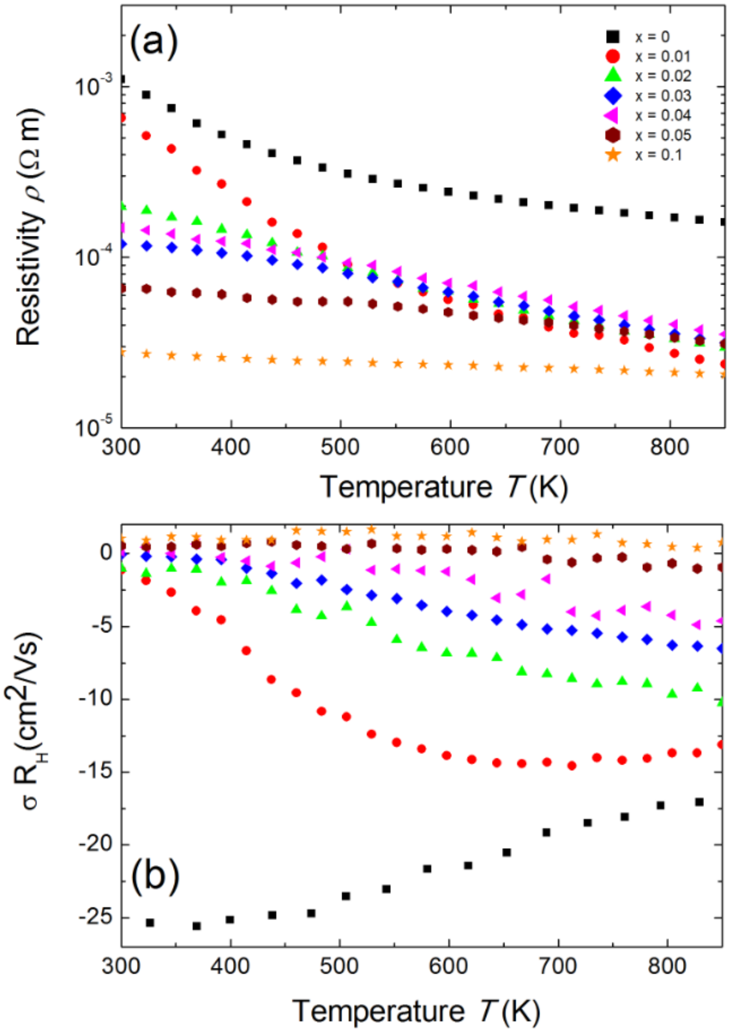

Figure 5-2: Temperature dependence of a) the electrical resistivity ρ and b) the $\sigma \cdot R_H$ product (in units of mobility) for the $Zr_{1-x}Sc_xNiSn$ solid solution. The true Hall mobility at 300 K is largest for the intrinsic, n-type ZrNiSn sample (Figure 2b). With increasing Sc content, the magnitude of $\sigma \cdot R_H$ decreases as a result of the influence of the low mobility holes.

With regards to the origin of the low mobility in the samples which show p-type character, we should consider how the Hall coefficient varies as a function of carrier mobility and concentration when both electrons and holes are present (in the bipolar region) [121]:

$$\boldsymbol{R_H} = \frac{\boldsymbol{n_p}\,\boldsymbol{\mu_p^2} - \boldsymbol{n_n}\mu_{\boldsymbol{n}}^{\boldsymbol{2}}}{\boldsymbol{e}(\boldsymbol{n_p}\,\boldsymbol{\mu_p} - \boldsymbol{n_n}\mu_{\boldsymbol{n}})^2} \qquad \text{Equation 5-2}$$

Here, n_n and n_p are the electron and hole concentrations, respectively, and μ_n and $\mu_p$are the electron and hole mobilities, respectively. If μ_n> μ_p, the sign for the Hall coefficient R_H can be negative even if n_p > n_n. In order to obtain a positive value for the Hall coefficient, $n_p\ \mu_p^2$ needs to exceed $n_n\mu_n^2$. Because the individual carrier contributions, n_n and μ_n, are unknown and difficult to determine, $n_H = \frac{1}{R_H e}$ can be used assuming a single carrier type, but it will result in a value that is greater than either the true value for n_p or n_n.

The Seebeck coefficient (S) for the $Zr_{1-x}Sc_xNiSn$ solid solution are presented in Figure 5-3. The pure ZrNiSn compound, without any Sc doping, displays a large negative Seebeck coefficient at room temperature, indicating a significant *n*-type defect concentration in the intrinsic ZrNiSn. With increasing Sc content, the value of the thermopower decreases as compensating *p*-type defects (Sc^{3+} on Zr^{4+} sites) are added to the naturally *n*-type material. It can be seen from the change in sign of the Seebeck coefficient from negative to positive that holes become the predominant charge carriers. This sign change occurs at lower Sc contents than observed for the sign change of $\sigma \cdot R_H$ (Figure 5-2b), indicating that in this region of mixed conduction, the holes probably outnumber electrons. However, because the electrons are more mobile, the Hall coefficient does not change sign until x > 0.05 (note that the mobilities are squared, in Equation 5-2), whereas the Seebeck coefficient is weighted by mobility to the first power [121]. As observed in the Hall coefficient measurements, ambipolar conduction of both electrons and holes is most likely responsible for the decrease in the thermopower at high temperatures.

In addition to indicating the onset of bipolar conduction, the maximum of the thermopower can be used for the estimation of the Goldsmid-Sharp band gap, E_g, according to Equation 5-1 [51], where we obtained values on the order of 0.05 eV. This is much smaller than the band gap suggested by Aliev *et al.* from electrical resistivity measurements (0.18 eV) [237]. The discrepancy between the estimation from our thermopower data and the literature estimates for the size of E_g in these compounds will be discussed in detail later and is the main topic of this chapter.

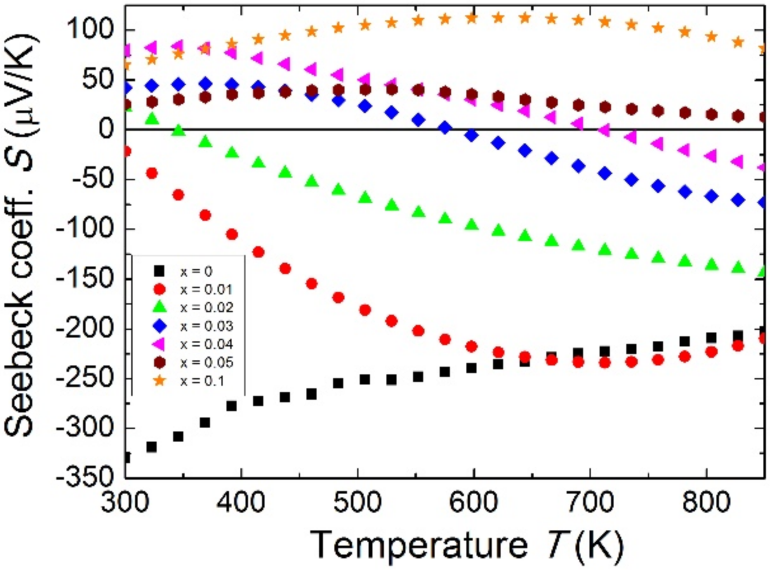

Figure 5-3: Temperature dependence of the Seebeck coefficient for the $Zr_{1-x}Sc_xNiSn$ solid solution. The Seebeck coefficient shows a rollover due to ambipolar conduction.

The temperature-dependent total thermal conductivity (κ_{tot}) is shown in Figure 5-4. The room temperature thermal conductivity is reduced by 40% for $Zr_{0.9}Sc_{0.1}NiSn$ as compared with the undoped ZrNiSn. Because this is accompanied by a decrease in resistivity (Figure 5-2a), it is clear that this must be due to scattering of phonons as a result of increased disorder in the material, which reduces the lattice thermal conductivity (which is much greater than the electronic thermal conductivity at room temperature for all Sc compositions). Above room temperature, we can see an increasing thermal conductivity for the doped samples, which is consistent with the existence of both electrons and holes (which is also shown by the other transport properties in Figure 5-2b and Figure 5-3). This effect occurs at lower and lower temperatures as the Sc content is increased. Although the bipolar effects are less pronounced for the Seebeck coefficient measurements, thermal conductivity is quite sensitive to bipolar conduction because it is affected both by the decrease of the resistivity (increasing κ_e) and by the increasing magnitude of the bipolar term of the thermal conductivity (κ_b).

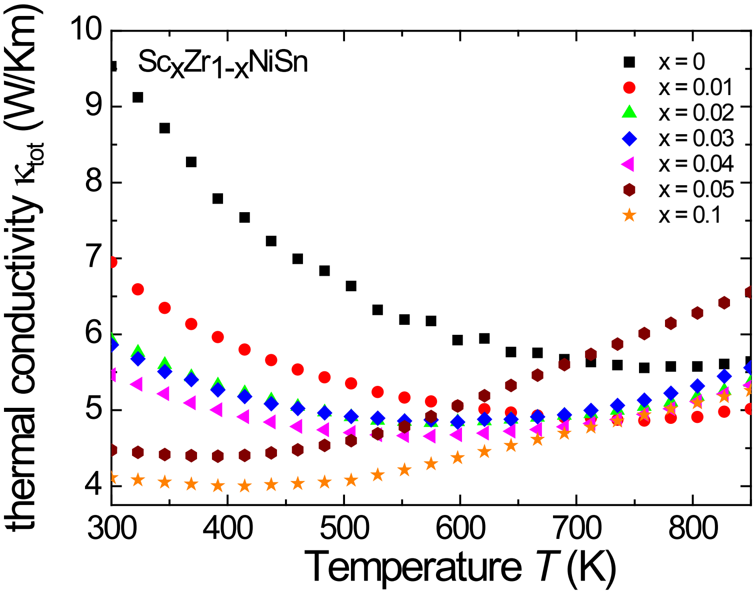

Figure 5-4 The total thermal conductivity of the $Zr_{1-x}Sc_xNiSn$ solid solution as a function of temperature and Scandium content.

Optical Absorption Edge

Optical properties were also measured to get information about the band structure, as displayed in Figure 5-5. Undoped ZrNiSn was measured in diffuse reflectance at room temperature; the indirect optical band gap was extracted using the Tauc extrapolation method (as discussed in Chapter 2) [46, 95]. The estimated value of the indirect optical band gap was 0.13 eV. Aliev et al. measured ZrNiSn samples previously using optical techniques, and they reported a minimum in the absorption coefficient of approximately 2000 cm^{-1} (~0.25 eV)—a value quite a bit larger than the 0.13 eV measured in this work. The most likely reason for this discrepancy is due to the large difference in room temperature resistivity.

It should be understood that the properties of ZrNiSn seem to depend significantly upon the method of synthesis for the sample. I performed similar DRIFTS measurements on intrinsic ZrNiSn samples synthesized by another collaborator using levitation melting/spark plasma sintering (Xie et al. [230, 238]), which yielded a minimum in the absorption coefficient around 0.2 eV (which agrees with Aliev's results). However, I attribute the higher absorption edge to a higher carrier concentration (which increases free-carrier absorption and possibly induces a Burstein Moss shift, see Chapter 3) than those samples presented here (synthesized using arc-melting). ZrNiSn from both Xie et al. and Aliev et al. show a much lower room temperature resistivity ($\sim 10\ m\Omega - cm$) in comparison to samples from this thesis chapter (intrinsic ZrNiSn showed resistivity near $100\ m\Omega - cm$). The lower resistivities from Xie, Aliev et al. resulted in free carrier absorption, which pushed the minimum absorption coefficient to higher energies.

Band gaps extracted from the temperature dependent resistivity both in this work and from Aliev et al. show values near 0.18 eV [237]. The large range of different values for the band gap obtained from different methods (Goldsmid-Sharp, temperature-dependent resistivity, optical, and DFT) suggest that a self-consistent model for this material should be developed. The remainder of this section will investigate the origins of the spread in values as well as the nature of the valence band. Recent literature suggests that the valence band is composed of Ni-states which arise from disorder within the material (specifically Ni disorder onto the vacancy site) [239], which will be discussed in detail later.

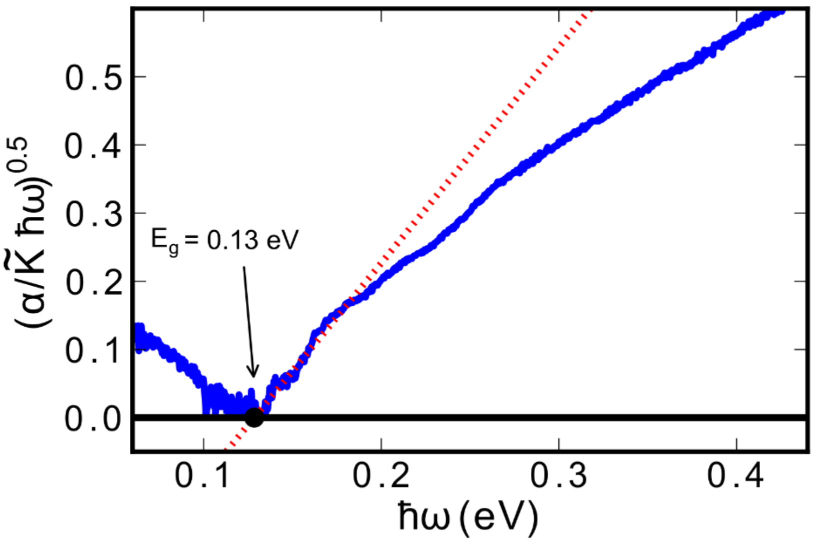

Figure 5-5: Optical diffuse reflectance data plotted as the indirect band gap transformation of the Kubelka Munk function for pure ZrNiSn. A linear fit (red dotted line) was used to estimate the band gap by extrapolating to zero absorption, indicating that the band gap is ~0.13 eV.

5.2c - Discussion

When considering the transition from heavily doped to intrinsically semiconducting behavior ($E_{g,thermal} < \sim 5\ k_BT$), the Seebeck coefficient is an important indicator of the excitation of minority charge carriers across the band gap. In between these two regions, the thermopower will reach a maximum (as shown in Figure 5-3), which can be used to estimate the band-gap via the Goldsmid-Sharp formula (Equation 5-1). The thermopower band gaps for the $Zr_{1-x}Sc_xNiSn$ solid solution are compared to those of a series of *n*-type *X*NiSn samples from the literature, as shown in Figure 5-6.

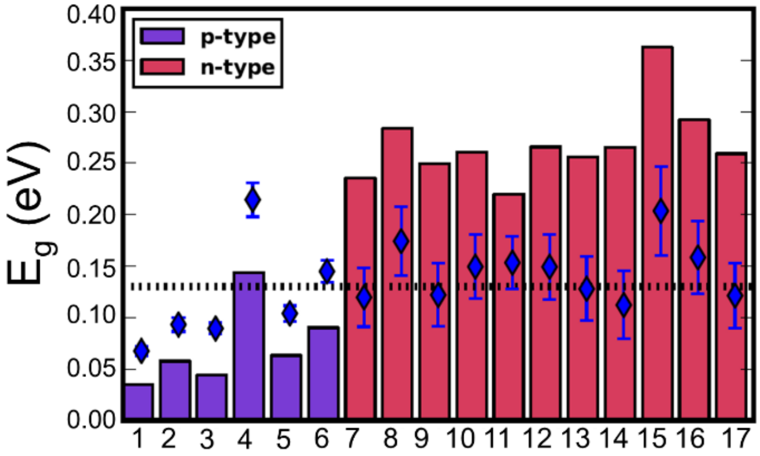

Figure 5-6: Estimation of the band gap for different n-*type (red bars) and* p-*type (purple bars) half-Heusler compounds using the Goldsmid-Sharp formula (E_g=2e$S_{max}T_{max}$) in units of eV* versus *the numerated HH compounds. The dotted line indicates the optical measured band gap of 0.13 eV for pure ZrNiSn from DRIFTS. The diamonds represent the estimated true band gap value that yields the experimental* S_{max} *and* T_{max} *when using the full relation derived by Goldsmid and Sharp for an electron-to-hole weighted mobility ratio of* A=*5 : 1) $Sc_{0.03}Zr_{0.97}NiSn$, 2) $Sc_{0.04}Zr_{0.96}NiSn$, 3) $Sc_{0.0.5}Zr_{0.95}NiSn$, 4) $Sc_{0.1}Zr_{0.9}NiSn$, 5) $ZrCo_{0.08}Ni_{0.92}Sn$ [230], 7) $Zr_{0.75}Hf_{0.25}NiSn$ [240], 8) $Zr_{0.5}Hf_{0.5}NiSn$ [240], 9) $Zr_{0.25}Hf_{0.75}NiSn$ [240], 10) HfNiSn [240], 11) $Ti_{0.95}Hf_{0.05}NiSn$ [241], 12) $Ti_{0.95}Hf_{0.05}NiSn_{0.995}Sb_{0.005}$ [241], 13) $Ti_{0.95}Hf_{0.05}NiSn_{0.99}Sb_{0.01}$ [241], 14) $Ti_{0.95}Hf_{0.05}NiSn_{0.98}Sb_{0.02}$ [241] , 15) $Hf_{0.75}Zr_{0.25}NiSn_{0.99}Sb_{0.01}$ [242], 16) $Hf_{0.5}Ti_{0.25}Zr_{0.25}NiSn_{0.99}Sb_{0.01}$ [242], and 17) $Hf_{0.25}Ti_{0.5}Zr_{0.25}NiSn_{0.99}Sb_{0.01}$ [242].*

A large difference in the Goldsmid-Sharp thermopower band gap is apparent when comparing Sc-doped *p*-type samples from this work and *n*-type literature results; both are much smaller than those estimated by *ab initio* calculations (~0.5 eV) [232, 233]. Here, we note that even though X (in XNiSn samples) varies through Zr, Hf, and Ti for n-type samples in Figure 5-6, the band structures and band gaps are expected to be the same (for DFT calculations) [243]. Although the large difference in Goldsmid-Sharp band gap between p-type and n-type samples might lead one to the conclusion that the choice of dopant will affect the size of the gap, it is important to consider the limitations of the simple Goldsmid-Sharp band gap estimation and the parameters that might affect the results. Following the derivation from Goldsmid and Sharp, the Seebeck coefficient for a mixed semiconductor is given as:

$$\boldsymbol{S = \frac{1}{1+\frac{\sigma_n}{\sigma_p}}\left(S_p + \frac{\sigma_n}{\sigma_p} S_n\right)} \qquad \text{Equation 5-3}$$

where $S_{n,p}$ and $\sigma_{n,p}$ represent the thermopower and the electrical conductivities of the two different carrier types, respectively. Goldsmid and Sharp derived a simple model assuming classical statistics [51], which estimates the electron-to-hole conductivity ratio as

$$\boldsymbol{\frac{\sigma_n}{\sigma_p} = A\, exp(\eta_n - \eta_p)} \qquad \text{Equation 5-4}$$

where η_n and η_p are the electron and hole dimensionless chemical potentials ($\eta = \xi / k_B T$). A is defined as the weighted mobility ratio:

$$\boldsymbol{A = \frac{\mu_{0,n} N_{v,n}}{\mu_{0,p} N_{v,p}} \left(\frac{m^*_{b,n}}{m^*_{b,p}}\right)^{3/2}} \qquad \text{Equation 5-5}$$

where $\mu_{0,n,p}$ is the electron or hole mobility parameter, $N_{v,n,p}$ is the valley degeneracy of the electron or hole pocket (both are N_v=3 in this case), and $m^*_{b,np}$is the single valley effective mass (not including the degeneracy of the valence or conduction bands). By substituting Equation 5-5 into Equation 5-4 and taking the classical limit for the thermopower and determining its maximum, Goldsmid and Sharp obtained:

$$\boldsymbol{S = \frac{k_B}{e} \frac{2(\eta_n - \lambda - 2)\left(\frac{E_g}{k_B T} + 2\lambda + 3\right) - \left(-\eta_n - \frac{E_g}{k_B T} - \lambda - 2\right)}{1 + 2\left(\frac{E_g}{k_B T} + 2\lambda + 3\right)}} \qquad \text{Equation 5-6}$$

And

$$\boldsymbol{A\exp\left(2\eta_n+\frac{E_g}{k_BT}\right) = \left(\frac{E_g}{k_BT}+2\lambda+3\right)\left[1\pm\sqrt{1-\frac{1}{\left(\frac{E_g}{k_BT}+2\lambda+3\right)^2}}\right]}$$

Equation 5-7

where $\frac{E_g}{k_BT}$ is the dimensionless band gap, and λ is the scattering exponent ($\tau = \tau_0\left(\frac{E}{k_BT}\right)^{\lambda-1/2}$, where $\lambda = 0$ is assumed here, which represents acoustic phonon scattering). In light of the large mobility difference between the *n*-type undoped sample (~25 cm^2/V·s) and the heavily Sc-doped samples (*p*-type mobility approximately ~1-2 cm^2/V·s), a weighted mobility ratio (*A*) that is larger than unity should be considered. In order to investigate this, we first gathered estimates of the Goldsmid-Sharp band gap for a series of *p*- and *n*-type ZrNiSn samples, as shown by the bars in Figure 5-6. A clear separation is observed between *p*-type samples (~0.05 eV) in purple and *n*-type ones in red (>~0.2 eV). For reference, the results from the optical measurements (Figure 5-5) are also plotted as a dashed line at ~ 0.13 eV in Figure 5-6. By numerically solving Equation 5-6 and Equation 5-7 with *A* = 5 (a reasonable value considering the large mobility difference between electrons and holes), I determined the required true band gap that would yield the experimentally measured S_{max} and T_{max}, the results of which are shown as blue diamonds in Figure 5-6 for each of *n*- and *p*-type ZrNiSn-based HH materials. All of these values are close to the measured optical results of 0.13 eV, indicating that the large weighted mobility ratio between electrons and holes is likely responsible for the difference in the Goldsmid-Sharp thermopower band gap when comparing *n*- and *p*-type samples.

Although Goldsmid and Sharp state that even with a large mobility ratio value (*A = 10*), the simple band gap estimatie should hold to within ~ 20%, I note that they assume a band gap of 10 k_BT_{max} to derive this value. This is a poor assumption for most materials, as the band gap in our system (and many others) is less than 5 k_BT_{max}. In order to illustrate this point, I have plotted

$2eS_{max}T_{max}/E_g$ versus S_{max} for a mobility ratio parameter $A = 5$ using Equation 5-6 and Equation 5-7 (Figure 5-7). The red line is the result for the *n*-type doping and the blue line displays the result for *p*-type doping. Data points in their corresponding colors were taken from their Goldsmid-Sharp band gap ratio to the optical band gap measured in this work (0.13 eV). The displayed error bars assume an error of ±10% in the thermopower and the optical band gap. Figure 5-7 shows a positive deviation to $2eS_{max}T_{max}/E_g$ (relative to 1.0) for the *n*-type samples, whereas we observe a negative deviation for *p*-type ones. Qualitatively, this is because the more mobile electrons dominate the Seebeck coefficient equation because it is weighted by their conductivity; this forces the thermopower of the *p*-type samples to roll over at lower values, whereas *n*-type samples maintain higher thermopower at higher temperatures.

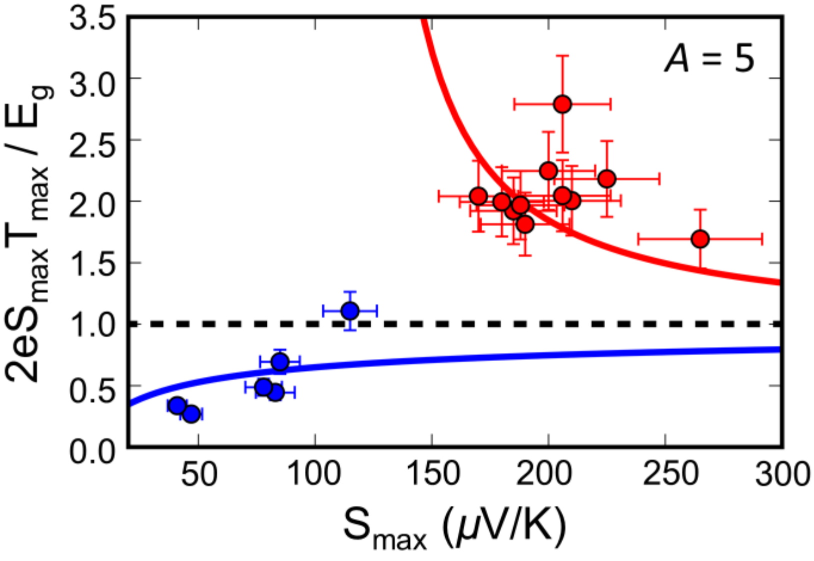

Figure 5-7: A plot of the ratio of the Goldsmid-Sharp band gap (2eSmaxTmax) to the true band gap for different p- and n-type half-Heusler compounds in red and blue, respectively, for an electron-to-hole weighted mobility ratio of A=5. The solid lines use Goldsmid and Sharp's full derived equation (Equation 5-6) to estimate this ratio. Experimental points use the observed maximum Seebeck coefficient (Smax) and temperature (Tmax) and the optical band gap (Eg,optical). An error of ±10% was assumed for the thermopower measurements and the band gap estimations.

To probe the supposition that $A \approx 5$ in ZrNiSn, an estimate for the weighted mobility ratio was obtained using a single parabolic band model as fit from the measured Seebeck coefficient and resistivity. Rather than fitting the effective mass and μ_0 (or equivalently E_{def}), in the absence of Hall data the weighted mobility (or in our case reliable estimates of the carrier concentrations in either the valence or conduction band), σ_0 can be fit. σ_0 is the conductivity pre-factor (a constant that does not depend on Fermi level that scales the conductivity) which can be expressed as:

$$\boldsymbol{\sigma_0 = n_0 e \mu_0 = \frac{\sqrt{2}(k_B T)^{3/2} e}{\pi^2 \hbar^3} \mu_0 {m_d^*}^{3/2}} \qquad \text{Equation 5-8}$$

which defines the relationship between the weighted mobility ($\mu_0 {m_d^*}^{3/2}$) and σ_0. This can be fit in a similar way to the effective mass for a single parabolic band (as detailed in Chapter 2) by first using the measured Seebeck coefficient to estimate the reduced chemical potential (η), then solving for σ_0 using the measured conductivity and the relation:

$$\boldsymbol{\sigma = \sigma_0 F_0(\eta)} \qquad \text{Equation 5-9}$$

The weighted mobility ratio (*A*) can then simply be defined as the ratio of the σ_0 terms of *n*-type and *p*-type samples. I gathered data from both this thesis and XNiSn literature results (with both donor and acceptor doping) to estimate σ_0 values as a function of the measured electrical conductivityl the results are shown in Figure 5-8. In order to minimize the effect of bipolar conduction, it is desirable to estimate σ_0 for the samples with their Fermi levels as far from the opposing band as possible; this is accomplished in Figure 5-8 by taking our estimates for $\sigma_{0,CB}$ and $\sigma_{0,VB}$ for samples with the highest electrical conductivities (far left or far right of the plot respectively). This yields 1.1 and 0.15 $(m\Omega - cm)^{-1}$ for $\sigma_{0,CB}$ and $\sigma_{0,VB}$ respectively. I estimate a weighted mobility ratio given these values of σ_0 of $\frac{1.1}{0.15} \approx 7$, which agrees well with our estimate of 5 when considering the maximum Seebeck coefficients in Figure 5-6 and Figure 5-7. I should note that the exact values of σ_0 may depend on the method of synthesis (ideally we would obtain $\sigma_{0\ n,p}$ for data that all used the same synthesis procedure).

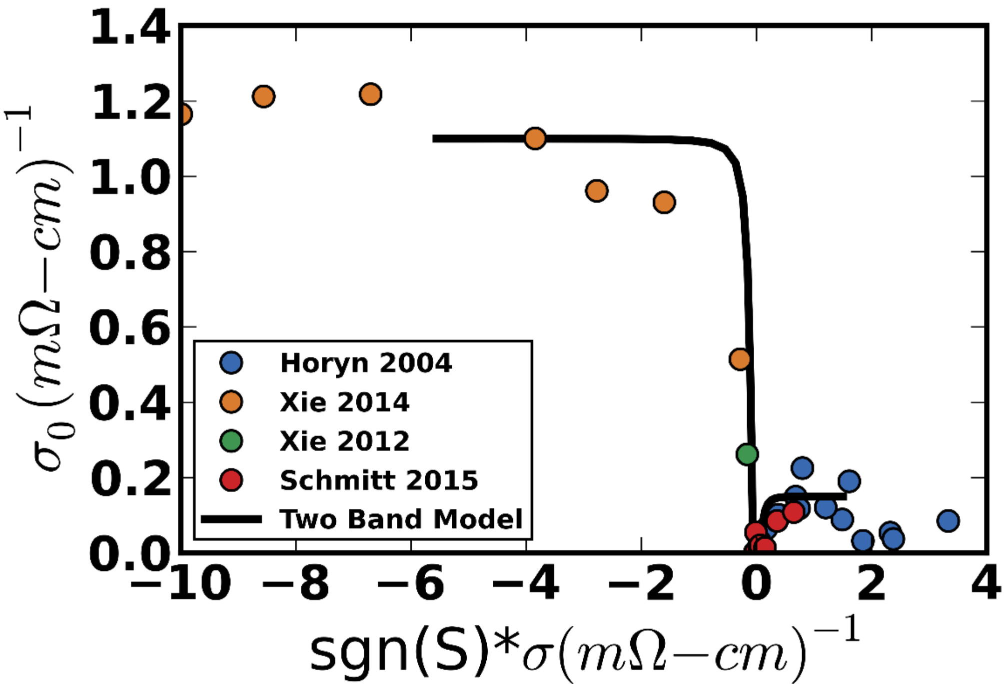

Figure 5-8: Estimated conductivity prefactor using the single parabolic band model for a series of ZrNiSn samples across the p-type to n-type transition for several literature results [52, 230, 231, 238] and results from this thesis. On the x-axis I have multiplied the measured conductivity by the sign of the measured Seebeck coefficient in order to represent the sign change. I have plotted these results along with a two-band (valence/conduction) model that uses a $\sigma_{0,CB} = 1.1$ *and a* $\sigma_{0,VB} = 0.15$ *and a band gap of 0.128 eV (as measured optically).*

5.2d - Electronic Structure Origin of the Weighted Mobility

Recent HH literature provides a self-consistent explanation as to the origin of the valence band states, which we have found to yield low weighted mobility. XNiSn materials upon addition of one more Ni atom per unit cell form the full-Heusler analog (XNi_2Sn). This crystal structure is known to be stable and produces a metallic material. Experimental evidence using synchrotron XRD and hard x-ray photoemission spectroscopy (HAXPES) confirms the existence of both in-gap states [239, 244] and up to ~10% of the Ni atoms disordering onto vacancy sites [239, 245]. Defect calculation results [246-249] confirm this theory, and the observed narrow gaps obtained from transport are sometimes attributed to these states [248, 250] in the literature.

With regards to the optical properties, the proposed picture of in-gap Ni states induced by disorder is consistent with the results obtained here. Even hydrogenic impurities, which contain a single energy level rather than a band of states, can result in an absorption edge below the fundamental one which shows similar energy dependence to indirect transitions [45]. In the case of ZrNiSn, though, the Ni-vacancy interstitial defects result in an addition of a continuous band of states within the gap [249], which can also lead to appreciable absorption below the fundamental edge (as shown in $Zn_{1-x}Mn_xO$ [251]). The narrow gap observed both optically and electronically imply that these “in-gap” Ni-interstital states simply compose the valence band from which we observe optical transitions and bipolar effects. Further, the electronic properties and weighted mobility ratio could also be explained in this context. Specifically, the inherently disordered impurity band would likely have lower mobility than the conduction band states which are likely a result of the underlying HH framework and are probably less effected by the disorder.

While the very small mobility in *p*-type ZrNiSn may be disheartening, it beneficially results in suppressed bipolar effects in the *n*-type ZrNiSn system. Thus, the low mobility minority carrier enables the *n*-type material to maintain a high thermopower at high temperatures, despite its narrow band gap. This is contrary to the high band gaps found in other *p*-type HHs, like TiCoSb or the recently identified $FeV_{0.6}Nb_{0.4}Sb$, where the band gap estimated from the Goldsmid-Sharp formula is around 0.57 eV and 0.4 eV, respectively [22, 252].

5.2e - Conclusions

In this section, the thermoelectric transport properties of Sc-substituted ZrNiSn HH solid solutions were systematically studied. The substitution of Zr by Sc led to the successful introduction of holes into the system, resulting in a *p*-type material with a maximum thermopower of +115 μV/K at 650 K. Owing to the introduction of holes into the system, the Seebeck coefficient became positive and increased with increasing temperature, reaching a maximum as the higher mobility *n*-type carriers were thermally activated. Generally, the transport properties are dominated by the high mobility of the electrons over that of the lower mobility holes, which can be seen from the $R_H\sigma$ product (in units of mobility). Both *p*-type data from this work and *n*-type literature data for the thermopower gap deviated significantly from the optical measurements (0.13 eV), but I have shown that this can be simply explained by a large difference in the weighted mobility between electrons and holes. A high electron-to-hole weighted mobility ratio leads to a suppression of the bipolar effect in the thermoelectric transport properties, which is essential for high zT values in n-type XNiSn (X = Ti, Zr, Hf) HH compounds.

5.2f - Methods

The solid solution $Zr_{1-x}Sc_xNiSn$ (x = 0, … , 0.10) was prepared by arc melting of stoichiometric amounts of Zr (99.99%), Ni (99.999%), Sn (99.999%), and Sc (99.999%) in an Ar atmosphere on a water-cooled crucible. To ensure compositional homogeneity, samples were flipped and remelted five times. The as-cast samples were annealed in evacuated quartz tubes at 1220 K for 7 d, followed by quenching in ice water to ensure the crystalline order. The crystal structure of the samples was studied by *X*-ray diffraction (*XRD*) on a Siemens D5000 diffractometer using Cu Kα radiation (wavelength of 1.5418 Å). The powder *XRD* patterns of all samples showed that they were a single phase with cubic $C1_b$ structure [233].

The total thermal conductivity was calculated from the thermal diffusivity (D) with $\kappa = C_P D d$, where C_p is assumed to be the Dulong–Petit heat capacity and d the density calculated from the molar mass and the lattice parameter for each sample obtained from XRD.

5.3 - Extending the Weighted Mobility Ratio/Goldsmid-Sharp Gap Analysis to Low Gap Materials

5.3a - Introduction

In the previous section, I have shown how to obtain an accurate estimate of the band gap using optical and electronic properties in ZrNiSn, which has a large difference in electron and hole weighted mobility. In this section, I extend the analysis beyond the non-degenerate limit to probe its applicability for narrow-gap semiconductors using full Fermi statistics. I also explore some of the assumptions made by Goldsmid and Sharp to show when the relation breaks down and what the expected error might be.

As mentioned in the previous section, band gap is an important parameter in thermoelectric materials because at high temperatures, bipolar excitation of carriers across the gap leads to a drastic drop in thermoelectric efficiency. This can be seen by plotting *zT* versus temperature for a good (representative) thermoelectric material (Figure 5-9 inset), the *zT* will rise until reaching a peak value after which it decreases. Since the peak *zT* values are often the metric by which materials are compared, it is worthwhile to understand the origins of the peak and what factors can influence it. Typical degenerate thermoelectric semiconductors display thermopowers which rise linearly with temperature to a maximum (Figure 5-9) followed by a decrease. Because the Seebeck coefficient is squared in the formula for *zT*, a maximum in the thermopower also results in a maximum in the temperature dependent *zT*.

It is well known that the origin of the thermopower peak is most often related to the onset of bipolar conduction which involves thermal excitation of both electrons and holes across the band gap. The contribution to the overall Seebeck coefficient by both the positive and negative charge carriers can be described by the conductivity weighted average (analogous to Equation 5-3):

$$\boldsymbol{S} = \frac{\boldsymbol{\sigma_p S_p} - \boldsymbol{\sigma_n}|\boldsymbol{S_n}|}{\boldsymbol{\sigma_p} + \boldsymbol{\sigma_n}} \qquad \text{Equation 5-10}$$

Because the minority carriers are (by definition) fewer in number, they will also have higher thermopower contributions (Seebeck coefficient is inversely proportional to carrier concentration). However, at low temperatures the population of minority carriers is small (low σ), meaning that they will not contribute much to the overall S. At higher temperatures, though, a broadening Fermi distribution leads to an exponential increase in minority carrier conductivity, resulting in a reduction (and therefore peak) in the thermopower [51].

The strength of bipolar conduction is determined by the value of the semiconductor band gap. Goldsmid and Sharp developed an analytical expression relating the band gap and the maximum thermopower, $|S|_{max}$, and the temperature at which it occurs (T_{max}) in the bipolar regime: $E_g=2e|S|_{max}T_{max}$ (Equation 5-1) [51]. This simple method of estimating the band gap is ubiquitous in the thermoelectrics community because temperature dependent Seebeck coefficient is so commonly measured. Figure 5-9 shows a calculated temperature dependent Seebeck coefficient and corresponding zT (inset) for a valence (VB) and conduction band (CB) model with a band gap of 0.13 eV at various carrier concentrations. We can see that the Goldsmid-Sharp band gap formula accurately predicts the maximum thermopower over a wide range of carrier concentrations and temperatures (as demonstrated by the dashed line in Figure 5-9, which serves as a good upper bound for the thermopower at a particular temperature regardless of extrinsic doping concentration). For example, Bi_2Te_3 has a band gap of E_g~0.13 eV [253, 254] at room temperature (T_{max} = 300K), yielding a maximum Seebeck coefficient near 230 μV/K—a reasonable estimate [255-258].

While the Goldsmid-Sharp gap serves as a quick estimate of the band gap in a given material, it is important to understand where deviations might occur when using this analysis. In Goldsmid-Sharp's full equation (Equation 5-5), the weighted mobility ratio, A, is an important parameter that governs how closely the Goldsmid-Sharp gap reflects the true gap. We can also consider *A* as the ratio of the quality factors, *B* (Equation 2-6), between the majority and minority bands. In the previous section, I showed that the Goldsmid-Sharp band gap can deviate by 50-100% of the optical band gap value mainly due to the large *A* values (*A*=5 for ZrNiSn) and an ϵ_g which is much less than 10 (<5 $k_B T$ in ZrNiSn) [52]. Further, the non-degenerate limit (as assumed by Goldsmid and Sharp) is not applicable for many common thermoelectric materials: in Bi_2Te_3 [259, 260], PbSe [65, 261], and PbTe [28, 34], where the value of the band gap is actually 5-6 $k_B T$ at T_{max}. In this section, I investigate the effects of a narrow ϵ_g by replacing Maxwell-Boltzmann statistics, applied in Goldsmid-Sharp's derivation, with Fermi-Dirac statistics which can more accurately represent semiconductor processes in narrow-gap ($\epsilon_g < 10$), doped materials. Ultimately, I present a chart that can be used to quickly estimate the relationship between the true gap and the Goldsmid-Sharp band gaps depending on *A* and S_{max}.

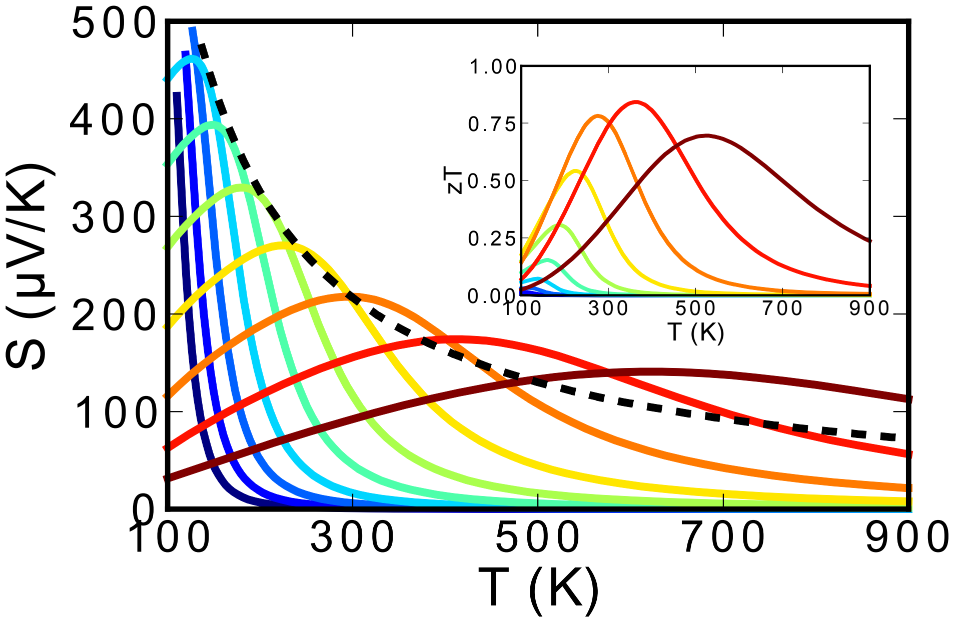

Figure 5-9: Calculated temperature dependent Seebeck coefficient and zT (inset) for various defect concentrations (N_A=p-n=1×10^{15} cm^{-3} in blue to 1×10^{20} cm^{-3} in red) for two parabolic bands with a band gap of 0.13 eV, m^*=1.0 m_0, and $\mu_0(300\ K) = 820\ cm^2/Vs$ (VB and CB). Dashed line indicates the Goldsmid-Sharp band gap: $S = E_g/2eT$. The lattice thermal conductivity was estimated as $\kappa_L(T) = 1.7\ (300/T)$ W/m-K, and the following Umklapp scattering is used for the zT estimate.

5.3b - Theory

The Seebeck coefficient in a multi band (valence/conduction) system can be expressed by Equation 5-3 [62]. In the interest of maintaining general relationships applicable for either p or n-type materials, we chose to use the majority and minority carrier labels by changing the n- and p-type terms in Equation 5-3 into the majority (maj) and minority (min) charge carrier contributions; S_{maj}, and S_{min}, and σ_{maj} and σ_{min} are the majority and minority carrier Seebeck coefficients and conductivities, respectively. In the case of a primarily p-type material, the majority carrier will be holes. While Goldsmid and Sharp proceed assuming Maxwell-Boltzmann, non-degenerate statistics, $\frac{\sigma_{maj}}{\sigma_{min}} = A\exp\left(\eta_{maj} - \eta_{min}\right)$ (Equation 5-4), where $A = \frac{\mu_{0,maj} N_{v,maj}}{\mu_{0,min} N_{v,min}} \left(\frac{m^*_{b,maj}}{m^*_{b,min}}\right)^{3/2}$, we will consider the Fermi integral solution to the Boltzmann transport equation (assuming scattering by acoustic phonons and parabolic bands) as presented in Chapter 2 for parabolic bands. In this context, the electrical conductivity ratio between the majority and minority carriers can be written as a function of the dimensionless chemical potential η in terms of the Fermi integral, F_j (as expressed in Chapter 2):

$$\boldsymbol{\frac{\sigma_{maj}}{\sigma_{min}} = A\frac{F_0\left(\eta_{maj}\right)}{F_0\left(\eta_{min}\right)}} \qquad \text{Equation 5-11}$$

Table 5-2 Description of the three different methods of estimating the maximum thermopower in this work.

Method Name	Criterion for Maximum	Statistics
Goldsmid-Sharp	$dS/d\eta = 0$	Maxwell-Boltzmann
Fermi	$dS/d\eta = 0$	Fermi
Exact	$dS/dT = 0$	Fermi

In order to find the maximum thermopower, several methods can be used as differentiated in Table 5-2. The derivation of the Goldsmid-Sharp band gap does not explicitly find the maximum in thermopower with temperature; rather, Goldsmid-Sharp find a maxima with respect to reduced chemical potential, $dS/d\eta = 0$ which is equivalent to dS/dT=0 when $d\eta/dT$ is much larger than $\frac{d(\epsilon_g)}{dT}$ as pointed out by Goldsmid and Sharp [51]. In this work, the "Fermi" method also assumes $dS/d\eta = 0$, as in the "Goldsmid-Sharp" method, but it uses Fermi-Dirac rather than Maxwell-Boltzmann statistics. We can test the $dS/d\eta = 0$ approximation by performing a full temperature dependent calculation of the Seebeck coefficient: the "Exact" method. This is accomplished by applying a charge counting balance, $N_A - N_D = p - n$ (as described initially in Chapter 2, and in a later section of this chapter), at various temperatures, where N_A and N_D are the number of electron acceptors and donors, respectively (the difference of which was used as an input parameter), and p and n are the number of holes and electrons, respectively (for simplicity we have assumed that $A_{m^*} = \frac{m^*_{b,maj}}{m^*_{b,min}} = 1$, but we discuss the alternative later in this section; Figure 5-15). The full temperature-dependent, numerically calculated results ("Exact" method) will be presented along with the simpler $dS/d\eta$=0 solutions using both Maxwell-Boltzmann ("Goldsmid-Sharp") and Fermi-Dirac ("Fermi") statistics.

5.3c - Results

First, in order to probe the applicability Golsmid-Sharp's assumption of Maxwell-Boltzmann (non-degenerate) statistics, Figure 5-10 considers a weighted mobility ratio of *A*=1. Figure 5-10a shows the chemical potential dependent Seebeck coefficient (with η=0 being the valence band edge, $\eta = \epsilon_g = 5$ being the conduction band edge). As expected, the "Goldsmid-Sharp" result overlaps well with the "Fermi" result for chemical potentials in the gap (0 < η < 5), but deviations begin for chemical potentials of about 1.5 k_BT from either band edge, which become larger as the chemical potential becomes degenerate (chemical potential within the band, $\eta < 0$ or $\eta > \epsilon_g$). Upon varying the band gap, the value of chemical potential (η_{max}) that yields $dS/d\eta = 0$ can be obtained; the results are plotted in Figure 5-10b. For E_g>6 k_BT, η_{max} yield the same value for the "Goldsmid Sharp" and "Fermi" methods, but deviations occur at smaller ϵ_g. Figure 5-10c shows the magnitude of the maximum Seebeck coefficient predicted using the three different methods (as shown in Table 5-2). The result is useful for estimating the maximum attainable thermopower at a given temperature (which would be set to T_{max}) for a material which has an electron-to-hole weighted mobility ratio (A) near 1.0 and a known band gap.

Figure 5-10d quantifies the effectiveness of the $2e|S|_{max}T_{max}$ estimate for band gap at different ϵ_g for the three cases of interest: the $dS/d\eta = 0$ models using both the "Fermi" and "Goldsmid-Sharp" methods, as well as the $dS/dT = 0$ (or "Exact") case. For large ϵ_g, the "Fermi" and "Goldsmid-Sharp" solutions ($dS/d\eta = 0$) converge to $2e|S|_{max}T_{max}/E_g$ very near 1.0 (although the exact value is ~5% less at $\epsilon_g = 10$). However, as the band gap becomes small, (ϵ_g<~5), $2e|S|_{max}T_{max}/E_g$ increases for all three methods. The divergence for small gaps is a consequence of increasingly degenerate chemical potentials which yield the maximum thermopower. Experimentally, this would be observed for heavily doped samples that do not reach a maximum thermopower until very high temperatures (these details will be discussed thoroughly in a later section).

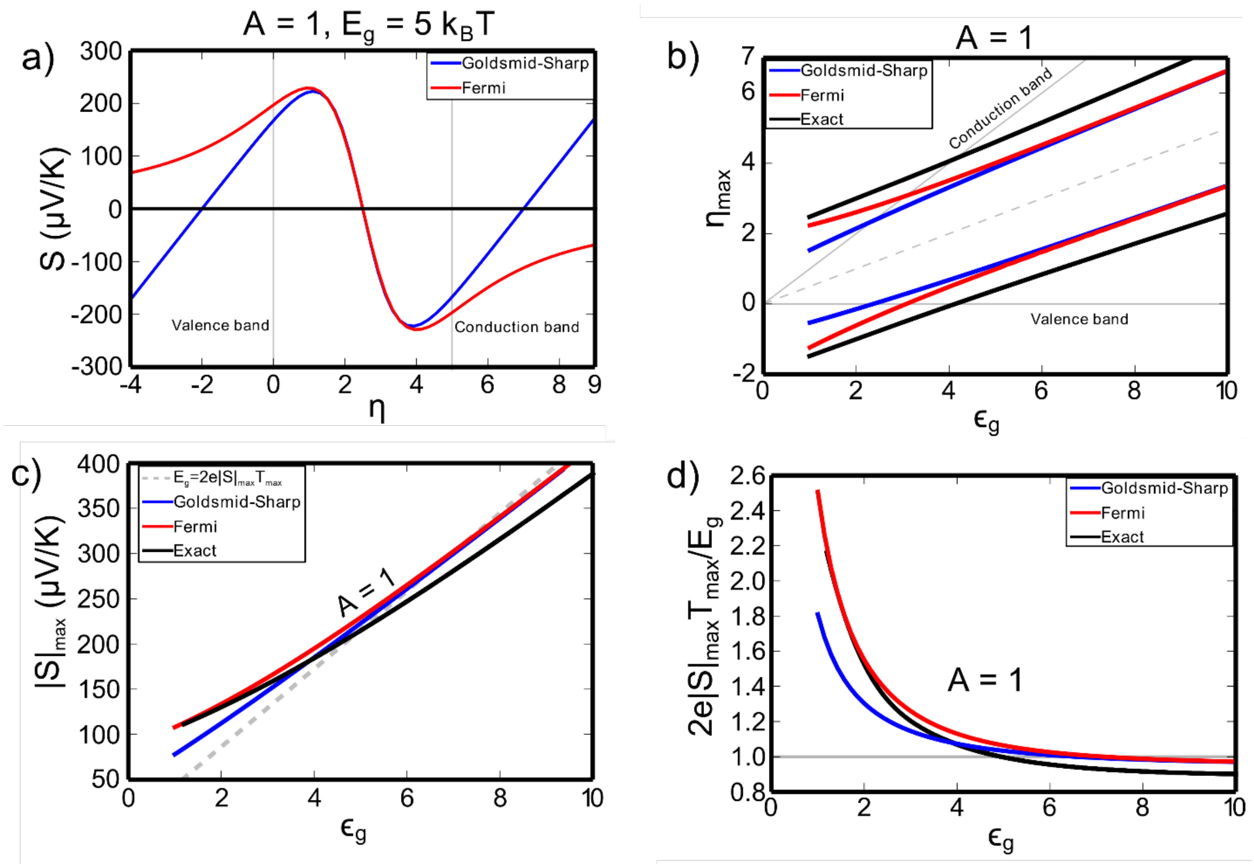

Figure 5-10: Result of the "Exact", "Fermi", and "Goldsmid-Sharp" methods calculated assuming ϵ_g= 5 and A=1 for a) Seebeck coefficient as a function of η. b) The reduced chemical potential which yields the maximum thermopower as a function of reduced band gap (at the rollover temperature) for A=1. c) Maximum attainable thermopower as a function of the reduced band gap (at A=1) for each method. d) the ratio of the $2e|S|_{max}T_{max}$ estimate to E_g as a function of the dimensionless band gap ϵ_g. The dashed line in c) represents the Goldsmid-Sharp band gap equation result. The dashed line in Figure (b) represents the halfway point between the VB and CB, and the solid grey lines represent the position of the valence and conduction bands. All calculations are done for a majority-to-minority carrier weighted mobility ratio of A=1.0.

The weighted mobility ratio (*A*) can also lead to deviations in the Goldsmid-Sharp band gap as illustrated in the previous section for ZrNiSn. While Bi_2Te_3 has similar majority and minority carrier weighted mobility [262, 263], other systems such as Si, Ge, and others [264] are believed to have values that exceed two (5 in the case of ZrNiSn). Figure 5-11 shows the *A*=5 and *A*=1/5 results for temperature dependent Seebeck coefficient ("Exact" method), analogous to Figure 5-9. It is clear that for *A*>1, the maximum Seebeck coefficient is larger than the Goldsmid-Sharp band gap result (dashed line) and that the converse is true for *A*<1.

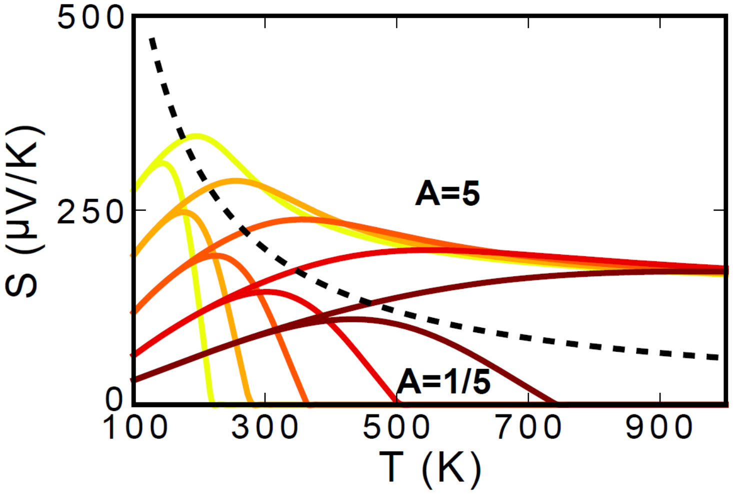

Figure 5-11: Temperature dependent Seebeck coefficient for various carrier concentrations (corresponding to Figure 1) for A=5 and A=1/5. Dashed line represents the Goldsmid-Sharp band gap: $S_{max} = E_g/2eT_{max}$ for various values of the carrier concentration; calculation details are the same as for Figure 5-9.

In order to illustrate the effect of an increasing weighted mobility ratio, the η-dependent Seebeck is plotted for ZrNiSn (ϵ_g~5 at room temperature) in Figure 5-12a. We see that the magnitude of the maximum Seebeck coefficient obtained for p-type ZrNiSn (A=1/5) is significantly lower than that for n-type ZrNiSn (A=5). The effect of having an A different from one is that the magnitude of the maximum Seebeck coefficient ($|S|_{max}$), as well as the temperature where it occurs (T_{max}), is increased for the carrier type with higher weighted mobility, while those of the lower weighted mobility carrier are decreased. So in a system like ZrNiSn, the n-type material maintains a high thermopower to much higher temperatures than might be expected from its narrow band gap (~0.13 eV) and therefore can reach an impressive zT from 0.5 – 1.0 [215, 265]. On the other hand, the p-type ZrNiSn prematurely experiences reduced thermopower due to compensating high-mobility electrons. Figure 5-12b shows the value of the maximum Seebeck coefficient for the three methods, a clear split in the A=5 and A=1/5 is observed. An alternative representation is shown in Figure 5-12c; here it is obvious that $2e|S|_{max}T_{max}/E_g$ is larger than 1.0 for all values of ϵ_g when A=5, while it is less than 1.0 for all ϵ_g for A=1/5 (except at quite low ϵ_g, the reasons for which will be discussed later). Figure 5-12d shows how $2e|S|_{max}T_{max}/E_g$ increases with increasing A value; larger deviations are observed as E_g/k_BT becomes smaller. In comparison with Goldsmid-Sharp's conclusion that only ~20% deviation is observed for *A*=10, we find that 50-100% errors in the estimated gap can be obtained for ϵ_g values reasonable for many relevant thermoelectric materials (ϵ_g~3-5).

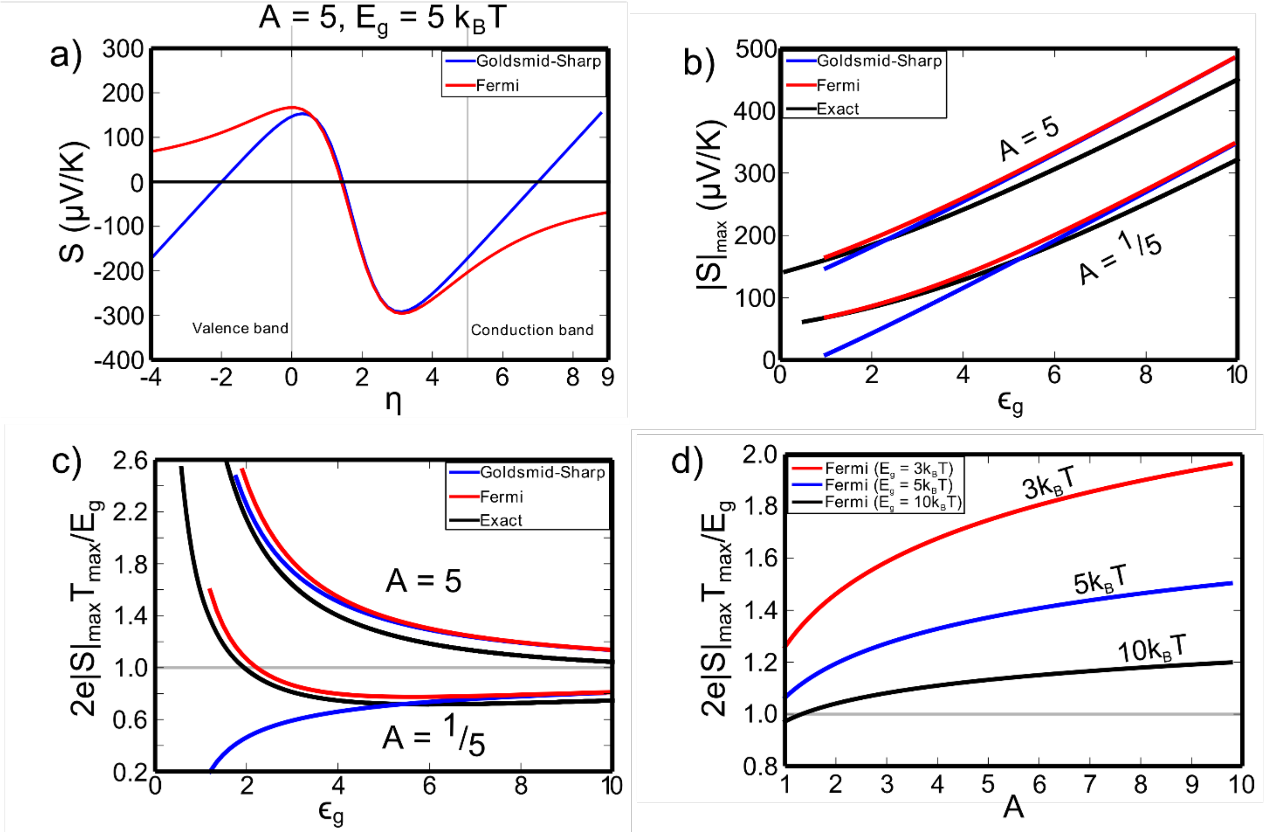

Figure 5-12: Result of the "Exact", "Fermi", and "Goldsmid-Sharp" methods assuming ϵ_g = 5 and A=5 (weighted mobility ratio) for a) Seebeck coefficient as a function of η,. b) The ratio of the 2e|S|maxTmax estimate to the actual model Eg as a function of ϵ_g, and c) the same ratio with respect to the weighted mobility ratio A at different Eg values (3, 5, and 10 kBT as indicated on the figure).

While the Goldsmid-Sharp band gap has proven to be a simple and useful estimate for the real band gap, it is not without its limitations. In this section, I have shown several cases for which this simple approximation breaks down. Figure 5-13 shows the deviation between the Goldsmid-Sharp band gap and the true band gap for a wide variety of these parameters. Ultimately, we observe that the magnitude of the deviation is largest for materials with large differences between the weighted mobility of electrons and holes (*A* ≠ 1). From an experimental perspective, *A* ≠ 1 will result in a larger value of $2e|S|_{max}T_{max}$ for the higher weighted mobility species, and a lower value for the one with lower weighted mobility. In the case of ZrNiSn, the more mobile electrons (A=5) result in an observation of about a five-fold difference in the p-type (~0.05 eV) and the n-type (~0.25 eV) Goldsmid-Sharp band gaps as shown in the previous section[52].

Figure 5-13 can be useful in determining either an unknown A value for a material if the true band gap is known, or it can show the expected deviations of the Goldsmid-Sharp band gap relative to the true band gap for a given A value. For instance, in the case of n-type ZrNiSn with $2e|S|_{max}T_{max}/E_g$ = 2.1 (using $E_{g,optical}$=0.13 eV [52]) and observed maximum Seebeck coefficient (~200 μV/K), we determine A~5. Alternatively, if the A is known, one can (based on the magnitude of the maximum Seebeck coefficient) obtain an estimate a value for $2e|S|_{max}T_{max}/E_g$ from Figure 5-13, which can be used to estimate the true band gap (as described in the numbered list below).

1. Measure temperature dependent thermopower and obtain a maximum
2. Calculate the Goldsmid-Sharp band gap: $E_g = 2e|S|_{max}T_{max}$
3. If $|S|_{max}$<150 μV/K, be aware that the true E_g may significantly differ from $2e|S|_{max}T_{max}$ (see below)
4. For $|S|_{max}$>150 μV/K, estimate the majority-to-minority carrier weighted mobility ratio, A.
5. Find the $2e|S|_{max}T_{max}/E_g$ ratio (r) from Figure 5-13 that is consistent with that A and S_{max} value to then calculate the corrected E_g=$2e|S|_{max}T_{max}/r$

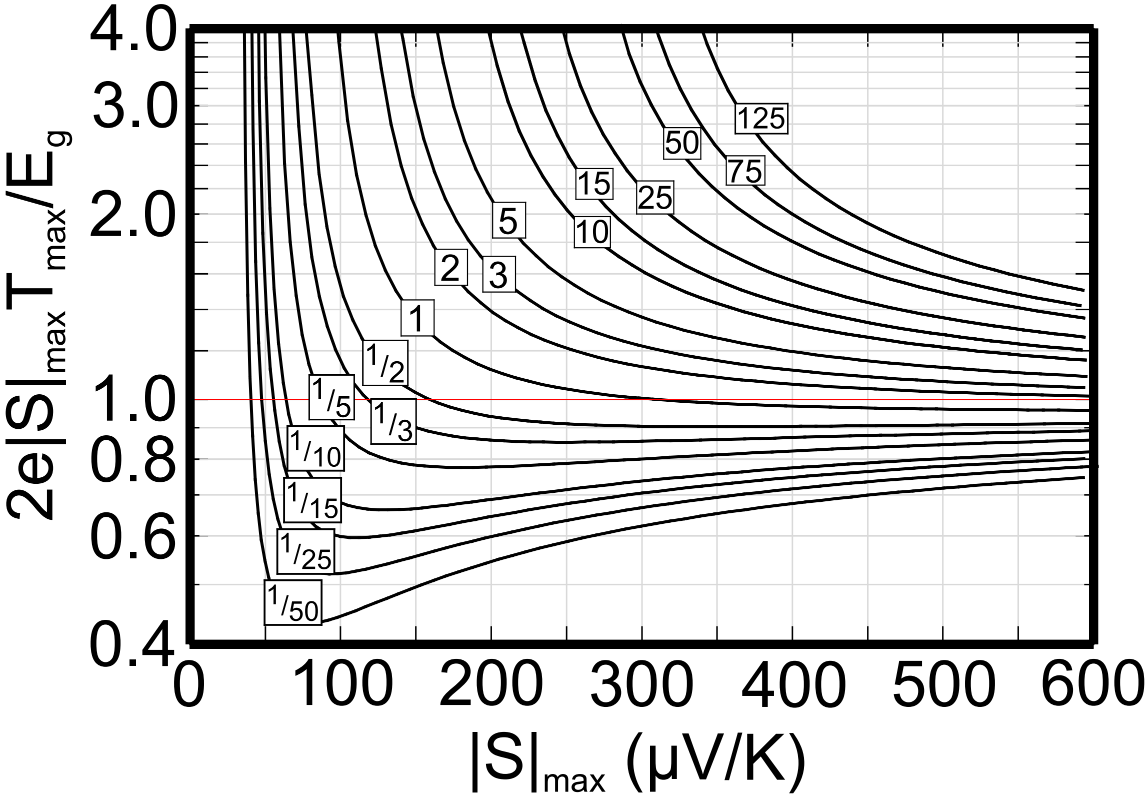

Figure 5-13: The ratio of the 2e|S|$_{max}$T$_{max}$ estimate to the actual model E$_g$ as a function of thermopower for a wide variety of A and S$_{max}$. A values are noted in a rectangular box laid on top of each black solid lines.

S$_{max}$<150 μV/K describes the degenerate crossover that leads to the upward trend in Figure 5-10, Figure 5-12, and Figure 5-13 mentioned previously for low values of *S$_{max}$*. For degenerate, heavily doped samples (η_{max} in the majority band) *E$_g$/k$_B$T$_{max}$* becomes a poor metric for describing the bipolar effects; rather, we believe the thermal band gap ($\frac{E_{g,thermal}}{k_B T} = \epsilon_g + \eta$) is the relevant parameter that describes the gap. This effect is even more pronounced as *A* is decreased because the lower mobility majority carrier requires a chemical potential deep within the band (large η) to mitigate the effects of a highly mobile minority carrier (see Figure 5-12b). In order to show the effects of degeneracy, I determined when the band gap that yielded a maximum thermopower and corresponded to a degenerate chemical potential (η_{max} within the band—see Figure 5-10b). I generate the analogous “Engineer’s Guide” figure for determining the effectiveness of the Goldsmid-Sharp band gap (as a predictor of the thermal gap) as a function of the maximum Seebeck coefficient, as shown in Figure 5-14. For many thermoelectrically relevant maximum Seebeck coefficients, the crossover to degenerate behavior (as indicated by a kink in $2eS_{max}T_{max}/E_{g,thermal}$) occurs. For nearly all A values, the kink (which means that degenerate η is required to reach $|S|_{max}$) occurs for Seebeck coefficients that are approximately 150 μV/K (which corresponds to a band gap of ~3 k_BT for the A=1 case as shown in Figure 5-10b). While the result seems to diverge for heavily-doped samples, nearly degenerate samples (S_{max}<150 μV/K) still give reasonable results in terms of relating the Goldsmid Sharp gap to the thermal band gap (rather than the true value) for the A=1 case.

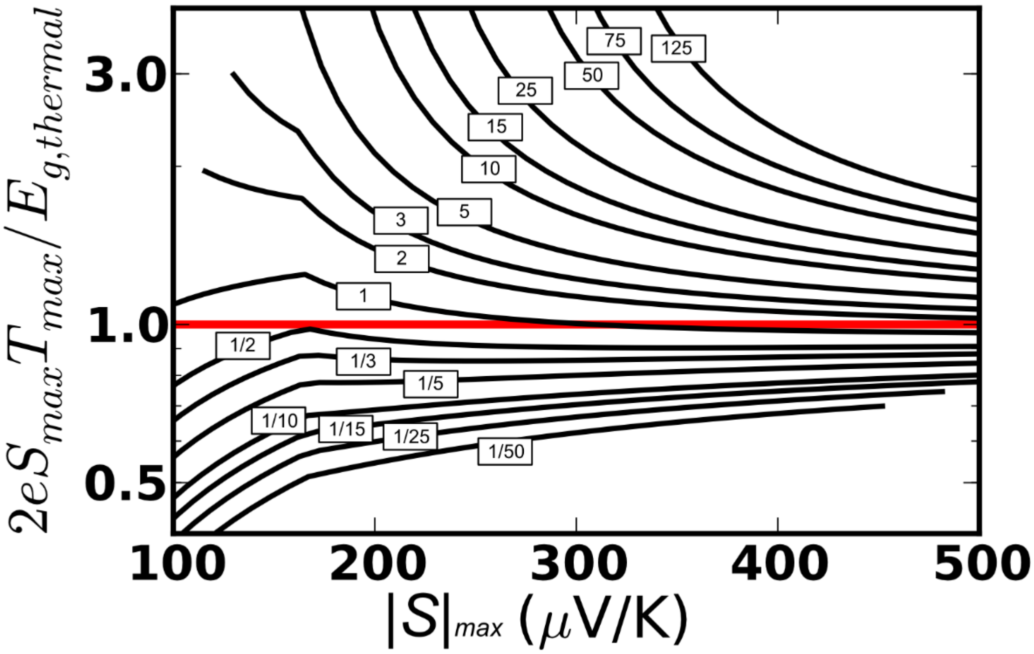

Figure 5-14: This engineer's guide is analogous to Figure 5-13; however, the predicted band gap in this case is ratioed to the thermal band gap ($\epsilon_g + \eta$, for degenerate or simply ϵ_g otherwise) instead of the true gap.

In terms of the weighted mobility ratio, up until this point we have not considered whether the difference in the weighted mobility ratio is due to the mobility (i.e., deformation potential) or effective mass: $A = A_{\mu}A_{m^*}^{3/2} = \left(\frac{\mu_{maj}}{\mu_{min}}\right)\left(\frac{m^*_{d,maj}}{m^*_{d,min}}\right)^{3/2}$. For the η-dependent Seebeck coefficient (and therefore the Goldsmid-Sharp and Fermi methods which use $\frac{dS}{d\eta} = 0$ as a criteria for a maximum), these separate pieces are always coupled: $S = \frac{1}{1+\frac{\sigma_{maj}}{\sigma_{min}}}\left(S_{min} + \frac{\sigma_{maj}}{\sigma_{min}} S_{maj}\right) = \frac{1}{1+A_{\mu}A_{m^*}^{3/2}\frac{F_0(\eta_{maj})}{F_0(\eta_{min})}}\left(S_{min} + A_{\mu}A_{m^*}^{3/2}\,\frac{F_0(\eta_{maj})}{F_0(\eta_{min})} S_{maj}\right)$; but this is not the case for the charge neutrality equation. The charge neutrality equation can be expressed as $N_A - N_D = p - n$, which upon substituting the single parabolic band expression for *n* (Equation 2-8):

$$\boldsymbol{N_A - N_D = \frac{(2k_BT)^{\frac{3}{2}}}{{m_{d,p}^{*}}^{3/2} 2\pi^2\hbar^3}\left(F_{1/2}(\eta_p) - A_{m^*}^{3/2} F_{1/2}(\eta_n)\right)} \qquad \text{Equation 5-12}$$

While the “Fermi” and “Goldsmid-Sharp” methods do not explicitly use the charge neutrality equation, since they determine the maximum thermopower from $\frac{dS}{d\eta} = 0$, the “Exact” method uses charge neutrality to determine the maximum via $\frac{dS}{dT} = 0$. In order to probe the effects of a varying effective mass ratio (while keeping the overall *A* value equal to either 1 or 5), I have solved the *dS/dT*=0 “Exact” method for a variety of cases as shown below. First, I solved for the *A*=1 case, meaning that the majority and minority carriers have the same weighted mobility, but I vary $A_{m^*} = \frac{m^*_{maj}}{m^*_{min}}$ to smaller and larger values (while also varying A_{μ} to keep *A*=1) as shown in Figure 5-15a. On increasing the effective mass of the majority carrier band ($A_{m^*} > 1$), $2eS_{max}T_{max}/E_g$ increases slightly but is still close to the same chemical potential and S_{max} as in the $A_{m^*} = 1$ case. On the other hand, when the majority carrier band has a significantly lower effective mass ($A_{m^*} < 1$), the shift away from the $A_{m^*} = 1$ case is larger. The reduced chemical potential position (Figure 5-15b) seems to indicate that the reason for the shift in S_{max} is likely due to a shift in η_{max} towards the majority carrier band edge. This makes sense in the context of an increasing minority carrier effective mass which would push η away from the minority carrier band to maintain the same carrier concentration.

For the *A*=5 case (Figure 5-15c,d), a similar trend is observed. However, when the majority carrier has a much lower weighted mobility than the minority (*A*=1/5), the result is not affected as significantly by a varying A_{m^*}. In the case where the majority carrier has higher mobility (*A*=5), though, if the majority carrier effective mass is much smaller ($A_{m^*} < 1$) then reductions in the maximum Seebeck coefficient can occur (similar to the *A*=1 case). For these studies we have considered A_{m^*} of 2 or 5 (or the inverse), which is a feasible range of values for real semiconductors. In summary, we should expect larger, negative deviations in the Goldsmid-Sharp band gap if the majority carrier has higher weighted mobility (as in the *A*=5 case) but significantly lower effective mass ($A_{m^*} < 1$). Nearly negligible deviations occur in the other cases (either *A*<1 or $A_{m^*} > 1$).

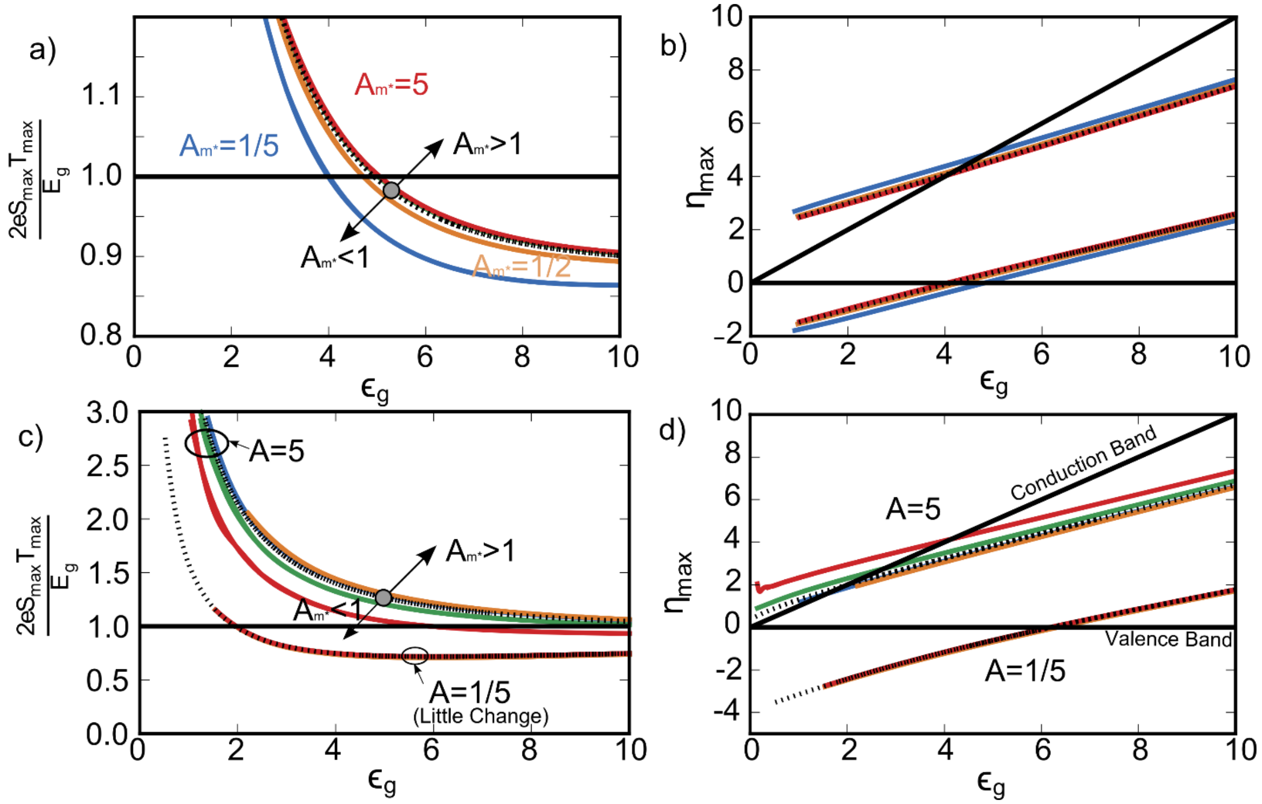

Figure 5-15: Comparison of results when the origin of A derives from a changing effective mass ratio (rather than purely mobility related). a) Goldsmid sharp effectiveness ($2eS_{max}T_{max}/E_g$) for A=1 with varying A_{m^*}. b) The varying chemical potential position for the parameters in a). c) $2eS_{max}T_{max}/E_g$ for A=5 and A=1/5 as a function of a changing contribution due to A_{m^*}. d) The resulting shift in the chemical potential that yields the maximum Seebeck coefficient as a function of reduced band gap for the A=5 and A=1/5 (colors correspond to c).

5.3d - Conclusions

In this section, I have developed the relevant theory for extending the Goldsmid-Sharp band gap to narrow gap semiconductors using the full Fermi statistics and an exact solution of the temperature-dependent transport integrals. I have investigated the effect of the weighted mobility ratio and narrow band gaps on the results, and I have shown several examples where the deviations can be quite large. These results should be generally applicable to any semiconductors (although the Engineer's guide should be rederived for alternative scattering mechanisms), but they should be particularly useful for the thermoelectrics community, which routinely measures the temperature-dependent Seebeck coefficient and utilizes the Goldsmid-Sharp band gap as a descriptor of the material's band structure. This analysis takes this one step further and allows us to more thoroughly describe discrepancies in this estimate.

5.4 - Conclusions

In summary, the Goldsmid-Sharp band gap ($E_g = 2e|S|_{max}T_{max}$) is an extremely useful tool for obtaining an estimate for a material's band gap through temperature dependent Seebeck measurements. However, in the case of ZrNiSn, these estimates yielded drastically different results when considering n-type and p-type material (a factor of 5 difference in the band gap). While most researchers understand that this is not an exact estimate, it is important to understand when and why the simple relation can break down and to what extent. In this work, we show that large deviations can occur for several reasons: a breakdown of Maxwell-Boltzmann statistics (used to derive the Goldsmid-Sharp band gap) for materials with narrow gaps, or materials with very large (or small) majority-to-minority carrier weighted mobility ratio (A). We use these analyses to explain the seemingly strange result in ZrNiSn in the context of a significantly larger weighted mobility for electrons than holes, which is likely a result of the nature of the valence band states which seem to be a result of Ni disorder. Because bipolar conduction is detrimental to thermoelectric performance, results from this work using the Goldsmid-Sharp gap could be used to validate strategies for suppressing bipolar effects beyond altering band gap and doping [21, 110, 260, 266], but also by other methods (including nanostructures [11, 267-269]) given that both n-type and p-type samples are obtainable.

I would like to acknowledge the contributions of my collaborators, Jennifer Schmitt [52] and Hyun-Sik Kim [50], who were equally contributing coauthors on the paper’s published based on work from this thesis chapter.

Chapter 6: $CoSb_3$ and other Thermoelectric Materials with Optical Evidence of Multiple Bands

6.1 - Introduction

As has been a theme in previous chapters of this thesis, many of the best thermoelectric materials contain multiple valence and/or conduction bands. In this chapter, we will investigate a few examples where these features are directly observable in the optical properties. The first example of this will be for $CoSb_3$, which exists in a well-studied class of thermoelectric materials known as the skutterudites. Skutterudites have received a lot of attention in recent literature due to their ability to accommodate filler atoms, which can drastically lower their thermal conductivities (many authors attribute this to rattling of the atom within its cage). Combined with reasonable electronic properties, these materials have achieved good *zT*s of up to ~1.0 for p-type and 1.5 for n-type—resulting in a significant amount of academic and commercial interest. In this chapter, I explore Yb filled n-type $CoSb_3$ optically, electronically, and using *ab-initio* calculations to provide an alternative explanation for their good performance which utilizes multiple conduction bands that participate in transport (increasingly so at high temperatures), similar to the features observed in the IV-VI materials (Chapter 4). This is contrary to many literature reports which attribute the high *zT*s mainly to thermal conductivity reduction, while the electronic properties are not generally understated.

Beyond $CoSb_3$, one other group of materials have yielded optical evidence of multi-band behavior. Zintl compounds, which have inherently low thermal conductivity due to their structural complexity, show optical evidence of multiple band features. Unfortunately, in this case the electronic properties do not reflect this fact, but this is likely because the secondary bands are too far away to access at reasonable temperatures. However, this section indicates the presence of multiple bands and opens the door for future band engineering studies in this class of materials.

6.2 - $CoSb_3$ – The Electronic Origin of High *zT*

6.2a - Introduction

Among the best thermoelectric materials, *n*-type filled skutterudites have been widely studied after it was found that the addition of filler atoms (La, Ce, and others), which can be filled into the one void site per primitive cell, can lead to high *zT* by reducing the thermal conductivity while simultaneously doping the material [270-272]. The $CoSb_3$ skutterudite structure is the Im3 (space group 204) which has the general formula AX_3 where A=Co, Rh, Ir and X=P, As, Sb. In this structure, the metal atom is octahedrally coordinated by 6 X atoms, the arrangement of which in 3D space leads to interstitial sites that can be filled with an additional atom [273]. This interstitial site can be filled as in the case of $LaFe_4Sb_{12}$, which maintains charge balance by compensating the change from Co to Fe (which has one fewer electron) by inserting the interstitial lanthanum atom. In this chapter, I will discuss the binary $CoSb_3$, which is semiconducting as synthesized, but can be doped n-type by partially filling the interstitials with filler atoms. This filling is then accompanied by a reduction in thermal conductivity, leading to good thermoelectric performance.

Since the 1990's, there has been much progress in the field of *n*-type filled skutterudites as thermoelectric materials resulting in high *zT* values of around 1.3 (and up to 1.7) at 850 K for single filling (with filler atoms being La [274], Na [275], In [276-278], Yb [279, 280], Nd [281], and others) and multiple filling (In+Ba [282], In+Pr [283], In+Nd [284], Ba+Yb [285], Ba+La+Yb [286]) respectively. The excellent thermoelectric performance of skutterudites at intermediate temperature ranges (400-600 °C) and their superior mechanical properties [287-289] make them ideal candidates for heat-recovery applications in the automobile industry [290]. High *zT* in skutterudites is mostly attributed to the addition of the filler atoms and subsequent reduction in thermal conductivity [291-293]. These reductions are thought to be a result of the filler atom rattling within the interstitial space that it occupies [274]; however, at least part of the reduction is believed to be due to point-defect scattering of phonons [274].

With regards to the good performance in these materials, the increased *zT* is often attributed to the beneficial thermal properties as a result of filling, whereas the influence of the intrinsic electronic structure is often understated or ignored completely. Band engineering approaches to enhancing *zT* have been a theme of this thesis; it has become increasingly apparent that complex band structures including multi-valley Fermi surfaces [16, 21, 34], convergence of bands (PbSe as shown in Chapter 4 for $Pb_{1-x}Sr_xSe$ [25], Mg_2Si [26], or PbTe [16]), or even threads of Fermi surface connecting band extrema (which will be discussed further in Chapter 7) [294, 295], are key features of many good thermoelectric materials.

Regarding the electronic structure in $CoSb_3$, Singh et al. has shown that valence band of $CoSb_3$ is very light with approximately linear (rather than the usual parabolic) character. The light bands explain the high mobility in lightly doped p-type $CoSb_3$ [296], but this does not explain why n-type $CoSb_3$ has substantially higher *zT* than p-type. For *n*-type $CoSb_3$ skutterudites, the non-parabolic (Kane) band concept has been borrowed to explain the apparent increase in effective mass measured by Seebeck coefficient (m_S^* as defined in previous chapters) as a function of doping level [271, 275, 281, 297-300]. However, I will show evidence of why the increasing effective mass cannot be due to non-parabolic bands, and that the effect is instead the result of multiple conduction bands.

While good thermal properties certainly contribute to the thermoelectric performance in $CoSb_3$, I show in this work that the electronic structure in $CoSb_3$ is also conducive to high *zT* for many of the reasons mentioned previously regarding band convergence and band engineering. In this chapter, I thoroughly investigate the electronic properties of Yb filled $CoSb_3$ in the context of complex conduction band behavior. I show both electronic and optical evidence of the existence of a second, multi-valley conduction band which increases the effective valley degeneracy. This band is also observed to shift as a function of temperature, resulting in its convergence towards the conduction band minimum as temperature increases, resulting in important contributions to the performance of *n*-type filled skutterudites.

I would like to acknowledge contributions to this work from Yinglu Tang (Caltech Snyder Group), who will be an equally contributing first author on this paper once it is submitted, and from Luis Agapito (University of North Texas).

6.2b - Multi-conduction Band Behavior in *n*-type CoSb$_3$ Skutterudite

Multiple band effects in CoSb$_3$ materials are observable through several methods, both experimental and theoretical, as presented in Figure 6-1. A clear demonstration of complex band behavior is seen in the doping dependent Seebeck coefficient (Pisarenko plot at 300K) shown in Figure 6-1a. At low carrier concentrations (n_H less than ~1×10^{19} cm^{-3}) CoSb$_3$ shows light mass behavior ($m_S^* {\sim} 0.7\, m_e$); as the carrier concentration increases, the system transitions to a much heavier mass, requiring a second band with $m_S^* = 4.8\, m_e$ in the heavily doped regime (larger than 3×10^{20} cm^{-3}). In the degenerate limit the relationship between *S*, m_S^*, and *n* can be described by the degenerate limit of the Mott relation [301]:

$$\boldsymbol{S = \frac{2k_B^2T}{3e\hbar^2}\left(\frac{\pi}{3n}\right)^{2/3} m_S^*(1+\lambda)} \qquad \text{Equation 6-1}$$

where λ is the scattering parameter (λ = 0 for acoustic phonon scattering, which is quite common above 300K and is most appropriate for CoSb$_3$) and m_S^* is the density of states (DOS) effective mass obtained from Seebeck measurements using the single parabolic band (SPB) model (method detailed in Chapter 2). By considering two conduction bands and one valence band in a three-band transport model with a conduction band offset (ΔE) of ~0.08 eV, consistent with optical measurements in this work, we capture the behavior of both the lightly and the heavily doped regions (Black line in Figure 6-1a). In addition to the 300 K Seebeck coefficient, several other experimental and theoretical results indicate multi-band behavior [302-307].

a)

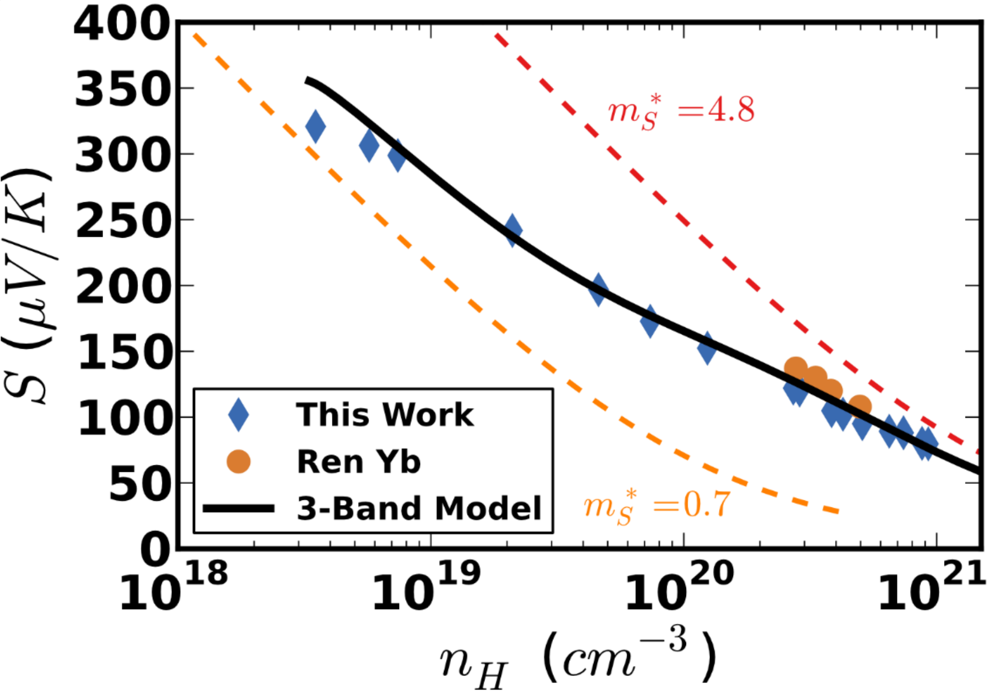

400
350
300
250
200
150
100
50
0
$S\ (\mu V/K)$
10^{18}
10^{19}
10^{20}
10^{21}
$n_H\ (cm^{-3})$
$m_S^* = 4.8$
$m_S^* = 0.7$
This Work
Ren Yb
3-Band Model

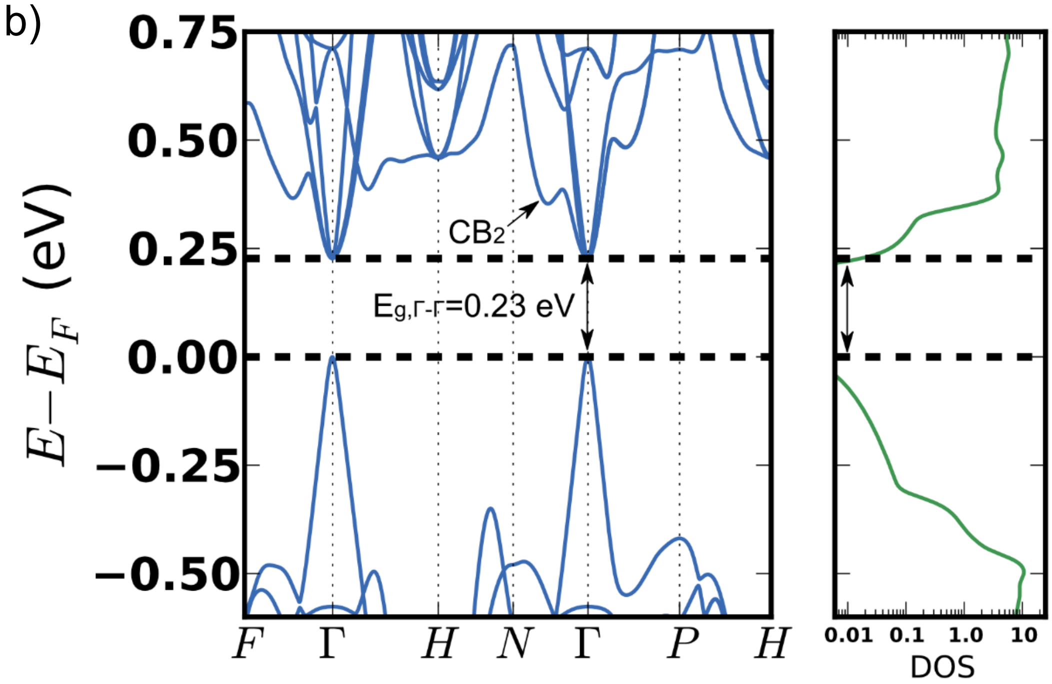
b)
0.75
0.50
0.25
0.00
−0.25
−0.50
$E\!-\!E_F$ (eV)
CB2
$E_{g,\Gamma\text{-}\Gamma}$=0.23 eV
F
Γ
H
N
Γ
P
H
0.01
0.1
1.0
10
DOS

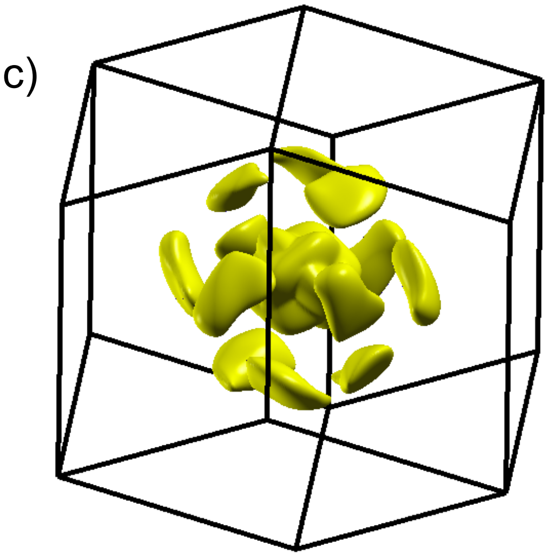
c)

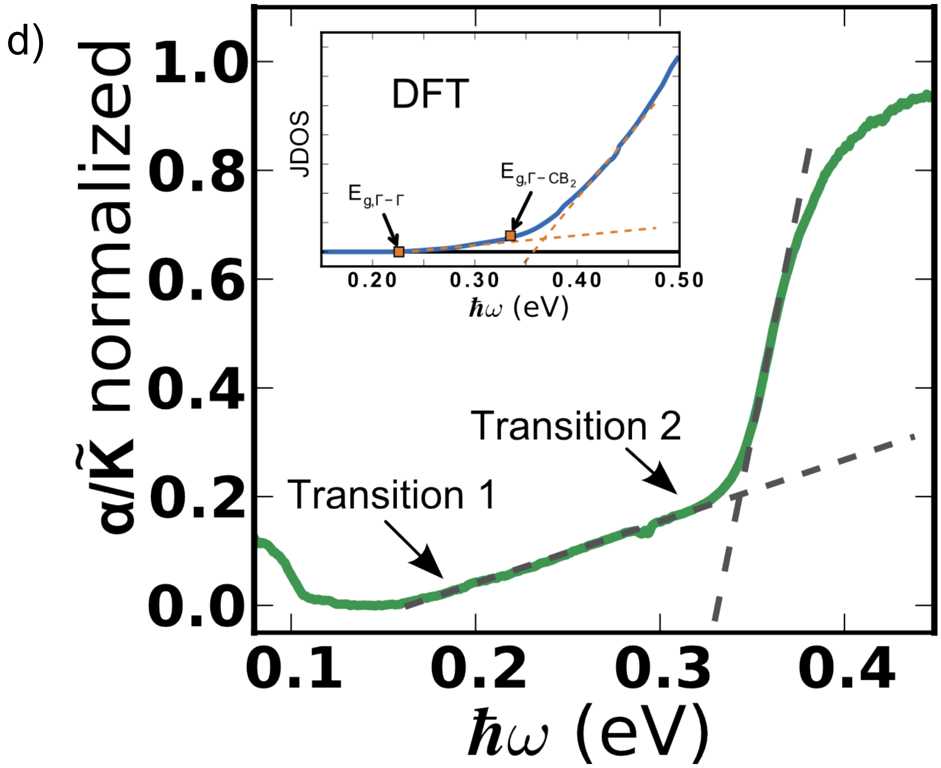

Figure 6-1: a) Pisarenko plot of Seebeck coefficient vs Hall carrier concentration at 300K. Black line is a two-band model with density of state effective mass for the light and heavy bands being 1.1 m_0 and 3.9 m_e, respectively. Orange and red lines are for single parabolic band models with the individual band masses. b) The DFT calculated electronic band structure for $CoSb_3$. c) Fermi surface calculation for Fermi levels 0.12 eV above the conduction band edge. d) Room temperature optical absorption measurement (Kubelka Munk function) with estimated joint density of states from DFT.

The calculated electronic band structure is consistent with an m_S^* that becomes gradually heavier as long we consider not only the primary conduction bands (Γ point), but also the bands higher in energy (labelled CB_2 in Figure 6-1b) for heavily doped $CoSb_3$. In $CoSb_3$, the *ab-initio* density functional theory (DFT) calculated band structure (Figure 6-1b) shows a direct band gap at the Γ point ($E_{g,\Gamma-\Gamma} = 0.23\ eV$), which yields a triply degenerate (N_v=3) conduction band edge. As a result of the heavily doping (and relatively low mass for CB_Γ), the Fermi level quickly moves deep into the conduction band, allowing a large population of electrons to develop in secondary conduction bands, i.e., CB_2. Our calculations show that this secondary conduction band (CB_2) begins about 0.12 eV above the conduction band edge along the $\Gamma - N$ line. The calculated iso-energy Fermi surface for a Fermi level just inside of CB_2 (Figure 6-1c) is also consistent with previous Fermi surface calculations by Chaput et al which show a highly degenerate Fermi surface with ~12 pockets (although they do not discuss its significance to the electronic properties beyond the Hall coefficient, r_H) [308]. Regarding the CB_2 $(\Gamma - N, N_v = 12)$ minima, only PbTe, which reaches a maximum *zT* of ~2 [16], has such a high value of N_v; this high degeneracy is also found to play a crucial role in the high temperature Seebeck and *zT* values. Modeled *zT* in Figure 6-4c shows that much of the *zT* is due to this high valley degeneracy band, which will be discussed later in this work.

Additional conduction band minima observed along $\Gamma - F$ (N_v=24, 0.012 eV above CB_2) and $\Gamma - H$ (N_v=6, 0.034 eV above CB_2) have high degeneracy and likely also contribute to thermoelectric transport. Even though Chaput et al. presented Fermi surfaces that show the formation of threads (along the $\Gamma - F$ direction) connecting the $\Gamma - N$ pockets (as shown in Figure 6-1c), this second region of complexity is generally not plotted in DFT calculations because the *F* point is not a common symmetry point in the $Im\overline{3}$ space group's Brillouin zone. A third set of bands at the *H*-point (triply degenerate each with N_v=1) lays ~0.08 eV above the $\Gamma - H$ minimum. Other DFT calculations from Puyet et al. suggest a secondary conduction band, but they show a qualitatively different conduction band structure (with the primary minimum at *H*) [305, 306]. Despite the complex secondary conduction band structure, simply considering two conduction bands $(\mathrm{CB}_\Gamma$ and $\mathrm{CB}_2)$ with their appropriate degeneracies seems to qualitatively capture the Seebeck Pisarenko behavior (Figure 6-1) and the optical results.

In support of thermoelectric transport and DFT calculations, multi-band features in $CoSb_3$ can be directly observed by IR optical absorption. Optical absorption edge spectra for a nearly intrinsic sample of $CoSb_3$ $(n_H = 1.7 \times 10^{17} cm^{-3})$ shows two distinct features (Figure 6-1d). The lower energy transition (which begins at ~0.16 eV optically and is computed to be 0.23 eV from DFT) is likely associated with the direct, $\Gamma - \Gamma$ transition; the second transition (which begins at ~0.3 eV optically, 0.34 eV from DFT) indicates the onset of a $\Gamma - CB_2$ transition. While direct transitions often result in more than 10x as strong of absorption when compared to indirect ones

[48], it is important to remember that the transition rate is also proportional to the density of states. Because both VB_{Γ} and CB_{Γ} are extremely light (see density of states in Figure 6-1b, right panel), the $\Gamma - \Gamma$ transition, despite the fact that it is a direct transition, may occur with a lower intensity than the $\Gamma - \mathrm{CB}_2$. I roughly estimate the strength of all transitions by calculating the joint density of states (JDOS, inset Figure 6-1d), which shows reasonable agreement with the two slopes observed in the optical measurements.

Other possibilities exist for the two distinct absorption edges which should be considered. First, a shallow absorption feature before the primary gap can be observed either in the case of intrinsic disorder/alloying in the sample (Chapter 4, PbSe/SrSe alloys showed long Urbach edges) or by intrinsic defect states which lay in the gap. However, because optical measurements were performed on the undoped sample that showed nearly intrinsic behavior, we do not expect the effects due to alloying or disorder. The possibility of a deep, intrisnic defect state laying within the band gap is possible; to exclude this as a possibility a series of lightly doped samples was also measured. I measured both extrinsically doped (filled with Yb or Na) and intrinsically doped (Co rich, Sb rich, Co poor, Sb poor) to encourage any intrinsic or extrinsic defect states to grow in number. Absorption edge measurements indicated no appreciable change in the strength of transition 1 relative to transition 2 that was not consistent with the addition of free carriers into the sample alone; therefore, I conclude that transition 1 is not a result of defect states.

Historically, optical measurements in the skutterudite system have been limited to Ackermann and Wold, who report an optical band gap for CoP_3 of 0.45 eV; they note that $CoSb_3$ and $CoAs_3$ do not show an absorption edge [309]. This was likely because the lowest light frequency that they had measured was 0.4 eV (our results suggest a lower band gap). Other optical measurements have focused on very low frequencies (<0.1 eV) in order to probe optical phonons [310, 311]—just missing the frequency range important for interband transitions. One recent thesis report by Ni shows that photoacoustic measurements on undoped $CoSb_3$

compounds can yield an absorption edge around 0.3 eV [312] (although he is not able to detect the absorption due to transition 1 that we observe here). In skutterudite systems other than $CoSb_3$, the literature has been sparse regarding optical absorption edge data, although Slack did publish a result for $IrSb_3$ which suggested a large optical gap (more than 1 eV) [313]. Optical measurements have also been performed over a wide range of frequencies by Matsunami et al. on Ce-filled skutterudites (with Fe, Ru, and Os rather than Co); these show band gaps within 0.2-0.3 eV, although additional analysis regarding other the nature of these interband transitions near the fundamental absorption edge is not discussed [314].

6.2c - Effective Mass in Systems with Non-parabolic Bands

The unexpectedly high thermopower at high carrier density in $Yb_xCo_4Sb_{12}$ observed in the Pisarenko plot of Figure 6-1a can also be represented as an increase in m_S^* (the Seebeck effective mass) as a function of carrier concentration as shown in Figure 6-2a. This apparent increase in effective mass with doping has previously been attributed to highly non-parabolic (Kane) bands [281, 315, 316] rather than multi-band effects. A non-parabolic dispersion (shown in Figure 6-2b, Equation 6-2) can arise as a result of interaction between the valence and conduction bands, which is common in narrow gap semiconductors, which can be described using $k \cdot p$ perturbation theory [58, 63, 64] (As mentioned in Chapter 2 and 3). Such bands are often described by the dispersion relation where the band is approximately parabolic (with band edge effective mass m_0^*) near the band edge, but becomes more linear as the electron energy, *E*, become larges large relative to the band gap E_g.

$$\boldsymbol{E\left(1+\frac{E}{E_g}\right)=\frac{\hbar^2k^2}{2m_0^*}} \qquad \text{Equation 6-2}$$

here *k* is the electron wave vector. This relation is expressed in terms of dimensional quantities, unlike the non-parabolic models in previous chapters which the dimensionless: $\beta = \frac{k_B T}{E_g}$ and $\epsilon = E/k_B T$. For non-parabolic bands, effective mass is not well defined because it can be derived from a number of classical relationships. In non-parabolic transport theory the commonly used energy dependent effective mass, derived from the electron momentum, is

$$\boldsymbol{m_P^*(E) = \hbar^2 k \left(\frac{dE}{dk}\right)^{-1} = m_0^*(1 + \frac{2E}{E_g})} \qquad \text{Equation 6-3}$$

This is a different definition than that found in most solid state physics textbooks $m^* = \hbar^2 \left(\frac{d^2E}{dk^2}\right)^{-1}$, which relates the effective mass to the band curvature directly. Many common semiconducting materials are reported to show $m^*(E)$ increasing with energy (Fermi level, E_F), including InSb [317], InAs [318], GaAs [319], PbTe [320], and others in a variety of different measurements, including electrical susceptibility (measured using optical reflectance) [320, 321], Shubnikov-De Haas/De Haas-Van Alphen oscillations [322], Faraday rotation [317, 318], and combined galvano thermomagnetic measurements (Seebeck and Nernst coefficients) [323]. In general these measurements are able to provide an estimate of the effective electronic mass, which is then compared to $m_P^*(E)$ of Equation 6-3 to determine the degree of non-parabolicity.

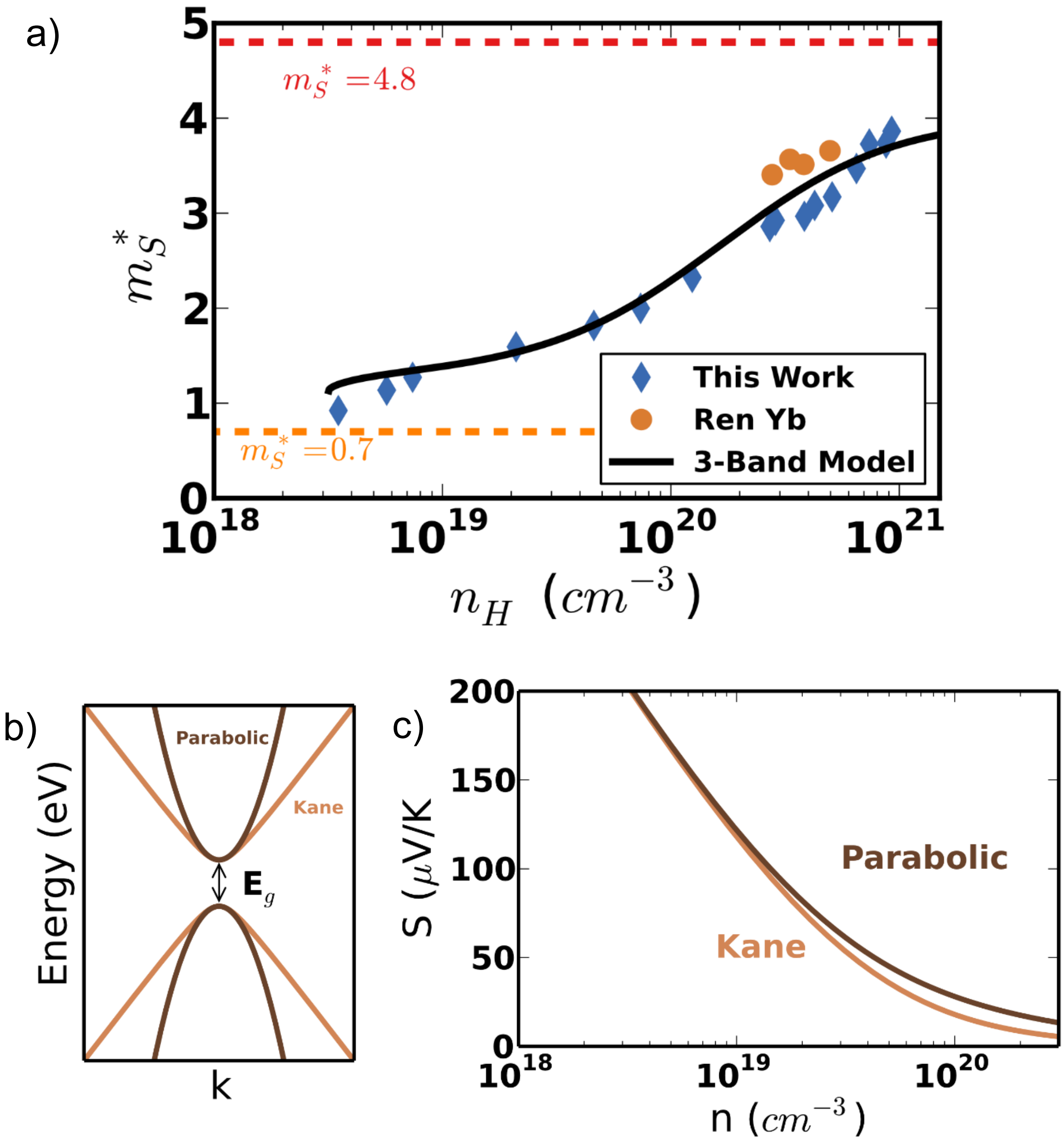

Figure 6-2: Effective mass calculation (equivalent single parabolic band effective mass) in a) n-type CoSb3 computed for experimental data along with the three-band model. The two individual band masses are also plotted to show the transition between them. b) Parabolic and Kane dispersions plotted with the same band edge effective mass showing the increasing effective mass (as the Kane band becomes linear). c) Seebeck Pisarenko plot for both Kane and Parabolic bands (full, Fermi integral calculation) illustrating that the Pisarenko mass actually decreases for Kane bands at high carrier concentration.

For thermoelectric materials we frequently define $m_S^*(E)$ from measurements of Seebeck coefficient and Hall carrier concentration ($n_H = 1/eR_H$) as the equivalent parabolic band mass that would give the measured Seebeck coefficient with the measured n_H (assuming λ = 0 from acoustic phonon scattering commonly observed in TE materials at 300K and above). In $CoSb_3$, this carrier concentration dependent effective mass $m_S^*(E)$ is observed to increase in both *n*-type (Figure 6-2a) and *p*-type materials, which is commonly attributed to band non-parabolicity using Equation 6-2 and Equation 6-3 [271, 315, 316, 324]. However, we must realize that these are two distinct definitions of effective mass that, in this case, are both qualitatively and quantitatively different. The degenerate limit of the Seebeck coefficient for a material whose bands display a Kane dispersion (the equivalent of Equation 6-1 obtained by applying Equation 6-2) can be expressed as [301, 325]:

$$\boldsymbol{S = \frac{2k_B^2 T}{3e\hbar^2}\left(\frac{\pi}{3n}\right)^{\frac{2}{3}} m_P^*(E)(1 + \lambda - \phi)} \qquad \text{Equation 6-4}$$

where and additional correction factor, $\phi = \frac{\frac{4E}{E_g}\left(1+\frac{E}{E_g}\right)}{\left(1+\frac{2E}{E_g}\right)^2}$, has been added to the equation for that of a parabolic band (Equation 6-1). For a general scattering mechanism, Equation 6-4 can be simplified upon substation of $m_P^*(E)$:

$$\boldsymbol{S = \frac{2k_B^2 T}{3e\hbar^2}\left(\frac{\pi}{3n}\right)^{\frac{2}{3}} m_0^* \left(\lambda\left(1 + \frac{2E}{E_g}\right) + \frac{1}{1 + \frac{2E}{E_g}}\right)} \qquad \text{Equation 6-5}$$

In the case where λ = 0, as is commonly found in TE materials, the m_S^* mass in a Kane band should actually decrease according to:

$$\boldsymbol{m_S^*(E) = \frac{m_0^*}{1 + \frac{2E}{E_g}}} \qquad \text{Equation 6-6}$$

Thus the Seebeck mass, as computed from most thermoelectric studies, does not necessarily increase with doping or Fermi level as the momentum mass. The Seebeck effective mass is derived by inspection when comparing Equation 6-5 for the non-parabolic band and the expression for the parabolic band (Equation 6-1).

The η-dependent Seebeck effective mass can also be derived for alternative scattering mechanisms as presented in Figure 6-3a. Here, we can see that only for the case of acoustic phonon scattering does the mass decrease in the degenerate limit. All other scattering mechanisms show an increase. In this sense, it is not difficult to understand why Equation 6-3 is so widely used to show increasing effective mass with chemical potential over a wide range of measurement techniques (which includes thermomagnetic and thermoelectric measurements, such as the Seebeck coefficient). While I do not dispute the fact that measurements that probe the conductivity effective mass (m_c^*) should increase with reduced Fermi level because the density of states for a Kane band is in fact larger (as evidenced by the lower curvature in Figure 6-2b at higher energies), I am saying that this effect is cancelled out when considering the Seebeck coefficient and the m_S^* (Figure 6-2c and Figure 6-3a) in the acoustic phonon scattering ($\lambda = 0$) case. If we consider some literature data for systems that are known to show Kane-like behavior, we can observe this trend. The m_S^* is extracted using (zero field) Seebeck Pisarenko data (S vs n_H) from several sources in InSb [64, 326] and InAs [64], and the results are plotted in Figure 6-3b. It has been observed that the primary mechanism for scattering in these materials is by polar optical phonons that have an $E^{1/2}$ energy dependence ($\lambda = 1$), indicating that the effective mass should increase as shown in Figure 6-3a. In fact, experimental results show that the mass does increase with doping level and that Equation 6-5 works reasonably with the substituted room temperature band gaps of 0.35 and 0.18 eV and band edge effective masses of 0.03 and 0.018 m_e for InAs and InSb, respectively. In order to investigate the hypothesis of whether m_S^* increases with increasing chemical potential, we should consider a system where acoustic phonon scattering dominates.

Doping dependent m_S^* is also considered for PbTe, PbSe, and SnTe, which are known to show acoustic phonon scattering at room temperature, as shown in Figure 6-3c. n-type PbTe and PbSe both show a doping-dependent effective mass that does not change too much with doping level (PbTe shows ~10% increase, while PbSe stays relatively constant). SnTe and p-type PbTe, however, show a decreasing mass with doping. These materials show a mass that decreases from ~0.2 and ~0.5 m_e in the lighter doped samples to to 0.1 m_e and 0.32 in the more heavily doped samples in SnTe and PbTe respectively (before the effects of the second bands are reached). As shown in Chapter 4 of this thesis, both p-type SnTe and PbTe are known to exhibit multi-band behavior with a secondary valence band about 0.4 and 0.12 eV below the primary at room temperature, respectively; however, in this plot, I have compiled data where the Seebeck coefficient still decreases with doping. These results seems to support our claim in Equation 6-6 that the Seebeck effective mass does decrease with doping level, although it is not clear why n-type PbTe and PbSe do not obey the same trends. In order to confirm the result, this analysis should be extended to other systems, but it is difficult to find quality Seebeck data across a range of doping for materials that show both Kane band behavior and acoustic phonon scattering. However, as more information is gathered, this effect could be investigated further.

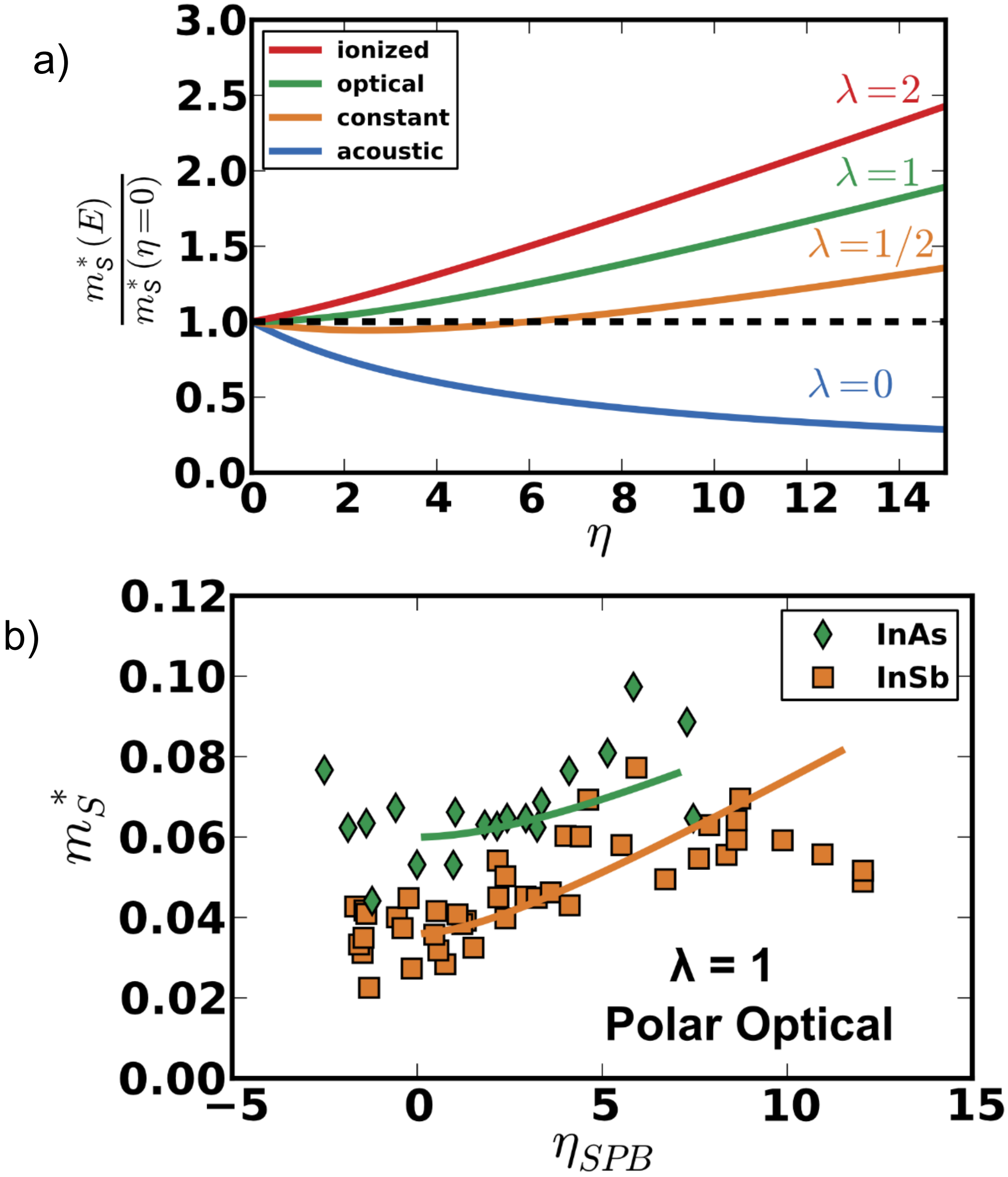
a)
ionized
optical
constant
acoustic
$\lambda=2$
$\lambda=1$
$\lambda=1/2$
$\lambda=0$
$\frac{m_S^*(E)}{m_S^*(\eta=0)}$
3.0
2.5
2.0
1.5
1.0
0.5
0.0
0
2
4
6
8
10
12
14
η
b)
InAs
InSb
λ = 1
Polar Optical
m_S^*
0.12
0.10
0.08
0.06
0.04
0.02
0.00
−5
0
5
10
15
η_{SPB}

c)

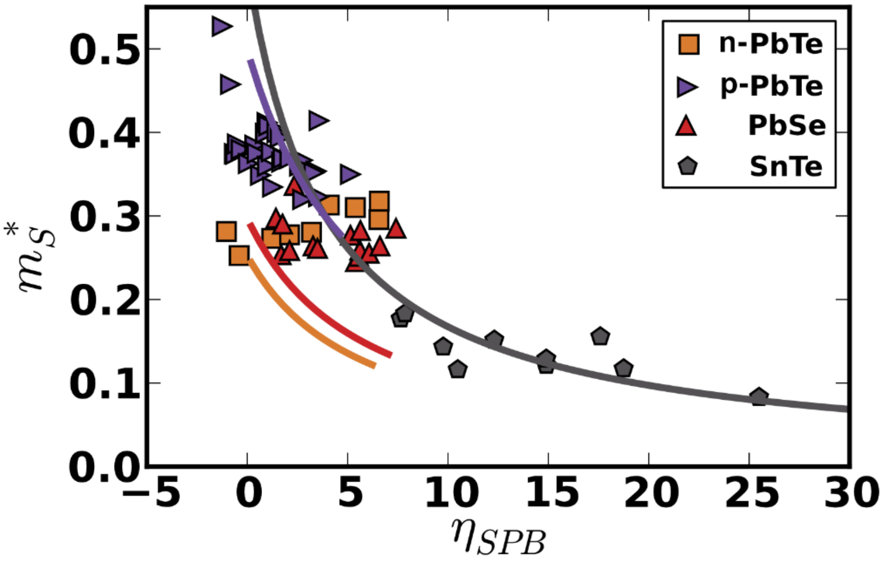

Figure 6-3: a) Calculated theoretical effective mass (ratioed to the value for reduced Fermi level at the band edge) derived using the Mott relation for different scattering mechanisms (Equation 6-5); the dashed line indicates an energy independent effective mass. A $\beta = \frac{k_B T}{E_g}$ value of 0.083 (consistent with PbTe at 300K) was used. b) Calculated SPB Seebeck effective mass (m_S^*) versus the reduced chemical potential calculated using the SPB model (η_{SPB}) for experimental examples at 300 K (InAs [64] and InSb [64, 326]) which are believed to be dominated by polar scattering. c) m_S^* versus η_{SPB} for n-type PbTe [28], p-type PbTe [34], n-type PbSe [65], and p-type SnTe [128].The solid lines in B and C indicate the best fit of the band edge mass along with the appropriate scattering mechanism plugged into Equation 6-5.

Even though $m_P^*(E)$ increases with energy in a Kane band, I have shown that in CoSb$_3$, we expect that the Seebeck coefficient and $m_S^*(E)$ should actually decrease relative to that of a parabolic band in the degenerate limit, as shown in Figure 6-2c. This may be surprising because, according to the Mott relation (Figure 6-1), a higher density of states leads is often expected to result in a higher Seebeck coefficient. Instead Equation 6-6 shows that the Kane band dispersion, and linear bands in general, does not benefit thermoelectric performance relative to a parabolic band with the same band-edge effective mass. For CoSb$_3$, Equation 6-6 demonstrates that the increasing m_S^* in Figure 6-2a is not evidence of Kane-type behavior, but rather that multiple conduction bands are necessary to explain the properties of CoSb$_3$ (as evidenced by the fitting performed in Figure 6-1a where 2 parabolic conduction bands are considered).

6.2d - Band Convergence in $CoSb_3$—High Temperature Transport Properties

We have shown evidence that a second band is required to explain the room temperature transport and optical properties. However, it is at high temperatures that the performance of $CoSb_3$ excels. At high temperatures, the electronic structure of $CoSb_3$ is expected to be even more exceptional as optical absorption edge measurements indicate that the two conduction bands approach each other with an extrapolated $T_{cvg} \approx 900\ K$. The effective valley degeneracy is further increased as a result of the multi band behavior (even below 900 K) to $N_v \approx 12 - 15$. The optical absorption measured from 20 – 450 °C clearly shows the stronger $\Gamma - CB_2$ absorption edge decreasing in onset energy (Figure 6-4a). The extrapolated absorption edges (Figure 6-4b) indicate that the primary ($\Gamma - \Gamma$, direct) transition does not shift as much with temperature (~-0.6×10^{-4} eV/K, and actually is overtaken by free carrier absorption at high temperatures), while the secondary band ($\Gamma - CB_2$) shows a clear temperature dependent decrease in energy at a rate of ~-2.0×10^{-4} eV/K. Depending on the method of extrapolation, the resulting estimations of the band gap were slightly different, which resulted in a range of possible values for the primary ($\Gamma - \Gamma$) and secondary ($\Gamma - CB_2$) transitions indicated by the error bars in Figure 6-4b (the details of which are described in the methods section). Figure 6-4b shows that as the temperature increases, CB_Γ and CB_2 are becoming closer in energy. As the two bands, CB_Γ and CB_2, become closer in energy (i.e., differ by less than 2 k_BT for T>400 K), both bands will contribute significantly to thermoelectric transport and improve the thermoelectric quality factor and zT in the same way that band convergence enables high zT in p-type PbTe [15, 16].

The high temperature zT reflects this conclusion; Figure 6-4c shows the carrier concentration dependent zT for a series of Yb-doped samples at 800 K along with the calculated results of a three-band model (two converged conduction bands, assuming $\Delta E \approx 0$). From this plot, we can see the benefits that having a second conduction band allows, resulting in a significantly higher zT than the primary conduction band at Γ can provide alone. If we consider both the primary (CB_Γ, N_v=3) and the secondary band (CB$_2$, $N_v = 12$) in the context of band engineering and the quality factor $B = \frac{2k_B^2\hbar}{3\pi}\frac{N_v C_L}{m_c^* E_{def}^2 \kappa_L} T$ ($m_{\Gamma,\mathrm{d}}^* \approx 0.7$, $m_{CB_2,d}^* \approx 4.8$ at 300 K), we can see that B_{CB2} is about four times that of B_Γ (as indicated by the much larger maximum *zT* in Figure 6-4c at 800 K). Because CB_Γ and *CB$_2$* are converged at high temperatures ($\Delta E = 0.2\ k_B T \approx 0$ for 800 K), the overall quality factor is enhanced by the presence of a second band since both pockets can be thought to conduct in parallel, thereby increasing the electrical conductivity without being detrimental to the Seebeck coefficient (in the limit of converged bands, $B_{eff} = B_1 + B_2$ [327]). At 800 K, bipolar effects are significant as a result of the highly mobile valence band and relatively narrow gap—reducing the overall *zT*, especially at the lower carrier concentrations. Future studies regarding CoSb$_3$ might build on this understanding by attempting to shift these bands together at lower temperatures to provide a further *zT* enhancement, as was the case for PbSe/SrSe alloys shown in Chapter 4.

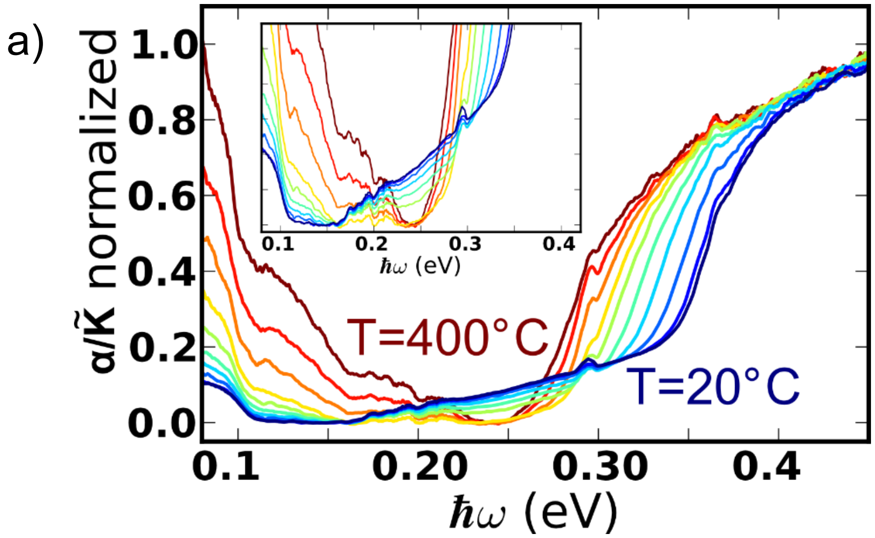

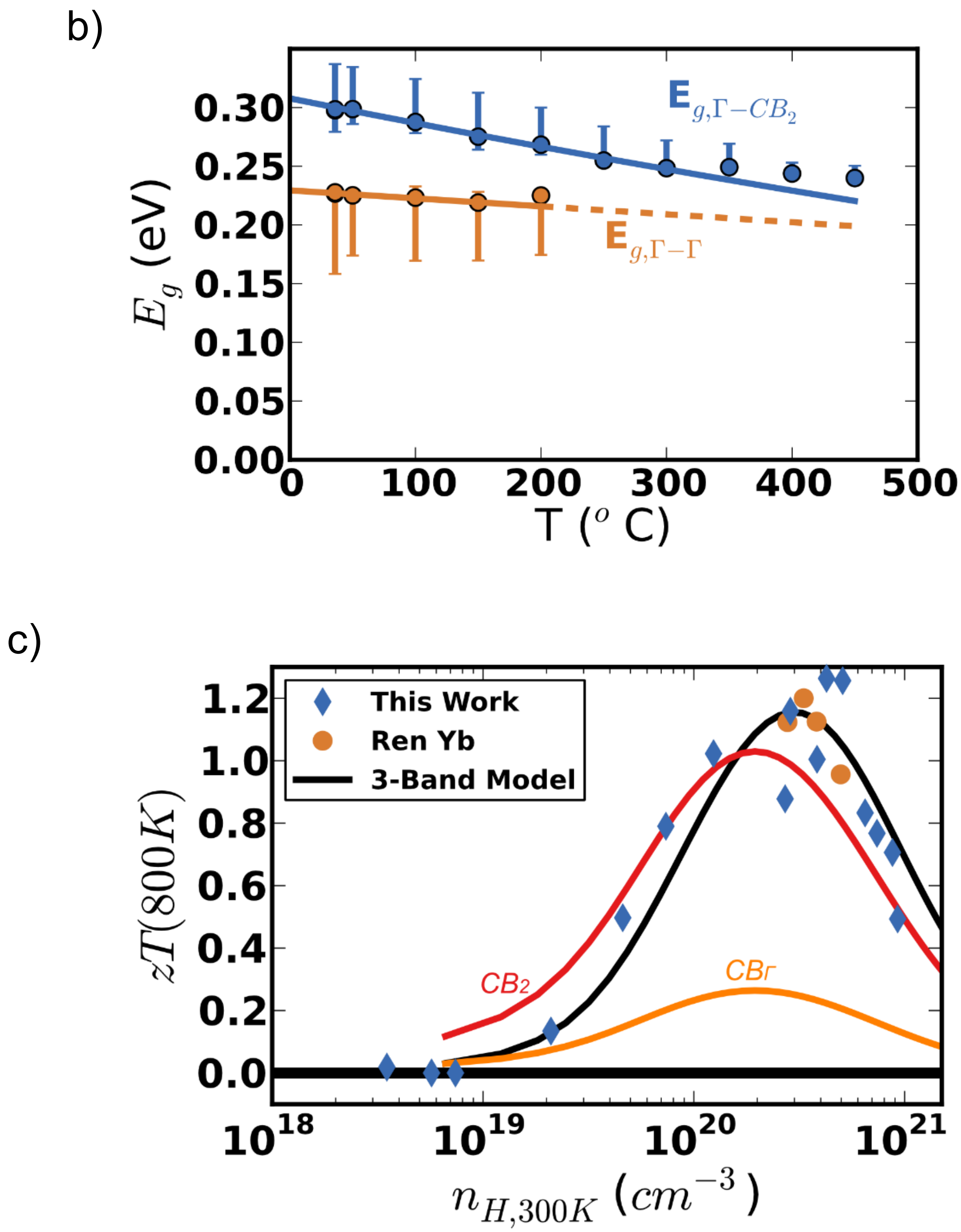

Figure 6-4: a) Temperature dependent optical absorption edge spectrum for CoSb$_3$ from 25 to 400°C. b) Temperature dependent extrapolated band gap for the direct ($E_{g,\Gamma-\Gamma}$) and indirect ($E_{g,\Gamma-CB_2}$) transitions, error bars represent a range of possible values depending on the extrapolation technique, dashed line is a continuation of the low temperature behavior of the direct gap which is overcome by free carriers for T>200°C. c) Experimental data represents zT (at 800 K) vs. room temperature n_H, along with the corresponding results for the three band model ($\Delta E = 0$) shown as the black line. The individual band contributions from CB_Γ and CB$_2$ are computed as shown in the methods section.

Temperature-dependent optical absorption spectra in lightly doped samples can also yield other interesting information in the form of absorption due to inter-conduction band transitions [116, 127, 328-330]. Temperature-dependent absorption spectra were measured for a lightly Yb-doped ($Co_4Yb_xSb_{12}$, x=0.0025, $n_{H,300K} = 6.8 \times 10^{17}\ cm^{-3}$) sample as presented in Figure 6-5. Here, the small amount of doping allows a small population of electrons in the primary conduction band which can participate in interband transitions to the secondary conduction band, CB_2. This feature is not observable upon further Yb doping because the free carrier absorption from intraband transitions increases too much. The free carrier contribution (which is expected to decay with $(\hbar\omega)^{-2}$ as discussed in Chapter 3), is fit using a power law (dashed lines in Figure 6-5a). This feature is subtracted to show the growing interband contribution as temperature increases in Figure 6-5b. Following Spitzer and Fan [329], I also consider the possibility that these features may arise from transitions to or from in-gap defect states. If we consider the free carrier absorption from the intrinsic sample (Figure 6-4a) at high temperatures, we might expect to see some of these features. At high temperatures, the intrinsic sample does indicate a small bump between 0.1 and 0.15 eV (where valence-conduction band transitions occur) relative to the decaying free carrier absorption. Another feature is observed in the intrinsic sample at 0.05 – 0.1 eV which exists even at room temperature (above the relatively flat free carrier background) and grows larger as temperature increases; however, it is difficult to resolve the difference between this feature and the growing free carrier absorption. To confirm the character of the intrinsic sample's features, better resolution at lower photon energies would be preferred (0.01 – 0.2 eV). These measurements have been performed to investigate optically active phonon modes in the Far IR (100-400 cm^{-1}, 0.001 – 0.05 eV) by Kliche et al [310], and it is possible that the 0.05-0.1 eV feature is related to these phonon modes.

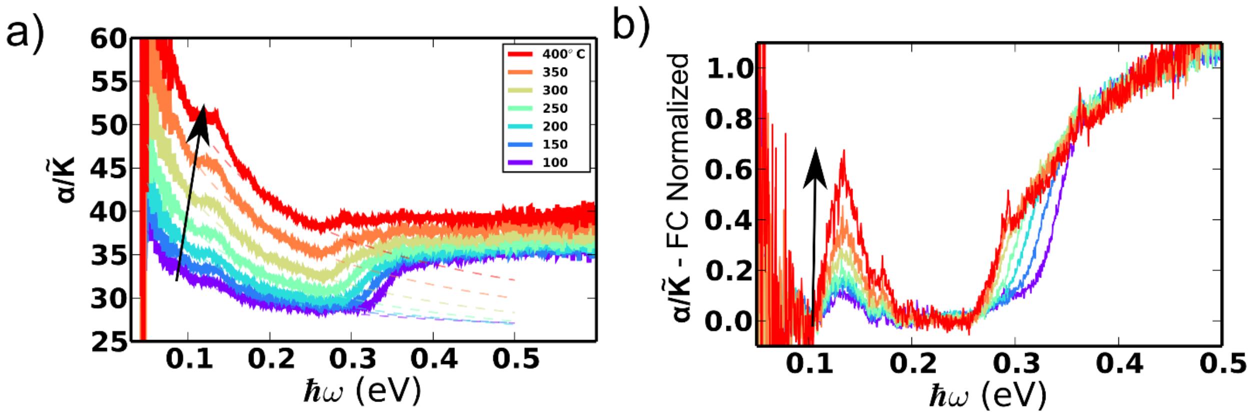

Figure 6-5: Temperature-dependent absorption edge measurements in a lightly Yb-doped (x=0.0025) $CoSb_3$ sample from 100-400°C. a) Raw Kubelka Munk transformed absorption data an arrow indicates the possible inter-conduction band absorption feature. Dashed lines indicate a power law fit for the free-carrier absorption. b) Resulting spectra after subtracting the free carrier contribution (FC) and normalizing, and an that arrow indicates the growing inter-band contribution.

6.2e - Conclusion

A unified picture explaining the extraordinary thermoelectric properties of skutterudites has emerged from a combined analysis of transport measurements, optical absorption, and theoretical calculations on a series of $Yb_xCo_4Sb_{12}$ samples. The primary light conduction bands at Γ, and have a good thermoelectric quality factor, but they are significantly aided by a secondary conduction band with extremely high valley degeneracy $N_v = 12$. At high temperatures these two bands converge, enabling the extraordinarily high $zT > 1$ that is observed in many $CoSb_3$ based skutterudites with a variety of filling and doping elements. The contribution of band convergence to the performance at high temperatures suggests that band engineering methods to converge the two conduction bands at lower temperatures would improve the low temperature zT. The analysis of linear and Kane bands presented here suggests that such non-parabolic band dispersions do not lead to an increase in thermopower (Seebeck coefficient) and are not beneficial to thermoelectric performance.

6.2f - Methods

Sample Synthesis

Samples were prepared by a process of melting and quenching followed by annealing at various temperatures for one week in order to achieve the equilibrium state, with details described previously [331] (and in Chapter 2 of this thesis). Phase purity was checked with SEM and SEM analysis in the same way as described in previous work [252, 276, 331]. Annealed samples were hot pressed according to the procedure outlined in Chapter 2.

Electrical transport properties, including electrical conductivity (σ) and Seebeck coefficient (S) were measured using the ZEM-3 (ULVAC Co. Ltd.) apparatus under a helium atmosphere from 300 to 850 K. Thermal conductivity (κ) was calculated using $\kappa = dD_TC_P$, with the thermal diffusivity D_T measured along the cross-plane direction by the laser flash method (Netzsch LFA 457) under argon flow with the Cowan model plus pulse correction. The specific heat capacity C_P was determined using the Dulong - Petit law $C_P = 3k_B$ per atom throughout the temperature range 300K to 850K.

Optical Absorption Edge

DRIFTS measurements were performed both at room temperature and high temperature for a series of $CoSb_3$ samples according to the details outlined in Chapter 2 of this thesis. Different extrapolation techniques led to different values of the band gap, hence the error bars in Figure 6-4b. First, regarding transition 1 (believed to be the direct gap, $\Gamma - \Gamma$ transition), several extrapolation techniques were considered. Linear regions were obtained for the three extrapolation techniques direct (α^2), indirect ($\alpha^{1/2}$), and forbidden [43] ($\alpha^{2/3}$) transitions, each giving a slightly different value of the band gap, the direct being the largest at around 0.23 eV. Because PbX (Chapter 4) also showed linear absorption regions for both direct and indirect transitions, I concluded that the direct gap extrapolation should be used (Figure 6-4b orange circles). The error bars in the figure correspond to the actual onset of absorption (as determined through linear extrapolation to the minimum), which should give a good lower bound for the value of $E_{g,\Gamma-\Gamma}$. With increasing temperature, the estimate for the direct gap did not change much (approximately constant at 0.22 eV). At high temperatures (T>200°C), the optical absorption spectra contained a considerable amount of free carrier absorption which overshadowed the first transition (as indicated by the dashed line above these temperatures). The free carrier absorption was fit to a power law and subtracted from the Kubelka Munk function in order to perform the absorption edge extrapolation fitting.

Regarding Transition 2, it was fit after subtracting both the free carrier absorption and either the direct extrapolation or linear extrapolation from transition 1 from the spectrum. This transition was fit as an indirect gap using either Tauc method, $(\alpha\hbar\omega)^{1/2}$, or simply $\alpha^{1/2} \propto \left(\hbar\omega - (E_g \pm E_{ph}\right)$ (both gave similar results for the gap). This method yielded two slopes which, according to theoretical analyses, indicate the onset of phonon absorption ($-E_{ph}$) and phonon emission ($+E_{ph}$) [43]. The band gap was extracted as either half-way between the absorption and emission intersections or simply as the emission intersection (as indicated by the symbols and error bars respectively in Figure 6-4b).

The joint density of states (JDOS) was computed numerically using the density of states (Figure 6-1b, right side). The JDOS was estimated using $JDOS(\hbar\omega) = \int\int \sqrt{D_{VB}(E_{VB})D_{CB}(E_{CB})}\delta(E_{CB} - E_{VB} - \hbar\omega)\, dE_{VB}dE_{CB}$ where $D_{VB,CB}$ is the density of states of the conduction or valence band respectively and δ is the Dirac delta function (selecting only energies where the valence and conduction band energies are separated by the desired photon energy).

Band Model

Here I consider transport properties of $Yb_xCo_4Sb_{12}$ using a rigid band approximation [332], meaning that the conduction band structure does not significantly change with doping (Yb content) from that of unfilled $CoSb_3$. Experimentally, similar electronic properties are obtained whether $CoSb_3$ is doped through filling or by substitution on the Co or Sb sites [281, 333] (both showing optimum thermoelectric performance at about 3×10^{20} cm^{-3} or 0.5 electrons per unit cell) [286, 334, 335] which justifies the use of the rigid band model. In other thermoelectric materials such as PbTe, rigid band models have been used quite successfully and have been confirmed theroetically [105]. Filled $Yb_xCo_4Sb_{12}$ is shown theoretically to be an essentially rigid band up to x=0.25 (0.5 electrons per unit cell [335]) although deviations appear at higher concentrations and for different fillers [305, 306].

In this work, a three band transport model was used to calculate the thermoelectric properties for $CoSb_3$ at T=300 and 800 K. The properties were calculated assuming acoustic phonon scattering [58] for all bands by solving the chemical potential dependent Boltzmann transport equations detailed in Ravich's appendix [58] for non-parabolic bands (parabolic bands were modelled assuming $\beta = 0$). The appropriate transport integrals were computed numerically (Python) to determine the η-dependent Seebeck, mobility, carrier concentration, etc. for each band [24]. The overall properties computed using conductivity weighted averages given by Putley et al. (as detailed in Chapter 2 for multi-band semiconductors) [62] for a system of two conduction bands (CB_Γ and CB_2) and one valence band.

We determine the room temperature density of states effective masses of CB_Γ and CB_2 to be 0.7 and 4.8 m_e with deformation potentials of 37.2 and 20.4 eV, respectively, and a band offset of 0.08 eV. The valley degeneracies for these bands were assumed to be 3 and 12, respectively. The anisotropy factor was assumed to be 5.0 for CB_Γ to reflect the three widely varying effective masses of the converged bands at the conduction band minimum. Including the valence band in the calculations was necessary (particularly at high temperatures); the best fit of its parameters were found to be: $N_v = 1$ (valence band maximum exists at Γ), $m_d^* = 0.6\, m_e$, $\beta = 0$ (parabolic), and $E_{def} = 7.8$ eV with a band gap of 0.22 eV.

At high temperatures (800K), the conduction band offset was taken to be $\Delta E = 0.0$ eV, in accordance with the optical observation of band convergence. The density of states effective masses were fit to 0.42 and 2.88 m_e with deformation potentials of 44.5 and 24.4 eV for the CB_Γ and CB_2, respectively. The valley degeneracy and anisotropy parameters were taken to be the same as at 300 K. The valence band parameters were adjusted at these high temperatures to accommodate for the much larger bipolar effect; the effective mass was taken to be 0.6 m_e with a deformation potential of 20 eV and a band gap of 0.22 eV (which is shown to be approximately constant from optical measurements). Because of the large bipolar effects, high temperature Hall-effect measurements (and carrier concentrations) are not reliable; room temperature n_H was plotted instead (even for high temperature properties). In order compute the room temperature Hall carrier concentration for the three band model, the charge neutrality equation $N_A - N_D = \sum_i p_i(\eta, T) - \sum_i n_i(\eta, T)$ was solved at high temperature to determine the intrinsic defect concentration (N_A-N_D as a function of η at 800 K), which was then projected back to room temperature (solved for an equivalent η_{300K}) from which the room temperature Hall coefficient (R_H) and n_H could be calculated.

*zT*s are plotted for each band (Figure 6-4c) assuming that the lattice thermal conductivity is equal to the value obtained where the maximum *zT* is obtained. The contribution for each individual band is computed as: $zT_i = \frac{S_i \sigma_i S}{\kappa_L + \kappa_e}$, where S_i and σ_i represent the contributions from each band and S is the conductivity weighted average over all bands (defined in Chapter 2) and $\kappa_e = \sum L_i \sigma_i$.

We should note that while these values yielded acceptable fits of the properties at these particular temperatures, the fits are not unique. In other words, other sets of parameters may provide adequate fits for the masses. In fact, the electronic structure calculations suggest that the states are more complicated than simply considering two conduction bands; however, we obtain both a quantitative and qualitative fit that seems to adequately reflect the nature of both transport and optical measurements.

Ab-initio DFT calculation and ultrafine evaluation of Fermi surfaces

Ab-initio calculations were performed by a collaborator, Luis Agapito (University of North Texas, Denton). The position of the 16 atoms in the $CoSb_3$ unit cell (with conventional lattice constant of 9.07 Å) is relaxed using norm-conserving pseudopotentials and the Perdew-Burke-Ernzerhof [336] density functional, as implemented in the *ab-initio* package Quantum Espresso [337]. The plane-wave basis set is defined by an energy cutoff of 270 Ry.

A 9x9x9 Monkhorst-Pack sampling of the reciprocal space is sufficient to converge the DFT calculations. However, an ultrafine *k*-mesh, containing 200x200x200 *k*-points in the reciprocal unit cell, is needed in order to obtain smooth isosurfaces. Highly accurate real-space tight-binding Hamiltonian matrices are built by projecting the DFT Bloch states onto a "small" set of atomic orbitals (4*p*, 3*d*, 4*s* for Co; and 5*p*, 5*s* for Sb) while filtering out states of low projectability [338, 339]. The reciprocal-space Hamiltonian matrices are obtained by Fourier transformation and then diagonalized at each point in the ultrafine mesh to obtain the Eigen energies. The tight-binding and the actual DFT eigenvalues are numerically the same for all practical purposes. We use the parallel implementation of the method that is available in the WanT code [340]. XCrySDen [341] is used for visualizing the isosurfaces.

6.3 - Zintl $A_5M_2Sb_6$ Materials

6.3a - Introduction

Due to their complex crystal structures, tunable transport properties, and high temperature stability, Zintl compounds such as $Yb_{14}MnSb_{11}$ (*zT* ~1.4 at 1200 K), Sr_3GaSb_3 (*zT* ~0.9 at 1000 K), and $Ca_5In_2Sb_6$ (*zT* ~0.7 at 1000 K) are promising candidates for use in thermoelectric applications [342-347]. While the complex unit cells of Zintl compounds reduce the velocity of the optical phonon modes, which lowers the lattice thermal conductivity [348], their covalently-bonded polyanionic structures also allow them to maintain good high electronic conductivity [349]. Through doping, these phases become extrinsic semiconductors with carrier concentrations in the range of 10^{19}-10^{21} carriers/cm^3, resulting in good thermoelectric *zT*s [350].

The $A_5M_2Sb_6$ Zintl phases (*A* = Ca or Sr, *M* = Al, Ga, In), which will be investigated in this section, also benefit from a complicated crystal structure and a resulting low lattice thermal conductivity. This family of compounds can be doped p-type by partial substitution of the metal site with Zn to optimize their charge carrier concentration. In this section, I will continue with the theme of this chapter, which has been identifying multi-band behavior using optical absorption edge measurements.

6.3b - Results and Discussion

Optical absorption edge measurements in $Ca_5In_2Sb_6$ and $Sr_5In_2Sb_6$ (Figure 6-6a) indicate two slopes in the absorption coefficient (similar to $CoSb_3$ shown in the previous section) which could be evidence of multiple band behavior. In both systems, the optical absorption edge spectra show a slow rise for energies above ~0.3 eV followed by a faster rise above ~0.55 eV and ~0.65 eV for the $Sr_5In_2Sb_6$ and $Ca_5In_2Sb_6$ variants, respectively. By examining the calculated $Sr_5In_2Sb_6$ electronic band structure shown in Figure 6-6b [351], we can determine which possible interband (valence-conduction band) transitions can occur that might correspond to the features in the optical absorption edge spectrum. The computed interband transition with the lowest energy corresponds to the direct band gap near the *X* point with a calculated value of ~ 0.44 eV and 0.48 eV for $Sr_5In_2Sb_6$ and $Ca_5In_2Sb_6$, respectively [351]. While the shallow rise at low energy in the optical data seems to indicate a weaker absorption feature (possibly an indirect gap or even mid-gap impurity states), we believe that this feature ($\hbar\omega_1$ as indicated in Figure 6-6a and b) is due to the direct $X - X$ transition. The second increase in absorption ($\hbar\omega_2$) is possibly due to an indirect interband transition from one of several lower laying valence bands (the first of which is centered at the Γ point) to the conduction band edge (at X). As is commonly understood, direct gaps usually yield substantially higher optical absorption coefficients than indirect ones [352]; however, in this case the density of states for the lower-laying secondary valence bands at Γ is significantly higher (by about a factor of 10) than the band edge states at *X* [351], similar to what was observed in $CoSb_3$. The (linear) extrapolation of the second absorption edge resulted in $\hbar\omega_2$ values of ~0.55 and 0.64 eV (see Figure 6-6a) for $Sr_5In_2Sb_6$ and $Ca_5In_2Sb_6$, respectively. In comparison, DFT results for the $\Gamma - X$ transition energy are ~0.73 and 0.75 eV, respectively, which shows reasonable agreement with the optical and theoretical results. We can compare the optical results with other experimental estimations of the electronic band gap. The temperature dependent resistivity approximation of the band gap calculated from $\rho \propto e^{E_g/2k_BT}$ is ~0.26 eV at low temperatures and ~0.58 eV at high, which corroborates the optical absorbance data [248]. The Goldsmid-Sharp band gap estimated from the maximum Seebeck coefficient (~380 μV/K at 500 K for the undoped sample) using the Goldsmid-Sharp band gap: $E_g = 2eS_{max}T_{max}$ is 0.38 eV [50]. Both estimates agree approximately with the optical and DFT results [353]. It is well known that multiple-band effects can lead to excellent thermoelectric performance, as is the case in PbTe [126, 354] and PbSe (Chapter 4 of this thesis). However, for $Sr_5In_2Sb_6$ the offset between the two bands is too large to improve the properties, requiring a chemical potential of ~0.25 eV to reach the second valence band which corresponds to a carrier concentration of about 10^{21} holes/cm^3 (assuming single parabolic band at T = 300 K and $m^* = 1.3\, m_e$). Further investigation into whether the suggested offset is either a function of temperature or alloying, as in Pb*X* (*X* = S, Se, Te) [126], can be performed to develop strategies towards band engineering in this system.

In this case, we have not thoroughly investigated the possibility that $\hbar\omega_1$ may be a result of intrinsic defect levels (as we had in $CoSb_3$), which might indicate that the primary gap is actually associated with $\hbar\omega_2$. However, when considering the combination of the gaps estimated from transport properties and the theoretical calculations which indicate relatively narrow gaps, we believe that the current explanation is reasonable.

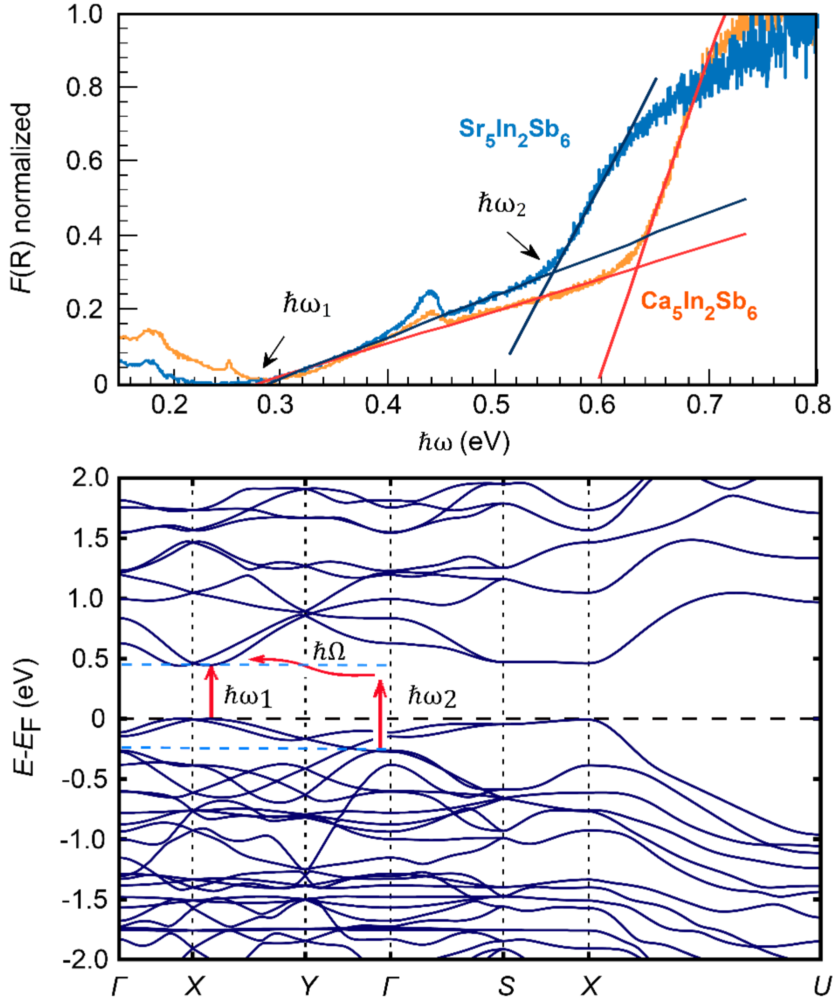

Figure 6-6: a) Optical absorption edge results showing $F(R)$ or $(\frac{\alpha}{K})$, the normalized Kubelka Munk function, for $Sr_5In_2Sb_6$ and $Ca_5In_2Sb_6$ where $\hbar\omega$ is the light energy in eV [355]. The two transitions at 0.3 eV and 0.55 eV are observed and are indicated by $\hbar\omega_n$. F(R) is the Kubelka Munk function (previously represented as $\frac{\alpha}{K}$. b) Calculated DFT band structure of $Sr_5In_2Sb_6$ with the suggested direct ($\hbar\omega_1$ ~0.48 eV) and indirect ($\hbar\omega_2$ ~0.73 eV) transitions indicated [351]. Both calculations indicate a difference of ~0.25 eV between the direct and indirect band gaps despite discrepancies in the band gap values. The peak at ~0.44 eV is indicative of O-H stretching vibrations consistent with some water adsorbed to the powder surface.

Additional measurements were performed over several different 5-2-6 compositions, each of which indicated semiconducting behavior [356]. Of these, $Eu_5In_2Sb_6$ exhibits the lowest measured band gap with an absorption edge around 0.25 eV, which agrees with previous calculations and experimental literature [357]. While the two-slope features are less pronounced in the Eu-containing compound, it is possible that they still exist but with a smaller offset (<0.1 eV), indicating that this might be a promising compound for band engineering. Of the other compounds, each begins absorbing light at ~0.3 eV and exhibits a secondary absorption edge at a different, higher energy. This is true for each system except the $Ca_5Ga_2Sb_6$, which shows the largest free-carrier absorption and a resulting minimum in *F(R)* at ~0.28 eV (indicating that the first absorption edge begins at a bit lower energy). Previous literature results agrees with this finding because they show a smaller gap (estimated from electronic properties) in $Ca_5Ga_2Sb_6$ than the other 5-2-6 compounds [358]; the valence band offset in the Ga compound is the smallest (other than the Eu-containing compound) with a value of ~0.15 eV. Literature Seebeck data on $Ca_5Ga_2Sb_6$ does not show deviation from the SPB model, but careful studies have not been performed. The In and Al containing compounds have a similar offset of ~0.35-0.4 eV which, as mentioned previously, is likely too far to be accessible through doping.

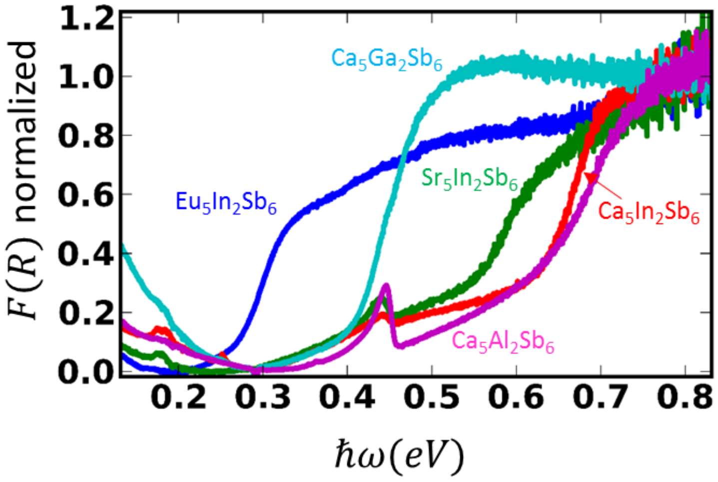

Figure 6-7: Optical absorption edge measurements in various Zintl 5-2-6 compounds. F(R) is the Kubelka Munk function (previously represented as $\frac{\alpha}{K}$.

6.3c - Conclusions

Further band structure calculations of intrinsic defects might provide some insight as to whether in-gap states might arise upon substitutions/vacancies/interstitials, as was the case for ZrNiSn in Chapter 5, which might suggest whether transition 1 is in fact related to a defect state. Based on a combination of optical, electronic, and computed properties, however, this conclusion of multiple band features seems to reasonably match the results. In order to confirm these suppositions of multiple band behavior, additional doping and transport measurement experiment should be performed, particularly in the $Eu_5In_2Sb_6$ and $Ca_5Ga_2Sb_6$ compounds, which seem to have the most promising band structures to utilize these multi-band effects through band engineering.

6.3d - Methods

The $Sr_5In_{2-x}Zn_xSb_6$ (x = 0, 0.025, 0.05, 0.1) series was synthesized using ball milling followed by hot pressing [359]. An InSb precursor was prepared using stoichiometric amounts of In shot (99.999%, Alfa Aesar) and Sb shot (99.9999%, Alfa Aesar). The elements were vacuum sealed in a quartz ampoule and heated to 900 K at a rate of 150 K/h and annealed there for 12 h, then slowly cooled to room temperature. In an argon-filled glove box, stoichiometric quantities of InSb, Sb, dendritic Sr (99.9%, Sigma Aldrich), and Zn foil (99.99%, Alfa Aesar) were weighed and placed in a stainless-steel vial with two 0.5 inch diameter stainless-steel balls. The Sr was cut into 1-3 mm pieces before it was weighed. The samples were then ball milled using a high energy SPEX Sample Prep 8000 Series Mixer/Mill for one hour. Each resulting powder was loaded into a high-density graphite die (POCO) with a 12 mm inner diameter and hot pressed in an argon environment at 823 K for 2 hours under 110 MPa of pressure. The samples were then cut into 1 mm thick disks.

Optical measurements were obtained and analyzed as outlined in Chapter 2. Absorption edges were extrapolated to the zero (or previous transition) in order to estimate the transition onset energies. Both direct (n=2) and indirect (n=1/2) extrapolations: $(F(R)\hbar\omega)^n \propto (\hbar\omega - E_g)$ were considered, each of which produced a linear region over which to fit (for each absorption edge). Because both direct and indirect extrapolations each yielded reasonable fits, we use the calculated band structure to help us determine which interband transitions are likely responsible for the absorption edge features.

6.4 - Conclusions

Multiple transitions can be observed optically in a variety of systems as shown in this chapter. $CoSb_3$ is particularly interesting because of its widespread use in commercial applications. While the electronic structure of $CoSb_3$ is not generally touted as one that is conducive to great thermoelectric properties, in this chapter I show that a multiple band transport is required to indicate the increasing Seebeck effective mass. We have fit the band parameters for the second band based on both optical measurements, and the behavior is consistent with a two conduction band transport model at both room and high temperature. Temperature dependent optical measurements indicate a decreasing energy of the second transition ($E_{g,\Gamma-CB_2}$), suggesting that, at high temperatures, the offset between the primary and secondary bands becomes even smaller until the bands are converged. We attribute a portion of the good thermoelectric performance to the shifting band structure and multi-band behavior, in addition to the reduction in lattice thermal conductivity upon Yb filling the voids in the $CoSb_3$ structure.

In addition to the $CoSb_3$ system, which shows multi-band behavior which is measurable through both the optical and electronic properties, the Zintl 5-2-6 system indicates the possibility of multi-band behavior as well. Optical measurements show two distinct absorption edges for a variety of compounds within this class of materials. In contrast to $CoSb_3$, the electronic properties in the Zintl compounds do not reflect a second band, likely because of the large band offset energies and large effective masses; although more studies should be performed to attempt to increase the doping concentration until the Fermi level reaches the secondary bands.

As has been a theme of this thesis, the combination of optical properties, electronic properties, and electronic band structure calculations has allowed us to develop relationships between the electronic structure and the good thermoelectric properties in $CoSb_3$. We provide necessary insight into the electronic structure of $CoSb_3$, which should provide the thermoelectrics community with a direction for further optimizing these materials. Only by understanding the electronic structure can we perform the appropriate carrier concentration optimization and band engineering to further enhance the thermoelectric properties.

Chapter 7: The "Fermi Surface Complexity Factor" and Band Engineering using *Ab-Initio* Boltzmann Transport Theory

7.1 - Introduction:

The calculation of electronic and thermoelectric properties from electronic band structure has received much attention lately with the increasing availability of computational algorithms and resources. *Ab-initio* calculations are very important from a materials' design perspective in that they provide insight into the underlying electronic states which give rise to the experimentally measurable thermoelectric properties. However, the correlation between calculated properties and experimental results is usually qualitative at best. Therefore, it is important to understand the methods that experimentalists use to characterize the thermoelectric performance, specifically in the context of what the results indicate about the electronic band structure. In this chapter, I develop a new metric for determining the viability of thermoelectric materials whose electronic band structures have been computed using *ab-initio* techniques. The approach is rooted in the Boltzmann transport equation, but is based on semi-empirical band engineering models and techniques which have been discussed in detail in this thesis (Single Parabolic Band model, Chapter 2). I will also give examples where band engineering (and degeneracy) simply cannot capture the behavior, which is most often observed in systems where additional topological features (in addition to individual isolated carrier pockets) arise. I apply the technique over a large database of compounds to show its validity in high-throughput screening of thermoelectric materials, allowing computations to overcome the limitations of the constant relaxation time approximation (CRTA).

One of the primary modes of improving thermoelectric materials as described in this thesis is through band engineering and carrier concentration tuning, which are often explained using the SPB model where the material properties are assumed to be described by a “free electron”-like band which has a certain effective mass (m_S^*). In terms of the thermoelectric figure of merit, zT, the optimum value can be found to scale with the quality factor (assuming acoustic phonon scattering, “APS”), $B_{APS} = \frac{2k_B^2\hbar}{3\pi}\frac{N_v C_l}{m_c^* E_{def}^2\,\kappa_L}T$ (Equation 2-6) [18]. Of the parameters in *B*, the valley degeneracy (N_v) has been shown to be critical for improving *zT* and has been a theme of this thesis (Chapter 4, 6) [16, 26, 132, 169, 170].

7.2 - Theory

7.2a - Effective Valley Degeneracy (N_v^*)

The valley degeneracy, N_v, is defined as the number of distinct Fermi surfaces that exist at the Fermi level. The origin of these degeneracies can be broken down into two parts: $N_v = N_{v,symmetry}N_{v,band}$, where $N_{v,symmetry}$ is related to the degeneracy of a given point in the Brillouin zone and $N_{v,band}$ is the number of individual bands that are converged at that energy. Valley degeneracy manifests itself by increasing the density of states effective mass, $m_d^* = N_v^{2/3}m_b^*$, relative to the single valley effective mass (m_b^*). This is beneficial for the thermoelectric properties because each individual pocket conducts in parallel while the overall Fermi level does not rise too quickly (allowing the material to simultaneously maintain a high Seebeck coefficient and high mobility). In order to maximize N_v, a highly symmetric Brillouin zone (usually found in high symmetry materials) with band extrema that exist at low symmetry points lead to the highest degeneracy. As described in Figure 7-1, for PbTe and other IV-VI materials, the primary valence band exists at the L-point with $N_{v,symmetry}$=4, and a $N_{v,band}$=1, and a secondary along the Σ line with a high degeneracy of $N_{v,symmetry}$=12, and a $N_{v,band}$=1.

While many semiconductors have their band extrema at the Γ point (the point of highest symmetry in the Brillouin zone), this point only has a $N_{v,symmetry}$ of 1 (although some have multiple degenerate bands, $N_{v,band}$>1). The lead chalcogenides, on the other hand, have their primary valence band (and conduction band) at the *L*-point with $N_{v,symmetry} = 4$ and a secondary valence band along the Σ line, which shows high degeneracy of 12 (see Figure 7-1a). While utilizing the first Brillouin zone's symmetry to simply count the number of degenerate valleys for a given material's primary band is useful for determining whether multiple Fermi surfaces might benefit the thermoelectric performance, it is not always clear how to quantify how much nearby bands contribute. Because electron transport is dominated by charge carriers with energies within a few k_BT of the Fermi level, additional bands must be in this range to lead to *zT* enhancement: for example, if E_F is well within the first *L*-band, but is more than a few k_BT from the Σ band, then the transport properties will only reflect that of the *L*-band (as we observed for low carrier concentrations in SnTe—Chapter 4).

In this thesis chapter, I develop a metric that can serve as an estimate of valley degeneracy in the regions where multiple bands participate in conduction. The "effective valley degeneracy", N_v^*, describes the Fermi level-dependent valley degeneracy in order to estimate the benefit to thermoelectric properties (and quality factor, *B*) as a result of these multi-band effects. This concept has been used before to indicate band convergence: for example, in PbTe, where the *L* and Σ bands are converged the effective degeneracy is thought to be ≈ 16 [16, 18]. Beyond cases where well-defined, individual charge carrier pockets exist, additional enhancements to thermoelectric performance can occur as a result of non-trivial topological features.

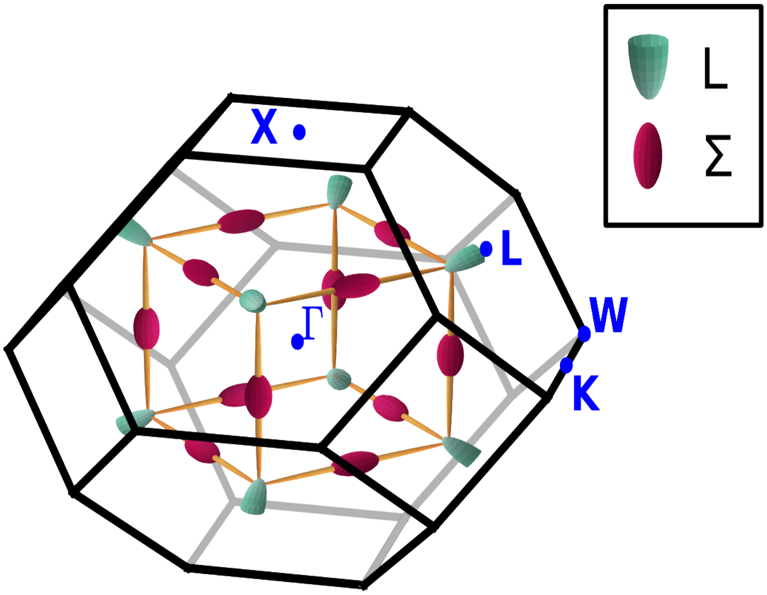

Figure 7-1: Fermi surfaces in p-type PbTe a) showing the separate ellipsoids of the L and Σ bands (leading to an increase in Nv) and b) showing the more complex Fermi surface once both the L and Σ bands have been reached, which leads to an increase in K*.*

7.2b - Effective Anisotropy Factor (K^*)

The single parabolic band model (SPB model) has an electron energy dispersion given by $E = \frac{\hbar^2 k^2}{2m^*}$, where *k* is the electron wave vector. The common definition for the effective mass is defined by the curvature of the band in k-space $m^* = \hbar^2 \left(\frac{d^2E}{dk^2}\right)^{-1}$ (light bands have high curvature, heavy bands have shallow). However, real systems often show deviations from the single parabolic band case and require a more complicated description (possibly anisotropic Fermi surfaces, non-parabolic bands, as shown in Chapters 3,4, and 6, multiple valley contributions, and/or more complicated topological features), and the band curvature definition of effective mass is not necessarily applicable nor does it even display the expected trend for the property of interest for systems that display these complex features.

In terms of Fermi surface anisotropy, only in the simplest cases can Fermi surfaces can be described as spherical pockets; many materials contain more complicated Fermi surfaces. The next level of complexity involves ellipsoidally shaped pockets where the anisotropy parameter, $K = \frac{m_\parallel^*}{m_\perp^*}$, quantifies the degree of anisotropy. Many systems show Fermi surface anisotropy both experimentally and theoretically, such as Si/Ge [55, 56], IV-VI materials [58, 59, 360], III-V materials [57], and others [61]. The conductivity effective mass (which is a single valley harmonic average along each direction): $m_c^* = 3\left({m_\parallel^*}^{-1} + 2{m_\perp^*}^{-1}\right)^{-1}$ determines the carrier mobility ($\mu = \frac{e\tau}{m_c^*}$). m_c^* is equal to the m_b^* (geometric average: $m_b^* = \left(m_\parallel^* {m_\perp^*}^2\right)^{1/3}$) for spherical pockets ($K = \frac{m_\parallel^*}{m_\perp^*} = 1$), although in general they are different. For ellipsoidally shaped Fermi surfaces ($K \neq 1$), the effective anisotropy K^* parameter can be expressed as:

$$\boldsymbol{K^*} = \left(\frac{\boldsymbol{m_b^*}}{\boldsymbol{m_c^*}}\right)^{3/2} = \frac{(\boldsymbol{2K+1})^{3/2}}{\boldsymbol{3^{3/2}K}} \qquad \text{Equation 7-1}$$

If the density of states mass is held constant, increasing *K* (and *K**) is good for thermoelectrics because it implies that the conductivity mass would decrease (corresponding to an increased mobility and conductivity). While anisotropy is generally beneficial, some Fermi surface anisotropy cannot be captured by simply considering ellipsoidally shaped carrier pockets.

The ellipsoidal description of the Fermi surface works well in many cases, and it is easily extendible to systems with N_v>1 (or to systems with a Fermi-level dependent effective valley degeneracy, N_v^*). However, some materials exhibit additional non-trivial topological features in their Fermi surface which cannot be accounted for in the ellipsoidal framework. For example, in PbTe, once the Fermi level becomes sufficiently degenerate, narrow threads are calculated to connect the individual L and Σ bands, which results in an increasingly complex Fermi surface (as illustrated by the orange features in Figure 7-1b) [294, 295]. In cases where the Fermi surface has additional complexity, simply estimating the N_v^* is not sufficient to capture the potential enhancement to the thermoelectric quality factor, requiring the introduction of “the effective anisotropy factor”, *K**, which can be expressed explicitly for ellipsoidally shaped pockets (Equation 7-1) but must be computed from the electronic structure in general. Recent work from several groups has shown that additional thermoelectric enhancement can occur as a result of Fermi surface complexity beyond simple spherically shaped, isolated pockets in the valence bands of both IV-VI [59, 294, 295] compounds and Si [361] (and perhaps other group IV or III-V materials with similar valence band structures). This can occur as a result of oddly shaped topological features such as threads (Figure 7-1) [294] or warping resulting from multiple extrema with drastically different masses [59].

7.2c - Fermi Surface Area to Volume Ratio

While Parker et al. have attributed topological enhancements to thermoelectric performance in the IV-VI systems to low dimensional Fermi-surface features, I propose an alternative explanation involving the Fermi surface area to volume ratio. If we consider the Boltzmann transport equation:

$$\boldsymbol{\sigma_{ij} = \int_{BZ}\left(-\frac{df}{dE}\right) v_i v_j \tau(k) d^3k = \int_{BZ}\left(-\frac{df}{dE}\right) v_i v_j \tau A_k \frac{dE}{dE/dk}} \qquad \text{Equation 7-2}$$

where *f* is the Fermi distribution function, v_i is the electron group velocity (in the i^{th} direction), τ is the scattering time, *k* is proportional to the electron momentum, *E* is the electron energy, and A_k is the Fermi surface area (derived by simply substituting $d^3k = dV_k = A_k dk$ where *V* is the volume of the Fermi surface). In the usual, energy-dependent, form of the Boltzmann transport equation, the density of states is substituted $D(E) = \frac{dn}{dE} = \frac{1}{(2\pi)^3}\frac{dV}{dE} = \frac{1}{(2\pi)^3}A_k\frac{dE}{dE/dk}$. However, this form allows us to see that the in the degenerate limit (i.e., where $(-\frac{df}{dE}) \approx \delta(E - E_F))$ the electrical conductivity is simply proportional to the Fermi surface area.

If we can also consider the carrier concentration:

$$\boldsymbol{n} = \frac{\boldsymbol{V_k}}{(\boldsymbol{2\pi})^3} \qquad \text{Equation 7-3}$$

which is simply equal to the volume enclosed by the Fermi surface divided by the volume of a single *k*-point (which the particle in a box model states is $\left(\frac{2\pi}{L^*}\right)^2$, where L^* is the sample dimension). The ratio of the electronic conductivity to the carrier concentration gives a value proportional to the mobility; therefore, mobility is increased if the surface area to volume ratio of the Fermi surface is large, as is the case for many complex Fermi surface features (such as the threads in Figure 7-1). This effect will benefit *zT* by allowing a larger electronic conductivity without drastically altering the Fermi level. Recent work by Pei et al. shows that low effective mass (i.e., high mobility) is desirable for thermoelectric band engineering, contrary to popular opinion which suggests high mass is good [106]. I believe that these complex topological features likely produce high quality factors owing to their large surface area to volume ratios, and that in the case where appreciable amounts of carriers exist in these states, they can contribute significantly to *zT*.

7.2d - Fermi Surface Complexity Factor $(N_v^* K^*)$

In this thesis chapter, I will attempt to describe the effects of valley degeneracy (and more broadly Fermi surface complexity) with a single parameter which we will call the “Fermi surface complexity factor”, $(N_v^* K^*)$. I define the “Fermi surface complexity factor” as $(N_v^* K^*) = \left(\frac{m_S^*}{m_c^*}\right)^{3/2}$ where the conductivity mass, m_c^*, and m_S^* is the effective mass obtained from Seebeck coefficient and carrier concentration using the SPB model. These two parameters are simply estimated from outputted Boltztrap calculation results and reflect parameters that are observed directly in the thermoelectric quality factor. Using transport properties estimated from the Boltztrap code in conjunction with the calculated band structure properties, we show how to obtain a chemical potential dependent estimate of $(N_v^* K^*)$ for any compound that does not depend on the assumed scattering mechanism. We apply this technique across a large number of materials from the Materials Project high-throughput thermoelectric properties database to validate the theory.

Single Parabolic Band Model from Boltztrap (m_S^*)

Calculated Boltztrap data will be analyzed in the context of the Seebeck Pisarenko plot (*S* vs *n*), which is commonly used when analyzing experimental data. Using the Pisarenko plot, the data can easily be understood in the context of a single parabolic band model (also assuming constant scattering time) with the relevant fitting parameter being the effective mass (m_d^*). The equations are shown for the thermoelectric parameters as a function of the reduced chemical potential: $\eta = \frac{\xi}{k_B T}$ are shown below for an arbitrary power law dependence of the scattering time $\tau(\epsilon) = \tau_0 \epsilon^{\lambda - 1/2}$ ($\lambda = 1/2$ for constant scattering time as is assumed in Boltztrap) [24]:

$$\boldsymbol{S}(\boldsymbol{\eta}) = \frac{\boldsymbol{k_B}}{\boldsymbol{e}}\left[\frac{(\mathbf{2}+\boldsymbol{\lambda})}{(\mathbf{1}+\boldsymbol{\lambda})}\frac{\boldsymbol{F}_{\mathbf{1}+\boldsymbol{\lambda}}(\boldsymbol{\eta})}{\boldsymbol{F}_{\boldsymbol{\lambda}}(\boldsymbol{\eta})} - \boldsymbol{\eta}\right] \quad \text{Equation 7-4}$$

$$\boldsymbol{n}(\boldsymbol{\eta}) = \frac{\mathbf{1}}{\mathbf{2}\boldsymbol{\pi}^{\mathbf{2}}}\left(\frac{\mathbf{2}\boldsymbol{m}_{\boldsymbol{d}}^{*}\boldsymbol{k_B}\boldsymbol{T}}{\hbar^{\mathbf{2}}}\right)^{\frac{\mathbf{3}}{\mathbf{2}}}\boldsymbol{F}_{\mathbf{1/2}}(\boldsymbol{\eta}) \quad \text{Equation 7-5}$$

where λ determines the scattering exponent, n is the charge carrier concentration, and m_d^* is the density of states effective mass. The effective mass can be determined using experimental parameters by supplying a measured Seebeck coefficient and *n* and solving for both η and m_d^*. This method can also be applied to calculated Boltztrap data (*S* vs *n*) to get an estimate for m_d^*, which we will call m_S^* (effective mass from Seebeck coefficient).

Boltztrap Conductivity Mass (m_c^*)

The conductivity effective mass is calculated directly from Boltztrap data by considering the electrical conductivity, σ. Boltztrap estimates the conductivity tensor (divided by τ) by solving the Boltzmann transport equation (Equation 7-2) for a given calculated electronic structure and temperature. The conductivity effective mass tensor can be calculated as $\boldsymbol{m_c^*} = ne^2(\boldsymbol{\sigma}/\tau)^{-1}$, where n is the carrier concentration, e is the fundamental electron charge, and $\boldsymbol{\sigma}/\tau$ is the conductivity tensor divided by the scattering time. Interestingly, because Boltztrap computes the ratio of the conductivity tensor to the scattering time ($\boldsymbol{\sigma}/\tau$), the conductivity mass tensor ($\boldsymbol{m_c^*}$) should represent the band structure and should not depend on the scattering time. One complaint about Boltztrap thermoelectric transport results is that they use the CRTA, which we know to not be valid for most experimental systems that show APS. By computing m_S^* and $\boldsymbol{m_c^*}$, which presumably do not depend on scattering, we hope to improve the applicability of the Boltztrap method to experimental results, especially in the context of band engineering, effective valley degeneracy (N_v^*), and effective anisotropy factor (K^*).

7.3 - Results and Discussion

7.3a - III-V Materials

N_v^*, the effective valley degeneracy, can be described as the number of valleys which conduct in parallel. In the case where only a single carrier pocket participates in conduction (not considering symmetry), $N_v^* = N_v$. Many real semiconducting systems have multiple band extrema within 1.0 eV of the band edge, implying that a Fermi-level dependent effective valley degeneracy should be defined which more accurately represents the changing number of degenerate pockets. N_v^* would reflect a smooth transition from one value of N_v to another as the carrier density the secondary pocket increases; this can be compared to the step-change in N_v that might be expected as the energy of the secondary band is reached just by considering the symmetry of the extrema alone (green line in Figure 7-2a, $N_v(E_F) = \sum N_{v,i}\mathrm{H}(E_F - E_i)$ where H is the Heaviside step function and E_i is the energy of the i^{th} band extrema). As the first example of where the Fermi surface complexity factor is applied, we have considered AlAs, shown in Figure 7-2.

The calculated DFT electronic band structure and Boltztrap data analyzed using the $(N_v^* K^*)$ method (Materials Project, mp-2172) for AlAs are shown in Figure 7-2 along with the true valley degeneracy (N_v) computed directly from the band extrema positions and the Brillouin zone symmetry. The primary conduction band minimum occurs at the X-point ($X_{\text{-c}}$ N_v=3), which agrees with the computed $(N_v^* K^*) = 3.5$ within the band gap near the conduction band edge. As the Fermi level moves into the conduction band, we reach the Γ_{-c} (N_v=1, 0.28 eV above $X_{\text{-c}}$) and $L_{\text{-c}}$ (N_v=4, 0.51 eV above $X_{\text{-c}}$) bands, the actual N_v increases to 4 and 8, respectively. The Fermi surface complexity factor $(N_v^* K^*)$ increases steadily from the band edge resulting in a value of 3.5 and 6.1 at the Γ_{-c} and $L_{\text{-c}}$ band edge energies, respectively. $(N_v^* K^*)$ continues to increase reaching a maximum value of ~12.5. This is not quite as high as one might expect based on the high degeneracy of the $K_{\text{-c}}$ extrema (N_v=12, 0.75 eV below $X_{\text{-c}}$) or the additional $X_{2\text{-}c}$ band (N_v=3, 0.78 eV below $X_{\text{-}c}$). It is not readily apparent why the full 23 valleys are not observed through $(N_v^* K^*)$, but it could be related to the fact that the thermopower is quite low (less than 20 μV/K) for these Fermi levels, meaning that we may be reaching the limit of the calculation resolution. Up until high energies, though, the thermoelectric Fermi surface complexity factor $(N_v^* K^*)$ seems to mirror the true N_v both qualitatively and quantitatively—indicating an anisotropy component, K^*, that is likely near unity.

If we consider the valence band of AlAs, it, like all of the III-V materials calculated in this chapter, consists of three degenerate bands, $\Gamma_{1,2,3-\mathrm{v}}$, each of which vary significantly in effective mass (light hole, heavy hole, and split-off band). As a result, the Fermi surface, even though it is centered at the $\mathit{\Gamma}$ point, will have a non-trivial topology (as suggested by Mecholsky et al. for silicon [361]), which will result in a larger K^* component to the Fermi surface complexity factor. For the valence band, $(N_v^* K^*) = 9$, which is an overestimate relative to the expected degeneracy of N_v=3 for $\Gamma_{1,2,3-v}$. Mecholsky et al. shows that the warped Fermi surfaces, which result from the combination of light and heavy holes in silicon, lead to interesting consequences for the effective mass and conductivities in these systems [361], consistent with inflated $(N_v^* K^*)$ observed for $\Gamma_{1,2,3-v}$ here.

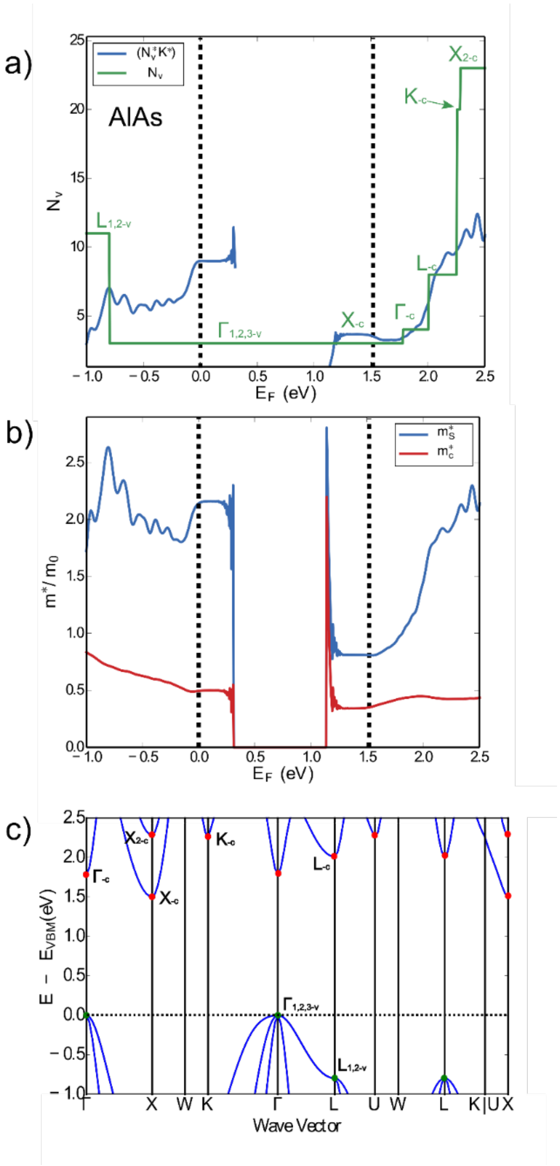

Figure 7-2: Boltztrap (300 K) and band structure calculation results for AlAs. a) "Fermi surface complexity factor" and true valley degeneracy plotted as functions of the Fermi level across the valence and conduction band. b) The conductivity (m_c^*) and density of states (as estimated from Seebeck coefficient, m_S^*) effective masses plotted as a function of Fermi energy. c) Band structure calculation results for AlAs with the near-edge extrema indicated and labelled.

Upon calculating the Fermi surface complexity factor for other III-V compounds, we can see many analogs to the AlAs results. AlP (Figure 7-3a) shows a primary extrema at $X_{\text{-}c}$ (N_v=3), which $(N_v^*K^*)$ matches well; this is followed by the $K_{\text{-}c}$ (N_v=12, at 0.83 eV above $X_{\text{-}c}$) and $X_{2\text{-}c}$ (N_v=3, at 0.85 eV above $X_{\text{-}c}$) bands, which result in a small increase in $(N_v^*K^*)$ up to >10.0 (although not until ~1.2 eV above $X_{\text{-}c}$ edge, which is not plotted). The conduction band of AlSb in Figure 7-3b shows three near-converged bands with the primary L_{-c} band (N_v=4) accompanied by a $(\Gamma - X)_{-c}$ (N_v=6 at 0.03 eV above L_{-c}) and Γ_{-c} (N_v=1 at 0.05 eV above L_{-c}). Because these two bands are so close in energy (within 2 k_BT at 300 K) to the conduction band edge, it is not surprising that $(N_v^*K^*)$ more closely reflects the sum of the degeneracy for these bands; even within the band gap, $(N_v^*K^*) \approx 14$. This value is slightly larger than the expected N_v of 11, but it is possible that the nearby X_{-c} band with N_v=3 could also be contributing as well. The conduction bands of GaN and GaSb are a bit simpler in that their primary conduction band lays at Γ_{-c}, resulting in both yielding $(N_v^*K^*) \approx 1$, as expected. In the case of GaAs, a secondary band at L_{-c} (N_v=4, at 0.69 eV above Γ_{-c}) results in an abrupt jump in the Fermi surface complexity factor up to about 7.0 around this energy. The details of each of the n-type III-V compounds' effective masses, expected valley degeneracy, and Fermi surface complexity factors are included in Table 7-3. The valence bands of all of the III-V compounds in this work showed the same triply degenerate at the $\Gamma_{1,2,3-v}$ behavior as in AlAs (Figure 7-2c), some were followed by a doubly degenerate at L_{12-v}; however, the L_{12-v} extrema were usually much lower in energy and did not effect $(N_v^*K^*)$ much. In all cases, $(N_v^*K^*)$ was between 6 and 10 at the valence band edge ($\Gamma_{1,2,3-v}$), which is greater than the expected N_v of 3.0, which should be attributed to the effective anisotropy factor (K^*) as mentioned previously for AlAs.

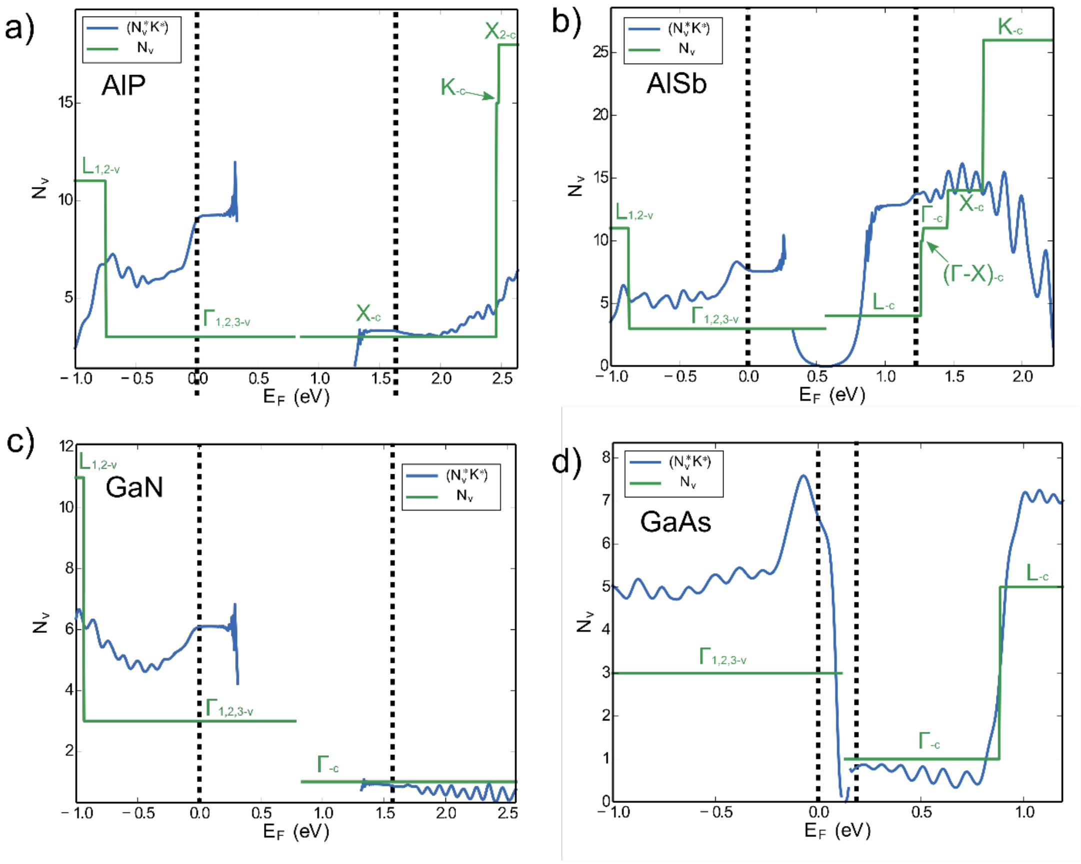

Figure 7-3: Fermi surface complexity factor computed for several III-V compounds along with their expected valley degeneracies for a) AlP (mp-1550), b) AlSb (mp-2624), c) GaN (mp-830, Zinc Blende structure), and d) GaAs (mp-2534).

Table 7-3: III-V semiconductor results regarding their true valley degeneracy extracted from band structure (CBM Loc, CB Deg), and their conductivity/Seebeck effective masses and Fermi surface complexity factors computed at the energy of the contributing band. E_g (band gap) is in eV, and MPID corresponds to the mp-id parameter used to store data within the Materials Project (materialsproject.org).

	MPID	E_g	CBM Loc	CB Deg	m_S^*	m_c^*	$N_v^*K^*$
AlN	1700	3.31	X, Γ(0.69)	3, 1	0.81, 0.96	0.39, 0.47	3.0, 3.0
AlP	1550	1.63	X, K (0.83), X (0.85)	3, 12, 3	0.77, 1.39, 1.46	0.35, 0.51, 0.51	3.3, 4.5, 4.9
AlAs	2172	1.5	X, Γ (0.28), L (0.51), K (0.75), X (0.78)	3, 1, 4, 12, 3	0.81, 0.97, 1.49, 1.94, 2.00	0.35, 0.42, 0.45, 0.42, 0.42	3.6, 3.5, 6.1, 9.8, 10.2
AlSb	2624	1.23	L, Γ-X (0.03), Γ (0.05), X (0.23), K (0.49)	4, 6, 1, 3, 12	1.37, 1.49, 1.53, 2.01, 2.05	0.24, 0.26, 0.27, 0.32, 0.36	13.7, 13.8, 13.9, 15.5, 13.7
GaN	830	1.57	Γ	1	0.15	0.16	0.9

GaP	2490	1.59	L, Γ (0.00), Γ-X (0.05), X (0.26), K (0.63)	4, 1, 6, 3, 12	1.23, 1.23, 1.40, 1.93, 2.08	0.22, 0.22, 0.24, 0.33, 0.39	13.0, 13.0, 14.1, 14.2, 12.3
GaAs	2534	0.19	Γ, L (0.69)	1, 4	0.03, 0.25	0.04, 0.12	0.8, 3.1
GaSb	1156	0	Γ, L (0.32), Γ-X (0.93)	1, 4, 6	0.02, 0.24, 0.89	0.03, 0.09, 0.22	0.5, 4.7, 8.4
InN	20411	0	Γ	1	0.09	0.12	0.66
InP	20351	0.47	Γ, L (0.93)	1, 4	0.055, 0.47	0.06, 0.27	0.84, 2.6
InAs	20305	0	Γ, L (0.84)	1, 4	0.03, 0.43	0.05, 0.24	0.6, 2.4
InSb	20012	0	Γ, L (0.44)	1, 4	0.03, 0.31	0.05, 0.13	0.5, 3.5

7.3b - IV-VI Materials – The Lead Chalcogenides

As mentioned previously (Chapter 4), the lead chalcogenides (including PbSe [65, 261], PbS [13], and their alloys [12, 19, 25, 121, 362-366]) are known to be good thermoelectric materials. Much of this is attributed to their high valley degeneracy resulting from an accessible Σ_{-v} band. I have applied the Fermi surface complexity factor analysis to both PbSe and PbS, the results of which are shown in Figure 7-4. The Σ_{-v} band lays 0.34 and 0.48 eV below L_{-v} in PbSe and PbS, respectively (which agree with previous experiment [25, 261, 367] and theory [25, 126, 294]); the computed band offsets, expected valley degeneracies, and observed $(N_v^* K^*)$ are tabulated in Table 7-4. Both PbSe and PbS show good agreement with the expected N_v of 4 for both the conduction and valence bands within the band gap. As the Fermi level moves deeper into the valence band, the Σ_{-v} results in a peak in $(N_v^* K^*)$ of ~19 and 14 for PbSe and PbS, respectively (close to the expected value of 16). Additional extrema at the W_{-v} (and $(\Gamma - X)_{-v}$ in the case of PbSe) result in another large peak in $(N_v^* K^*)$ up to values of ~41 (at 0.75 eV below L_{-v}) and ~16 (at 0.94 eV below L_{-v}) for PbSe and PbS, respectively. Each of the peak values agrees qualitatively with the expected N_v from band structure, although $(N_v^* K^*)$ is higher than expected for the W_{-v}/$(\Gamma - X)_{-v}$ in PbSe, implying that K^*>1. K^* is likely larger due to non-trivial topological features that are well-known to occur in the valence band of the lead chalcogenides beginning below the Σ_{-v} band (as mentioned in a previous section and shown schematically in Figure 7-1) [121, 294, 295]. For PbSe and PbS, the conduction band only shows some deviations from $(N_v^* K^*) = 4$ within the gap as expected from the primary conduction band, L_{-c}, but they do show some increase as the secondary conduction band (Σ_{-c}) arises at 0.79 and 0.88 eV above the band edge, respectively (although the value does not reach the expected value of N_v=16).

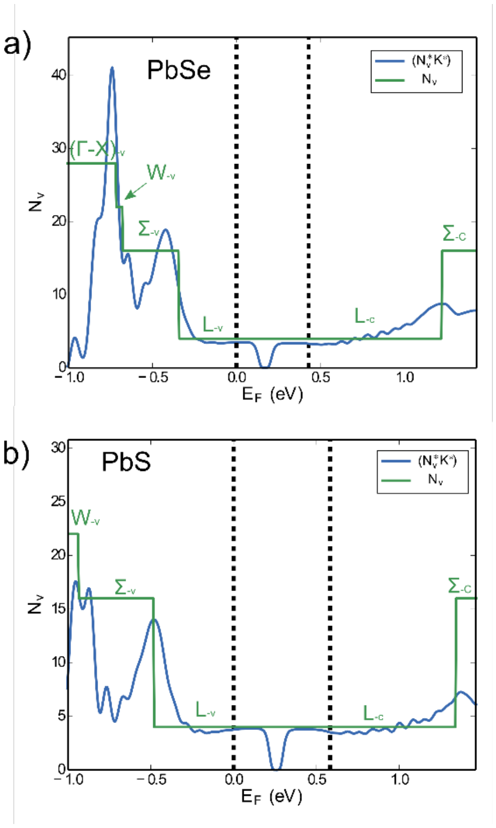

Figure 7-4: The Fermi surface anisotropy factor and valley degeneracy plotted for a) PbSe (mp-2201) and b) PbS (mp-21276).

Table 7-4: Valence band parameters for several IV-VI materials of thermoelectric interest. Band gaps (E_g) is listed in eV. VBM locations are given by their position in k-space (which also corresponds to Figure 7-5 and Figure 7-4) as well as their energy offset relative to the valence band edge. We have included their degeneracy (individual band degeneracy, not cumulative, which is plotted in Figure 7-4a), the Seebeck/conductivity effective mass (m_c^*, m_{Seeb}^*), and the calculated effective valley degeneracy, N_v^*, at each corresponding band *edge energy. For SnTe, which had a very low band gap, values for the L band were taken 0.1 eV below the band edge so as to avoid strong bipolar effects.*

	MPID	E_g	VBM Loc	VBM N_v	m^*_{Seeb}	m^*_c	N_v^*
PbTe	19717	0.81	L, Σ (0.12), Γ-X (0.30), W (0.30), Σ_2 (0.64), $L_{2,3}$ (0.76)	4, 12, 6, 6, 12, 4x2	0.71, 2.29, 4.82, 1.37, 1.78	0.17, 0.23, 0.33, 0.41, 0.45	8.7, 30.8, 56.9, 6.0, 7.9
PbSe	20667	0.43	L, Σ (0.34), W (0.68), Γ-X (0.72)	4, 12, 6, 6	0.37, 1.49, 2.87, 5.22	0.16, 0.30, 0.47, 0.49	3.5, 11.1, 14.9, 34.6
PbS	21276	0.46	L, Σ (0.48), W (0.94), Γ-X (1.00)	4, 12, 6, 6	0.48, 2.19, 4.13, 2.69	0.20, 0.38, 0.63, 0.62	3.8, 14.0, 16.9, 9.0
SnTe	1883	0.04	L, Σ (0.36), Γ-X (0.80), W (0.82)	4, 12, 6, 6	0.16, 1.13, 2.58, 3.16	0.07, 0.15, 0.32, 0.32	3.6, 21.7, 22.4, 30.7

Of the lead chalcogenides, PbTe has been shown to yield the best thermoelectric performance. Experimentally, p-type PbTe stands out from PbSe and PbS mainly due to its relatively small band offset between the L_{-v} and Σ_{-v} bands and lower thermal conductivity [16, 123-126, 162]. Figure 7-5 shows the computed band structure, the Fermi surface complexity factor $(N_v^*K^*)$, and computed effective masses for PbTe. Figure 7-5c shows the large number of near-edge bands that exist in PbTe in both the valence and conduction band. I show the calculated $(N_v^*K^*)$ along with the expected valley degeneracy contributions for the different extrema (Figure 7-5a). Upon the Fermi level entering the valence band, we observe an $(N_v^*K^*)$ of ~9, which continues to increase as the Fermi level moves further into the band. While in the case of PbSe and PbS $(N_v^*K^*) \approx N_v(L_{-v}) = 4$ within the gap near the L_{-v} edge, PbTe shows a larger band edge Fermi surface complexity factor. It is not clear whether this is due to some influence of the Σ_{-v} band (which is computed to be only ~0.12 eV or 4.8 k_BT at 300 K away from L_{-v}), which would imply N_v^*>4, or whether it may be due to the fact that the L_{-v} bands for PbTe are more ellipsoidal (K^*>1) than in PbSe and PbS (observed in the literature [58, 59, 360].) As E_F moves further into the valence band, we can see a rapid increase in m_S^* (Figure 7-5b) because of the additional influence of the high degeneracy Σ_{-v} band. Despite the large increase in m_S^*, the conductivity mass increases only modestly, resulting in a rapid increase in $(N_v^* K^*)$. Once the Fermi level reaches the Σ_{-v} band, $(N_v^* K^*)$ reaches values near 30, much greater than the expected N_v of 16. The Fermi surface complexity factor continues to increase rapidly as we reach the W_{-v}, $(\Gamma - X)_{-v}$, Σ_{2-v}, and $L_{2,3-v}$ at 0.3, 0.3, 0.64, 0.76 eV below L_{-v}, respectively, ultimately achieving an extremely large value around 60. While a large N_v is expected from the many valence bands (reaching a value of ~50, green line Figure 7-5a), $(N_v^* K^*)$ rises very quickly and reaches a peak value that is much higher than expected (from the actual N_v). It is clear that $(N_v^* K^*)$ cannot be explained by simply considering N_v^* alone, implying that $K^*>1$. As mentioned previously, it is well-known that the lead chalcogenides exhibit a complicated Fermi surface that involves a merging of the separate pockets (L_{-v} and Σ_{-v}) [59, 121, 294, 295], which is likely causing the large K^* value (threads shown in Figure 7-1). As mentioned in the theory section, recent work from Parker et al. suggests that cylindrical "threads" that connect the L_{-v} and Σ_{-v} pockets result in a significantly larger Fermi surface area, which is suggested to benefit thermoelectric properties [295]. While Parker et al. attribute this to a reduced-dimensional Fermi surface, my explanation involves the large surface area to volume ratio of the states which these charge carriers occupy; this results in these thread-like states having an inherently large mobility and quality factor (and corresponding large K^*).

The conduction band also benefits from a large number of additional carrier pockets with high degeneracy. A corresponding analog of the Σ_{-v} valence band is calculated to exist in the conduction band (Σ_{-c}) at ~0.54 eV above the band edge. This band is accompanied by a doubly degenerate L-band ($L_{2,3-c}$). Each of these bands increase $(N_v^* K^*)$, resulting in a peak around this energy. It is important to note that experimentally in *n*-type PbTe, it is difficult to dope to high enough carrier concentration to reach any secondary conduction bands [28]; Boltztrap calculations suggest that carrier concentrations of >$2 \times 10^{21}\ cm^{-3}$ to reach the Σ_{-c} band (whereas experimentally, the maximum attainable n_H has been shown to be an order of magnitude less [28]).

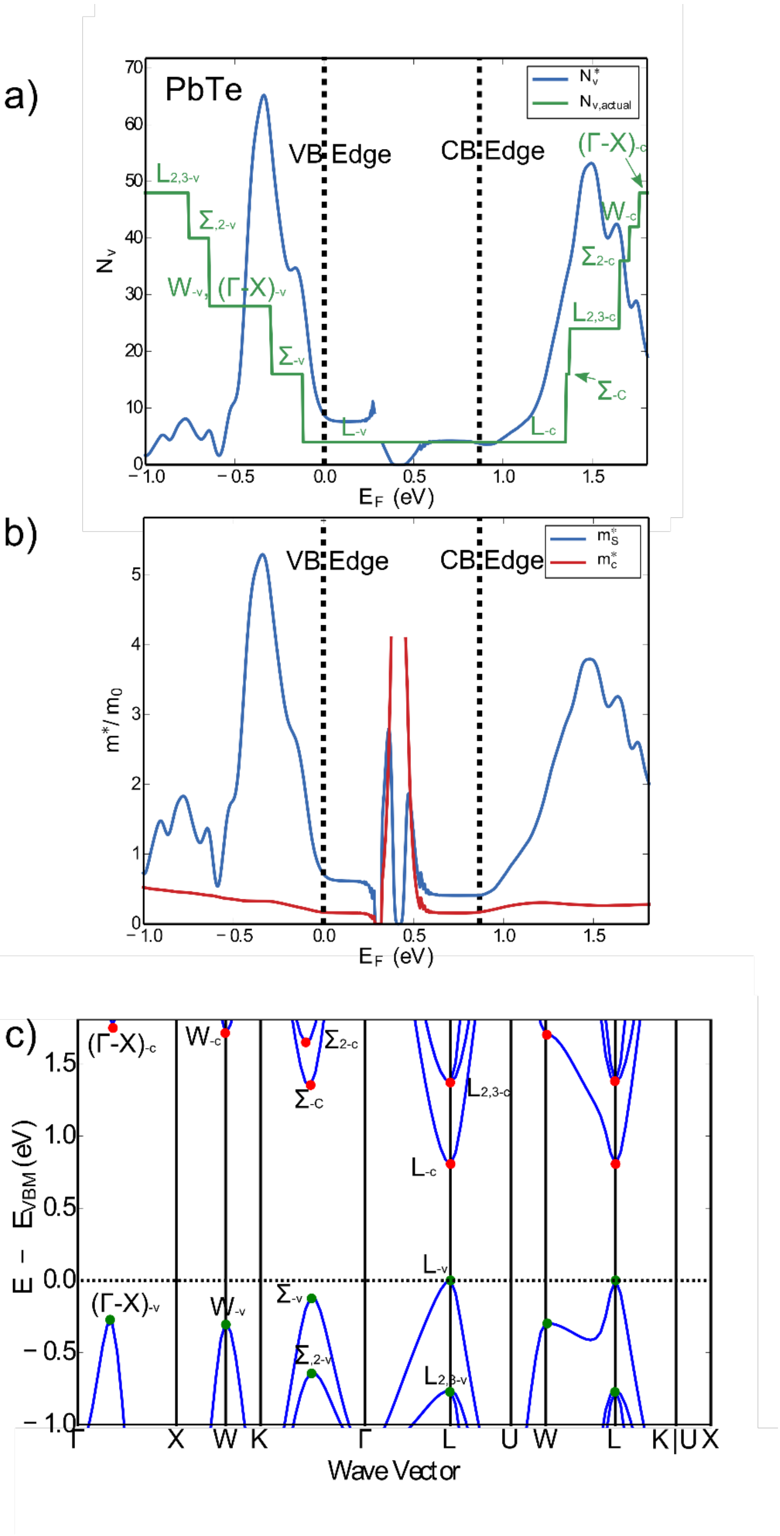

Figure 7-5: PbTe (mp-19717) calculated results for a) effective valley degeneracy (N_v^*), b) density of states (m^*_S), and conductivity effective mass (m^*_c), as well as the near-edge band structure including the marked and labeled band extrema. The valence and conduction band edge is shown in a,b, as a dashed line (anything between the dashed lines exists within the band gap). c) The computed electronic structure of PbTe with the extrema indicated.

7.3c - High Throughput Computation

The thermoelectric quality factor (*B*) which scales both the maximum carrier concentration dependent power factor and *zT* is well-known for the acoustic phonon scattering regime (Equation 2-6, the most commonly observed experimental scattering mechanism for thermoelectric materials at T>300 K) as outlined in the introduction of this chapter. While acoustic phonon scattering is the most common scattering mechanism for high temperature materials, constant scattering time (CRTA) is simpler to implement from a computational perspective (in Boltztrap) and is very commonly used to gauge a material's thermoelectric performance directly from *ab-initio* calculations. Here, the thermoelectric quality factor can be derived as:

$$\mathbf{B}_{\tau=\mathbf{constant}} = \frac{\mathbf{k}_{\mathbf{B}}^{7/2}\mathbf{2}^{3/2}}{\mathbf{3}\pi^{2}\hbar^{3}}\left(\frac{\mathbf{m}_{\mathbf{d}}^{*\,3/2}}{\mathbf{m}_{\mathbf{c}}^{*}}\right)\frac{\tau}{\kappa_{\mathbf{L}}}\mathbf{T}^{5/2} = \frac{\mathbf{k}_{\mathbf{B}}^{7/2}\mathbf{2}^{3/2}}{\mathbf{3}\pi^{2}\hbar^{3}}\frac{(\mathbf{N}_{\mathbf{v}}^{*}\mathbf{K}^{*})^{2/3}\mathbf{m}_{\mathbf{d}}^{*\,1/2}\tau}{\kappa_{\mathbf{L}}}\mathbf{T}^{5/2} \qquad \text{Equation 7-6}$$

For constant scattering time, $B_{\tau=constant} \propto (N_v^* K^*)^{2/3} m_d^{*\,1/2}$, indicating that systems with higher effective mass will lead to a higher predicted power factor and *zT* from Boltztrap calculations. The result is qualitatively different than B_{APS}, which yields an inverse effective mass dependence proportional to $\frac{N_v}{m_c^*}$ (or $\frac{(N_v^* K^*)}{m_b^*} = \frac{N_v^*}{m_c^*}$); this implies that light mass, high mobility materials with high valley degeneracy are the best for thermoelectrics [106]. We propose the "Fermi surface complexity factor" $(N_v^* K^*)$ as a better predictor of thermoelectric performance than Boltztrap computed Seebeck coefficient or power factor because it scales directly with thermoelectric quality factor in both the APS and CRTA cases. Further, $(N_v^* K^*)$ links the desired thermoelectric quantities (*B*, conductivity, Seebeck coefficient) directly to the computed electronic band structure, specifically through the valley degeneracy and effective anisotropy. Also, it captures the effects that complex Fermi surfaces can have on the thermoelectric performance through K^*.

The vast electronic structure database constructed through the Materials Project allows for large-scale screening of thermoelectric materials using Boltztrap (using the CRTA). Figure 7-6 shows the correlation between $(N_v^* K^*)$ and the calculated maximum (Fermi level-dependent) power factor for the large group of compounds (~2300 isotropic compounds) assuming a specific scattering time ($\tau = 1 \times 10^{-14}\ s$) at 600 K. We can see a good correlation between the calculated Fermi surface complexity factor and the maximum attainable power factor; this is expected since the quality factor for constant relaxation time is expected to scale as $B_{\tau=constant} \propto (N_v^* K^*)^{2/3}$. The line on Figure 7-6 indicates a 2/3 power slope, which is expressed well for the dataset.

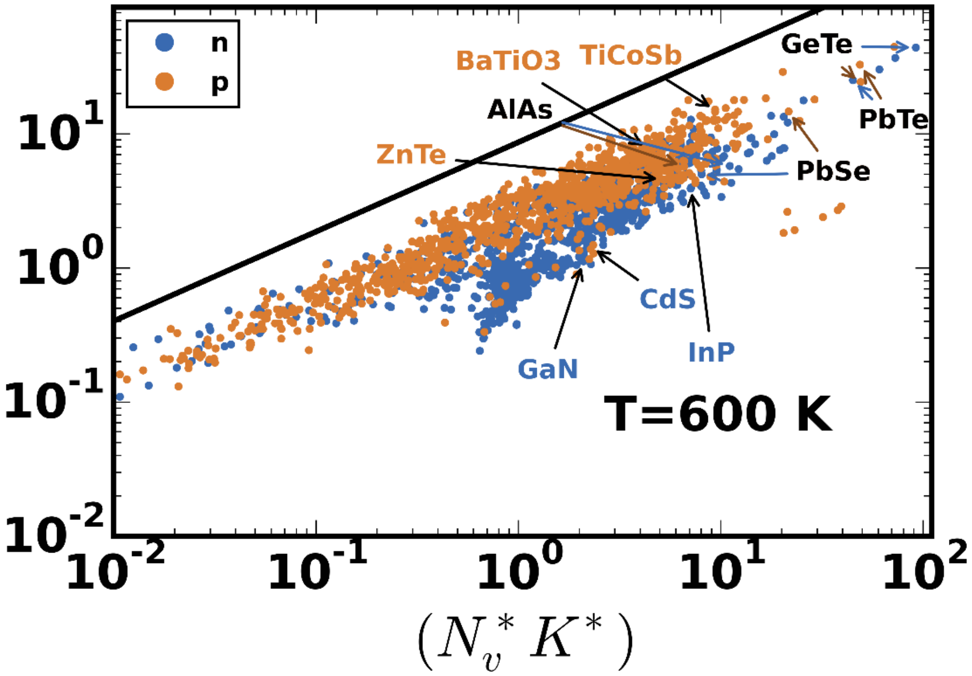

Figure 7-6: Maximum power factor for ~2300 cubic compounds plotted as a function of the Fermi surface complexity factor (evalulated at the Fermi level that yields the maximum power factor) at T=600 K).

7.4 - Conclusions

I have introduced and examined the Fermi surface complexity factor $(N_v^*K^*)$ and its relation to the valley degeneracy. I have conceptually separated the components of the Fermi surface complexity factor into the effective valley degeneracy (N_v^*) and the effective anisotropy factor (K^*) by examining several known material systems (III-V and IV-VI semiconductors). We infer that the valence bands in both the III-V and IV-VI have a larger than expected Fermi surface complexity factor which exceeds the expected degeneracy, likely as a result of non-trivial topological features which enhance *K**. We have also shown that $(N_v^*K^*)$ should not depend on the particular scattering time assumptions, making results from it more consistent with experimental observations that tend to exhibit acoustic phonon scattering. We have analyzed the maximum power factors and *zT*'s for a large set (>2300) cubic compounds from the Materials Project to show that $(N_v^*K^*)$ seems to correlate well with both the maximum power factor (and also the quality factor). Correlation of experiments and theory is of critical importance both for validating theoretical calculations and for interpretation of experimental results. High throughput Boltztrap calculations have the potential for high-impact in the community for their predictive power, by understanding these calculated properties in the context of band engineering they can have an even broader use.

7.5 - Methods

Ab-initio computations in this section are from the Materials Project database [368] and use DFT within the generalized gradient approximation (GGA) in the Perdew-Burke-Ernzheroff (PBE) formulation [336]. Calculations were performed using the VASP software and projector augmented-wave pseudopotentials [369]. Bolztrap calculations were computed using the open-source code [30] along with analysis and plotting software from pymatgen [370].

When considering the IV-VI materials, all materials are calculated in their most stable configuration (unit cells relaxed in the rock salt—space group 225—structure). In PbTe in particular, the calculated band gap from GGA is much larger than the experimental band gap (~0.3 eV at 300K for PbTe [126]). Literature suggests that if spin-orbit coupling (SOC) was considered, the gap shrinks to near the experimental values [85]; however, we have neglected SOC contributions in this work. Regardless, because Boltztrap calculations are done at T=300 K, the band gap itself should not greatly affect the results; the results would be affected most for Fermi levels within the band gap, which is not where the interesting valley degeneracy effects occur. The effect is also present in PbSe and PbS, although to a lesser extent.

Specifically considering the III-V materials, we have assumed that each is crystallized in the zinc-blende crystal structure (Space group 216), even though the nitrides are more stable in the hexagonal Wurtzite structure [57, 371]. We also should point out that standard DFT calculations do not always provide the correct ordering of the conduction band minima (at the L, X, Γ, and K points) [57, 372, 373], but for simplicity and to illustrate the effectiveness of the Fermi surface complexity factor, we have assumed that these are the correct band structures and have interpreted all of the results with that assumption in mind (Wang et al. suggest the use of the modified Becke-Johnson semilocal exchange for values that more accurately represent experimental values [373, 374]). Further, while the valence band structure is similar among all of the III-V materials (triply degenerate at the Γ point in the absence of spin-orbit coupling), we realize that if we had included spin-orbit coupling that one of the bands (the one with the intermediate effective mass) would split off from the other two (with the energy offset increasing with the mass of the elements).

High throughput calculations of the Fermi surface complexity factor are analyzed in Figure 7-6, but we limit the analysis to cubic compounds (maximum deviation in the eigenvalues of the power factor tensor of less than 3% along any direction) and those with a maximum optimum carrier concentration less than $1 \times 10^{22}\ cm^{-3}$. We also chose to remove compounds that were not particularly stable or those that were metallic (we required that the energy above the convex hull be <0.05 eV, and that the band gap be >0.03 eV).

Chapter 8: Conclusions and Future Directions

In this work, I have shown several examples where band engineering concepts have been utilized to understand and optimize the thermoelectric properties over a range of material systems. Band structure characterization using optical properties, electronic/thermoelectric properties (as a function of doping), and ab-initio computed band structures provide detailed description of the electronic band structure in three important material systems.

First, in the lead chalcogenides I have used optical and *ab-initio* techniques to characterize the temperature-dependent band gap. I conclude that the gap increase is due to both lattice expansion and electron-phonon interaction, and that a convergence temperature around 700 K is consistent with optical and *ab-initio* results. This realization that the convergence temperature is larger than previously believed is important and will likely lead to more well-refined temperature-dependent transport models, and it can be used to help distinguish the effectiveness of different band engineering strategies in these materials.

Second, in the half Heusler (ZrNiSn) system I have considered several estimates for the band gap using optical, electronic, and *ab-initio* techniques. The optical absorption edge results allow us to obtain the true band gap value (0.13 eV), which we can use to resolve the weighted mobility ratio (A=5) between electrons and holes. I explain the excellent high temperature zT in n-type ZrNiSn by suppressed bipolar effects due to the low weighted mobility for holes in the system. I develop a chart to quickly determine the deviation of the Goldsmid Sharp band gap as the A value is varied. Future work can apply what was learned from the large A value in ZrNiSn, particularly with respect to how it affects the estimate of the Goldsmid Sharp band gap, to rank bipolar suppression strategies in other classes of materials.

$CoSb_3$ is an important thermoelectric material with excellent thermoelectric properties upon filling of the internal voids. In this thesis, I have shown a series of Yb-filled $CoSb_3$ skutterudite samples, which displayed a rapidly rising carrier concentration dependent effective mass (as obtained from the Seebeck coefficient). I have explained this rise in the context of multiple conduction band transport, which is supported by optical results that show two distinct absorption edges and *ab-initio* electronic structure calculations that show a high valley degeneracy (N_v=12) secondary conduction band. Further, these bands are found to shift together with temperature, resulting in convergence for T>700 K. While skutterudites are not often explored in detail for their electronic structure, this work suggests that the high degeneracy secondary conduction band plays a critical role in the electronic transport in filled $CoSb_3$, particularly at high temperature. Future directions from this work will likely involve engineering the conduction band structure (possibly through alloying); $CoSb_3$ shares many similar traits to other IV-VI materials where band engineering strategies have led to successful zT improvements.

Lastly, the Fermi surface complexity factor ($N_v^* K^*$), as computed from Boltztrap results (and effective mass estimates), is a simple way to obtain an estimate of the Fermi-level dependent effective valley degeneracy (N_v^*). Further, complex Fermi surface features (such as threads or tubes) also manifest themselves by increasing the effective anisotropy factor (K^*). This section provides an alternative to traditional presentation of computed Boltztrap data that is independent of the assumed scattering mechanism and directly reflects the electronic structure. I believe that this alternative is a better way to compare materials from a band structure perspective in a high-throughput sense.

While optical properties measurements in the thermoelectrics community are not commonplace, this thesis provides several important examples where they are critical in determining the band positions. By combining electronic, optical, and *ab-initio* computed properties, multiple band effects can be identified and ultimately utilized to improve the thermoelectric properties. Band engineering and multiple bands are a viable route towards improving *zT*, and future material enhancements will likely utilize these features.

References

1. Salvador, J.R., J.Y. Cho, Z. Ye, J.E. Moczygemba, A.J. Thompson, J.W. Sharp, J.D. König, R. Maloney, T. Thompson, J. Sakamoto, H. Wang, A.A. Wereszczak, and G.P. Meisner, *Thermal to Electrical Energy Conversion of Skutterudite-Based Thermoelectric Modules.* Journal of Electronic Materials, 2013. **42**(7): p. 1389-1399.
2. Liebl, J., S. Neugebauer, A. Eder, M. Linde, B. Mazar, and W. Stütz, *The thermoelectric generator from BMW is making use of waste heat.* MTZ Worldwide, 2009. **70**(4): p. 4-11.
3. Kristiansen, N.R. and H.K. Nielsen, *Potential for Usage of Thermoelectric Generators on Ships.* Journal of Electronic Materials, 2010. **39**(9): p. 1746-1749.
4. Kristiansen, N.R., G.J. Snyder, H.K. Nielsen, and L. Rosendahl, *Waste Heat Recovery from a Marine Waste Incinerator Using a Thermoelectric Generator.* Journal of Electronic Materials, 2012. **41**(6): p. 1024-1029.
5. Kaibe, H., K. Takeshi, F. Schinichi, K. Makino, and H. Hirokuni, *Recovery of Plant Waste Heat by a Thermoelectric Generating System.* Komatsu Technical Report, 2011. **57**(164): p. 26-30.
6. Bell, L.E., *Cooling, heating, generating power, and recovering waste heat with thermoelectric systems.* Science, 2008. **321**(5895): p. 1457-1461.
7. Carstens, T.A., M.L. Corradini, J.P. Blanchard, and M. Zhenqiang, *Thermoelectric Powered Wireless Sensors for Spent Fuel Monitoring.* Nuclear Science, IEEE Transactions on, 2012. **59**(4): p. 1408-1413.
8. Prilepo, Y.P., A.A. Pustovalov, V.V. Sinyavskiy, N.M. Sudak, and O.B. Yatsenko, *Problems of designing radioisotope thermoelectric power generators with a service life of decades for use in outer space exploration vehicles.* Thermal Engineering, 2012. **59**(13): p. 981-983.
9. Thomas, S., D. Leonard, H. John, and Z. June, *NASA's Radioisotope Power Systems and Technologies - A Forward Look*, in *9th Annual International Energy Conversion Engineering Conference*. 2011, American Institute of Aeronautics and Astronautics.
10. Popoola, L., A. Grema, G. Latinwo, B. Gutti, and A. Balogun, *Corrosion problems during oil and gas production and its mitigation.* International Journal of Industrial Chemistry, 2013. **4**(1): p. 35.
11. Minnich, A.J., M.S. Dresselhaus, Z.F. Ren, and G. Chen, *Bulk nanostructured thermoelectric materials: current research and future prospects.* Energy & Environmental Science, 2009. **2**(5): p. 466-479.
12. Zhao, L.D., J.Q. He, S.Q. Hao, C.I. Wu, T.P. Hogan, C. Wolverton, V.P. Dravid, and M.G. Kanatzidis, *Raising the Thermoelectric Performance of p-Type PbS with Endotaxial Nanostructuring and Valence-Band Offset Engineering Using CdS and ZnS.* Journal of the American Chemical Society, 2012. **134**(39): p. 16327-16336.
13. Kanatzidis, M.G., S. Johnsen, J.Q. He, J. Androulakis, V.P. Dravid, I. Todorov, and D.Y. Chung, *Nanostructures Boost the Thermoelectric Performance of PbS.* Journal of the American Chemical Society, 2011. **133**(10): p. 3460-3470.
14. Biswas, K., J.Q. He, I.D. Blum, C.I. Wu, T.P. Hogan, D.N. Seidman, V.P. Dravid, and M.G. Kanatzidis, *High-performance bulk thermoelectrics with all-scale hierarchical architectures.* Nature, 2012. **489**(7416): p. 414-418.
15. Pei, Y.Z., A.D. LaLonde, N.A. Heinz, X.Y. Shi, S. Iwanaga, H. Wang, L.D. Chen, and G.J. Snyder, *Stabilizing the Optimal Carrier Concentration for High Thermoelectric Efficiency.* Advanced Materials, 2011. **23**(47): p. 5674-5678.

16. Pei, Y.Z., X.Y. Shi, A. LaLonde, H. Wang, L.D. Chen, and G.J. Snyder, *Convergence of electronic bands for high performance bulk thermoelectrics.* Nature, 2011. **473**(7345): p. 66-69.
17. Pei, Y., H. Wang, Z.M. Gibbs, A.D. LaLonde, and G.J. Snyder, *Thermopower enhancement in Pb1-xMnxTe alloys and its effect on thermoelectric efficiency.* NPG Asia Mater, 2012. **4**: p. e28.
18. Pei, Y., H. Wang, and G.J. Snyder, *Band Engineering of Thermoelectric Materials.* Advanced Materials, 2012. **24**(46): p. 6125-6135.
19. Yamini, S.A., H. Wang, Z.M. Gibbs, Y.Z. Pei, S.X. Dou, and G.J. Snyder, *Chemical composition tuning in quaternary p-type Pb-chalcogenides - a promising strategy for enhanced thermoelectric performance.* Physical Chemistry Chemical Physics, 2014. **16**(5): p. 1835-1840.
20. Biswas, K., J.Q. He, G.Y. Wang, S.H. Lo, C. Uher, V.P. Dravid, and M.G. Kanatzidis, *High thermoelectric figure of merit in nanostructured p-type PbTe-MTe (M = Ca, Ba).* Energy & Environmental Science, 2011. **4**(11): p. 4675-4684.
21. Zhao, L.D., H.J. Wu, S.Q. Hao, C.I. Wu, X.Y. Zhou, K. Biswas, J.Q. He, T.P. Hogan, C. Uher, C. Wolverton, V.P. Dravid, and M.G. Kanatzidis, *All-scale hierarchical thermoelectrics: MgTe in PbTe facilitates valence band convergence and suppresses bipolar thermal transport for high performance.* Energy & Environmental Science, 2013. **6**(11): p. 3346-3355.
22. Fu, C., T. Zhu, Y. Pei, H. Xie, H. Wang, G.J. Snyder, Y. Liu, Y. Liu, and X. Zhao, *High Band Degeneracy Contributes to High Thermoelectric Performance in p-Type Half-Heusler Compounds.* Advanced Energy Materials, 2014. **4**(18).
23. Chen, S. and Z. Ren, *Recent progress of half-Heusler for moderate temperature thermoelectric applications.* Materials Today, 2013. **16**(10): p. 387-395.
24. May, A.F. and G.J. Snyder, *Introduction to Modeling Thermoelectric Transport at High Temperatures*, in *CRC Handbook of Thermoelectrics*, D.M. Rowe, Editor. 2011, CRC Press.
25. Wang, H., Z.M. Gibbs, Y. Takagiwa, and G.J. Snyder, *Tuning bands of PbSe for better thermoelectric efficiency.* Energy & Environmental Science, 2014. **7**: p. 804-811.
26. Liu, W., X. Tan, K. Yin, H. Liu, X. Tang, J. Shi, Q. Zhang, and C. Uher, *Convergence of Conduction Bands as a Means of Enhancing Thermoelectric Performance of n-Type Mg2Si1-xSnx Solid Solutions.* Physical Review Letters, 2012. **108**(16): p. 166601.
27. Tauber, R.N., A.A. Machonis, and I.B. Cadoff, *Thermal and Optical Energy Gaps in Pbte.* Journal of Applied Physics, 1966. **37**(13): p. 4855-4860.
28. LaLonde, A.D., Y.Z. Pei, and G.J. Snyder, *Reevaluation of PbTe(1-x)I(x) as high performance n-type thermoelectric material.* Energy & Environmental Science, 2011. **4**(6): p. 2090-2096.
29. Jain, A., S.P. Ong, G. Hautier, W. Chen, W.D. Richards, S. Dacek, S. Cholia, D. Gunter, D. Skinner, G. Ceder, and K.A. Persson, *Commentary: The Materials Project: A materials genome approach to accelerating materials innovation.* APL Materials, 2013. **1**(1): p. 011002.
30. Madsen, G.K.H. and D.J. Singh, *BoltzTraP. A code for calculating band-structure dependent quantities.* Computer Physics Communications, 2006. **175**(1): p. 67-71.
31. Borup, K.A., E.S. Toberer, L.D. Zoltan, G. Nakatsukasa, M. Errico, J.-P. Fleurial, B.B. Iversen, and G.J. Snyder, *Measurement of the electrical resistivity and Hall coefficient at high temperatures.* Review of Scientific Instruments, 2012. **83**(12): p. 123902.

32. Iwanaga, S., E.S. Toberer, A. LaLonde, and G.J. Snyder, *A high temperature apparatus for measurement of the Seebeck coefficient.* Review of Scientific Instruments, 2011. **82**(6).
33. Wang, H., W.D. Porter, H. Bottner, J. Konig, L. Chen, S. Bai, T.M. Tritt, A. Mayolett, C. Smith, F. Harris, J. Sharp, J. Lo, H. Keinke, and L.I. Kiss, *International Round-Robin Testing of Bulk Thermoelectrics.* ORNL/TM-2011/393, 2011.
34. Pei, Y., A. LaLonde, S. Iwanaga, and G.J. Snyder, *High thermoelectric figure of merit in heavy hole dominated PbTe.* Energy & Environmental Science, 2011. **4**(6): p. 2085-2089.
35. Wendlandt, W. and H. Hecht, *Reflectance Spectroscopy*. Chemical Analysis, ed. P.J. Elving and I.M. Kolthoff. 1966, New York: Interscience Publishers.
36. Gibson, A.F., *The Absorption Spectra of Single Crystals of Lead Sulphide, Selenide and Telluride.* Proceedings of the Physical Society of London Section B, 1952. **65**(389): p. 378-388.
37. Scanlon, W.W., *Recent Advances in the Optical and Electronic Properties of Pbs, Pbse, Pbte and Their Alloys.* Journal of Physics and Chemistry of Solids, 1959. **8**: p. 423-428.
38. Riedl, H.R., *Free-Carrier Absorption in P-Type Pbte.* Physical Review, 1962. **127**(1): p. 162-166.
39. Prakash, V., *The optical absorption edge in the lead salts and its variation with temperature and pressure*. Division of Engineering: Applied Physics1967, Harvard University.
40. Nikolic, P.M., *Optical Energy Gaps Lattice Parameters and Solubility Limits of Solid Solutions of Snse and Gese in Pbte and Gese in Snte.* British Journal of Applied Physics, 1965. **16**(8): p. 1075-1079.
41. Nikolic, P.M., *Solid Solution of Lead-Germanium Chalcogenide Alloys and Some of Their Optical Properties.* Journal of Physics D-Applied Physics, 1969. **2**(3): p. 383-&.
42. Drabkin, I.A., G.F. Zakharyugina, and I.V. Nelson, *Optical Width of the Forbidden Band of Pb1-xMnxTe Solid Solutions.* Soviet Physics Semiconductors-Ussr, 1971. **5**(2): p. 277-278.
43. Yu, P.Y. and M. Cardona, *Fundamentals of Semiconductors*. 1996, Berlin: Springer.
44. Basu, P.K., *Theory of Optical Processes in Semiconductors*. Series on Semiconductor Science and Technology, ed. H. Kamimura, R.J. Nicholas, and R.H. Williams. 1997: Oxford University Press. 447.
45. Seeger, K., *Semiconductor Physics: An Introduction*. 6th ed, ed. Lotsch. 1997, Hedelberg: Springer.
46. Tauc, J., *Optical properties and electronic structure of amorphous Ge and Si.* Materials Research Bulletin, 1968. **3**(1): p. 37-46.
47. Schmid, P.E., *Optical-Absorption in Heavily Doped Silicon.* Physical Review B, 1981. **23**(10): p. 5531-5536.
48. Gnutzman, U. and K. Clauseck, *Theory of Direct Optical-Transitions in an Optical Indirect Semiconductor with a Superlattice Structure.* Applied Physics, 1974. **3**(1): p. 9-14.
49. Nolas, G.S., J. Sharp, and H.J. Goldsmid, *Thermoelectrics: Basic Principles and New Materials Developments*. Springer Series in Materials Science, ed. R. Hull, et al. 2001, Dallas: Springer.
50. Gibbs, Z.M., H.-S. Kim, H. Wang, and G.J. Snyder, *Band gap estimation from temperature dependent Seebeck measurement—Deviations from the 2e|S|maxTmax relation.* Applied Physics Letters, 2015. **106**(2): p. 022112.

51. Goldsmid, H.J. and J.W. Sharp, *Estimation of the thermal band gap of a semiconductor from Seebeck measurements.* Journal of Electronic Materials, 1999. **28**(7): p. 869-872.
52. Schmitt, J., Z.M. Gibbs, G.J. Snyder, and C. Felser, *Resolving the True Band Gap of ZrNiSn Half-Heusler Thermoelectric Materials.* Materials Horizons, 2015. **2**: p. 68-75.
53. May, A.F., E.S. Toberer, A. Saramat, and G.J. Snyder, *Characterization and analysis of thermoelectric transport in n-type Ba8Ga16-xGe30+x.* Physical Review B, 2009. **80**(12): p. 125205.
54. May, A.F., *High-Temperature Transport in Lanthanum Telluride and Other Modern Thermoelectric Materials*. Chemical Engineering. Doctor of Philosophy. 2010, California Institute of Technology: Pasadena, CA.
55. Dresselhaus, G., A.F. Kip, and C. Kittel, *Cyclotron Resonance of Electrons and Holes in Silicon and Germanium Crystals.* Physical Review, 1955. **98**(2): p. 368-384.
56. Dexter, R.N., H.J. Zeiger, and B. Lax, *Cyclotron Resonance Experiments in Silicon and Germanium.* Physical Review, 1956. **104**(3): p. 637-644.
57. Vurgaftman, I., J.R. Meyer, and L.R. Ram-Mohan, *Band parameters for III–V compound semiconductors and their alloys.* Journal of Applied Physics, 2001. **89**(11): p. 5815-5875.
58. Ravich, Y.I., B.A. Efimova, and I.A. Smirnov, *Semiconducting Lead Chalcogenides* Monographs In Semiconductor Physics, ed. L.S. Stil'bans. Vol. 5. 1970, New York-London: Plenum Press. 377.
59. Chen, X., D. Parker, and D.J. Singh, *Importance of non-parabolic band effects in the thermoelectric properties of semiconductors.* Sci. Rep., 2013. **3**: p. 3168.
60. Nimtz, G. and B. Schlicht, *Narrow-Gap Lead Salts.* Springer Tracts in Modern Physics, 1983. **98**: p. 1-117.
61. Lerner, L.S., *Shubnikov-de Haas Effect in Bismuth.* Physical Review, 1962. **127**(5): p. 1480-1492.
62. Putley, E.H., *Galvano- and thermo-magnetic coefficients for a multi-band conductor.* Journal of Physics C: Solid State Physics, 1975. **8**(12): p. 1837.
63. Kane, E.O., *Band Structure of Indium Antimonide.* Journal of Physics and Chemistry of Solids, 1957. **1**(4): p. 249-261.
64. Zawadzki, W., *Electron transport phenomena in small-gap semiconductors.* Advances in Physics, 1974. **23**(3): p. 435-522.
65. Wang, H., Y. Pei, A.D. LaLonde, and G.J. Snyder, *Weak electron–phonon coupling contributing to high thermoelectric performance in n-type PbSe.* Proceedings of the National Academy of Sciences, 2012. **109**(25): p. 9705-9709.
66. LaLonde, A.D., T. Ikeda, and G.J. Snyder, *Rapid consolidation of powdered materials by induction hot pressing.* Review of Scientific Instruments, 2011. **82**(2): p. 025104.
67. Aw, S.E., H.S. Tan, and C.K. Ong, *Optical-Absorption Measurements of Band-Gap Shrinkage in Moderately and Heavily Doped Silicon.* Journal of Physics-Condensed Matter, 1991. **3**(42): p. 8213-8223.
68. Luo, H.T., W.Z. Shen, Y.H. Zhang, and H.F. Yang, *Study of band gap narrowing effect in n-GaAs for the application of far-infrared detection.* Physica B-Condensed Matter, 2002. **324**(1-4): p. 379-386.
69. Kanatzidis, M.G., K. Ahn, C.P. Li, and C. Uher, *Improvement in the Thermoelectric Figure of Merit by La/Ag Cosubstitution in PbTe.* Chemistry of Materials, 2009. **21**(7): p. 1361-1367.

70. Li, Y.P., Q.S. Meng, Y. Deng, H. Zhou, Y.L. Gao, Y.Y. Li, J.F. Yang, and J.L. Cui, *High thermoelectric performance of solid solutions CuGa1-xInxTe2 (x=0-1.0).* Applied Physics Letters, 2012. **100**(23): p. 231903, 1-4.
71. Lyden, H.A., *Measurement of Conductivity Effective Mass in Semiconductors Using Infrared Reflection.* Physical Review a-General Physics, 1964. **134**(4A): p. 1106-1112.
72. Kaiser, W. and H.Y. Fan, *Infrared Absorption of Indium Antimonide.* Physical Review, 1955. **98**(4): p. 966-968.
73. Spitzer, W.G. and H.Y. Fan, *Determination of Optical Constants and Carrier Effective Mass of Semiconductors.* Physical Review, 1957. **106**(5): p. 882-890.
74. Stern, F., *Optical Properties of Lead-Salt and Iii-V Semiconductors.* Journal of Applied Physics, 1961. **32**: p. 2166-2173.
75. Palik, E.D., D.L. Mitchell, and J.N. Zemel, *Magneto-Optical Studies of Band Structure of Pbs.* Physical Review, 1964. **135**(3A): p. 763-778.
76. Drabkin, I.A., Y.Y. Eliseeva, and I.V. Nelson, *Fundamental Absorption Edge of Heavily Doped n-type PbTe.* soviet Physics Semiconductors-Ussr, 1975. **8**(7): p. 900.
77. N. Piccoli, J.M.B., M. Balkanski *Optical Constants and Band Gap of PbTe from thin film studies between 25 and 300K.* Journal of physical chemistry of Solids, 1974. **35**: p. 971-977.
78. Charache, G.W., D.M. DePoy, J.E. Raynolds, P.F. Baldasaro, K.E. Miyano, T. Holden, F.H. Pollak, P.R. Sharps, M.L. Timmons, C.B. Geller, W. Mannstadt, R. Asahi, A.J. Freeman, and W. Wolf, *Moss-Burstein and plasma reflection characteristics of heavily doped n-type InxGa1-xAs and InPyAs1-y.* Journal of Applied Physics, 1999. **86**(1): p. 452-458.
79. Bugajski, M. and W. Lewandowski, *Concentration-Dependent Absorption and Photoluminescence of N-Type Inp.* Journal of Applied Physics, 1985. **57**(2): p. 521-530.
80. Vanoverstraeten, R.J. and R.P. Mertens, *Heavy Doping Effects in Silicon.* Solid-State Electronics, 1987. **30**(11): p. 1077-1087.
81. Lanir, M., A.H. Lockwood, and H. Levinstein, *Absorption-Edge Shift in Lead-Tin Telluride.* Solid State Communications, 1978. **27**(3): p. 313-316.
82. Herrmann, K.H., V. Melzer, and U. Muller, *Interband and Intraband Contributions to Refractive-Index and Dispersion in Narrow-Gap Semiconductors.* Infrared Physics, 1993. **34**(2): p. 117-136.
83. Husain, M., S. Kumar, M.A.M. Khan, and M. Zulfequar, *Optical, structural and electrical investigations on PbTe1-xSx alloys.* Journal of Materials Science, 2007. **42**(1): p. 363-367.
84. Wei, S.H. and A. Zunger, *Electronic and structural anomalies in lead chalcogenides.* Physical Review B, 1997. **55**(20): p. 13605-13610.
85. Hummer, K., A. Gruneis, and G. Kresse, *Structural and electronic properties of lead chalcogenides from first principles.* Physical Review B, 2007. **75**(19): p. 195211, 1-9.
86. Lusakowski, A., P. Boguslawski, and T. Radzynski, *Calculated electronic structure of Pb1-xMnxTe (0 <= x < 11%): The role of L and Sigma valence band maxima.* Physical Review B, 2011. **83**(11): p. 115206, 1-7.
87. Baleva, M., T. Georgiev, and G. Lashkarev, *On the Temperature-Dependence of the Energy-Gap in Pbse and Pbte.* Journal of Physics-Condensed Matter, 1990. **2**(13): p. 2935-2940.

88. Delaire, O., J. Ma, K. Marty, A.F. May, M.A. McGuire, M.H. Du, D.J. Singh, A. Podlesnyak, G. Ehlers, M.D. Lumsden, and B.C. Sales, *Giant anharmonic phonon scattering in PbTe.* Nature Materials, 2011. **10**(8): p. 614-619.
89. Dash, W.C. and R. Newman, *Intrinsic Optical Absorption in Single-Crystal Germanium and Silicon at 77-Degrees-K and 300-Degrees-K.* Physical Review, 1955. **99**(4): p. 1151-1155.
90. Veis, A.N. and Y.I. Ukhanov, *Study of Absorption-Coefficient of P-Type Pbte.* Soviet Physics Semiconductors-Ussr, 1976. **10**(7): p. 780-783.
91. Ekuma, C.E., D.J. Singh, J. Moreno, and M. Jarrell, *Optical properties of PbTe and PbSe.* Physical Review B, 2012. **85**(8): p. 085205, 1-7.
92. Huang, H.C., S. Yee, and M. Soma, *The Carrier Effects on the Change of Refractive-Index for N-Type Gaas at Lambda = 1.06, 1.3, and 1.55-Mu-M.* Journal of Applied Physics, 1990. **67**(3): p. 1497-1503.
93. Munoz, M., F.H. Pollak, M. Kahn, D. Ritter, L. Kronik, and G.M. Cohen, *Burstein-Moss shift of n-doped In0.53Ga0.47As/InP.* Physical Review B, 2001. **63**(23): p. 233302.
94. Kudman, I. and T. Seidel, *Absorption Edge in Degenerate P-Type Gaas.* Journal of Applied Physics, 1962. **33**(3): p. 771-773.
95. Gibbs, Z.M., A. LaLonde, and G.J. Snyder, *Optical band gap and the Burstein–Moss effect in iodine doped PbTe using diffuse reflectance infrared Fourier transform spectroscopy.* New Journal of Physics, 2013. **15**(7): p. 075020.
96. Mahan, G.D., *Energy-Gap in Si and Ge - Impurity Dependence.* Journal of Applied Physics, 1980. **51**(5): p. 2634-2646.
97. Berggren, K.F. and B.E. Sernelius, *Band-Gap Narrowing in Heavily Doped Many-Valley Semiconductors.* Physical Review B, 1981. **24**(4): p. 1971-1986.
98. Pankove, J.I. and P. Aigrain, *Optical Absorption of Arsenic-Doped Degenerate Germanium.* Physical Review, 1962. **126**(3): p. 956-962.
99. Casey, H.C. and F. Stern, *Concentration-Dependent Absorption and Spontaneous Emission of Heavily Doped Gaas.* Journal of Applied Physics, 1976. **47**(2): p. 631-643.
100. Lu, J.G., S. Fujita, T. Kawaharamura, H. Nishinaka, Y. Kamada, T. Ohshima, Z.Z. Ye, Y.J. Zeng, Y.Z. Zhang, L.P. Zhu, H.P. He, and B.H. Zhao, *Carrier concentration dependence of band gap shift in n-type ZnO : Al films.* Journal of Applied Physics, 2007. **101**(8): p. 083705, 1-7.
101. Mahan, G.D., *Condensed Matter in a Nutshell*. 2010: Princeton University Press.
102. Kalt, H. and M. Rinker, *Band-Gap Renormalization in Semiconductors with Multiple Inequivalent Valleys.* Physical Review B, 1992. **45**(3): p. 1139-1154.
103. Khoklov, D. and Y.I. Ravich, *Lead Chalcogenides: Physics Applications*. Optoelectronic Properties of Semiconductors and Superlattices, ed. M.O. Manasreh. Vol. 18. 2003, New York: Taylor & Francis.
104. Lee, M.S. and S.D. Mahanti, *Validity of the rigid band approximation in the study of the thermopower of narrow band gap semiconductors.* Physical Review B, 2012. **85**(16): p. 165149, 1-8.
105. Takagiwa, Y., Y.Z. Pei, G. Pomrehn, and G.J. Snyder, *Validity of rigid band approximation of PbTe thermoelectric materials.* Apl Materials, 2013. **1**(1): p. 011101.
106. Pei, Y., A.D. LaLonde, H. Wang, and G.J. Snyder, *Low effective mass leading to high thermoelectric performance.* Energy & Environmental Science, 2012. **5**(7): p. 7963-7969.

107. White, D.R. and R.L. White, *Isoconversion Effective Activation Energy Profiles by Variable Temperature Diffuse Reflection Infrared Spectroscopy.* Applied Spectroscopy, 2008. **62**(1): p. 116-120.
108. White, R.L., *Variable Temperature Infrared Study of Copper Sulfate Pentahydrate Dehydration.* Thermochimica Acta, 2012. **528**: p. 58-62.
109. Boldish, S.I. and W.B. White, *Optical Band Gaps of Selected Ternary Sulfide Minerals.* American Mineralogist, 1998. **83**: p. 865-871.
110. LaLonde, A.D., Y. Pei, H. Wang, and G. Jeffrey Snyder, *Lead telluride alloy thermoelectrics.* Materials Today, 2011. **14**(11): p. 526-532.
111. Pei, Y., A.D. LaLonde, N.A. Heinz, and G.J. Snyder, *High Thermoelectric Figure of Merit in PbTe Alloys Demonstrated in PbTe-CdTe.* Advanced Energy Materials, 2012. **2**(6): p. 670-675.
112. Biswas, K., J. He, I.D. Blum, C.-I. Wu, T.P. Hogan, D.N. Seidman, V.P. Dravid, and M.G. Kanatzidis, *High-performance bulk thermoelectrics with all-scale hierarchical architectures.* Nature, 2012. **489**(7416): p. 414-418.
113. Kanatzidis, M.G., *Nanostructured Thermoelectrics: The New Paradigm?†.* Chemistry of Materials, 2010. **22**(3): p. 648-659.
114. Snyder, G.J. and E.S. Toberer, *Complex thermoelectric materials.* Nature Materials, 2008. **7**(2): p. 105-114.
115. Crocker, A.J. and L.M. Rogers, *Valence Band Structure Of PbTe.* Journal De Physique, 1968. **11-12**(29): p. C4 - 129.
116. Veis, A.N., M.N. Vinogradova, N.L. Ivanchukova, and Y.I. Ukhanov, *Investigation of Infrared Reflection from P-Type Pbte.* Soviet Physics Semiconductors-Ussr, 1975. **8**(11): p. 1461-1462.
117. Singh, D.J., *Doping-dependent thermopower of PbTe from Boltzmann transport calculations.* Physical Review B, 2010. **81**(19): p. 195217, 1-6.
118. Ahmad, S., S.D. Mahanti, K. Hoang, and M.G. Kanatzidis, *Ab initio studies of the electronic structure of defects in PbTe.* Physical Review B, 2006. **74**(15): p. 155205.
119. Hoang, K. and S.D. Mahanti, *Electronic structure of Ga-, In-, and Tl-doped PbTe: A supercell study of the impurity bands.* Physical Review B, 2008. **78**(8): p. 085111, 1-8.
120. Biswas, K., J.Q. He, Q.C. Zhang, G.Y. Wang, C. Uher, V.P. Dravid, and M.G. Kanatzidis, *Strained endotaxial nanostructures with high thermoelectric figure of merit.* Nature Chemistry, 2011. **3**(2): p. 160-166.
121. Jaworski, C.M., M.D. Nielsen, H. Wang, S.N. Girard, W. Cai, W.D. Porter, M.G. Kanatzidis, and J.P. Heremans, *Valence-band structure of highly efficient p-type thermoelectric PbTe-PbS alloys.* Physical Review B, 2013. **87**(4): p. 045203, 1-10.
122. Androulakis, J., I. Todorov, D.Y. Chung, S. Ballikaya, G.Y. Wang, C. Uher, and M. Kanatzidis, *Thermoelectric enhancement in PbTe with K or Na codoping from tuning the interaction of the light- and heavy-hole valence bands.* Physical Review B, 2010. **82**(11): p. 115209, 1-8.
123. Allgaier, R.S., *Valence Bands in Lead Telluride.* Journal of Applied Physics, 1961. **32**: p. 2185-2189.
124. Allgaier, R.S. and B.B. Houston, *Hall Coefficient Behavior and 2nd Valence Band in Lead Telluride.* Journal of Applied Physics, 1966. **37**(1): p. 302-309.
125. Kolomoets, N.V., M.N. Vinogradova, and L.M. Sysoeva, *Valence Band of PbTe.* Soviet Physics Semiconductors-Ussr, 1968. **1**(8): p. 1020-1024.
126. Gibbs, Z.M., H. Kim, H. Wang, R.L. White, F. Drymiotis, M. Kaviany, and G. Jeffrey Snyder, *Temperature dependent band gap in PbX (X = S, Se, Te).* Applied Physics Letters, 2013. **103**(26): p. 262109.

127. Veis, A.N., V.I. Kaidanov, R.F. Kuteinikov, S.A. Nemov, S.A. Rudenko, and Y.I. Ukhanov, *Investigation of Structure of Valence Band of Lead Selenide.* Soviet Physics Semiconductors-Ussr, 1978. **12**(2): p. 161-163.
128. Zhou, M., Z.M. Gibbs, H. Wang, Y. Han, C. Xin, L. Li, and G.J. Snyder, *Optimization of thermoelectric efficiency in SnTe: the case for the light band.* Physical Chemistry Chemical Physics, 2014. **16**(38): p. 20741-20748.
129. Brebrick, R.F. and A.J. Strauss, *Anomalous Thermoelectric Power as Evidence for Two-Valence Bands in SnTe.* Physical Review, 1963. **131**(1): p. 104-110.
130. Rogers, L.M., *Valence band structure of SnTe.* Journal of Physics D: Applied Physics, 1968. **1**(7): p. 845.
131. Zhao, L.D., S.Q. Hao, S.H. Lo, C.I. Wu, X.Y. Zhou, Y. Lee, H. Li, K. Biswas, T.P. Hogan, C. Uher, C. Wolverton, V.P. Dravid, and M.G. Kanatzidis, *High Thermoelectric Performance via Hierarchical Compositionally Alloyed Nanostructures.* Journal of the American Chemical Society, 2013. **135**(19): p. 7364-7370.
132. Zhao, L.D., V.P. Dravid, and M.G. Kanatzidis, *The panoscopic approach to high performance thermoelectrics.* Energy & Environmental Science, 2014. **7**(1): p. 251-268.
133. Rogers, L.M., *Drift Mobility of Light-Mass Holes in Pbte Heavily Doped with Na.* Journal of Physics D-Applied Physics, 1968. **1**(8): p. 1067-1070.
134. Airapetyants, S.V., M.N. Vinogradova, I.N. Dubrovskaya, N.V. Kolomoets, and I.M. Rudnik, *Structure of Valence Band of Heavily Doped Lead Telluride.* Soviet Physics Solid State,Ussr, 1966. **8**(5): p. 1069-1072.
135. Andreev, A.A. and V.N. Radionov, *Determination of Band Structure of Lead Telluride from Measurements of Hall Effect at High Temperatures.* Soviet Physics Semiconductors-Ussr, 1967. **1**(2): p. 145-148.
136. Devyatkova, E.D. and V.A. Saakyan, *Forbidden Band Width of PbSe at High Temperatures.* Soviet Physics Solid State,Ussr, 1968. **9**(9): p. 2163-2164.
137. Vinogradova, M.N., N.V. Kolomoets, I.M. Rudnik, and L.M. Sysoeva, *Valence Band of PbSe.* Soviet Physics Semiconductors-Ussr, 1969. **3**(2): p. 231-232.
138. Gibson, A.F., *The Absorption Spectra of Solid Lead Sulphide, Selenide and Telluride.* Proceedings of the Physical Society of London Section B, 1950. **63**(370): p. 756-767.
139. Paul, W., D.A. Jones, and R.V. Jones, *Infra-Red Transmission of Galena.* Proceedings of the Physical Society of London Section B, 1951. **64**(378): p. 528-529.
140. Avery, D.G., *The optical constants of Lead Sulphide, Lead Selenide and Lead Telluride in the 0.5-3 micron region of the spectrum.* Proceedings of the Physical Society of London Section B, 1952. **64**.
141. Clark, M.A. and R.J. Cashman, *Transmission and Spectral Response of Lead Sulfide and Lead Telluride.* Physical Review, 1952. **85**(6): p. 1043-1044.
142. Moss, T.S., *Photoelectromagnetic and Photoconductive Effects in Lead Sulphide Single Crystals.* Proceedings of the Physical Society of London Section B, 1953. **66**(408): p. 993-1002.
143. Paul, W. and R.V. Jones, *Absorption Spectra of Lead Sulphide at Different Temperatures.* Proceedings of the Physical Society of London Section B, 1953. **66**(399): p. 194-200.
144. Lasser, M.E. and H. Levinstein, *Optical Properties of Lead Telluride.* Physical Review, 1954. **96**(1): p. 47-52.
145. Smith, R.A., *The electronic and optical properties of the lead sulphide group of semi-conductors.* Physica, 1954. **20**(7-12): p. 910-929.

146. Cardona, M. and D.L. Greenaway, *Optical Properties and Band Structure of Group 4-6 and Group 5 Materials.* Physical Review, 1964. **133**(6A): p. 1685-1697.
147. Dixon, J.R. and H.R. Riedl, *Optical Dispersion of Lead Sulfide in Infrared.* Physical Review, 1965. **140**(4A): p. 1283-&.
148. Nikolic, P.M., *Solid Solutions of Cdse and Cdte in Pbte and Their Optical Properties.* British Journal of Applied Physics, 1966. **17**(3): p. 341-&.
149. Aspnes, D.E. and M. Cardona, *Electro-Optic Measurements of Pbs Pbse and Pbte.* Physical Review, 1968. **173**(3): p. 714-728.
150. Massimo, M. and I.B. Cadoff, *Pb1-Xgexte Solubilities, Electrical and Optical-Properties.* Journal of Electronic Materials, 1976. **5**(6): p. 601-620.
151. Anderson, W.W., *Absorption Constant of Pb1-xSnxTe and Hg1-xCdxTe Alloys.* Infrared Physics, 1980. **20**: p. 363-373.
152. Faradzhev, F.E., *Optical-Properties of Pbse1-Xtex Solid-Solutions.* Soviet Physics Semiconductors-Ussr, 1984. **18**(11): p. 1311-1312.
153. Nikolić, P.M., *Some optical Properties of lead-tin-chalcogenide alloys.* Publications de la Faculte Delectrotechnique De L'Universite A Belgrade, 1971. **354-356**: p. 51-121.
154. Toulouse, B., F. Morales, and S. Rolland, *TEMPERATURE-DEPENDENCE OF THE ENERGY-GAP IN PBTE.* Journal De Physique, 1985. **46**(6): p. 959-964.
155. Veis, A.N., V.I. Kaidanov, Y.I. Ravich, I.A. Ryabtseva, and Y.I. Ukhanov, *Investigation of the Absorption Coefficient of Indium-doped PbTe.* Soviet Physics Semiconductors-Ussr, 1976. **10**(1): p. 62-65.
156. Bocharova, T.V., A.N. Veis, Z. Dashevsky, V.A. Kotelnikov, and R.Y. Krupitskaya, *Investigation of the Absorption Coefficient of Thin Indium-Doped PbTe Films.* Soviet Physics Semiconductors-Ussr, 1981. **15**(1): p. 103-105.
157. Kaidanov, V.I. and Y.I. Ravich, *Deep and Resonance States in a(Iv)B(Vi) Semiconductors.* Soviet Physics Uspekhi, 1985. **28**(1): p. 31-53.
158. Nemov, S.A. and Y.I. Ravich, *Thallium Dopant in Lead Chalcogenides: Investigation Methods and Peculiarities.* Physics - Uspekhi, 1998. **41**(8): p. 735-759.
159. Suzuki, N. and S. Adachi, *Optical constants of Pb1-xSnxTe alloys.* Journal of Applied Physics, 1996. **79**(4): p. 2065-2069.
160. Wang, J.F., J.J. Hu, X.C. Sun, A.M. Agarwal, L.C. Kimerling, D.R. Lim, and R.A. Synowicki, *Structural, electrical, and optical properties of thermally evaporated nanocrystalline PbTe films.* Journal of Applied Physics, 2008. **104**(5): p. 053707, 1-5.
161. Miller, E., I. Cadoff, and K. Komarek, *Interrelation of Electronic Properties and Defect Equilibria in Pbte.* Journal of Applied Physics, 1961. **32**(11): p. 2457-2465.
162. Kim, H. and M. Kaviany, *Effect of Thermal Disorder on High Figure of Merit in PbTe.* Physical Review B, 2012. **86**(4): p. 045213, 1-10.
163. Xu, L.Q., Y.P. Zheng, and J.C. Zheng, *Thermoelectric transport properties of PbTe under pressure.* Physical Review B, 2010. **82**(19): p. 195102:1-16.
164. Zemel, J.N., J.D. Jensen, and R.B. Schoolar, *Electrical and Optical Properties of Epitaxial Films of Pbs Pbse Pbte and Snte.* Physical Review, 1965. **140**(1A): p. A330-A342.
165. Laff, R.A., *Photoeffects in Lead Telluride P-N Junctions.* Journal of Applied Physics, 1965. **36**(10): p. 3324-3329.
166. Saakyan, V.A., E.D. Devyatkova, and I.A. Smirnov, *Determining Forbidden Gap Width of PbTe at HIgh Temperatures.* Soviet Physics Solid State,Ussr, 1966. **7**(10): p. 2541-2542.

167. Veis, A.N., *Investigation of the Fundamental Absorption-Coefficient of N-Type PbTe at High Temperatures.* Soviet Physics Semiconductors-Ussr, 1982. **16**(6): p. 724-725.
168. Vesnin, Y.I. and Y.V. Shubin, *On the Constancy of the Average Crystal-Lattice Parameter in the Decay of the Solid-Solutions Pbs - Pbte.* Materials Research Bulletin, 1984. **19**(10): p. 1355-1359.
169. Tan, G., F. Shi, J.W. Doak, H. Sun, L.-D. Zhao, P. Wang, C. Uher, C. Wolverton, V.P. Dravid, and M.G. Kanatzidis, *Extraordinary role of Hg in enhancing the thermoelectric performance of p-type SnTe.* Energy & Environmental Science, 2015. **8**(1): p. 267-277.
170. Tan, G., L.-D. Zhao, F. Shi, J.W. Doak, S.-H. Lo, H. Sun, C. Wolverton, V.P. Dravid, C. Uher, and M.G. Kanatzidis, *High Thermoelectric Performance of p-Type SnTe via a Synergistic Band Engineering and Nanostructuring Approach.* Journal of the American Chemical Society, 2014.
171. Globus, T.R. and A.O. Olesk, *OPTICAL-ABSORPTION SPECTRA AND ENERGY-BAND STRUCTURE OF PBSE.* Soviet Physics Semiconductors-Ussr, 1985. **19**(4): p. 385-388.
172. Smirnov, I.A., B.Y. Moizhes, and E.D. Nensberg, *THE EFFECTIVE CARRIER MASS IN LEAD SELENIDE.* Soviet Physics-Solid State, 1961. **2**(8): p. 1793-1804.
173. Veis, A.N., R.F. Kuteinikov, S.A. Kumzerov, and Y.I. Ukhanov, *Investigation of Valence Band-Structure of Lead Selenide by Optical Methods.* Soviet Physics Semiconductors-Ussr, 1976. **10**(11): p. 1320-1321.
174. Shen, W.Z., H.F. Yang, L.F. Jiang, K. Wang, G. Yu, H.Z. Wu, and P.J. McCann, *Band gaps, effective masses and refractive indices of PbSrSe thin films: Key properties for mid-infrared optoelectronic device applications.* Journal of Applied Physics, 2002. **91**(1): p. 192-198.
175. Lambrecht, A., N. Herres, B. Spanger, S. Kuhn, H. Bottner, M. Tacke, and J. Evers, *MOLECULAR-BEAM EPITAXY OF PB1-XSRXSE FOR THE USE IN IR DEVICES.* Journal of Crystal Growth, 1991. **108**(1-2): p. 301-308.
176. Majumdar, A., H.Z. Xu, F. Zhao, J.C. Keay, L. Jayasinghe, S. Khosravani, X. Lu, V. Kelkar, and Z. Shi, *Bandgap energies and refractive indices of Pb1-xSrxSe.* Journal of Applied Physics, 2004. **95**(3): p. 939-942.
177. Vinogradova, M.N., I.M. Rudnik, L.M. Sysoeva, and N.V. Kolomoets, *Investigation of Thermoelectric Power and Carrier Mobility in p-type PbSe.* Soviet Physics Semiconductors-Ussr, 1969. **2**(7): p. 892-893.
178. Wang, H., A.D. LaLonde, Y. Pei, and G.J. Snyder, *The Criteria for Beneficial Disorder in Thermoelectric Solid Solutions.* Advanced Functional Materials, 2013. **23**(12): p. 1586-1596.
179. Akai, H., *Electronic-structure of Ni-Pd Alloys Calculated by the Self-consistent KKR-CPA Method.* Journal of the Physical Society of Japan, 1982. **51**(2): p. 468-474.
180. Akai, H., *Fast Korringa-Kohn-Rostoker coherent potential approximation and its application to FCC Ni-Fe systems.* Journal of Physics: Condensed Matter, 1989. **1**(43): p. 8045.
181. Schr√∂ter, M., H. Ebert, H. Akai, P. Entel, E. Hoffmann, and G.G. Reddy, *First-principles investigations of atomic disorder effects on magnetic and structural instabilities in transition-metal alloys.* Physical Review B, 1995. **52**(1): p. 188-209.
182. Heremans, J.P., B. Wiendlocha, and A.M. Chamoire, *Resonant levels in bulk thermoelectric semiconductors.* Energy & Environmental Science, 2012. **5**: p. 5510-5530.

183. Jaworski, C.M., B. Wiendlocha, V. Jovovic, and J.P. Heremans, *Combining alloy scattering of phonons and resonant electronic levels to reach a high thermoelectric figure of merit in PbTeSe and PbTeS alloys.* Energy & Environmental Science, 2011. **4**(10): p. 4155-4162.
184. Jaworski, C.M., J. Tobola, E.M. Levin, K. Schmidt-Rohr, and J.P. Heremans, *Antimony as an amphoteric dopant in lead telluride.* Physical Review B, 2009. **80**(12): p. -.
185. HERMAN, F., R. KORTUM, L., I. ORTENBURGER, B., and J.P. VAN DYKE, *RELATIVISTIC BAND STRUCTURE OF GeTe, SnTe, PbTe, PbSe, AND PbS.* J. Phys. Colloques, 1968. **29**(C4): p. C4-62-C4-77.
186. Vedeneev, V.P., S.P. Krivoruchko, and E.P. Sabo, *Tin telluride based thermoelectrical alloys.* Semiconductors, 1998. **32**(3): p. 241-244.
187. Bernick, R.L. and L. Kleinman, *ENERGY BANDS, EFFECTIVE MASSES AND G-FACTORS OF LEAD SALTS AND SNTE.* Solid State Communications, 1970. **8**(7): p. 569-&.
188. Santhanam, S. and A. Chaudhuri, *Transport properties of SnTe interpreted by means of a two valence band model.* Materials Research Bulletin, 1981. **16**(8): p. 911-917.
189. Gonzalez, P., J. Agapito, and D. Pardo, *Two-band model parameters deduced from Hall coefficient measurements in polycrystalline films of SnTe.* Journal of Physics C: Solid State Physics, 1986. **19**(6): p. 899.
190. Singh, D.J., *Thermopower OF SnTe From Boltzmann Transport Calculation.* Functional Materials Letters, 2010. **3**(4): p. 223-226.
191. Hsieh, T.H., H. Lin, J.W. Liu, W.H. Duan, A. Bansil, and L. Fu, *Topological crystalline insulators in the SnTe material class.* Nature Communications, 2012. **3**.
192. Rabe, K.M. and J.D. Joannopoulos, *Abinitio Relativistic Pseudopotential Study of the Zero-Temperature Structural-Properties of Snte and Pbte.* Physical Review B, 1985. **32**(4): p. 2302-2314.
193. Zhu, H., W. Sun, R. Armiento, P. Lazic, and G. Ceder, *Band structure engineering through orbital interaction for enhanced thermoelectric power factor.* Applied Physics Letters, 2014. **104**(8): p. 082107.
194. Khokhlov, D., L. Ryabova, A. Nicorici, V. Shklover, S. Ganichev, S. Danilov, and V. Bel'kov, *Terahertz photoconductivity of Pb1−xSnxTe(In).* Applied Physics Letters, 2008. **93**(26): p. -.
195. Khokhlov, D.R., I.I. Ivanchik, S.N. Raines, D.M. Watson, and J.L. Pipher, *Performance and spectral response of Pb1−xSnxTe(In) far-infrared photodetectors.* Applied Physics Letters, 2000. **76**(20): p. 2835-2837.
196. Gumenjuk-Sichevskaya, J.V. and F.F. Sizov, *Currents in narrow-gap photodiodes.* Semiconductor Science and Technology, 1999. **14**(12): p. 1124-1131.
197. Xu, S.Y., C. Liu, N. Alidoust, M. Neupane, D. Qian, I. Belopolski, J.D. Denlinger, Y.J. Wang, H. Lin, L.A. Wray, G. Landolt, B. Slomski, J.H. Dil, A. Marcinkova, E. Morosan, Q. Gibson, R. Sankar, F.C. Chou, R.J. Cava, A. Bansil, and M.Z. Hasan, *Observation of a topological crystalline insulator phase and topological phase transition in Pb1-xSnxTe.* Nature Communications, 2012. **3**.
198. Safdar, M., Q.S. Wang, M. Mirza, Z.X. Wang, K. Xu, and J. He, *Topological Surface Transport Properties of Single-Crystalline SnTe Nanowire.* Nano Letters, 2013. **13**(11): p. 5344-5349.
199. Zhang, Q., B. Liao, Y. Lan, K. Lukas, W. Liu, K. Esfarjani, C. Opeil, D. Broido, G. Chen, and Z. Ren, *High thermoelectric performance by resonant dopant indium in nanostructured SnTe.* Proceedings of the National Academy of Sciences, 2013. **110**(33): p. 13261-13266.

200. Brebrick, R.F., *Deviations from Stoichiometry and Electrical Properties in Snte.* Journal of Physics and Chemistry of Solids, 1963. **24**(1): p. 27-&.
201. Rogacheva, E. and O. Nashchekina, *Non-stoichiometry and properties of SnTe（Cd） semiconducting phase of variable composition.* physica status solidi (a), 2006. **203**(11): p. 2856-2860.
202. Story, T., M. Gorska, A. Lusakowski, M. Arciszewska, W. Dobrowolski, E. Grodzicka, Z. Golacki, and R. Galazka, *New Mechanism of f-f Exchange Interactions Controlled by Fermi Level Position.* Physical review letters, 1996. **77**: p. 3447-3450.
203. Trifonova, E. and L. Karagiozov, *On iodine behaviour in bulk crystals of PbTe and SnTe synthesized by the iodide method.* Crystal Research and Technology, 1983. **18**(3): p. 315-320.
204. Moldovanova, M., E.P. Trifonova, R. Assenov, and L. Karagiozov, *On Some Paramaters of Annealed Tin Telluride Prepared by the Iodide Method.* Physica Status Solidi-Rapid Research Letters, 1980. **58**: p. K47-50.
205. Assenov, R., V.A. Moshinikov, and D.A. Yaskov, *On the Behaviour of Iodine in PbTe and SnTe.* Physica status solidi (a), 1985. **88**: p. K27-30.
206. Wang, H., E. Schechtel, Y. Pei, and G.J. Snyder, *High Thermoelectric Efficiency of n-type PbS.* Advanced Energy Materials, 2013. **3**(4): p. 488-495.
207. Chen, Y., M.D. Nielsen, Y.-B. Gao, T.-J. Zhu, X. Zhao, and J.P. Heremans, *SnTe-AgSbTe2 Thermoelectric Alloys.* Advanced Energy Materials, 2012. **2**(1): p. 58-62.
208. Han, M.K., J. Androulakis, S.J. Kim, and M.G. Kanatzidis, *Lead-Free Thermoelectrics: High Figure of Merit in p-type AgSnmSbTem+ 2.* Advanced Energy Materials, 2012. **2**(1): p. 157-161.
209. Wagner, M., *Simulation of thermoelectric devices.* These de doctorat, Universität Wien, 2007.
210. Rowe, D.M., *CRC Handbook of Thermoelectrics*. 2010: Taylor & Francis.
211. Rogers, L.M., *HALL MOBILITY AND THERMOELECTRIC POWER OF P-TYPE LEAD TELLURIDE.* British Journal of Applied Physics, 1967. **18**(9): p. 1227-&.
212. Uher, C., J. Yang, S. Hu, D.T. Morelli, and G.P. Meisner, *Transport properties of pure and doped MNiSn (M =Zr, Hf).* Physical Review B, 1999. **59**(13): p. 8615-8621.
213. Culp, S.R., J.W. Simonson, S.J. Poon, V. Ponnambalam, J. Edwards, and T.M. Tritt, *(Zr,Hf)Co(Sb,Sn) half-Heusler phases as high-temperature (>700°C)p-type thermoelectric materials.* Applied Physics Letters, 2008. **93**(2): p. 022105.
214. Lee, P.-J. and L.-S. Chao, *High-temperature thermoelectric properties of Ti0.5(ZrHf)0.5−xNbxNi0.9Pd0.1Sn0.98Sb0.02 half-Heusler alloys.* Journal of Alloys and Compounds, 2010. **504**(1): p. 192-196.
215. Shen, Q., L. Chen, T. Goto, T. Hirai, J. Yang, G.P. Meisner, and C. Uher, *Effects of partial substitution of Ni by Pd on the thermoelectric properties of ZrNiSn-based half-Heusler compounds.* Applied Physics Letters, 2001. **79**(25): p. 4165-4167.
216. Koehne, M., T. Graf, H.J. Elmers, and C. Felser, *Semi-heusler/heusler alloys having tailored phase separation*, 2011, Google Patents.
217. Sakurada, S., N. Shutoh, and S. Hirono, *thermoelectric material having a higher ZT value, ZT value is "dimensionless figure of merit" and therefore has higher thermoelectric conversion efficiency; specified metallic compound with little or no toxic metals such as lead*, 2010, Google Patents.
218. Shutoh, N., S. Sakurada, N. Kondo, and N. Takezawa, *Thermoelectric material and thermoelectric element*, 2012, Google Patents.

219. Krez, J., J. Schmitt, G. Jeffrey Snyder, C. Felser, W. Hermes, and M. Schwind, *Optimization of the carrier concentration in phase-separated half-Heusler compounds.* Journal of Materials Chemistry A, 2014. **2**(33): p. 13513-13518.
220. Xie, W., A. Weidenkaff, X. Tang, Q. Zhang, J. Poon, and T. Tritt, *Recent Advances in Nanostructured Thermoelectric Half-Heusler Compounds.* Nanomaterials, 2012. **2**(4): p. 379-412.
221. Tritt, T.M. and M.A. Subramanian, *Thermoelectric Materials, Phenomena, and Applications: A Bird's Eye View.* MRS Bulletin, 2006. **31**(03): p. 188-198.
222. Tritt, T.M., *Recent Trends in Thermoelectric Materials Research II*. 2001, San Diego, CA, USA: Academic Press.
223. Graf, T., C. Felser, and S.S.P. Parkin, *Simple rules for the understanding of Heusler compounds.* Progress in Solid State Chemistry, 2011. **39**(1): p. 1-50.
224. Xie, H., H. Wang, Y. Pei, C. Fu, X. Liu, G.J. Snyder, X. Zhao, and T. Zhu, *Beneficial Contribution of Alloy Disorder to Electron and Phonon Transport in Half-Heusler Thermoelectric Materials.* Advanced Functional Materials, 2013. **23**(41): p. 5123-5130.
225. Liu, Y., A. Page, P. Sahoo, H. Chi, C. Uher, and P.F.P. Poudeu, *Electronic and phonon transport in Sb-doped Ti0.1Zr0.9Ni1+xSn0.975Sb0.025 nanocomposites.* Dalton Transactions, 2014. **43**(21): p. 8094-8101.
226. Yan, X., G. Joshi, W. Liu, Y. Lan, H. Wang, S. Lee, J.W. Simonson, S.J. Poon, T.M. Tritt, G. Chen, and Z.F. Ren, *Enhanced Thermoelectric Figure of Merit of p-Type Half-Heuslers.* Nano Letters, 2011. **11**(2): p. 556-560.
227. Takas, N., P. Sahoo, D. Misra, H. Zhao, N. Henderson, K. Stokes, and P.P. Poudeu, *Effects of Ir Substitution and Processing Conditions on Thermoelectric Performance of p-Type Zr0.5Hf0.5Co1−x Ir x Sb0.99Sn0.01 Half-Heusler Alloys.* Journal of Electronic Materials, 2011. **40**(5): p. 662-669.
228. Lee, M.-S., F.P. Poudeu, and S.D. Mahanti, *Electronic structure and thermoelectric properties of Sb-based semiconducting half-Heusler compounds.* Physical Review B, 2011. **83**(8): p. 085204.
229. Populoh, S., O. Brunko, K. Gałązka, W. Xie, and A. Weidenkaff, *Half-Heusler (TiZrHf)NiSn Unileg Module with High Powder Density.* Materials, 2013. **6**(4): p. 1326-1332.
230. Xie, H.-H., C. Yu, B. He, T.-J. Zhu, and X.-B. Zhao, *Thermoelectric Properties and n- to p-Type Conversion of Co-Doped ZrNiSn-Based Half-Heusler Alloys.* Journal of Electronic Materials, 2012. **41**(6): p. 1826-1830.
231. Horyn, A., O. Bodak, L. Romaka, Y. Gorelenko, A. Tkachuk, V. Davydov, and Y. Stadnyk, *Crystal structure and physical properties of (Ti,Sc)NiSn and (Zr,Sc)NiSn solid solutions.* Journal of Alloys and Compounds, 2004. **363**(1): p. 10-14.
232. Ouardi, S., G.H. Fecher, B. Balke, X. Kozina, G. Stryganyuk, C. Felser, S. Lowitzer, D. Ködderitzsch, H. Ebert, and E. Ikenaga, *Electronic transport properties of electron- and hole-doped semiconducting C1_b Heusler compounds: NiTi1-xMxSn (M=Sc, V).* Physical Review B, 2010. **82**(8): p. 085108.
233. Jeitschko, W., *Transition metal stannides with MgAgAs and MnCu2Al type structure.* Metallurgical Transactions, 1970. **1**(11): p. 3159-3162.
234. Yu, C., T.-J. Zhu, R.-Z. Shi, Y. Zhang, X.-B. Zhao, and J. He, *High-performance half-Heusler thermoelectric materials Hf1−x ZrxNiSn1−ySby prepared by levitation melting and spark plasma sintering.* Acta Materialia, 2009. **57**(9): p. 2757-2764.
235. Kimura, Y., T. Tanoguchi, and T. Kita, *Vacancy site occupation by Co and Ir in half-Heusler ZrNiSn and conversion of the thermoelectric properties from n-type to p-type.* Acta Materialia, 2010. **58**(13): p. 4354-4361.

236. Wang, J.L., H. Wang, G.J. Snyder, X. Zhang, Z.H. Ni, and Y.F. Chen, *Characteristics of lattice thermal conductivity and carrier mobility of undoped PbSe-PbS solid solutions.* Journal of Physics D: Applied Physics, 2013. **46**(40): p. 405301.

237. Aliev, F.G., N.B. Brandt, V.V. Moshchalkov, V.V. Kozyrkov, R.V. Skolozdra, and A.I. Belogorokhov, *Gap at the Fermi Level in the Intermetallic Vacancy System Tinisn, Zrnisn, Hfnisn.* Zeitschrift Fur Physik B-Condensed Matter, 1989. **75**(2): p. 167-171.

238. Xie, H., H. Wang, C. Fu, Y. Liu, G.J. Snyder, X. Zhao, and T. Zhu, *The intrinsic disorder related alloy scattering in ZrNiSn half-Heusler thermoelectric materials.* Sci. Rep., 2014. **4**.

239. Miyazaki, H., T. Nakano, M. Inukai, K. Soda, Y. Izumi, T. Muro, J. Kim, M. Takata, M. Matsunami, S.-i. Kimura, and Y. Nishino, *Electronic and Local Crystal Structures of the ZrNiSn Half-Heusler Thermoelectric Material.* MATERIALS TRANSACTIONS, 2014. **55**(8): p. 1209-1214.

240. Yu, C., H. Xie, C. Fu, T. Zhu, and X. Zhao, *High performance half-Heusler thermoelectric materials with refined grains and nanoscale precipitates.* Journal of Materials Research, 2012. **27**(19): p. 2457-2465.

241. Kim, S.W., Y. Kimura, and Y. Mishima, *High temperature thermoelectric properties of TiNiSn-based half-Heusler compounds.* Intermetallics, 2007. **15**(3): p. 349-356.

242. Joshi, G., T. Dahal, S. Chen, H. Wang, J. Shiomi, G. Chen, and Z. Ren, *Enhancement of thermoelectric figure-of-merit at low temperatures by titanium substitution for hafnium in n-type half-Heuslers Hf0.75−xTixZr0.25NiSn0.99Sb0.01.* Nano Energy, 2013. **2**(1): p. 82-87.

243. Ogut, S. and K.M. Rabe, *Band-Gap and Stability in the Ternary Intermetallic Compounds Nisnm (M=Ti,Zr,Hf) - a First-Principles Study.* Physical Review B, 1995. **51**(16): p. 10443-10453.

244. Koji, M., K. Akio, S. Kazuaki, Y. Mao, C. Yitao, S. Kenya, N. Hirofumi, T. Masaki, F. Shin-ichi, S. Yuji, I. Eiji, K. Keisuke, T. Junichi, and K. Takeshi, *In-gap Electronic States Responsible for the Excellent Thermoelectric Properties of Ni-based Half-Heusler Alloys.* Applied Physics Express, 2008. **1**(8): p. 081901.

245. Xie, H.H., J.L. Mi, L.P. Hu, N. Lock, M. Chirstensen, C.G. Fu, B.B. Iversen, X.B. Zhao, and T.J. Zhu, *Interrelation between atomic switching disorder and thermoelectric properties of ZrNiSn half-Heusler compounds.* Crystengcomm, 2012. **14**(13): p. 4467-4471.

246. Larson, P., S.D. Mahanti, and M.G. Kanatzidis, *Structural stability of Ni-containing half-Heusler compounds.* Physical Review B, 2000. **62**(19): p. 12754-12762.

247. Qiu, P.F., J. Yang, X.Y. Huang, X.H. Chen, and L.D. Chen, *Effect of antisite defects on band structure and thermoelectric performance of ZrNiSn half-Heusler alloys.* Applied Physics Letters, 2010. **96**(15).

248. Simonson, J.W. and S.J. Poon, *Electronic structure of transition metal-doped XNiSn and XCoSb (X = Hf,Zr) phases in the vicinity of the band gap.* Journal of Physics: Condensed Matter, 2008. **20**(25): p. 255220.

249. Do, D.T., S.D. Mahanti, and J.J. Pulikkoti, *Electronic structure of Zr-Ni-Sn systems: role of clustering and nanostructures in half-Heusler and Heusler limits.* Journal of Physics-Condensed Matter, 2014. **26**(27): p. 275501.

250. Aliev, F.G., V.V. Kozyrkov, V.V. Moshchalkov, R.V. Scolozdra, and K. Durczewski, *Narrow band in the intermetallic compounds MNiSn (M=Ti, Zr, Hf).* Zeitschrift für Physik B Condensed Matter, 1990. **80**(3): p. 353-357.

251. Johnson, C.A., K.R. Kittilstved, T.C. Kaspar, T.C. Droubay, S.A. Chambers, G.M. Salley, and D.R. Gamelin, *Mid-gap electronic states in Zn1-xMnxO.* Physical Review B, 2010. **82**(11): p. 115202.
252. Qiu, P., X. Huang, X. Chen, and L. Chen, *Enhanced thermoelectric performance by the combination of alloying and doping in TiCoSb-based half-Heusler compounds.* Journal of Applied Physics, 2009. **106**(10): p. 103703.
253. Madelung, O., *Semiconductors: Data Handbook*. 2004: Springer Science & Business Media.
254. Nolas G. S., S.J., Goldsmid H. J., *Thermoelectrics: Basic Principles and New Materials Developments*. 2001: Springer Science & Business Media.
255. M, S., *Nichtparabolizitat des Valenzbandes von Bi2Te3 gegolgert adu Transporteigenschaften.* Phys. stat. sol. (b), 1975. **69**.
256. Testardi, L.R., J.N. Bierly Jr, and F.J. Donahoe, *Transport properties of p-type Bi2Te3□Sb2Te3 alloys in the temperature range 80–370°K.* Journal of Physics and Chemistry of Solids, 1962. **23**(9): p. 1209-1217.
257. Jeon, H.-W., H.-P. Ha, D.-B. Hyun, and J.-D. Shim, *Electrical and thermoelectrical properties of undoped Bi2Te3-Sb2Te3 and Bi2Te3-Sb2Te3-Sb2Se3 single crystals.* Journal of Physics and Chemistry of Solids, 1991. **52**(4): p. 579-585.
258. Plecháček, T., J. Navrátil, J. Horák, and P. Lošťák, *Defect structure of Pb-doped Bi2Te3 single crystals.* Philosophical Magazine, 2004. **84**(21): p. 2217-2228.
259. Austin, I.G., *The Optical Properties of Bismuth Telluride.* Proceedings of the Physical Society, 1958. **72**(4): p. 545.
260. Wang, S., G. Tan, W. Xie, G. Zheng, H. Li, J. Yang, and X. Tang, *Enhanced thermoelectric properties of* $Bi_2(Te_{1-x}Se_x)_3$*-based compounds as n-type legs for low-temperature power generation.* Journal of Materials Chemistry, 2012. **22**(39): p. 20943-20951.
261. Wang, H., Y.Z. Pei, A.D. LaLonde, and G.J. Snyder, *Heavily Doped p-Type PbSe with High Thermoelectric Performance: An Alternative for PbTe.* Advanced Materials, 2011. **23**(11): p. 1366-1370.
262. Madelung, O., *Semiconductors: Data Handbook*. 2004, Berlin: Springer-Verlag. p. 630.
263. Nolas, G.S., J. Sharp, and H.J. Goldsmid, *Thermoelectrics: Basic Principles and New Materials Developments*. 2001, Berlin: Springer-Verlag. p. 115, 118.
264. Mandrus, D., A. Migliori, T.W. Darling, M.F. Hundley, E.J. Peterson, and J.D. Thompson, *Electronic transport in lightly doped CoSb3.* Physical Review B, 1995. **52**(7): p. 4926-4931.
265. Hohl, H., A.P. Ramirez, C. Goldmann, G. Ernst, B. Wölfing, and E. Bucher, *Efficient dopants for ZrNiSn-based thermoelectric materials.* Journal of Physics: Condensed Matter, 1999. **11**(7): p. 1697.
266. Liu, W., K.C. Lukas, K. McEnaney, S. Lee, Q. Zhang, C.P. Opeil, G. Chen, and Z. Ren, *Studies on the Bi2Te3-Bi2Se3-Bi2S3 system for mid-temperature thermoelectric energy conversion.* Energy & Environmental Science, 2013. **6**(2): p. 552-560.
267. Poudel, B., Q. Hao, Y. Ma, Y. Lan, A. Minnich, B. Yu, X. Yan, D. Wang, A. Muto, D. Vashaee, X. Chen, J. Liu, M.S. Dresselhaus, G. Chen, and Z. Ren, *High-Thermoelectric Performance of Nanostructured Bismuth Antimony Telluride Bulk Alloys.* Science, 2008. **320**(5876): p. 634-638.
268. Yu, F., J. Zhang, D. Yu, J. He, Z. Liu, B. Xu, and Y. Tian, *Enhanced thermoelectric figure of merit in nanocrystalline Bi2Te3 bulk.* Journal of Applied Physics, 2009. **105**(9): p. 094303.

269. Bahk, J.-H. and A. Shakouri, *Enhancing the thermoelectric figure of merit through the reduction of bipolar thermal conductivity with heterostructure barriers.* Applied Physics Letters, 2014. **105**(5): p. 052106.
270. Sales, B.C., D. Mandrus, and R.K. Williams, *Filled Skutterudites Antimonides: A New Class of Thermoelectric Materials.* Science, 1996. **272**: p. 1325-1328.
271. Caillat, T., A. Borshchevsky, and J.P. Fleurial, *Properties of single crystalline semiconducting CoSb3.* Journal of Applied Physics, 1996. **80**(8): p. 4442-4449.
272. Nolas, G.S., G.A. Slack, D.T. Morelli, T.M. Tritt, and A.C. Ehrlich, *The effect of rare-earth filling on the lattice thermal conductivity of skutterudites.* Journal of Applied Physics, 1996. **79**(8): p. 4002.
273. Uher, C., *Skutterudites: Prospective Novel Thermoelectrics*, in *Semiconductors and Semimetals*. 2001. p. 139-253.
274. Nolas, G.S., J.L. Cohn, and G.A. Slack, *Effect of partial void filling on the lattice thermal conductivity of skutterudites.* Physical Review B, 1998. **58**(1): p. 164-170.
275. Pei, Y.Z., J. Yang, L.D. Chen, W. Zhang, J.R. Salvador, and J. Yang, *Improving thermoelectric performance of caged compounds through light-element filling.* Applied Physics Letters, 2009. **95**(4): p. 042101.
276. Tang, Y.L., Y.T. Qiu, L.L. Xi, X. Shi, W.Q. Zhang, L.D. Chen, S.M. Tseng, S.W. Chen, and G.J. Snyder, *Phase diagram of In-Co-Sb system and thermoelectric properties of In-containing skutterudites.* Energy & Environmental Science, 2014. **7**(2): p. 812-819.
277. Leszczynski, J., V. Da Ros, B. Lenoir, A. Dauscher, C. Candolfi, P. Masschelein, J. Hejtmanek, K. Kutorasinski, J. Tobola, R.I. Smith, C. Stiewe, and E. Muller, *Electronic band structure, magnetic, transport and thermodynamic properties of In-filled skutterudites InxCo4Sb12.* Journal of Physics D-Applied Physics, 2013. **46**(49).
278. Qin, Z., K.F. Cai, S. Chen, and Y. Du, *Preparation and electrical transport properties of In filled and Te-doped CoSb3 skutterudite.* Journal of Materials Science-Materials in Electronics, 2013. **24**(10): p. 4142-4147.
279. Tang, Y., S.W. Chen, and G.J. Snyder, *Temperature Dependent Solubility of Yb in Yb-CoSb$_3$ Skutterudite and its Effect on Preparation, Optimization and Lifetime of Thermoelectrics.* Journal of Materiomics, 2014. **1**(1).
280. Park, K.-H., I.-H. Kim, S.-M. Choi, W.-S. Seo, D.-I. Cheong, and H. Kang, *Preparation and Thermoelectric Properties of p-Type Yb-Filled Skutterudites.* Journal of Electronic Materials, 2013. **42**(7): p. 1377-1381.
281. Kuznetsov, V.L., L.A. Kuznetsova, and D.M. Rowe, *Effect of partial void filling on the transport properties of Nd x Co 4 Sb 12 skutterudites.* Journal of Physics: Condensed Matter, 2003. **15**(29): p. 5035.
282. Yu, J., W.Y. Zhao, B. Lei, D.G. Tang, and Q.J. Zhang, *Effects of Ge Dopant on Thermoelectric Properties of Barium and Indium Double-Filled p-Type Skutterudites.* Journal of Electronic Materials, 2013. **42**(7): p. 1400-1405.
283. Tang, G.D., W.C. Yang, F. Xu, and Y. He, *Synthesis and Thermoelectric Properties of In and Pr Double-Filled Skutterudites In (x) Pr (y) Co4Sb12.* Journal of Electronic Materials, 2014. **43**(2): p. 435-438.
284. Tang, G.D., D.W. Zhang, G. Chen, F. Xu, and Z.H. Wang, *Thermoelectric: properties in double-filled skutterudites InxNdyCo4Sb12.* Solid State Communications, 2012. **152**(24): p. 2193-2196.
285. Ballikaya, S. and C. Uher, *Enhanced thermoelectric performance of optimized Ba, Yb filled and Fe substituted skutterudite compounds.* Journal of Alloys and Compounds, 2014. **585**: p. 168-172.

286. Shi, X., J. Yang, J.R. Salvador, M. Chi, J.Y. Cho, H. Wang, S. Bai, J. Yang, W. Zhang, and L. Chen, *Multiple-filled skutterudites: high thermoelectric figure of merit through separately optimizing electrical and thermal transports.* J Am Chem Soc, 2011. **133**(20): p. 7837-46.
287. Rogl, G., A. Grytsiv, P. Rogl, E. Bauer, M. Hochenhofer, R. Anbalagan, R.C. Mallik, and E. Schafler, *Nanostructuring of p- and n-type skutterudites reaching figures of merit of approximately 1.3 and 1.6, respectively.* Acta Materialia, 2014. **76**: p. 434-448.
288. Yang, X.-q., P.-c. Zhai, L.-s. Liu, and Q.-j. Zhang, *Thermodynamic and mechanical properties of crystalline CoSb3: A molecular dynamics simulation study.* Journal of Applied Physics, 2011. **109**(12): p. 123517.
289. Ravi, V., S. Firdosy, T. Caillat, B. Lerch, A. Calamino, R. Pawlik, M. Nathal, A. Sechrist, J. Buchhalter, and S. Nutt, *Mechanical Properties of Thermoelectric Skutterudites.* AIP Conference Proceedings, 2008. **969**(1): p. 656-662.
290. Yang, J. and F.R. Stabler, *Automotive Applications of Thermoelectric Materials.* Journal of Electronic Materials, 2009. **38**(7): p. 1245-1251.
291. Geng, H., X. Meng, H. Zhang, and J. Zhang, *Lattice thermal conductivity of filled skutterudites: An anharmonicity perspective.* Journal of Applied Physics, 2014. **116**(16): p. 163503.
292. Li, W. and N. Mingo, *Thermal conductivity of fully filled skutterudites: Role of the filler.* Physical Review B, 2014. **89**(18).
293. Nolas, G.S., G. Fowler, and J. Yang, *Assessing the role of filler atoms on the thermal conductivity of filled skutterudites.* Journal of Applied Physics, 2006. **100**(4): p. 043705.
294. Svane, A., N.E. Christensen, M. Cardona, A.N. Chantis, M. van Schilfgaarde, and T. Kotani, *Quasiparticle self-consistent GW calculations for PbS, PbSe, and PbTe: Band structure and pressure coefficients.* Physical Review B, 2010. **81**(24): p. 245120:1-10.
295. Parker, D., X. Chen, and D.J. Singh, *High Three-Dimensional Thermoelectric Performance from Low-Dimensional Bands.* Physical Review Letters, 2013. **110**(14): p. 146601.
296. Caillat, T., A. Borshchevsky, and J.P. Fleurial, *Preparation and thermoelectric properties of p- and n-type CoSb3.* AIP Conference Proceedings, 1994. **316**(1): p. 58-61.
297. Morelli, D.T., G.P. Meisner, B. Chen, S. Hu, and C. Uher, *Cerium Filling and Doping of Cobalt Triantimonide.* Physical Review B, 1997. **56**: p. 7376-7383.
298. Pei, Y.Z., S.Q. Bai, X.Y. Zhao, W. Zhang, and L.D. Chen, *Thermoelectric properties of EuyCo4Sb12 filled skutterudites.* Solid State Sciences, 2008. **10**(10): p. 1422-1428.
299. Salvador, J.R., J. Yang, H. Wang, and X. Shi, *Double-filled skutterudites of the type Yb[sub x]Ca[sub y]Co[sub 4]Sb[sub 12]: Synthesis and properties.* Journal of Applied Physics, 2010. **107**(4): p. 043705.
300. Puyet, M., B. Lenoir, A. Dauscher, P. Pécheur, C. Bellouard, J. Tobola, and J. Hejtmanek, *Electronic, transport, and magnetic properties of CaxCo4Sb12 partially filled skutterudites.* Physical Review B, 2006. **73**(3).
301. Young, D.L., T.J. Coutts, and V.I. Kaydanov, *Density-of-states effective mass and scattering parameter measurements by transport phenomena in thin films.* Review of Scientific Instruments, 2000. **71**(2): p. 462-466.
302. Kajikawa, Y., *Analysis of high-temperature thermoelectric properties of p-type CoSb3 within a two-valence-band and two-conduction-band model.* Journal of Applied Physics, 2014. **115**(20): p. -.

303. Kajikawa, Y., *Refined analysis of the transport properties of Co1−xNixSb3 according to a model including a deep donor level and the second lowest valleys of the conduction band.* Journal of Alloys and Compounds, 2015. **621**(0): p. 170-178.

304. Liu, W.-S., L.-D. Zhao, B.-P. Zhang, H.-L. Zhang, and J.-F. Li, *Enhanced thermoelectric property originating from additional carrier pocket in skutterudite compounds.* Applied Physics Letters, 2008. **93**(4): p. -.

305. Puyet, M., A. Dauscher, B. Lenoir, M. Dehmas, C. Stiewe, E. Müller, and J. Hejtmanek, *Beneficial effect of Ni substitution on the thermoelectric properties in partially filled CayCo4−xNixSb12 skutterudites.* Journal of Applied Physics, 2005. **97**(8): p. -.

306. Puyet, M., A. Dauscher, B. Lenoir, C. Bellouard, C. Stiewe, E. Müller, J. Hejtmanek, and J. Tobola, *Influence of Ni on the thermoelectric properties of the partially filled calcium skutterudites CayCo4−xNixSb12.* Physical Review B, 2007. **75**(24): p. 245110.

307. Nagamoto, Y., K. Tanaka, and T. Koyanagi. *Transport properties of heavily doped n-type CoSb3*. in *Thermoelectrics, 1998. Proceedings ICT 98. XVII International Conference on*. 1998.

308. Chaput, L., P. Pecheur, J. Tobola, and H. Scherrer, *Transport in doped skutterudites: Ab initio electronic structure calculations.* Physical Review B, 2005. **72**(8).

309. Ackermann, J. and A. Wold, *The preparation and characterization of the cobalt skutterudites CoP3, CoAs3 and CoSb3.* Journal of Physics and Chemistry of Solids, 1977. **38**(9): p. 1013-1016.

310. Kliche, G. and H.D. Lutz, *Temperature dependence of the FIR reflection spectra of the skutterudites CoAs3 and CoSb3.* Infrared Physics, 1984. **24**(2–3): p. 171-177.

311. Lutz, H.D. and G. Kliche, *Far-Infrared Reflection Spectra, Optical and Dielectric Constants, Effective Charges, and Lattice Dynamics of the Skutterudites CoP3, CoAs3, and CoSb3.* physica status solidi (b), 1982. **112**(2): p. 549-557.

312. Ni, G., *Photoacoustic measurements of bandgaps of thermoelectric materials*. Mechanical Engineering. Master of Science. 2014, Massachusetts Institute of Technology

Massachusetts Institute of Technology.

313. Slack, G.A. and V.G. Tsoukala, *Some Properties of Semiconducting Irsb3.* Journal of Applied Physics, 1994. **76**(3): p. 1665-1671.

314. Matsunami, M., H. Okamura, K. Senoo, S. Nagano, C. Sekine, I. Shirotani, H. Sugawara, H. Sato, and T. Nanba, *Optical Conductivity and Electronic Structures in Ce-Filled Skutterudites.* Journal of the Physical Society of Japan, 2008. **77**(Suppl.A): p. 315-317.

315. Anno, H., K. Matsubara, Y. Notohara, T. Sakakibara, and H. Tashiro, *Effects of doping on the transport properties of CoSb3.* Journal of Applied Physics, 1999. **86**(7): p. 3780-3786.

316. Dyck, J.S., W. Chen, C. Uher, L. Chen, X. Tang, and T. Hirai, *Thermoelectric properties of the n-type filled skutterudite Ba0.3Co4Sb12 doped with Ni.* Journal of Applied Physics, 2002. **91**(6): p. 3698-3705.

317. Smith, S.D., T.S. Moss, and K.W. Taylor, *The energy-dependence of electron mass in indium antimonide determined from measurements of the infrared Faraday effect.* Journal of Physics and Chemistry of Solids, 1959. **11**(1–2): p. 131-139.

318. Cardona, M., *Electron Effective Masses of InAs and GaAs as a Function of Temperature and Doping.* Physical Review, 1961. **121**(3): p. 752-758.
319. Raymond, A., J.L. Robert, and C. Bernard, *The electron effective mass in heavily doped GaAs.* Journal of Physics C: Solid State Physics, 1979. **12**(12): p. 2289.
320. Dixon, J.R. and H.R. Riedl, *Electric-Susceptibility Hole Mass of Lead Telluride.* Physical Review, 1965. **138**(3A): p. A873-A881.
321. Dionne, G. and J.C. Woolley, *Optical Properties of Some Pb1-Xsnxte Alloys Determined from Infrared Plasma Reflectivity Measurements.* Physical Review B, 1972. **6**(10): p. 3898-3913.
322. Seiler, D.G., R.R. Galazka, and W.M. Becker, *Band Structure of HgSe: Band Parameter Determinations from Effective-Mass Data, and Concentration Dependence and Anisotropy of Beating Effects in the Shubnikov-de Haas Oscillations.* Physical Review B, 1971. **3**(12): p. 4274-4285.
323. Harman, T.C., *Galvano-thermomagnetic effects in semiconductors and semimetals—IV. mercury selenide.* Journal of Physics and Chemistry of Solids, 1964. **25**(9): p. 931-940.
324. Arushanov, E., M. Respaud, H. Rakoto, J.M. Broto, and T. Caillat, *Shubnikov-de Haas oscillations in CoSb3 single crystals.* Physical Review B, 2000. **61**(7): p. 4672-4676.
325. Young, D.L., T.J. Coutts, V.I. Kaydanov, A.S. Gilmore, and W.P. Mulligan, *Direct measurement of density-of-states effective mass and scattering parameter in transparent conducting oxides using second-order transport phenomena.* Journal of Vacuum Science & Technology A, 2000. **18**(6): p. 2978-2985.
326. Orlov, V.G. and G.S. Sergeev, *The key role of charge carriers scattering on polar optical phonons in semiconductors for thermoelectric energy conversion.* Solid State Communications, 2013. **174**(0): p. 34-37.
327. Pshenaĭ-Severin, D.A. and M.I. Fedorov, *Effect of the band structure on the thermoelectric properties of a semiconductor.* Physics of the Solid State, 2007. **49**(9): p. 1633-1637.
328. Dumke, W.P., M.R. Lorenz, and G.D. Pettit, *Intraband and Interband Free-Carrier Absorption and Fundamental Absorption Edge in N-Type Inp.* Physical Review B, 1970. **1**(12): p. 4668-&.
329. Spitzer, W. and H.Y. Fan, *Infrared Absorption in n-Type Silicon.* Physical Review, 1957. **108**(2): p. 268-271.
330. Haga, E. and H. Kimura, *Free-Carrier Infrared Absorption in III-V Semiconductors IV. Inter-Conduction Band Transitions.* Journal of the Physical Society of Japan, 1964. **19**(9): p. 1596-1606.
331. Tang, Y., S.-w. Chen, and G.J. Snyder, *Temperature dependent solubility of Yb in Yb–CoSb3 skutterudite and its effect on preparation, optimization and lifetime of thermoelectrics.* Journal of Materiomics, 2015. **1**(1): p. 75-84.
332. Zhou, A., L.S. Liu, P.C. Zhai, W.Y. Zhao, and Q.J. Zhang, *Electronic Structures and Transport Properties of Single-Filled CoSb3.* Journal of Electronic Materials, 2010. **39**(9): p. 1832-1836.
333. Alleno, E., E. Zehani, and O. Rouleau, *Metallurgical and thermoelectric properties in Co1-xPdxSb3 and Co(1-x)Ni(x)Sb3 revisited.* Journal of Alloys and Compounds, 2013. **572**: p. 43-48.
334. Shi, X., W. Zhang, L. Chen, J. Yang, and C. Uher, *Theoretical study of the filling fraction limits for impurities in CoSb3.* Physical Review B, 2007. **75**(23).
335. Yang, J., L. Xi, W. Zhang, L.D. Chen, and J.H. Yang, *Electrical Transport Properties of Filled CoSb3 Skutterudites: A Theoretical Study.* Journal of Electronic Materials, 2009. **38**(7): p. 1397-1401.

336. Perdew, J.P., K. Burke, and M. Ernzerhof, *Generalized Gradient Approximation Made Simple.* Physical Review Letters, 1996. **77**(18): p. 3865-3868.
337. Giannozzi, P., S. Baroni, N. Bonini, M. Calandra, R. Car, C. Cavazzoni, D. Ceresoli, G.L. Chiarotti, M. Cococcioni, I. Dabo, A. Dal Corso, S. De Gironcoli, S. Fabris, G. Fratesi, R. Gebauer, U. Gerstmann, C. Gougoussis, A. Kokalj, M. Lazzeri, L. Martin-Samos, N. Marzari, F. Mauri, R. Mazzarello, S. Paolini, A. Pasquarello, L. Paulatto, C. Sbraccia, S. Scandolo, G. Sclauzero, A. Seitsonen, P., A. Smogunov, P. Umari, and R.M. Wentzcovitch, *QUANTUM ESPRESSO: a modular and open-source software project for quantum simulations of materials.* Journal of Physics: Condensed Matter, 2009. **21**(39): p. 395502.
338. Agapito, L.A., A. Ferretti, A. Calzolari, S. Curtarolo, and M. Buongiorno Nardelli, *Effective and accurate representation of extended Bloch states on finite Hilbert spaces.* Physical Review B, 2013. **88**(16): p. 165127.
339. Agapito, L.A., S. Ismail-Beigi, S. Curtarolo, and M. Buongiorno Nardelli, *Accurate tight-binding Hamiltonian matrices from ab-initio calculations.* In preparation, 2015.
340. WanT code by A. Ferretti, B. Bonferroni, A. Calzolari, and M. Buongiorno Nardelli, (http://www.wannier-transport.org)
341. Kokalj, A., *Computer graphics and graphical user interfaces as tools in simulations of matter at the atomic scale.* Computational Materials Science, 2003. **28**(2): p. 155-168.
342. Wang, J., X.C. Liu, S.Q. Xia, and X.T. Tao, *Ca1-xRExAg1-ySb (RE = La, Ce, Pr, Nd, Sm; 0 <= x <= 1; 0 <= y <= 1): Interesting Structural Transformation and Enhanced High-Temperature Thermoelectric Performance.* Journal of the American Chemical Society, 2013. **135**(32): p. 11840-11848.
343. Guo, K., Q.G. Cao, and J.T. Zhao, *Zintl phase compounds AM(2)Sb(2) (A=Ca, Sr, Ba, Eu, Yb; M=Zn, Cd) and their substitution variants: a class of potential thermoelectric materials.* Journal of Rare Earths, 2013. **31**(11): p. 1029-1038.
344. Bhardwaj, A. and D.K. Misra, *Enhancing thermoelectric properties of a p-type Mg3Sb2- based Zintl phase compound by Pb substitution in the anionic framework.* Rsc Advances, 2014. **4**(65): p. 34552-34560.
345. Zevalkink, A., J. Swallow, and G.J. Snyder, *Thermoelectric properties of Zn-doped Ca5In2Sb6.* Dalton Trans., 2013. **42**: p. 9713-9719.
346. Zevalkink, A., W.G. Zeier, G. Pomrehn, E. Schechtel, W. Tremelb, and G.J. Snydera, *Thermoelectric properties of Sr3GaSb3 – a chain-forming Zintl compound.* Energy Environ. Sci., 2012. **5**: p. 9121-9128.
347. Brown, S.R., S.M. Kauzlarich, F. Gascoin, and G.J. Snyder, *Yb14MnSb11: New High Efficiency Thermoelectric Material for Power Generation.* Chemistry of Materials, 2006. **18**(7): p. 1873-1877.
348. Ohno, S., A. Zevalkink, Y. Takagiwa, S.K. Bux, and G.J. Snyder, *Thermoelectric properties of the Yb9Mn4.2−xZnxSb9 solid solutions.* Journal of Materials Chemistry A, 2014. **2**(20): p. 7478.
349. Snyder, G.J. and E.S. Toberer, *Complex Thermoelectric Materials.* Nature Mater, 2008. **7**: p. 105-114.
350. Toberer, E.S., A.F. May, and G.J. Snyder, *Zintl Chemistry for Designing High Efficiency Thermoelectric Materials.* Chemistry of Materials, 2010. **22**(3): p. 624-634.
351. Zevalkink, A., S. Chanakian, U. Aydemir, A. Ormeci, G. Pomrehn, S. Bux, J.-P. Fleurial, and J. Snyder, *Thermoelectric properties and electronic structure of the Zintl phase Sr5In2Sb6 and solid solution Ca5-xSrxIn2Sb6.* Journal of Physics: Condensed Matter, 2015. **27**(1).

352. Gnutzmann, U. and K. Clausecker, *Theory of direct optical transitions in an optical indirect semiconductor with a superlattice structure.* Applied Physics 1974. **3**(1): p. 9-14.
353. Schmitt, J., Z.M. Gibbs, G.J. Snyder, and C. Felser, *Resolving the true band gap of ZrNiSn half-Heusler thermoelectric materials.* Mater. Horiz., 2014. **2**(1): p. 68-75.
354. Pei, Y., X. Shi, A. LaLonde, H. Wang, L. Chen, and G.J. Snyder, *Convergence of electronic bands for high performance bulk thermoelectrics.* Nature, 2011. **473**(7345): p. 66-9.
355. Kubelka, P. and F. Munk, *Reflection characteristics of paints.* Z. Technische Physik, 1932. **12**: p. 593-601.
356. Zevalkink, A., G.S. Pomrehn, S. Johnson, J. Swallow, Z.M. Gibbs, and G.J. Snyder, *Influence of the Triel Elements (M = Al, Ga, In) on the Transport Properties of Ca5M2Sb6 Zintl Compounds.* Chemistry of Materials, 2012. **24**(11): p. 2091-2098.
357. Park, S.-M., E.S. Choi, W. Kang, and S.-J. Kim, *Eu5In2Sb6, Eu5In2-xZnxSb6: rare earth zintl phases with narrow band gaps.* Journal of Materials Chemistry, 2002. **12**(6): p. 1839-1843.
358. Johnson, S.I., A. Zevalkink, and G.J. Snyder, *Improved thermoelectric properties in Zn-doped Ca5Ga2Sb6.* Journal of Materials Chemistry A, 2013. **1**(13): p. 4244-4249.
359. Chanakian, S., A. Zevalkink, U. Aydemir, Z.M. Gibbs, G. Pomrehn, S. Bux, J.P. Fleurial, and G.J. Snyder, *Enhanced Thermoelectric Properties of Sr5In2Sb6 via Zn-doping.* Journal of Materials Chemistry A, 2015.
360. Allgaier, R.S., *Magnetoresistance in PbS, PbSe, and PbTe at 295, 77.4, and 4.2K.* Physical Review, 1958. **112**(3): p. 828-836.
361. Mecholsky, N.A., L. Resca, I.L. Pegg, and M. Fornari, *Theory of band warping and its effects on thermoelectronic transport properties.* Physical Review B, 2014. **89**(15): p. 155131.
362. Wang, H., J.L. Wang, X.L. Cao, and G.J. Snyder, *Thermoelectric alloys between PbSe and PbS with effective thermal conductivity reduction and high figure of merit.* Journal of Materials Chemistry A, 2014. **2**(9): p. 3169-3174.
363. Korkosz, R.J., T.C. Chasapis, S.-h. Lo, J.W. Doak, Y.J. Kim, C.-I. Wu, E. Hatzikraniotis, T.P. Hogan, D.N. Seidman, C. Wolverton, V.P. Dravid, and M.G. Kanatzidis, *High ZT in p-Type (PbTe)1–2x(PbSe)x(PbS)x Thermoelectric Materials.* Journal of the American Chemical Society, 2014.
364. Lee, Y., S.-H. Lo, J. Androulakis, C.-I. Wu, L.-D. Zhao, D.-Y. Chung, T.P. Hogan, V.P. Dravid, and M.G. Kanatzidis, *High-Performance Tellurium-Free Thermoelectrics: All-Scale Hierarchical Structuring of p-Type PbSe–MSe Systems (M = Ca, Sr, Ba).* Journal of the American Chemical Society, 2013.
365. Zhang, Q., F. Cao, W. Liu, K. Lukas, B. Yu, S. Chen, C. Opeil, D. Broido, G. Chen, and Z. Ren, *Heavy Doping and Band Engineering by Potassium to Improve the Thermoelectric Figure of Merit in p-Type PbTe, PbSe, and PbTe1–ySey.* Journal of the American Chemical Society, 2012. **134**(24): p. 10031-10038.
366. Kanatzidis, M., J. Androulakis, I. Todorov, J.Q. He, D.Y. Chung, and V. Dravid, *Thermoelectrics from Abundant Chemical Elements: High-Performance Nanostructured PbSe-PbS.* Journal of the American Chemical Society, 2011. **133**(28): p. 10920-10927.
367. Chasapis, T.C., Y. Lee, E. Hatzikraniotis, K.M. Paraskevopoulos, H. Chi, C. Uher, and M.G. Kanatzidis, *Understanding the role and interplay of heavy-hole and light-*

hole valence bands in the thermoelectric properties of PbSe. Physical Review B, 2015. **91**(8): p. 085207.

368. Jain, A., G. Hautier, C.J. Moore, S. Ping Ong, C.C. Fischer, T. Mueller, K.A. Persson, and G. Ceder, *A high-throughput infrastructure for density functional theory calculations.* Computational Materials Science, 2011. **50**(8): p. 2295-2310.
369. Kresse, G. and J. Furthmüller, *Efficiency of ab-initio total energy calculations for metals and semiconductors using a plane-wave basis set.* Computational Materials Science, 1996. **6**(1): p. 15-50.
370. Ong, S.P., W.D. Richards, A. Jain, G. Hautier, M. Kocher, S. Cholia, D. Gunter, V.L. Chevrier, K.A. Persson, and G. Ceder, *Python Materials Genomics (pymatgen): A robust, open-source python library for materials analysis.* Computational Materials Science, 2013. **68**(0): p. 314-319.
371. Fan, W.J., M.F. Li, T.C. Chong, and J.B. Xia, *Electronic properties of zinc-blende GaN, AlN, and their alloys Ga1−xAlxN.* Journal of Applied Physics, 1996. **79**(1): p. 188-194.
372. Adachi, S., *Optical dispersion relations for GaP, GaAs, GaSb, InP, InAs, InSb, AlxGa1−xAs, and In1−xGaxAsyP1−y.* Journal of Applied Physics, 1989. **66**(12): p. 6030-6040.
373. Wang, Y., H. Yin, R. Cao, F. Zahid, Y. Zhu, L. Liu, J. Wang, and H. Guo, *Electronic structure of III-V zinc-blende semiconductors from first principles.* Physical Review B, 2013. **87**(23): p. 235203.
374. Tran, F. and P. Blaha, *Accurate Band Gaps of Semiconductors and Insulators with a Semilocal Exchange-Correlation Potential.* Physical Review Letters, 2009. **102**(22): p. 226401.